

Plasmonic Enhancement of Nonlinear Optical Responses by Gold Nanorods

Jeong-Ah Lee

Dissertation submitted to the faculty of the
Virginia Polytechnic Institute and State University
in partial fulfillment of the requirements for the degree of

Doctor of Philosophy
In
Physics

James R. Heflin, Committee Chair
Hans D. Robinson, Committee Co-Chair
Jean J. Heremans
Kyungwha Park

December 15, 2016
Blacksburg, VA

Keywords: Nonlinear optics, Second harmonic generation, Gold nanoparticles, Gold nanorod,
Localized surface plasmon, Self-assembly, Thin Film, Polymer

Copyright 2016, Jeong-Ah Lee

Plasmonic Enhancement of Nonlinear Optical Responses by Gold Nanorods

Jeong-Ah Lee

Abstract

The increase in the magnitude of local electric fields through resonances of plasmonic excitations in metallic nanoparticles is a major area of current optical research. This dissertation is focused on plasmon-enhanced second harmonic generation of organic ionic self-assembled films via localized surface plasmon resonance of gold nanorods. By matching the plasmon resonance of the gold nanorods to the wavelength of the fundamental light, it is possible to greatly enhance the SHG efficiency. To demonstrate this, the surface of the gold nanorods was functionalized with a nonlinear-optical (NLO) polymer, PCBS, via the layer-by-layer method and deposited on a polymer thin film created on a glass substrate using the ionic self-assembled multilayer (ISAM) method.

The sample fabrication is divided into two parts: gold nanorod synthesis and functionalization. The gold nanorods were synthesized by the seed-mediated method with varying amounts of silver ions to control their LSPR wavelengths. The functionalization started by replacing the original thick CTAB bilayer on the surface of the gold nanorods by a thin PAH-DTC layer via dialysis. The nanorods were then alternately coated with PAH (polycation) and PCBS (NLO polyanion) up to three bilayers of PAH/PCBS. The number of polymer layers on the nanorods was chosen in consideration of the LSPR decay length (a few nm). The functionalized gold nanorods were then deposited on either PAH/PCBS or PAH/PSS ISAM films.

Characterization was performed via optical spectral measurement, zeta potential measurement, and field-emission scanning electron microscopy (FESEM). The LSPR wavelength shifted when the surrounding medium changed. It was red-shifted for each added polymer layer on the nanorod surface. However, when the functionalized nanorods were deposited on the ISAM film, the resonance peak blue-shifted. The zeta potential confirmed the proper electric charge of each polymer layer coated on the nanorods. Finally, FESEM was performed on the samples for visual inspection of the nanorod deposition and distribution after the SHG measurement was complete.

The SHG from the functionalized gold nanorods was measured using a Maker-like fringe method. In this method, second harmonic waves generated from the front and rear sides of the substrate interfere constructively and destructively when the sample is rotated with respect to the incoming pump wave. Electrical noise reduction techniques were implemented to improve the SHG signal readings. Signal processing was implemented using LabVIEW software in order to read a reliable SHG signal from the setup. The maximum tolerable fluence of the gold nanorods was determined in order to prevent optical damage. The interference fringe pattern was observed from the functionalized gold nanorods and compared with that from the conventional ISAM film. The enhancement from the gold nanorods was as high as 600 times compared to the bare films. Polarization dependent SHG measurements were conducted to ascertain the effect of coupling between p- or s-polarized fundamental incident light to the SH light. To further improve the SHG enhancement, the self-assembly method herein can be extended from a monolayer to multilayers of functionalized gold nanorods.

Plasmonic Enhancement of Nonlinear Optical Responses by Gold Nanorods

Jeong-Ah Lee

General Audience Abstract

The field of optics examines the interactions of light and matter. The most commonly observed optical phenomena are the reflection and refraction of light where the frequency of light remains unchanged. However, when light becomes intense, interesting optical phenomena occur where the frequency of the outgoing light differs from that of the incoming light. With the invention of the first working laser in 1960, many interesting nonlinear phenomena were experimentally confirmed, including second harmonic generation (SHG) which was the first nonlinear optical process to be observed. In the original SHG experiment, a visible ruby laser was illuminated into a quartz crystal which produced UV light. This demonstrated light frequency doubling corresponding to wavelength halving from 694 nm (ruby laser) to 347 nm (UV light).

Following progress in molecular engineering, many organic materials and polymers have been employed to study nonlinear optics for applications such as optical frequency conversion, electro-optic modulation, and second harmonic generation imaging microscopy. Nonetheless, the SHG conversion efficiency is very low due to phase-mismatch. This stems from frequency dispersion in a medium, where the incoming light and the generated light travel at different velocities. In the past, efforts toward enhancing the SHG conversion efficiency was focused on selecting specific crystals in which the incoming light and the second harmonic light pass through different effective path lengths in the medium.

Although the phase-matching method is the most effective method to achieve high conversion efficiency it is also important to increase the intrinsic nonlinearity of a material. A new multidisciplinary approach using the surface plasmon resonance has become an important technique for improving the

conversion efficiency. Plasmons are the collective oscillation of electrons on a metal surface. At the resonant optical frequency, the amplitude of the plasmon oscillation becomes maximized. When metallic nanoparticles are resonantly illuminated with light, the electric field can be locally intensified at the sharp boundaries of the nanoparticle. Since the intensity of SHG increases by the square of the incoming light intensity, the SHG efficiency can be greatly enhanced via surface plasmons on the metal nanoparticles.

In this dissertation, the fabrication of new optical materials incorporating gold plasmonic nanoparticles for SHG enhancement was demonstrated. The plasmonic nanomaterials were fabricated by coating the surface of gold nanorods with nonlinear polymer films and depositing them on another polymer thin film on a flat glass substrate. The enhanced SHG intensity was measured and compared with that of the conventional nonlinear polymer films alone. It was observed that the enhancement from the gold nanorods was as high as 600 times. To further improve the SHG enhancement, the surface modified gold nanorods can be extended from a single layer to multilayers on the polymer film substrate.

Acknowledgements

I would like to express my sincere gratitude to all of the amazing and wonderful people I met at Virginia Tech who helped me get through my graduate studies. First of all, I am grateful for my advisor, Dr. Randy Heflin, for his patience, kindness, and guidance during my studies. I overcame many research obstacles with his help, and my dissertation would not be the same without his caring and thoughtful revision. I would also like to thank Dr. Hans Robinson for his willingness to advise and help with my research. His expertise and critical discussions with me improved the work included in this dissertation. I acknowledge the support and participation of Dr. Kyungwha Park and Dr. Jean Heremans as the members of my committee.

I am deeply grateful for the financial support provided by the Institute of Critical Technology and Applied Science (ICTAS) and the Department of Physics. The ICTAS Doctoral fellowship allowed me to focus on coursework and research in the beginning of my graduate studies as a research assistant. The teaching assistantship I received afterwards from the Department of Physics trained me to become a better teacher and allowed me to work with amazing people—Alma Robinson and Dr. John Simonetti. Teaching physics gave me some of the biggest rewards, and I am happy that it became one of my career options. I very much enjoyed teaching the SCALE-UP courses with Alma for the past two and a half years and I will miss the grading parties with the SCALE-UP team—Alma, John and Dan Balbarin.

I would like to give thanks to Betty Wilkins and the late Chris Thomas for their kind help and efficient administration. They were kind and efficient. I am also very thankful for the members of the Physics Department Machine Shop—Scott Allen, Ron Stables, and John Miller. They were very helpful and handy when I needed to build small and specialized lab equipment. Travis Heath updated my “ancient” lab computer to a new one, which helped tremendously in collecting data. Sherri Collins, Michele Strauss, and Katrina Loan helped me with purchases regarding lab supplies.

My colleagues in the Heflin group and the Robinson group deserve my thanks. Jonathan Metzman was understanding and cooperative when we needed to share the optical table and the

room under darkness. Panupon Samaimongkol and Erich See readily shared their lab knowledge with me and made themselves available to assist. I enjoyed the get-togethers with Kirby Myers and Kelly Mccutcheon to share our trials and triumphs in graduate school. My collaborators at the University of Illinois, Urbana-Champaign, were very welcoming during my visit to learn the gold nanorod synthesis. Dr. Kathy Murphy sponsored my visit and organized my training with Joshua Hinman who demonstrated the nanorod synthesis to me.

Even from thousands of miles away, I felt the strong support of my family. My Mom and Dad always showed their faith in me and inspired me to continue. My sister, Hyunee, provided close companionship and selflessly offered her time to chat and commiserate. I hope that I will be able to visit them more often now that I am finished.

Finally, I am deeply and sincerely grateful to Michael Fraser for his unlimited and boundless help and support throughout my entire Ph.D. Without his help, it would not have been to this level of satisfaction. He helped me with numerous computer simulations and always made himself available for the discussion of my research. There were countless days and nights when he volunteered to help me with various problems regarding lasers, optical setups, experiments, etc. He gave me encouragement and moral support to finish my studies and dissertation, and I cannot express my gratitude enough. His contributions toward the improvement of my dissertation cannot be overlooked. Escaping outside the lab, I enjoyed our travel adventures together. I am very fortunate to spend all my years in graduate school with him and wish that our science discussions and whimsical travels continue.

I am also thankful for my birds—Kiwi and the late Mango. Their playful companionship and entertaining behaviors made me smile even after a hard day at lab.

Contents

List of Figures	xi
List of Tables	xvi
Acronyms and Abbreviations	xvii
Chapter 1 Introduction	1
1.1 Background and Motivation	1
1.2 Research Goals.....	8
1.3 Dissertation Outline	10
References.....	12
Chapter 2 Background and Literature Review.....	19
2.1 Nonlinear Optics	19
2.2 Second Harmonic Generation	21
2.3 Sum- and Difference-Frequency Generation	23
2.4 Second-Order Nonlinear Susceptibility	27
2.5 Coupled Wave Equation for Efficiency of Second Harmonic Generation	32
2.6 Nonlinear Optical Materials.....	36
2.6.1 Inorganic Materials for SHG	36
2.6.2 Organic Molecules for SHG	37
2.6.3 Organic Crystals.....	37
2.6.4 Poled Polymers	42
2.6.5 Langmuir-Blodgett Film	44
2.6.6 Covalent Self-Assembled Systems	46

2.6.7 Ionic Self-Assembled Multilayer (ISAM) Technique	47
2.6.8 Hybrid Covalent/Ionic Deposition.....	51
2.7 Applications of Second Order Nonlinear Optics	53
2.8 Plasmonics	54
2.9 Colloidal Gold.....	56
2.9.1 Historical Background	57
2.9.2 Optical Properties of Gold Nanorods.....	58
2.9.3 Synthesis of Gold Nanorods	61
2.10 Applications of Nanoparticles in Plasmonics	63
References.....	68
Chapter 3 Sample Fabrication Methods.....	81
3.1 Second-order NLO ISAM Film Deposition Process	82
3.2 Gold Nanorod Synthesis: Seed-mediated Growth Method.....	84
3.3 Hydroquinone Reduction of the Growth Solution	86
3.3.1 Materials	86
3.3.2 Solution Preparation.....	88
3.3.3 Gold Nanorod Synthesis Procedure	89
3.3.4 Characterization of Gold Nanorods	92
3.4 Functionalized Gold Nanorod Synthesis	95
3.4.1 PAH-DTC Preparation.....	95
3.4.2 CTAB Replacement with PAH-DTC via Dialysis.....	97
3.4.3 PCBS/PAH Functionalized Gold Nanorods	105
3.5 Functionalized Gold Nanorods on ISAM Film.....	114
3.5.1 Nanorod Density of PSS-coated GNRs on ISAM film.....	114
3.5.2 Nanorod Density of PAH/PCBS Functionalized GNRs on ISAM Film.....	117

3.5.3 PAH/PCBS Functionalized Gold Nanorods on ISAM Film.....	120
References.....	128
Chapter 4 Experimental Techniques and Measurements.....	132
4.1 Maker Fringe Method for ISAM Film.....	133
4.2 SHG Measurement Apparatus.....	136
4.3 Electrical Noise Reduction Methods.....	141
4.4 LabVIEW Programming for SHG Measurement.....	143
4.5 Pump Energy Threshold for Gold Nanorods.....	147
4.6 Preliminary SHG Measurement of PSS-coated Gold Nanorods.....	151
4.7 SHG Measurements of PAH/PCBS Functionalized GNRs on ISAM Film.....	157
4.7.1 Laser Warm-up.....	158
4.7.2 GNRs on PCBS ISAM Film (Pump Energy: 150 μ J).....	159
4.7.3 GNRs on PSS ISAM Film (Pump Energy: 150 μ J).....	162
4.7.4 GNRs on PCBS ISAM Film (Pump Energy: 35 μ J).....	165
4.7.5 GNRs on PSS ISAM Film (Pump Energy: 35 μ J).....	169
4.7.6 Summary of SHG Measurement.....	172
4.8 Polarization Dependent SHG Measurement.....	179
4.8.1 GNRs on PAH/PCBS ISAM Film.....	180
4.8.2 GNRs on PAH/PSS ISAM Film.....	182
4.8.3 Summary of Polarization Dependent SHG Measurement.....	184
References.....	186
Chapter 5 Conclusions and Future Work.....	187
References.....	191

List of Figures

Figure 1.1 Electric field pattern from a gold nanorod (aspect ratio 3.6) excited by a plane wave linearly polarized parallel to the plane of the page.	4
Figure 2.1 Waveforms of electric field and polarization fields in different media.	22
Figure 2.2 Illustration of Second Harmonic Generation.	23
Figure 2.3 Illustration of Sum-Frequency Generation.	25
Figure 2.4 Illustration of Difference-Frequency Generation.	26
Figure 2.5 The phase mismatch factor of second harmonic generation.	34
Figure 2.6 Normalized second harmonic intensity versus z for $\Delta k \neq 0$	35
Figure 2.7 Illustration of donor-acceptor group connected with a benzene ring.	37
Figure 2.8 Illustration of an asymmetric electronic response of the polarization for molecules with donor-acceptor groups.	38
Figure 2.9 Langmuir-Blodgett Deposition.	45
Figure 2.10 Illustration of ISAM film deposition.	48
Figure 2.11 Second order susceptibility of Poly S-119/PAH ISAM films versus salt concentration for several pH values.	49
Figure 2.12 Molecular structure of Mordant Orange 10.	50
Figure 2.13 Molecular structures of (a) Procion Red and (b) Procion Brown.	51
Figure 2.14 Illustration of traveling surface plasma wave at the metal-dielectric interface.	55
Figure 2.15 Localized plasmon resonance in gold nanospheres and gold nanorods.	59
Figure 2.16 Simulated extinction spectra of gold nanorod suspension in water with different aspect ratios.	61

Figure 2.17 Illustration of the seed-mediated method with CTAB as surfactant and hydroquinone as the reducing agent.....	63
Figure 3.1 Molecular structures of the polymers used in ISAM NLO film fabrication.	82
Figure 3.2 Polymer conformation: tails, loops, and trains.	84
Figure 3.3 The structures of the materials for gold nanorod synthesis.	87
Figure 3.4 Extinction spectra of hydroquinone reduced gold nanorods with various silver amounts: (a) 10, (b) 20, (c) 30, (d) 35, (e) 40 μ L.	94
Figure 3.5 Absorption spectrum of 1 mM PAH-DTC.	96
Figure 3.6 Extinction spectra of gold nanorod solution prior to and during dialysis (top). Normalized plasmon extinction of various dialysis times (bottom).	98
Figure 3.7 Extinction spectra of gold nanorod solution measured before dialysis, 20 minutes after dialysis, and after stirring in PAH-DTC for 3, 6, and 30 hours.....	100
Figure 3.8 Extinction spectrum of CTAB-coated long gold nanorod measured by a UV-Vis spectrometer.....	101
Figure 3.9 Normalized extinction spectra of CTAB-coated long gold nanorods during dialysis (top) and plasmon extinction of various dialysis times (bottom).	103
Figure 3.10 Illustration of the liquid layers surrounding a negatively charged gold nanoparticle.	104
Figure 3.11 Extinction spectra of GNR with various PAH-DTC concentrations.....	105
Figure 3.12 Zeta potential of various PAH-DTC concentration for GNR functionalization.....	106
Figure 3.13 Extinction spectra of GNR with various PCBS concentrations.	107
Figure 3.14 Zeta potential of CTAB-GNR, PAH-DTC coated GNR, and PAH-DTC/PCBS coated GNR with various PCBS concentrations.	108
Figure 3.15 Zeta potential graphs taken by Zetasizer (Malvern).	109
Figure 3.16 Illustration of the PAH/PCBS functionalized GNR procedure.	111
Figure 3.17 Normalized extinction spectra of PAH/PCBS functionalized GNR.	112

Figure 3.18 Zeta potential of PAH/PCBS functionalized GNR.....	113
Figure 3.19 GNR deposition by the dropcast method.....	115
Figure 3.20 Extinction spectra of PSS-coated nanorods: (a) in suspension and (b) on (PAH/PCBS) ₃ PAH film.....	116
Figure 3.21 FESEM images of PSS-coated GNRs deposited on a PAH film by dropcasting... ..	116
Figure 3.22 Extinction spectra of PAH-DTC/PCBS GNR of varying concentration deposited on (PAH/PCBS) ₃ PAH films.	118
Figure 3.23 FESEM images of (PAH-DTC/PCBS) functionalized gold nanorods deposited on (PAH/PCBS) ₃ PAH ISAM films.	119
Figure 3.24 ISAM films (3 or 3.5 bilayers of PAH/PCBS or PAH/PSS on glass slides) vertically immersed into the functionalized GNR solutions.....	121
Figure 3.25 Extinction spectra of PAH/PCBS Functionalized GNR suspension.	122
Figure 3.26 Functionalized GNR deposited on 3 or 3.5 bilayer PAH/PCBS (top) and PAH/PSS (bottom) films.	123
Figure 3.27 SEM images of functionalized GNRs deposited on (PAH/PCBS) ₃ and (PAH/PCBS) ₃ PAH films.	124
Figure 3.28 SEM images of functionalized GNRs deposited on (PAH/PSS) ₃ and (PAH/PSS) ₃ PAH films.	125
Figure 4.1 Maker fringe plots for (a) 9 μm thick NLO poled polymer film and (b) 1000 μm thick X-cut quartz.	134
Figure 4.2 Interference fringe pattern from a double-sided (PAH/PCBS) ₃ PAH sample.....	136
Figure 4.3 Experimental apparatus for second-harmonic generation measurement.....	137
Figure 4.4 Power measurement vs. angle rotation of waveplates.....	138
Figure 4.5 Transmittance spectra of filters: a long pass filter for $\lambda > 1000$ nm, a short pass filter for $380 \text{ nm} < \lambda < 600$ nm, and a spike filter at 532 nm.	140
Figure 4.6 Faraday cage (enclosing PMT and preamp) and ferrite rings and clip.....	141

Figure 4.7 Oscilloscope screenshot of waveforms of channel 1 (pump, yellow) and channel 2 (SHG, blue).....	143
Figure 4.8 Front panel of the LabVIEW program shows the initialization values (left column) and the display graphs for processed data (labeled (I), (II), (III), and (IV)).	144
Figure 4.9 Front panel of the LabVIEW program for SHG measurement of (a) GNRs and (b) (PAH/PCBS) ₃ PAH film.....	145
Figure 4.10 LabVIEW plots of SHG waveforms.....	146
Figure 4.11 SHG vs. Pump energy measurement.	147
Figure 4.12 Illustration of a focused Gaussian beam.....	148
Figure 4.13 FESEM image of PCBS ₃ GNRs deposited on (PAH/PSS) ₃ film.....	149
Figure 4.14 Laser fluences at various positions from focal point for pump energy 35 μ J.	150
Figure 4.15 SHG intensity of 3.5 bilayer PAH/PCBS films with and without PSS-coated GNRs.	152
Figure 4.16 SHG intensity plots for PSS-coated GNRs deposited on (PAH/PCBS) ₃ PAH film with insets showing FESEM images.....	153
Figure 4.17 SHG intensity from 3.5bi layer PAH/PCBS films with (red solid lines) and without (blue solid lines) PSS-coated GNRs.	154
Figure 4.18 Illustration of PSS-coated nanorods deposited on (PAH/PCBS) ₃ PAH film with an additional 3.5 bilayer PAH/PCBS film deposited on top.	155
Figure 4.19 Normalized SHG intensity of PSS-coated GNRs deposited on (PAH/PCBS) ₃ PAH film with an additional 3.5 bilayer (PAH/PCBS) film.	156
Figure 4.20 Laser pump reading of the photodiode from the oscilloscope over time.	158
Figure 4.21 Normalized SHG intensity of 3 or 3.5 bilayer PCBS film with and without nanorods (pump energy 150 μ J).	160
Figure 4.22 Normalized SHG intensity of 3.5 bilayer PAH/PCBS film with and without nanorods (pump energy 150 μ J).	161

Figure 4.23 Signal-to-noise ratio for the SHG intensity of 3 or 3.5 bilayer PAH/PSS film with nanorods (pump energy 150 μ J).	163
Figure 4.24 Signal-to-noise ratio for the SHG intensity of 3.5 bilayer PAH/PSS film with nanorods (pump energy 150 μ J).	164
Figure 4.25 (Top) Signal from the PMT when SHG measurement was conducted on PAH-DTC GNRs on (PAH/PCBS) ₃ film.	166
Figure 4.26 Normalized SHG intensity of 3.5 bilayer PCBS film with (left axis) and without (right axis) nanorods (pump energy 35 μ J for nanorods, 350 μ J for film)..	168
Figure 4.27 Normalized SHG intensity of 3 or 3.5 bilayer PCBS film with (left axis) and without (right axis) nanorods (pump energy 35 μ J for nanorods, 350 μ J for film).	170
Figure 4.28 Normalized SHG intensity of 3.5 bilayer PCBS film with (left axis) and without (right axis) nanorods (pump energy 35 μ J for nanorods, 350 μ J for film).	171
Figure 4.29 SHG intensity of PCBS-functionalized GNRs on 3.5 bilayer PAH/PCBS films... ..	174
Figure 4.30 SHG intensity of PCBS-functionalized GNRs on 3.5 bilayer PAH/PSS films.....	175
Figure 4.31 SHG intensity of PCBS-functionalized GNRs on (PAH/PSS) ₃ PAH and (PAH/PCBS) ₃ PAH films.	177
Figure 4.32 SHG intensity of the bare PCBS films compared to the SHG of the bare PSS films.	178
Figure 4.33 Top view and side view of the new SHG detection apparatus.	179
Figure 4.34 SHG intensity of (PAH/PCBS) ₃ PAH film for different fundamental and second-harmonic polarizations.....	180
Figure 4.35 SHG intensity of PCBS1 GNRs deposited on (PAH/PCBS) ₃ PAH film for different fundamental and second-harmonic polarizations.....	181
Figure 4.36 SHG intensity of (PAH/PSS) ₃ PAH film for different fundamental and second-harmonic polarizations.....	182

Figure 4.37 SHG intensity of PCBS1 GNRs deposited on (PAH/PSS) ₃ PAH film for different fundamental and second-harmonic polarizations.....	183
Figure 4.38 Illustration of fundamental and second-harmonic light passing through the substrate containing (a) ISAM film without nanorods and (b) with nanorods.	185

List of Tables

Table 2.1 Second-order optical nonlinear effects.....	24
Table 3.1 Materials for gold nanorod synthesis	87
Table 3.2 Solution Preparation for Gold Nanorod Synthesis.....	89
Table 3.3 PSS-coated GNR density on PAH film.....	117
Table 3.4 Functionalized GNR on ISAM films.	120
Table 3.5 Quantitative results of the functionalized GNRs on two different ISAM films.	127
Table 4.1 Summary of SHG enhancement from functionalized gold nanorods	172
Table 4.2 SHG multilayer factor normalized by the nanorod density	173
Table 4.3 SHG enhancement comparison from functionalized gold nanorods.....	176
Table 4.4 Comparison of the SHG intensity from the PCBS-functionalized GNRs on ISAM films.	178

Acronyms and Abbreviations

CAMAC	Computer automated measurement and control
CTAB	Cetyltrimethylammonium bromide
DC	Direct current
DFG	Difference-frequency generation
DTC	Dithiocarbamate
EFISH	Electric-field induced second harmonic
EO	Electro optic
FESEM	Field-emission scanning electron microscopy
GNR	Gold nanorod
GNS	Gold nanosphere
HCISAM	Hybrid covalent ionic self-assembled multilayer
ICP-AES	Inductively coupled plasma atomic emission spectroscopy
ISAM	Ionic self-assembled multilayer
LB	Langmuir-Blodgett
NLO	Nonlinear optical (Nonlinear optics)
LASER	Light amplification of stimulated emission of radiation
LED	Light emitting diode
LSP	Localized surface plasmons
LSPR	Localized surface plasmon resonance
OPA	Optical parametric amplification
OPO	Optical parametric oscillator
OR	Optical rectification
PAH	Poly(allylamine hydrochloride)
PAH-DTC	Poly(allylamine hydrochloride)-dithiocarbamate
PB	Procion brown
PR	Procion red
PCBS	Poly[carboxyhydroxyphenylazobenzenesulfonamidoethanediyl] sodium salt

PMT	Photomultiplier tube
PSS	Poly(sodium-p-styrenesulfonate)
QPM	Quasi-phase matching
RCA	Radio corporation of America (cleaning process)
SERS	Surface-enhanced Raman spectroscopy
SFG	Sum-frequency generation
SH	Second-harmonic
SHG	Second-harmonic generation
SNR	Signal-to-noise ratio
SPASER	Surface plasmon amplification of stimulated emission of radiation
SPP	Surface plasmon polaritons
TSPR	Transverse surface plasmon resonance
UPD	Underpotential deposition
UV	Ultraviolet
UV-Vis-NIR	Ultraviolet-Visible-Near-infrared

Chapter 1

Introduction

1.1 Background and Motivation

Since the advent of lasers in the 1960s so that coherent high intensity light sources became available, previously unexplored optical phenomena served as platforms of new fields of optics such as quantum optics, guided optics (e.g. fiber optics, planar waveguide optics) and nonlinear optics. Nonlinear optics is the study of optical phenomena where the polarization of light in a dielectric material responds nonlinearly to the applied electric field. Through nonlinear optics, laser radiation is not limited to monochromatic segments of the optical spectrum but can be converted from one frequency to another. The field of nonlinear optics was initiated by the second harmonic generation (SHG) experiment of Franken *et al.*¹ shortly after the demonstration of the first operating laser.

Second harmonic generation is one of the most important nonlinear optical effects. It is a special type of sum frequency generation where two incident photons of the same angular frequency ω combine to make one photon at angular frequency 2ω . This optical phenomenon is observed in specific (noncentrosymmetric) materials because in a centrosymmetric material the second-order nonlinear susceptibility, $\chi^{(2)}$, vanishes due to the symmetry of the material. For the past several decades, SHG has been researched in nonlinear optical (NLO) materials, such as inorganic crystals, organic crystals, poled polymers, Langmuir-Blodgett (LB) films, covalent self-assembled systems, ionic self-assembled monolayer (ISAM) polymer films, and hybrid-covalent/ionic self-assembled monolayer (HCISAM) films. Due to their flexibility in molecular engineering and fabrication, organic polymer films have been widely used for generating noncentrosymmetric structures required for SHG. Poled polymers are obtained by applying a strong electric field to align molecular dipoles. Unfortunately, after the electric field is removed,

they become thermally and environmentally unstable due to orientational relaxation.² LB films are synthesized by a layer-by-layer deposition technique using amphiphilic molecules which contain hydrophobic tails and hydrophilic heads. LB films possess a high degree of molecular orientation and provide precise film thickness control at the molecular level. However, the deposition is time consuming and requires expensive and specialized equipment. The resulting LB films also exhibit poor temporal and thermal stabilities.³ Covalent self-assembled films are created by covalently linked self-assembled chromophores. This method provides higher chromophore density and better alignment than the electric poling method.⁴ But the deposition process is also time consuming due to the chemical activation steps and thus it is difficult to make thick films.⁵

In contrast, ISAM films are created by alternately immersing a substrate in polyanion and polycation solutions. This simple method provides a swift way to make bilayers (~ 10 minutes per bilayer) without complicated equipment.⁶ In the past, our research group fabricated ISAM films incorporating an NLO-active polyelectrolyte which demonstrated excellent temporal stability (~ 3 years) of the second-order nonlinearity.⁷ The chromophore alignment was also thermally stable at 150 °C. The ISAM $\chi^{(2)}$ values were found to be 0.7 times that of quartz and did not show any measureable decay for more than a year. However, due to the binding of chromophores to the polycation above and below them, the bulk of the film showed a low degree of polar order.⁸ To overcome this, a covalent/ionic self-assembled monolayer technique was developed by our group.⁹ Polar ordering of the bulk NLO-active chromophores was achieved by alternating the deposition of the NLO-active chromophore and a polyelectrolyte layer via covalent reaction and electrostatic attraction. The ISAM technique can also be applied to a curved surface. From our team, Daengngam *et al.*¹⁰ demonstrated thermodynamically stable and significant $\chi^{(2)}$ from a cylindrically symmetric silica optical fiber. The ISAM films were deposited on a silica fiber taper where the alignment of the NLO chromophores was maintained via electrostatic interaction. The research in this dissertation uses the ISAM method to produce samples for SHG, which also incorporate nanoparticles for plasmonic enhancement of the nonlinear optical response to be discussed later in further detail.

The conversion efficiencies of SHG are typically extremely small due to frequency dispersion in which the second-harmonic and fundamental wave travel out at different velocities through a nonlinear optical medium. This is called phase-mismatch and several techniques have been

implemented in order to achieve phase-matching. One way of achieving phase-matching is to make use of birefringence.¹¹ Birefringent materials have different refractive indices for different polarizations. By using extraordinary polarization for the fundamental at angular frequency ω and ordinary polarization for the second harmonic at angular frequency 2ω , phase-matching can be achieved. However, this technique is not suitable for materials that have insufficient birefringence or no birefringence. There is another technique called quasi-phase matching in which a periodic structure in a nonlinear medium allows the second-harmonic signal to increase monotonically. For a fabrication of quasi-phase matched crystals, the most commonly used method is periodic poling. Some limitations of quasi-phase matching, however, come from the fabrication which requires specific crystal materials and properties, limited widths of grating period, and high cost and complex manufacturing especially using lithography. Taking a different approach recently in our group, Daengngam *et al.* reported the fabrication of a spatially periodic coating of ISAM film on a silica fiber taper by a UV ablation technique.¹² It was demonstrated that the taper with a periodic structure produced 15 times greater SHG signal than a fiber taper with a uniform coating.

In addition to increasing the conversion efficiency through phase-matching, there is significant interest in increasing the intrinsic nonlinear response of a material. One relatively new way to do this is through plasmonics. Plasmonics is a field of nanophotonics that involves interaction between electromagnetic radiation and conduction electrons at a metal/dielectric interface or the surface of metallic nanoparticles.¹³ This new approach makes use of optical confinement and enhancement in metallic nanoparticles, called localized surface plasmon resonance (LSPR), to locally increase the fundamental field strength. **Figure 1.1** shows the electric field pattern from a gold nanorod (aspect ratio 3.6) excited by a plane wave which is linearly polarized partly lengthwise and widthwise with respect to the rod.¹⁴ The electric field of the nanorod is most concentrated at the tips indicated by the bright regions. Since the intensity of the second harmonic wave grows quadratically with the intensity of the fundamental wave, it is possible to achieve high SHG intensity by concentrating fundamental power using localized surface plasmon enhancement when the wavelength of the fundamental light matches the resonant wavelength of a LSPR.

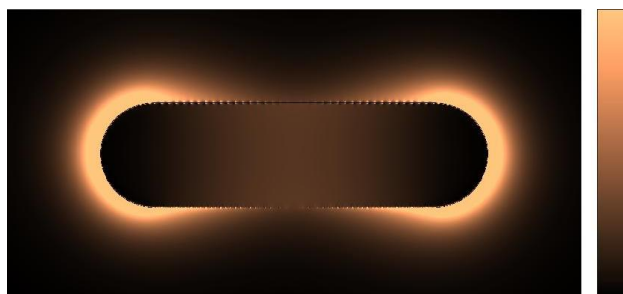


Figure 1.1 Electric field pattern from a gold nanorod (aspect ratio 3.6) excited by a plane wave linearly polarized parallel to the plane of the page. It was simulated using the metallic nanoparticles boundary element method (MNBEM) toolbox developed by F.J. Garcia.³

Since the first prediction of surface plasmons in 1957 by Rufus Ritchie,¹⁵ research in plasmonics began by studying how light scatters from molecules on metals^{16,17} and successfully advanced Raman spectroscopy to the ability detect smaller numbers of molecules. Plasmonic excitations can enhance nonlinear optical (NLO) effects in a couple of ways. First, plasmonic resonances are highly sensitivity to the dielectric properties of the metal and its surrounding medium and thus can be useful for sensors. For example, slight modifications of refractive index near a metal surface can modify the plasmonic resonance significantly. Second, the ability to concentrate and channel light using subwavelength structures can result in strong local electromagnetic fields. The enhanced electric field can then be applied to manipulate the interactions between light and materials, enhancing nonlinear phenomena. As mentioned earlier, surface-enhanced Raman spectroscopy (SERS)¹⁸⁻²¹ became possible thanks to the surface enhancement effect. Raman spectroscopy is intrinsically a weak Raman process but the enhancement factor of SERS can be as high as on the order of 10^4 in nanoparticle aggregates or fractal structures, enabling single molecule detection.^{18,21-25} Numerous applications other than SERS include near-field optics,²⁶ surface-enhanced phase shift,²⁷ solar cells,²⁸⁻³⁰ optical chips,³¹⁻³³ biological imaging,^{34,35} biochemical sensing,^{36,37} nanoshell therapy,^{38,39} SPASERS (Surface Plasmon Amplification of Stimulated Emission of Radiation)^{40,41} and LEDs.^{42,43}

While surface-enhanced Raman spectroscopy has been extensively explored, surface-enhanced second harmonic generation also has been of some interest to many scientists and engineers. In 1966, shortly after the first demonstration of optical harmonic generation, plasmon-enhanced second harmonic generation was observed on a silver surface with inversion symmetry by Brown *et al.*⁴⁴ They suggested that the principal source of second harmonic light was the conduction electron plasma in silver. In 1981, Chen *et al.* reported that the second harmonic generation at a rough surface silver-air interface was enhanced by a factor of 10^4 compared to the case of smooth evaporated films.⁴⁵

In recent decades, with growing interest in colloidal nanoparticles, there have been increasing reports regarding plasmonic enhancement for nonlinear optical applications. For third harmonic generation, Lippitz *et al.*⁴⁶ first observed third harmonic signals from individual gold colloids of 40 nm diameter excited with 1 ps pulses at 1500 nm. More recently Lassiter *et al.* investigated third harmonic generation from gold nanostripes coupled with a gold film and observed 4.8 orders of magnitude in enhancement compared to the case of bare gold film.⁴⁷

For second harmonic generation, however, it is more difficult to implement plasmonic enhancement because the material must lack global inversion symmetry. The atoms in plasmonic metals (gold, silver, or aluminum) are organized in a face-centered cubic lattice which is centrosymmetric, therefore SHG is forbidden in the bulk metal in the electric dipole approximation. But symmetry breaking is possible at a metal surface because of the finite dimension of the atomic lattice. Therefore, nanoscale SHG is possible at the surface of centrosymmetric nanoparticles in bulk isotropic solution which was demonstrated experimentally by Wang *et al.*⁴⁸ Several other techniques also have been applied to break the symmetry to achieve SHG from metal nanostructures. These techniques include imperfect spheres,⁴⁹ defects,⁵⁰ asymmetric shapes,⁵¹⁻⁵⁴ random metal nanostructures,^{55,56} asymmetric geometric arrangement,⁵⁷ and nanoparticle aggregates/arrays.⁵⁸⁻⁶⁵ Material surfaces coated with metal nanostructures are also suggested to act as a nonlinear conversion medium. Turkpence *et al.*⁶⁶ demonstrated strong modification of optical responses by quantum dots attached to a metallic nanoparticle.

However, nanoscale SHG from noble metals are weak and generally inefficient at such a small scale. In order to maximize the nonlinear efficiency, hybrid nanomaterials consisting of metal

nanoparticles and NLO materials have been utilized. Vidal *et al.*⁶⁷ detected SHG from a single isolated microsphere coated with NLO material. Clark *et al.* observed 20 times enhancement in SHG intensity using 100 nm gold nanoparticles coated with chromophore dye.⁶⁸ Core-shell structures were fabricated to demonstrate enhanced SHG by several groups. Pu *et al.* measured an enhanced SHG power of 500 times using core-shell nanocavities that consisted of a noncentrosymmetric crystalline core and a metallic shell.⁶⁹ More recently, Shen *et al.*⁷⁰ designed a nonlinear nanoruler which consists of a 55 nm gold core coated with silica shell of different thicknesses from 1 to 6 nm. They demonstrated that it can accomplish 1 nm resolution by using plasmon-enhanced second harmonic generation.

Self-assembled films also provide great enhancement factors of SHG. A two dimensional gold nanoparticle monolayer on a chemically modified substrate was created via self-assembly and SHG was demonstrated in a Maker-type fringe pattern.⁷¹ From our own research team, Chen *et al.*⁷² demonstrated large enhancements of NLO susceptibility of ionic self-assembled multilayer (ISAM) films by using nanosphere lithography to create silver nanoparticle structures on the ISAM film. Their hybrid film (ISAM + nanoparticles) generated 1600 times more SHG signal than the film without nanoparticles, making 3 bilayers of hybrid film equivalent to a 700 - 1000 bilayer conventional film. Dong *et al.*⁷³ deposited gold nanoparticles inside trenches of a gold film by using lithography and self-assembly to achieve SHG enhanced by 4200-fold compared to a densely packed gold nanoparticles on a smooth gold film. Self-assembly employing the “layer-by-layer” method can be advantageous for extending 2D nanoparticle structures to a 3D construction, which brings a variety of potential functions of nanoparticle arrays. Zdanowicz *et al.* fabricated nanocomposite samples consist of alternating layers of silver-decorated silica glass nanoparticles and pure silica glass deposited on a glass substrate and performed Maker-fringe measurements.^{74,75}

As so far explored, gold nanoparticles are an excellent candidate for enhancing optical second harmonic responses. Their unique chemical, electrical, optical, and physical properties have opened up a wide range of plasmonic applications including chemical catalysts,^{76,77} biochemical sensors and nanoscale electronics.⁷⁸⁻⁸⁰ Therefore, plasmonic enhancement of NLO material by incorporating gold nanoparticles into an NLO ISAM film system is the main interest of this dissertation. The aim is to develop NLO materials whose nonlinear optical responses are larger

than in conventional ISAM films for applications in frequency conversion, electro-optic modulation, or second harmonic generation spectroscopy.^{81,82}

There are a few important factors that need to be considered in this dissertation for maximizing the second-order nonlinearity. First, the excitation wavelength of the fundamental light should overlap the plasmon resonance peak of the nanoparticles. Gold nanorods were chosen because their resonance wavelengths are in the near-infrared region of the optical spectrum, whereas the resonances of gold nanospheres are in the visible region. Second, the SHG enhancement primarily comes from the interface second-order nonlinear susceptibility ($\chi^{(2)}$) (discussed more in detail below) and thus, only the top few bilayers of the films receive plasmonic enhancement. Lastly, to produce large $\chi^{(2)}$ at the metal-film interface, interface effects need to be considered when selecting NLO materials. One of the attractive features of gold nanorod synthesis is its ability to tune the longitudinal surface plasmon resonance (LSPR) peak to the desired wavelength by varying the amount of silver ions present during the synthesis. Therefore, the first consideration can be satisfied. In prior work from our team, interface effects in plasmon-enhanced SHG from ISAM films was investigated by Chen *et al.*⁸³ and it was discovered that the air-film interface was the dominant contribution to the SHG signal. In the preceding study by Chen *et al.* of plasmon-enhanced SHG from ISAM film onto which silver triangular nanoparticles were deposited, it was verified that the greatest enhancements in NLO coefficients were observed for a three-bilayer film. Hence, the number of ISAM bilayers in the present work will focus on 3 or 3.5 depending on the surface charge of the nanoparticles. Regarding the selection of NLO polymers, PCBS and Procion Brown (PB) have been widely used as polyanion in our group for the study of SHG from ISAM films. PB exhibits stronger SHG signal than PCBS due to its ability to achieve a high polar order by the hybrid covalent ISAM method. However, it was shown by Chen *et al.* that PAH/PB films are more susceptible to disruption at the interface by the nanoparticle deposition process and produce lower NLO efficiencies than PAH/PCBS films with nanoparticles. As a result, PCBS is selected as the NLO polymer in this work. In addition, we found in the course of this work that the most effective way of achieving plasmonic enhancement of SHG would be to attach NLO chromophore dipoles directly to the gold nanorods. Thus, a method of functionalizing gold nanorods with PCBS and PAH was adapted for this study.

1.2 Research Goals

The purpose of this research is to develop and test a new sort of nanomaterial that can plasmonically enhance second-order nonlinear optical susceptibilities from the conventional NLO ISAM films by incorporating the nanomaterials into the NLO films. The development of the nanomaterial was achieved by a bottom-up approach of self-assembly of gold nanorods. By tuning the localized surface resonance wavelength of gold nanorods close to the fundamental wavelength of the laser, the electric field is locally intensified at the ends of the nanorods. Therefore, for the same fundamental intensities provided by the laser, greater SHG signals can be generated from the NLO films coated on the gold nanorods than from the conventional NLO films on a glass substrate. The study was done by measuring the SHG from the gold nanorods in a Maker-like fringe optical setup using an Nd:YAG laser at the wavelength of 1064 nm. The research objectives are listed as follows.

- i. Synthesize gold nanorods whose LSPR wavelength is near the wavelength of the laser. Follow the seed-mediated method modified for hydroquinone reduction to yield nanorods with LSPRs in the near-infrared region. Adjust the amount of silver nitrate in the growth solution to tune the LSPR wavelengths to the desired wavelength.
- ii. Observe the LSPR wavelength shifts when the surrounding medium changes. The resonance peak red-shifts when the nanorods are functionalized, but the resonance peak blue-shifts when the functionalized nanorods are deposited on a polymer film. The final LSPR of the nanorods on the ISAM film is required to be near 1064 nm.
- iii. Develop and optimize a method for functionalizing gold nanorods with polymer films. Apply the Layer-by-Layer method to coat NLO-active polyanions (PCBS) and polycations (PAH) alternately on the nanorod surface. To achieve good particle stability, determine the optimum concentrations of PAH and PCBS and centrifugation parameters.
- iv. Investigate the method of dialysis to replace the thick physisorbed CTAB bilayer surrounding the gold nanorods with a thin chemisorbed PAH-DTC layer to reduce the distance between the nanorods and the NLO films on the nanorods.
- v. Characterize the functionalized gold nanorods to confirm their collective electric charge and LSPR wavelength. Zeta potential is measured on the slipping plane surface that moves with the particle. The zeta potential measurement provides a prime indicator of the stability

of colloidal dispersions. Optical spectrum measurement is a common characterization method to measure the LSPR wavelength of nanoparticle colloids.

- vi. Prepare the ISAM films by using two different polyanions, NLO-active anion PCBS and NLO-inactive anion PSS. The number of bilayers are determined in consideration of the LSPR decay length (a few nm) and our team's prior collaborative work done with silver nanotriangles on ISAM film.
- vii. Study the deposition of the functionalized nanorods on the ISAM film. Explore different particle deposition methods via dropcast or dipping. Vary the dilution of the nanorod solutions to observe the distributions and particle densities on the ISAM film using field-emission scanning electron microscopy (FESEM).
- viii. Design and assemble the Maker fringe optical setup for SHG measurement. Explore and implement various electrical noise reduction techniques to improve the SHG signal readings. Perform the SHG measurements both for the ISAM films containing the functionalized gold nanorods and for the ISAM films alone. To avoid the optical damage of gold nanorods, determine the maximum tolerable fluence by measuring SHG at various pump energies.
- ix. Compare the SHG intensities to verify whether the second-order nonlinear susceptibilities are enhanced by the functionalized gold nanorods. Observe and analyze the characteristics of each SHG interference fringe pattern.
- x. Conduct polarization dependent SHG measurements to study the coupling between p- or s-polarized incoming fundamental light and the PCBS chromophores either on gold nanorods or on a glass substrate. Include an additional polarizer to control the polarization of the measured SHG. Explain the differences between the samples of ISAM films with and without the functionalized gold nanorods.

1.3 Dissertation Outline

The following is an outline of the content and significance of this dissertation. This chapter provided a brief background on nonlinear optics and plasmonics and concluded with a synopsis of the key goals and results of this dissertation.

Chapter 2 is focused on the theoretical and experimental background of second-order nonlinear optics, ionic self-assembly, and plasmonics. An introduction to nonlinear optics is given and second-order nonlinear effects are described in detail by examining the second-order contribution to the polarization by an incident electric field. In doing so, the requirement for second harmonic generation of noncentrosymmetric order is revealed and a deeper look at the second-order nonlinear susceptibility tensor $\chi^{(2)}$ is provided. Finally, the efficiency of second harmonic generation is derived using a coupled wave equation. The chapter next considers the experimental background of second harmonic generation. Two types of materials, inorganic and organic, and their properties are covered here. Since organic materials are proven to be more promising than inorganic materials thanks to molecular engineering, organic materials are discussed in detail. Organic materials covered in this chapter include organic crystals, poled polymers, Langmuir-Blodgett films, and thin polymer films. For thin films, ionically self-assembled multilayer (ISAM) and hybrid covalent ISAM techniques are discussed in significant depth. Applications of second harmonic generation are discussed next. The chapter concludes with nonlinear plasmonics and applications using nanoparticles.

Chapter 3 describes sample fabrication methods. It is divided into four major parts: NLO ISAM film deposition, gold nanorod synthesis, functionalization of gold nanorods, and incorporation of functionalized gold nanorods into ISAM films. ISAM film deposition is explained in detail including the polymers and the method used. The procedure of the seed-mediated gold nanorod synthesis method by hydroquinone reduction is described. Resonance peak tuning is discussed in the synthesis process as well. Characterization methods are explained and the results of spectrum and zeta potential measurements are analyzed. Functionalization of gold nanorod with polymers (PCBS and PAH) by the Layer-by-Layer technique is illustrated and detailed procedures and optimized conditions are given. Replacement of CTAB bilayers with PAH-DTC is investigated via dialysis. The optimized concentration of each polymer used for functionalization

is determined. Finally, deposition of functionalized gold nanorods on the ISAM films are also illustrated and described. Detailed results of characterization via optical spectrum measurement and FESEM images are presented.

Chapter 4 describes experimental techniques and presents experiment results. The first half of the chapter regards the NLO experimental techniques. The SHG measurement apparatus based on a Maker-type fringe method is illustrated and explained in detail. Various techniques used to reduce electrical noise from the laser power supply are explored. The data acquisition method via a LabVIEW program is described for collection of SHG signals from the samples. Lastly, the pump energy threshold for gold nanorods is investigated and determined. The second half of the chapter displays the experimental results collected from the SHG measurement of functionalized gold nanorods. Preliminary data from PSS-coated gold nanorods are discussed and justify the new approach involving coating of NLO polymer directly onto the nanorods. The SHG intensities from gold nanorods are compared to the SHG intensities from ISAM films for two different chosen pump energies. The enhancement of SHG from gold nanorods is demonstrated when lower pump energy was used for gold nanorods. Characteristics of the SHG interference fringe pattern from gold nanorods are discussed. A polarization dependent SHG measurement reveals the difference in interference patterns between SHG from gold nanorods and ISAM film and SHG from the bare ISAM film.

Chapter 5 draws conclusions of the study of plasmonically enhanced SHG measurement from gold nanorods and proposes future work. Conclusions of the fabrication of nanostructures using plasmonic enhancement and applications are also provided and some ideas for future work are discussed.

References

1. Franken, P. A., Hill, A. E., Peters, C. W. & Weinreich, G. Generation of Optical Harmonics. *Phys. Rev. Lett.* **7**, 118–119 (1961).
2. *Nonlinear optics of organic molecules and polymers.* (CRC Press, 1997).
3. Ashwell, G. J. Langmuir-Blodgett films: molecular engineering of non-centrosymmetric structures for second-order nonlinear optical applications. *J. Mater. Chem.* **9**, 1991–2003 (1999).
4. Marks, T. J. & Ratner, M. A. Design, Synthesis, and Properties of Molecule-Based Assemblies with Large Second-Order Optical Nonlinearities. *Angew. Chem. Int. Ed. Engl.* **34**, 155–173 (1995).
5. Liu, Y. *et al.* Characterization of electrostatically self-assembled nanocomposite thin films. *Smart Mater. Struct.* **8**, 100–105 (1999).
6. Rosidian, A., Liu, Y. & Claus, R. O. Ionic Self-Assembly of Ultrahard ZrO₂/Polymer Nanocomposite Thin Films. *Adv. Mater.* **10**, 1087–1091 (1998).
7. Heflin, J. R., Figura, C., Marciu, D., Liu, Y. & Claus, R. O. Thickness dependence of second-harmonic generation in thin films fabricated from ionically self-assembled monolayers. *Appl. Phys. Lett.* **74**, 495–497 (1999).
8. Figura, C. *et al.* Control of Second-Order Nonlinear Optical Susceptibility in Ionically Self-Assembled Films by pH and Ionic Strength. *MRS Proc.* **598**, (1999).
9. Heflin, J. R. *et al.* Efficient, Thermally Stable, Second Order Nonlinear Optical Response in Organic Hybrid Covalent/Ionic Self-Assembled Films. *Langmuir* **22**, 5723–5727 (2006).
10. Daengngam, C. *et al.* Demonstration of a cylindrically symmetric second-order nonlinear fiber with self-assembled organic surface layers. *Opt. Express* **19**, 10326 (2011).
11. Boyd, R. W. *Nonlinear optics.* (Academic Press, 2008).
12. Daengngam, C. *et al.* Fabrication and characterization of periodically patterned silica fiber structures for enhanced second-order nonlinearity. *Opt. Express* **23**, 8113 (2015).

13. Kauranen, M. & Zayats, A. V. Nonlinear plasmonics. *Nat. Photonics* **6**, 737–748 (2012).
14. Hohenester, U. & Trügler, A. MNPBEM – A Matlab toolbox for the simulation of plasmonic nanoparticles. *Comput. Phys. Commun.* **183**, 370–381 (2012).
15. Ritchie, R. H. Plasma Losses by Fast Electrons in Thin Films. *Phys. Rev.* **106**, 874–881 (1957).
16. Fleischmann, M., Hendra, P. J. & McQuillan, A. J. Raman spectra of pyridine adsorbed at a silver electrode. *Chem. Phys. Lett.* **26**, 163–166 (1974).
17. Jeanmaire, D. L. & Van Duyne, R. P. Surface raman spectroelectrochemistry. *J. Electroanal. Chem. Interfacial Electrochem.* **84**, 1–20 (1977).
18. Nie, S. & Emory, S. R. Probing Single Molecules and Single Nanoparticles by Surface-Enhanced Raman Scattering. *Science* **275**, 1102–1106 (1997).
19. Haes, A. J. & Van Duyne, R. P. A Nanoscale Optical Biosensor: Sensitivity and Selectivity of an Approach Based on the Localized Surface Plasmon Resonance Spectroscopy of Triangular Silver Nanoparticles. *J. Am. Chem. Soc.* **124**, 10596–10604 (2002).
20. Doering, W. E. & Nie, S. Single-Molecule and Single-Nanoparticle SERS: Examining the Roles of Surface Active Sites and Chemical Enhancement. *J. Phys. Chem. B* **106**, 311–317 (2002).
21. Kneipp, K. *et al.* Single Molecule Detection Using Surface-Enhanced Raman Scattering (SERS). *Phys. Rev. Lett.* **78**, 1667–1670 (1997).
22. Michaels, A. M., Nirmal, M. & Brus, L. E. Surface Enhanced Raman Spectroscopy of Individual Rhodamine 6G Molecules on Large Ag Nanocrystals. *J. Am. Chem. Soc.* **121**, 9932–9939 (1999).
23. Kneipp, K., Kneipp, H. & Kneipp, J. Surface-Enhanced Raman Scattering in Local Optical Fields of Silver and Gold Nanoaggregates From Single-Molecule Raman Spectroscopy to Ultrasensitive Probing in Live Cells. *Acc. Chem. Res.* **39**, 443–450 (2006).
24. Michaels, A. M., Jiang & Brus, L. Ag Nanocrystal Junctions as the Site for Surface-Enhanced Raman Scattering of Single Rhodamine 6G Molecules. *J. Phys. Chem. B* **104**, 11965–11971 (2000).
25. Camden, J. P. *et al.* Probing the Structure of Single-Molecule Surface-Enhanced Raman Scattering Hot Spots. *J. Am. Chem. Soc.* **130**, 12616–12617 (2008).

26. Schnell, M. *et al.* Controlling the near-field oscillations of loaded plasmonic nanoantennas. *Nat. Photonics* **3**, 287–291 (2009).
27. Chen, L. *et al.* Observation of large positive and negative lateral shifts of a reflected beam from symmetrical metal-cladding waveguides. *Opt. Lett.* **32**, 1432 (2007).
28. Nakayama, K., Tanabe, K. & Atwater, H. A. Plasmonic nanoparticle enhanced light absorption in GaAs solar cells. *Appl. Phys. Lett.* **93**, 121904 (2008).
29. Catchpole, K. R. & Polman, A. Plasmonic solar cells. *Opt. Express* **16**, 21793 (2008).
30. Ferry, V. E., Sweatlock, L. A., Pacifici, D. & Atwater, H. A. Plasmonic Nanostructure Design for Efficient Light Coupling into Solar Cells. *Nano Lett.* **8**, 4391–4397 (2008).
31. Maier, S. A. *et al.* Plasmonics—A Route to Nanoscale Optical Devices. *Adv. Mater.* **13**, 1501–1505 (2001).
32. Lutz, T. *et al.* Molecular Orbital Gates for Plasmon Excitation. *Nano Lett.* **13**, 2846–2850 (2013).
33. Dionne, J. A., Diest, K., Sweatlock, L. A. & Atwater, H. A. PlasMOSstor: A Metal–Oxide–Si Field Effect Plasmonic Modulator. *Nano Lett.* **9**, 897–902 (2009).
34. Sokolov, K. *et al.* Real-Time Vital Optical Imaging of Precancer Using Anti-Epidermal Growth Factor Receptor Antibodies Conjugated to Gold Nanoparticles. *Cancer Res.* **63**, 1999–2004 (2003).
35. El-Sayed, I. H., Huang, X. & El-Sayed, M. A. Surface Plasmon Resonance Scattering and Absorption of anti-EGFR Antibody Conjugated Gold Nanoparticles in Cancer Diagnostics: Applications in Oral Cancer. *Nano Lett.* **5**, 829–834 (2005).
36. Anker, J. N. *et al.* Biosensing with plasmonic nanosensors. *Nat. Mater.* **7**, 442–453 (2008).
37. Feng, J. *et al.* Nanoscale Plasmonic Interferometers for Multispectral, High-Throughput Biochemical Sensing. *Nano Lett.* **12**, 602–609 (2012).
38. Hirsch, L. R. *et al.* Nanoshell-mediated near-infrared thermal therapy of tumors under magnetic resonance guidance. *Proc. Natl. Acad. Sci.* **100**, 13549–13554 (2003).
39. Bardhan, R., Lal, S., Joshi, A. & Halas, N. J. Theranostic Nanoshells: From Probe Design to Imaging and Treatment of Cancer. *Acc. Chem. Res.* **44**, 936–946 (2011).

40. Noginov, M. A. *et al.* Demonstration of a spaser-based nanolaser. *Nature* **460**, 1110–1112 (2009).
41. Oulton, R. F. *et al.* Plasmon lasers at deep subwavelength scale. *Nature* **461**, 629–632 (2009).
42. Kwon, M.-K. *et al.* Surface-Plasmon-Enhanced Light-Emitting Diodes. *Adv. Mater.* **20**, 1253–1257 (2008).
43. Lozano, G. *et al.* Plasmonics for solid-state lighting: enhanced excitation and directional emission of highly efficient light sources. *Light Sci. Appl.* **2**, e66 (2013).
44. Brown, F. & Parks, R. E. Magnetic-Dipole Contribution to Optical Harmonics in Silver. *Phys. Rev. Lett.* **16**, 507–509 (1966).
45. Chen, C. K., de Castro, A. R. B. & Shen, Y. R. Surface-Enhanced Second-Harmonic Generation. *Phys. Rev. Lett.* **46**, 145–148 (1981).
46. Lippitz, M., van Dijk, M. A. & Orrit, M. Third-Harmonic Generation from Single Gold Nanoparticles. *Nano Lett.* **5**, 799–802 (2005).
47. Lassiter, J. B. *et al.* Third-Harmonic Generation Enhancement by Film-Coupled Plasmonic Stripe Resonators. *ACS Photonics* **1**, 1212–1217 (2014).
48. Wang, H., Yan, E. C. Y., Borguet, E. & Eisenthal, K. B. Second harmonic generation from the surface of centrosymmetric particles in bulk solution. *Chem. Phys. Lett.* **259**, 15–20 (1996).
49. Nappa, J. *et al.* Electric dipole origin of the second harmonic generation of small metallic particles. *Phys. Rev. B* **71**, 165407 (2005).
50. Zayats, A. V., Kalkbrenner, T., Sandoghdar, V. & Mlynek, J. Second-harmonic generation from individual surface defects under local excitation. *Phys. Rev. B* **61**, 4545–4548 (2000).
51. Singh, A. K. *et al.* Nonlinear optical properties of triangular silver nanomaterials. *Chem. Phys. Lett.* **481**, 94–98 (2009).
52. Yildiz, B. C. *et al.* Enhanced second harmonic generation from coupled asymmetric plasmonic metal nanostructures. *J. Opt.* **17**, 125005 (2015).
53. Neacsu, C. C., Reider, G. A. & Raschke, M. B. Second-harmonic generation from nanoscopic metal tips: Symmetry selection rules for single asymmetric nanostructures. *Phys. Rev. B* **71**, 201402 (2005).

54. Czaplicki, R. *et al.* Second-Harmonic Generation from Metal Nanoparticles: Resonance Enhancement versus Particle Geometry. *Nano Lett.* **15**, 530–534 (2015).
55. O'Donnell, K. A., Torre, R. & West, C. S. Observations of second-harmonic generation from randomly rough metal surfaces. *Phys. Rev. B* **55**, 7985–7992 (1997).
56. Bozhevolnyi, S. I., Beermann, J. & Coello, V. Direct Observation of Localized Second-Harmonic Enhancement in Random Metal Nanostructures. *Phys. Rev. Lett.* **90**, 197403 (2003).
57. Canfield, B. K. *et al.* Local Field Asymmetry Drives Second-Harmonic Generation in Noncentrosymmetric Nanodimers. *Nano Lett.* **7**, 1251–1255 (2007).
58. Blau, G., Coutaz, J. L. & Reinisch, R. Second-harmonic generation by counterpropagating surface plasmons at a silver diffraction grating. *Opt. Lett.* **18**, 1352 (1993).
59. Sandrock, M. L., Pibel, C. D., Geiger, F. M. & Foss, C. A. Synthesis and Second-Harmonic Generation Studies of Noncentrosymmetric Gold Nanostructures. *J. Phys. Chem. B* **103**, 2668–2673 (1999).
60. Götz, T., Buck, M., Dressler, C., Eisert, F. & Träger, F. Optical second-harmonic generation by supported metal clusters: Size and shape effects. *Appl. Phys. A* **60**, 607–612 (1995).
61. McMahon, M. D., Lopez, R., Haglund, R. F., Ray, E. A. & Bunton, P. H. Second-harmonic generation from arrays of symmetric gold nanoparticles. *Phys. Rev. B* **73**, 041401 (2006).
62. Metzger, B. *et al.* Strong Enhancement of Second Harmonic Emission by Plasmonic Resonances at the Second Harmonic Wavelength. *Nano Lett.* **15**, 3917–3922 (2015).
63. Lesuffleur, A., Kumar, L. K. S. & Gordon, R. Enhanced second harmonic generation from nanoscale double-hole arrays in a gold film. *Appl. Phys. Lett.* **88**, 261104 (2006).
64. Atanasov, P. A., Nedyalkov, N. N., Sakai, T. & Obara, M. Localization of the electromagnetic field in the vicinity of gold nanoparticles: Surface modification of different substrates. *Appl. Surf. Sci.* **254**, 794–798 (2007).
65. Yang, M. *et al.* Plasmon-enhanced second-harmonic generation from hybrid ZnO-covered silver-bowl array. *J. Phys. Condens. Matter* **28**, 214003 (2016).
66. Turkpence, D., Akguc, G. B., Bek, A. & Tasgin, M. E. Engineering nonlinear response of nanomaterials using Fano resonances. *J. Opt.* **16**, 105009 (2014).

67. Vidal, X. *et al.* Nonlinear optical response from single spheres coated by a nonlinear monolayer. *Opt. Lett.* **33**, 699–701 (2008).
68. Clark, H. A., Campagnola, P. J., Wuskell, J. P., Lewis, A. & Loew, L. M. Second Harmonic Generation Properties of Fluorescent Polymer-Encapsulated Gold Nanoparticles. *J. Am. Chem. Soc.* **122**, 10234–10235 (2000).
69. Pu, Y., Grange, R., Hsieh, C.-L. & Psaltis, D. Nonlinear Optical Properties of Core-Shell Nanocavities for Enhanced Second-Harmonic Generation. *Phys. Rev. Lett.* **104**, 207402 (2010).
70. Shen, S. *et al.* Plasmon-Enhanced Second-Harmonic Generation Nanorulers with Ultrahigh Sensitivities. *Nano Lett.* **15**, 6716–6721 (2015).
71. Hayakawa, T., Usui, Y., Bharathi, S. & Nogami, M. Second Harmonic Generation from Coupled Surface-Plasmon Resonances in Self-Assembled Gold-Nanoparticle Monolayers Coated with an Aminosilane. *Adv. Mater.* **16**, 1408–1412 (2004).
72. Chen, K., Durak, C., Heflin, J. R. & Robinson, H. D. Plasmon-Enhanced Second-Harmonic Generation from Ionic Self-Assembled Multilayer Films. *Nano Lett.* **7**, 254–258 (2007).
73. Dong, Z. *et al.* Second-Harmonic Generation from Sub-5 nm Gaps by Directed Self-Assembly of Nanoparticles onto Template-Stripped Gold Substrates. *Nano Lett.* **15**, 5976–5981 (2015).
74. Zdanowicz, M. *et al.* Ordered multilayer silica-metal nanocomposites for second-order nonlinear optics. *Appl. Phys. Lett.* **103**, 251907 (2013).
75. Zdanowicz, M. *et al.* Second-harmonic response of multilayer nanocomposites of silver-decorated nanoparticles and silica. *Sci. Rep.* **4**, (2014).
76. Daniel, M.-C. & Astruc, D. Gold Nanoparticles: Assembly, Supramolecular Chemistry, Quantum-Size-Related Properties, and Applications toward Biology, Catalysis, and Nanotechnology. *Chem. Rev.* **104**, 293–346 (2004).
77. Thompson, D. T. Using gold nanoparticles for catalysis. *Nano Today* **2**, 40–43 (2007).
78. Gole, A. & Murphy, C. J. Seed-Mediated Synthesis of Gold Nanorods: Role of the Size and Nature of the Seed. *Chem. Mater.* **16**, 3633–3640 (2004).
79. Jana, N. R., Gearheart, L. & Murphy, C. J. Wet Chemical Synthesis of High Aspect Ratio Cylindrical Gold Nanorods. *J. Phys. Chem. B* **105**, 4065–4067 (2001).

80. Jain, P. K., Huang, X., El-Sayed, I. H. & El-Sayed, M. A. Review of Some Interesting Surface Plasmon Resonance-enhanced Properties of Noble Metal Nanoparticles and Their Applications to Biosystems. *Plasmonics* **2**, 107–118 (2007).
81. Tsuboi, K. *et al.* Second-harmonic spectroscopy of surface immobilized gold nanospheres above a gold surface supported by self-assembled monolayers. *J. Chem. Phys.* **125**, 174703 (2006).
82. Bautista, G. *et al.* Second-Harmonic Generation Imaging of Metal Nano-Objects with Cylindrical Vector Beams. *Nano Lett.* **12**, 3207–3212 (2012).
83. Chen, K. *et al.* Interface effects in plasmon-enhanced second-harmonic generation from self-assembled multilayer films. *J. Opt. Soc. Am. B* **27**, 92 (2010).

Chapter 2

Background and Literature Review

In this chapter, second-order nonlinear optics, nonlinear materials, plasmonics and colloidal gold are discussed. An introduction to nonlinear optics is given to explain the process of second harmonic generation. Nonlinear materials, from inorganic crystals to organic polymeric thin films and their applications, including nonlinear optical microscopy and electro-optic devices, are reviewed. Next, a review of plasmonics is given, followed by a background, the optical properties, and the synthesis of gold nanoparticles. Finally, applications of nanoparticles in plasmonics are discussed.

2.1 Nonlinear Optics

The optical response of a material can be expressed by the induced polarization P . For linear optics, the induced polarization depends linearly on the electric field strength as described as

$$P(t) = \varepsilon_0 \chi^{(1)} E(t), \quad (2.1)$$

where $\chi^{(1)}$ is known as the linear susceptibility and ε_0 is the permittivity of free space. This first approximation is suitable for most electromagnetic interactions with low incident electric field strengths.

In nonlinear optics, when a large incident electric field is applied to a material, the optical response can be described as a Taylor expansion of the polarization P in powers of the electric field E .

$$\begin{aligned}
P(t) &= \varepsilon_0(\chi^{(1)}E(t) + \chi^{(2)}E^2(t) + \chi^{(3)}E^3(t) + \dots) \\
&\equiv P^{(1)}(t) + P^{(2)}(t) + P^{(3)}(t) + \dots
\end{aligned} \tag{2.2}$$

The equation (2.2) is for a lossless and dispersionless material and $P(t)$ and $E(t)$ are scalar quantities and the n^{th} -order nonlinear susceptibilities $\chi^{(n)}$ are real. For a material with dispersion and/or loss, the nonlinear susceptibility becomes a complex quantity as in equation (2.3).

$$P_I = \varepsilon_0(\chi_{IJ}^{(1)}E_J + \chi_{IJK}^{(2)}E_JE_K + \chi_{IJKL}^{(3)}E_JE_KE_L + \dots) \quad I, J, K, L = 1, 2, 3 \tag{2.3}$$

By using the Einstein summation convention, each term is summed over repeated indices of the three components of Cartesian coordinates. The coefficients $\chi_{IJ\dots}^{(n)}$ correspond to the $(n+1)^{\text{th}}$ -rank tensor of the n^{th} order nonlinear susceptibility. The first coefficient, $\chi_{IJ}^{(1)}$, is the linear susceptibility, and the remaining quantities $\chi_{IJK}^{(2)}$ and $\chi_{IJKL}^{(3)}$ are the second-order and the third-order nonlinear optical susceptibilities, respectively.

For typical nonlinear crystals used in the visible and near infrared, components of $\chi^{(2)}$ are in the range of 0.5 to 5 pm/V.⁸⁴ The values of the nonlinear susceptibilities can be estimated to an order-of-magnitude for nonlinearities of electronic origin.⁸⁵ When the amplitude of the external electric field E is of the order of the atomic electric field strength $E_{\text{atomic}} = e/4\pi\varepsilon_0a_0^2$, where $a_0 = 4\pi\varepsilon_0\hbar^2/(m_e e^2)$ is the Bohr radius of the hydrogen atom, the second-order nonlinear response $P^{(2)}$ is comparable to the linear response $P^{(1)}$.¹¹ An example numerical value of the atomic electric field strength E_{atomic} is 5.14×10^{11} V/m. By applying an order-of-magnitude estimate,¹¹ $\chi^{(2)}$ is of the order of $\chi^{(1)}/E_{\text{atomic}}$ and $\chi^{(3)}$ is of the order of $\chi^{(1)}/E_{\text{atomic}}^2$. For condensed matter $\chi^{(1)}$ is roughly the product of atomic number density (of the order of a_0^{-3}) and atomic polarizability (of the order of a_0^3) and therefore $\chi^{(1)}$ is of the order of unity. Hence,

$$\chi^{(2)} \approx \frac{1}{E_{\text{atomic}}} = 1.94 \times 10^{-12} \text{ m/V} \tag{2.4.1}$$

$$\chi^{(3)} \approx \frac{1}{E_{\text{atomic}}^2} = 3.78 \times 10^{-24} \text{ m}^2/\text{V}^2. \tag{2.4.2}$$

2.2 Second Harmonic Generation

Consider the second-order term to calculate the second-order polarization for a harmonic field at angular frequency ω which is incident upon a crystal with nonzero $\chi^{(2)}$.¹¹ The electric field strength is given by

$$E(t) = Ee^{-i\omega t} + \text{c. c.} \quad (2.5)$$

The resulting second-order nonlinear polarization created in the crystal is

$$\begin{aligned} P^{(2)}(t) &= \varepsilon_0 \chi^{(2)} E^2(t) \\ &= 2\varepsilon_0 \chi^{(2)} EE^* + (\varepsilon_0 \chi^{(2)} E^2 e^{-i2\omega t} + \text{c. c.}). \end{aligned} \quad (2.6)$$

In equation (2.6) we can see that the second-order polarization contains a component at zero frequency in the first term and a component oscillating at twice the frequency of the incident light in the second term. The first term is a process known as optical rectification, in which an oscillating electric field is converted to a static electric field. The second term is referred to as second harmonic generation (SHG).

It is important to note that second-order nonlinear optical interactions can only occur in noncentrosymmetric materials. In a medium with inversion symmetry, the inversion process adds a minus sign to both the induced polarization $P \rightarrow -P$ and the applied electric field $E \rightarrow -E$. For the second-order nonlinear process, we obtain, $-P = \varepsilon_0 \chi^{(2)} (-E)^2$, which can be only true if $\chi^{(2)} = 0$. **Figure 2.1** shows how linear and nonlinear polarizations respond to the applied electric sinusoidal field in **Figure 2.1(a)**. While the polarization field for linear response has the same waveform pattern as the electric field, the polarization fields in nonlinear media show distortion in their waveforms. For a centrosymmetric medium in **Figure 2.1(c)** the induced polarization includes only odd harmonics of the fundamental frequency, but for a noncentrosymmetric medium in **Figure 2.1(d)** both even and odd harmonics exist in the waveform. Another difference between the waveforms (c) and (d) is the time-averaged response: zero for centrosymmetric medium and nonzero for noncentrosymmetric medium due to different responses to an electric field pointing in different directions.

This rule applies both on the molecular and on the macroscopic scale. Since polar molecules can be randomly oriented, a polar order should be induced in the macroscopic scale in order to achieve a second-order nonlinear optical response. This can be achieved by several methods such as electric poling, noncentrosymmetric crystal growth, and the Langmuir-Blodgett technique, which will be discussed in **Section 2.6**.

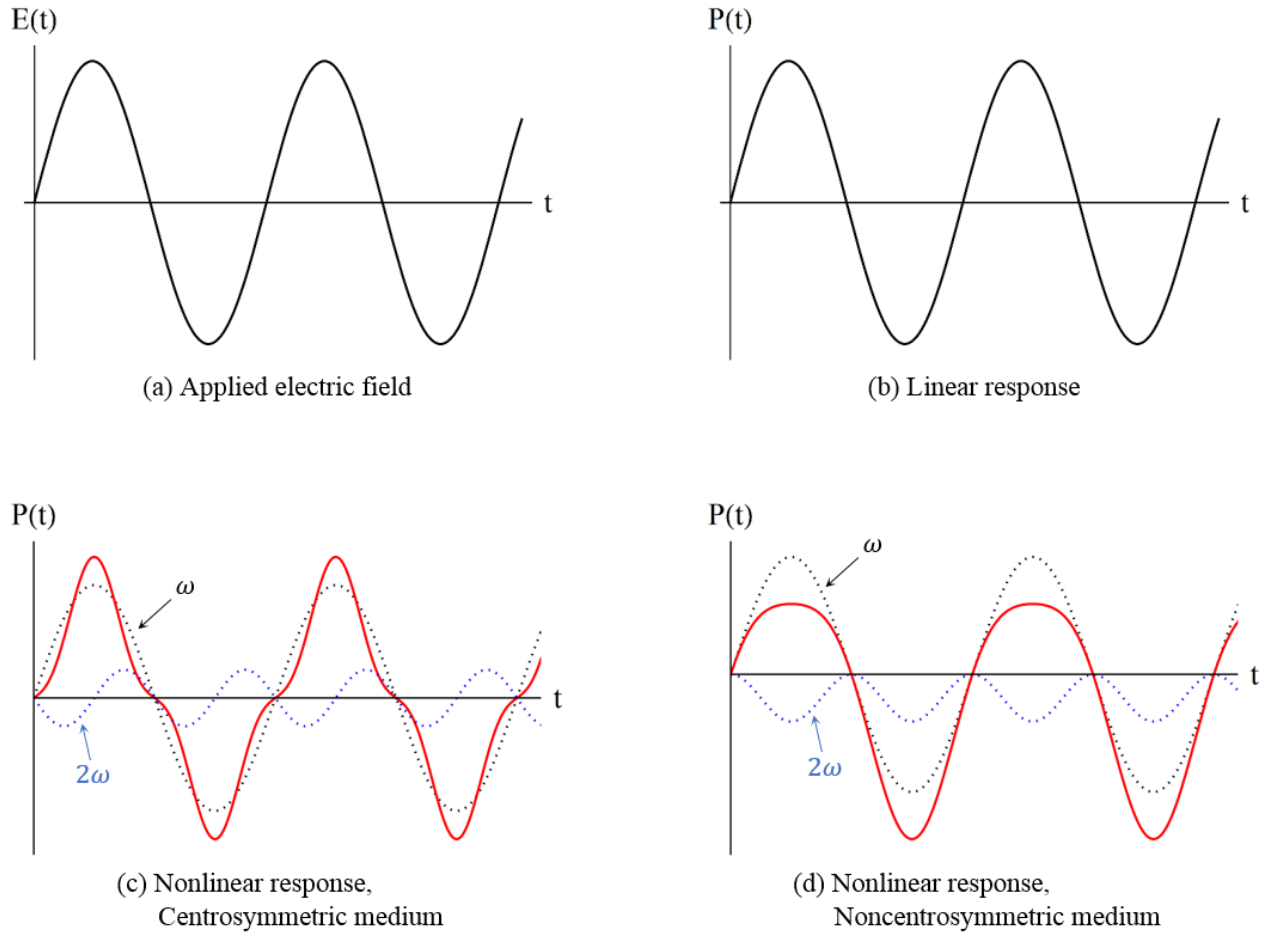


Figure 2.1 Waveforms of electric field and polarization fields in different media. (a) Applied electric field as a sinusoidal wave of frequency ω . (b) The generated polarization shows no distortion of the waveform. (c) In a nonlinear medium possessing a center of symmetry, the polarization (in red) is the sum of linear polarization of frequency ω (in black) and second-order polarization of frequency 2ω (in blue). The time-averaged response is zero. (d) In a noncentrosymmetric medium, the polarization (in red) is the sum of the linear polarization of frequency ω (in black) and second-order polarization of frequency 2ω (in blue). The time-averaged response is nonzero.

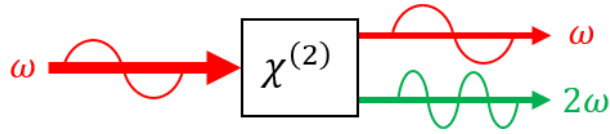


Figure 2.2 Illustration of Second Harmonic Generation

In the process of second harmonic generation two photons of frequency ω are annihilated and a photon of frequency 2ω is simultaneously created in a single quantum-mechanical process as shown in **Figure 2.2**. The second harmonic wave of frequency 2ω is induced by the polarization wave of frequency 2ω which is generated in the nonlinear medium by the fundamental wave of frequency ω .

This process can be efficient enough, in principle, to have all of the incident power at frequency ω converted to radiation at the second harmonic frequency 2ω . This is possible when the fundamental and second harmonic waves travel at the same velocity in the crystal. This process is called phase-matching which ensures the second harmonic wave generated at different positions in the crystal interfere constructively and therefore, the generated wave can extract energy most efficiently from the incident waves. However, it is most often the case that the conversion efficiencies are typically extremely small due to frequency dispersion in which the second harmonic and fundamental wave travel out of phase through the nonlinear optical medium. Conversion efficiency of second harmonic generation will be discussed in detail in **Section 2.5**.

2.3 Sum- and Difference-Frequency Generation

The second harmonic generation process is a special type of sum-frequency generation as shown in **Figure 2.3**. It is also a parametric process where energy and momentum are conserved, and thus, the nonlinear medium is in the same quantum state at the end as in the beginning.⁸⁶ Ideally parametric processes are lossless and the nonlinear susceptibility is real.

Now consider the case of the incident electric field with frequencies ω_1 and ω_2 and a static electric field E_0 in a medium with nonzero $\chi^{(2)}$ in the form

$$\vec{E}(t) = E_1 e^{-i\omega_1 t} + E_2 e^{-i\omega_2 t} + E_0 + \text{c. c.} \quad (2.7)$$

The second-order contribution to the nonlinear polarization can be written as follows.

$$\begin{aligned} \vec{P}^{(2)}(t) &= \varepsilon_0 \chi^{(2)} \vec{E}^2(t) \\ &= \varepsilon_0 \chi^{(2)} (2E_1 E_1^* + 2E_2 E_2^* + E_0^2 \\ &\quad + 2E_0 E_1 e^{-i\omega_1 t} + 2E_0 E_2 e^{-i\omega_2 t} + E_1^2 e^{-2i\omega_1 t} + E_2^2 e^{-2i\omega_2 t} \\ &\quad + 2E_1 E_2 e^{-i(\omega_1 + \omega_2)t} + 2E_1 E_2^* e^{-i(\omega_1 - \omega_2)t} + \text{c. c.}) \end{aligned} \quad (2.8.1)$$

Using the following notation¹¹

$$\vec{P}^{(2)}(t) = \sum_n P(\omega_n) e^{-i\omega_n t}, \quad (2.8.2)$$

where the summation extends over positive and negative frequencies ω_n , the various frequency components of the nonlinear polarization are shown in **Table 2.1**.

Table 2.1 Second-order optical nonlinear effects

Polarization amplitude	Effect
$P(2\omega_1) = \varepsilon_0 \chi^{(2)} E_1^2$ $P(2\omega_2) = \varepsilon_0 \chi^{(2)} E_2^2$	Second Harmonic Generation (SHG)
$P(\omega_1 + \omega_2) = 2\varepsilon_0 \chi^{(2)} E_1 E_2$	Sum-Frequency Generation (SFG)
$P(\omega_1 - \omega_2) = 2\varepsilon_0 \chi^{(2)} E_1 E_2^*$	Difference-Frequency Generation (DFG)
$P(\omega_1) = 2\varepsilon_0 \chi^{(2)} E_0 E_1$ $P(\omega_2) = 2\varepsilon_0 \chi^{(2)} E_0 E_2$	(Linear) Electro-optic Effect (EO)
$P(0) = 2\varepsilon_0 \chi^{(2)} (E_1 E_1^* + E_2 E_2^*) + E_0^2$	Optical Rectification (OR)

Although there are five different frequency components in the nonlinear polarization, typically only one of these are present with any observable intensity. This is because a phase-matching condition for a certain process cannot be satisfied for more than one frequency component of the nonlinear polarization.¹¹ Applications of each process are provided in the rest of this section.

The second-order nonlinear effects can be applied to create useful devices such as frequency up-converters, optical parametric oscillators (down-converters), spectroscopy, Pockels cell Q-switch, phase/amplitude modulators, and beam deflectors⁸⁷.

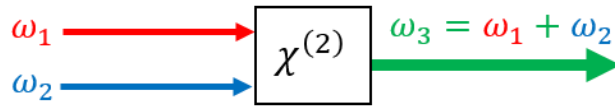


Figure 2.3 Illustration of Sum-Frequency Generation

Sum-frequency generation can be applied to produce visible or UV light. A yellow laser beam with a wavelength of 589 nm can be created by mixing the inputs of a laser with a wavelength 1064 nm and another with a wavelength 1319 nm.⁸⁸ Similarly, a UV laser beam with a wavelength 355 nm can be created by mixing the inputs of a laser with a wavelength 1064 nm and its second harmonic generation with a wavelength 532 nm.⁸⁹ A tunable source in the UV spectral region can be made by selecting one of the input beams (e.g., ω_1 in **Figure 2.3**) to be the output of a fixed-frequency visible laser and the other (e.g., ω_2 in **Figure 2.3**) to be the output of a frequency tunable visible laser. It can also be used to analyze surfaces and interfaces in SFG spectroscopy which is discussed in detail in **Section 2.7**.

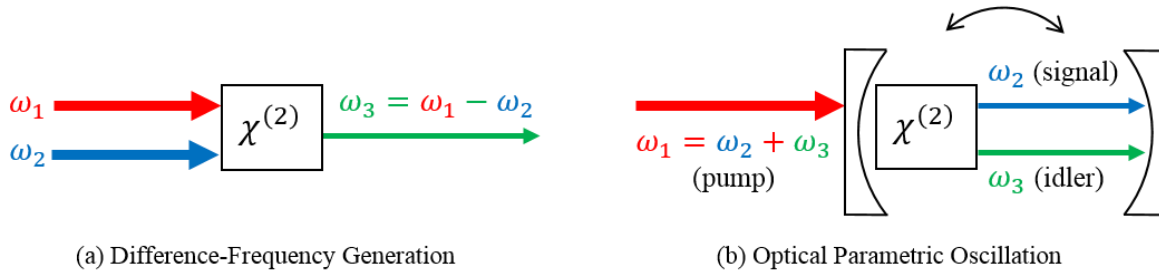


Figure 2.4 Illustration of Difference-Frequency Generation

Difference-frequency generation (DFG) can be applied to produce tunable infrared light by mixing a frequency of a tunable laser with a fixed frequency of a visible laser, i.e., generation of light of $4.5\ \mu\text{m}$ by mixing wavelengths $860\ \text{nm}$ and $1064\ \text{nm}$. In a DFG process, a photon at the higher input frequency (ω_1 in **Figure 2.4a**) is destroyed and a photon at a lower input frequency (ω_2 in **Figure 2.4a**) is created to form a photon at the difference frequency (ω_3 in **Figure 2.4a**).¹¹ As the higher input frequency (ω_1) is weakened, the lower output frequency (ω_3) is amplified by this process and thus the DFG process is also known as optical parametric amplification (OPA). If a nonlinear crystal used in DFG is placed in an optical resonator which has mirrors reflective at frequencies ω_2 and/or ω_3 , as in **Figure 2.4b**, coherent output at these frequencies can build up to large values. This device is known as an optical parametric oscillator (OPO), and it is tuned by changing the orientation of the crystal. The applied input frequency (ω_1) is called the pump frequency, the desired output (ω_2) is called the signal frequency, and the difference frequency generation output (ω_3) is called the idler frequency.

The electro-optic effect describes a change in the refractive index of a material caused by a static electric field. Noncentrosymmetric materials exhibit the linear electro-optic effect, also known as the Pockels effect, where the refractive index changes linearly with the applied electric field strength. All centrosymmetric materials exhibit only the quadratic electro-optic effect, also known as the Kerr effect, where the refractive index changes quadratically with the applied electric field strength, and it is weaker than the Pockels effect. Electro-optic materials refer to materials exhibiting the Pockels effect and will be discussed in **Section 2.7**.

Optical rectification can convert a sinusoidal electric field to a DC polarization. It was first reported by Bass *et al.*⁹⁰ in 1962 for ruby laser light passing through the crystals potassium dihydrogen phosphate (KDP) and potassium dideuterium phosphate (KD₂P). It also can be applied for the generation of terahertz radiation by using an ultrashort pulsed laser.

The time-dependent polarizations in equation (2.8) can act as the source term in the inhomogeneous electromagnetic wave equation

$$\nabla^2 \vec{E} - \frac{n^2}{c^2} \frac{\partial^2 \vec{E}}{\partial t^2} = \frac{1}{\epsilon_0 c^2} \frac{\partial^2 \vec{P}^{NL}}{\partial t^2}, \quad (2.9)$$

where n is the linear refractive index and c is the speed of light in vacuum.¹¹ The second derivative of the polarization with respect to time, $\partial^2 \vec{P}^{NL} / \partial t^2$, is a measure of the acceleration of the charges in the nonlinear medium that can generate electromagnetic radiation. The coupled wave equations will be studied to calculate the efficiency of the second harmonic generation in **Section 2.5**. The electromagnetic radiation generated by the second-order nonlinear polarization field in a nonlinear medium can be used in technological applications as explored in **Section 2.7**.

2.4 Second-Order Nonlinear Susceptibility

In a material with dispersion and/or loss, the nonlinear susceptibility becomes a complex quantity relating the complex amplitudes of the electric field and polarization.¹¹ The nonlinear polarization can be represented as the discrete sum of a number of frequency components as

$$\vec{P}(\vec{r}, t) = \sum_{n>0} \vec{P}_n(\vec{r}) e^{-i\omega_n t} + \text{c. c.} \quad (2.10.1)$$

$$\vec{P}_n(\vec{r}) = \vec{P}_n e^{i\vec{k}_n \cdot \vec{r}}. \quad (2.10.2)$$

If we introduce an alternative notation

$$\vec{P}_n(\vec{r}) = \vec{P}(\omega_n) \quad (2.11.1)$$

$$\vec{P}(-\omega_n) = \vec{P}(\omega_n)^* \quad (2.11.2)$$

then the total polarization becomes

$$\vec{P}(\vec{r}, t) = \sum_n \vec{P}(\omega_n) e^{-i\omega_n t}. \quad (2.12)$$

Similarly, the electric field can be expressed as

$$\vec{E}(\vec{r}, t) = \sum_n \vec{E}(\omega_n) e^{-i\omega_n t} \quad (2.13.1)$$

$$\vec{E}_n(\vec{r}) = \vec{A}_n e^{i\vec{k}_n \cdot \vec{r}} \text{ and } \vec{E}(-\omega_n) = \vec{E}(\omega_n)^* \quad (2.13.2)$$

where \vec{A}_n is a slowly varying amplitude.

The components of the second-order susceptibility tensor are defined as the proportionality constants relating the nonlinear polarization amplitude to the product of electric field amplitudes.

$$P_I(\omega_n + \omega_m) = \varepsilon_0 \sum_{JK} \sum_{nm} \chi_{IJK}^{(2)}(\omega_n + \omega_m, \omega_n, \omega_m) E_J(\omega_n) E_K(\omega_m). \quad (2.14)$$

The sum $\omega_n + \omega_m$ is held fixed, although ω_n and ω_m are allowed to vary. For second harmonic generation, if we take the input frequency as ω and the generated frequency as 2ω , we obtain

$$P_I(2\omega) = \varepsilon_0 \sum_{JK} \chi_{IJK}^{(2)}(-2\omega; \omega, \omega) E_J(\omega) E_K(\omega) \quad (2.15)$$

where the negative sign and semicolon indicate that 2ω is the output frequency.

In equation (2.14), $\chi_{IJK}^{(2)}$ is a 3rd-rank tensor of 27 components where indices IJK refer to the Cartesian components of the field (x, y, z or 1,2,3):

$$\begin{pmatrix} \chi_{xxx}^{(2)} & \chi_{xyy}^{(2)} & \chi_{xzz}^{(2)} & \chi_{xyz}^{(2)} & \chi_{xzy}^{(2)} & \chi_{xzx}^{(2)} & \chi_{xxz}^{(2)} & \chi_{xxy}^{(2)} & \chi_{xyx}^{(2)} \\ \chi_{yxx}^{(2)} & \chi_{yyy}^{(2)} & \chi_{yzz}^{(2)} & \chi_{yyz}^{(2)} & \chi_{yzy}^{(2)} & \chi_{yzz}^{(2)} & \chi_{yxx}^{(2)} & \chi_{yxy}^{(2)} & \chi_{yyx}^{(2)} \\ \chi_{zxx}^{(2)} & \chi_{zyy}^{(2)} & \chi_{zzz}^{(2)} & \chi_{zzy}^{(2)} & \chi_{zzy}^{(2)} & \chi_{zxx}^{(2)} & \chi_{zxx}^{(2)} & \chi_{zxy}^{(2)} & \chi_{zyx}^{(2)} \end{pmatrix}. \quad (2.16)$$

However, the number of independent and nonzero components of $\chi_{IJK}^{(2)}$ can be reduced by using four properties of nonlinear susceptibilities: complex-conjugation symmetry, time-reversal symmetry, permutation symmetry, and Kleinman's symmetry.⁹¹

Complex-conjugation symmetry

Since the polarization and the electric field are measurable quantities, they must be real and thus show a complex conjugation relationship between positive and negative frequency components as shown in equations (2.11.2) and (2.13.2). Similarly, the following is satisfied for the positive and negative frequency components of the susceptibility.

$$\chi_{IJK}^{(2)}(-\omega_n - \omega_m, -\omega_n, -\omega_m) = \left[\chi_{IJK}^{(2)}(\omega_n + \omega_m, \omega_n, \omega_m) \right]^* \quad (2.17)$$

Time-reversal symmetry

The susceptibility tensors are invariant for simultaneous change of sign for all frequency arguments. This is valid only for a nonresonant (nonabsorptive) interaction where the applied field frequencies ω_i are much smaller than the resonance frequency ω_0 . Because the nonlinear susceptibilities are real quantities in a nonresonant medium, we have

$$\left[\chi_{IJK}^{(2)}(\omega_n + \omega_m, \omega_n, \omega_m) \right]^* = \chi_{IJK}^{(n)}(\omega_n + \omega_m, \omega_n, \omega_m). \quad (2.18)$$

However, equation (2.17) is always true, therefore

$$\chi_{IJK}^{(2)}(\omega_n + \omega_m, \omega_n, \omega_m) = \chi_{IJK}^{(2)}(-\omega_n - \omega_m, -\omega_n, -\omega_m). \quad (2.19)$$

Permutation symmetry

There are two types of permutation symmetries, intrinsic permutation symmetry and full permutation symmetry. The intrinsic permutation is valid for both resonant and nonresonant interactions, while the full permutation symmetry holds only for nonresonant interactions.

In the intrinsic permutation symmetry, the elements of nonlinear susceptibility tensors are equal for all simultaneous interchanges of the last two Cartesian indices (J, K) and the corresponding frequency arguments (ω_n and ω_m).

$$\chi_{IJK}^{(2)}(\omega_n + \omega_m, \omega_n, \omega_m) = \chi_{IKJ}^{(2)}(\omega_m + \omega_n, \omega_m, \omega_n). \quad (2.20)$$

It states that the order of electric field components in equation (2.14) is irrelevant, i.e. $E_j(\omega_n)E_k(\omega_m) = E_k(\omega_m)E_j(\omega_n)$.

On the other hand, in a nonresonant, lossless medium where all of the nonlinear susceptibilities are real, full permutation symmetry is possible. Not only does the equation (2.20) hold, but the elements of nonlinear susceptibility tensors are also equal for all arbitrary simultaneous interchanges of subscript positions (I, J, K) and corresponding frequency arguments ($\omega_n + \omega_m, \omega_n, \omega_m$). The first frequency argument is always the sum of the other two and when it is interchanged with either of the two frequencies their signs must be inverted. Considering three waves of frequencies ω_1, ω_2 , and ω_3 , where $\omega_3 = \omega_1 + \omega_2$,

$$\chi_{IJK}^{(2)}(\omega_3 = \omega_1 + \omega_2) = \chi_{JKI}^{(2)}(-\omega_1 = \omega_2 - \omega_3) \quad (2.21)$$

By the complex-conjugated symmetry, $\chi_{JKI}^{(2)}(-\omega_1 = \omega_2 - \omega_3) = \left[\chi_{JKI}^{(2)}(\omega_1 = -\omega_2 + \omega_3) \right]^*$, and by the time-reversal symmetry $\left[\chi_{JKI}^{(2)}(\omega_1 = -\omega_2 + \omega_3) \right]^* = \chi_{JKI}^{(2)}(\omega_1 = -\omega_2 + \omega_3)$.

Hence, this leads to the result that

$$\chi_{IJK}^{(2)}(\omega_3 = \omega_1 + \omega_2) = \chi_{JKI}^{(2)}(\omega_1 = -\omega_2 + \omega_3). \quad (2.22)$$

Continuing with the procedure leads to the following

$$\begin{aligned} \chi_{IJK}^{(2)}(\omega_3 = \omega_1 + \omega_2) &= \chi_{JKI}^{(2)}(\omega_1 = -\omega_2 + \omega_3) = \chi_{KIJ}^{(2)}(\omega_2 = \omega_3 - \omega_1) \\ &= \chi_{IKJ}^{(2)}(\omega_3 = \omega_2 + \omega_1) = \chi_{KJI}^{(2)}(\omega_2 = -\omega_1 + \omega_3) = \chi_{JIK}^{(2)}(\omega_1 = \omega_3 - \omega_2). \end{aligned} \quad (2.23)$$

Kleinman's symmetry

If there is no dispersion of the susceptibility in a nonresonant medium, i.e. $\chi^{(2)}$ is independent of the frequencies, then it satisfies the Kleinman symmetry condition where the indices can be freely permuted without permuting the frequencies.

$$\chi_{IJK}^{(2)}(\omega_3) = \chi_{JKI}^{(2)}(\omega_3) = \chi_{KIJ}^{(2)}(\omega_3) = \chi_{IKJ}^{(2)}(\omega_3) = \chi_{KJI}^{(2)}(\omega_3) = \chi_{JIK}^{(2)}(\omega_3) \quad (2.24)$$

Since E_J and E_K can be exchanged in equation (2.14), the tensor is symmetric in the permutation of J and K , thus it follows that

$$\chi_{xyz}^{(2)} = \chi_{xzy}^{(2)}, \quad \chi_{yzx}^{(2)} = \chi_{yxz}^{(2)}, \quad \chi_{zxy}^{(2)} = \chi_{zyx}^{(2)}, \quad \dots \quad (2.25)$$

Then the tensor in equation (2.16) is reduced to the following 18 components

$$\begin{pmatrix} P_x^{2\omega} \\ P_y^{2\omega} \\ P_z^{2\omega} \end{pmatrix} = \varepsilon_0 \begin{pmatrix} \chi_{xxx}^{(2)} & \chi_{xyy}^{(2)} & \chi_{xzz}^{(2)} & \chi_{xyz}^{(2)} & \chi_{xzx}^{(2)} & \chi_{xxy}^{(2)} \\ \chi_{yxx}^{(2)} & \chi_{yyy}^{(2)} & \chi_{yzz}^{(2)} & \chi_{yyz}^{(2)} & \chi_{yzz}^{(2)} & \chi_{yyx}^{(2)} \\ \chi_{zxx}^{(2)} & \chi_{zyy}^{(2)} & \chi_{zzz}^{(2)} & \chi_{zyz}^{(2)} & \chi_{zzx}^{(2)} & \chi_{zxy}^{(2)} \end{pmatrix} \begin{pmatrix} E_x^2 \\ E_y^2 \\ E_z^2 \\ 2E_y E_z \\ 2E_x E_z \\ 2E_x E_y \end{pmatrix} \quad (2.26)$$

The second-order susceptibility tensor $\chi_{IJK}^{(2)}$ can be defined by

$$d_{IJK} = \frac{1}{2} \chi_{IJK}^{(2)} \quad (2.27)$$

which leads to

$$P_I(2\omega) = \varepsilon_0 \sum_{JK} 2d_{IJK} E_J(\omega) E_K(\omega). \quad (2.28)$$

where the nonlinear susceptibility tensor d_{IJK} is a 3×6 matrix

$$d_{IL} = \begin{pmatrix} d_{11} & d_{12} & d_{13} & d_{14} & d_{15} & d_{16} \\ d_{21} & d_{22} & d_{23} & d_{24} & d_{25} & d_{26} \\ d_{31} & d_{32} & d_{33} & d_{34} & d_{35} & d_{36} \end{pmatrix}. \quad (2.29)$$

The nonlinear optical coefficient d_{IJK} is symmetric in J and K , and therefore $d_{IJK} = d_{IKJ} = d_{IL}$ where $L = J$ for $J = K$ and $L = 9 - (J + K)$ otherwise.

L	1	2	3	4	5	6
JK	11	22	33	23 32	13 31	12 21

If the material is nonabsorbing and dispersionless, the Kleinman relation⁹² yields

$$\mathbf{d}_{IJK} = \mathbf{d}_{JKI} = \mathbf{d}_{KIJ} = \mathbf{d}_{JIK} = \mathbf{d}_{KJI} = \mathbf{d}_{IKJ}$$

$$d_{14} = d_{25} = d_{36}$$

$$d_{12} = d_{26}$$

$$d_{23} = d_{34}$$

$$d_{13} = d_{35}$$

$$d_{16} = d_{21}$$

$$d_{24} = d_{32}$$

$$d_{31} = d_{15}$$

For fixed propagation and polarization directions, the nonlinear polarization (with $\omega_3 = \omega_1 + \omega_2$) can be expressed by the scalar relationship

$$P(\omega_3) = 4\varepsilon_0 d_{\text{eff}} E(\omega_1) E(\omega_2). \quad (2.30.1)$$

And for second harmonic generation

$$P(2\omega) = 2\varepsilon_0 d_{\text{eff}} E(\omega)^2 \quad (2.30.2)$$

where $E(\omega) = |\vec{E}(\omega)|$, $P(\omega) = |\vec{P}(\omega)|$, and d_{eff} is the effective nonlinear optical susceptibility.

2.5 Coupled Wave Equation for Efficiency of Second Harmonic Generation

The conversion efficiency per unit length of second harmonic generation is a ratio of the second harmonic intensity to that of the fundamental. The intensity of second harmonic wave can be found by solving the wave equation (2.9). If the fundamental wave has a high intensity and not too much power is transferred into the second harmonic wave, we can neglect pump depletion (known as the slowly-varying amplitude approximation).⁸⁶ In this approximation, the field amplitudes vary slowly over distances comparable to a wavelength, and the second-order spatial derivative and the square of the first-order spatial derivative of their amplitude functions can be neglected.⁹¹

The wave equation (2.9) can be written for the electric fields propagating in the z direction

$$\frac{\partial^2 E_i(z, t)}{\partial z^2} - \frac{n_i}{c^2} \frac{\partial E_i(z, t)}{\partial t^2} = \frac{1}{\varepsilon_0 c^2} \frac{\partial^2 P_i}{\partial t^2} \quad i = 1, 2 \quad (2.31)$$

where $i = 1, 2$ represent the fundamental and the second harmonic wave, respectively.

The solution to the wave equation (2.31) for a second harmonic wave at frequency 2ω is a plane wave propagating in the z direction.

$$E_i(z, t) = A_i(z)e^{i(k_iz - \omega_it)} + \text{c. c.} \quad i = 1, 2 \quad (2.32)$$

where $k_i = n_i\omega_i/c$ and $A_i(z)$ is a slowly varying amplitude.

The nonlinear polarization is a source term in the wave equation and given by

$$P^{NL}(z, t) = P_1(z)e^{-i\omega_1t} + P_2(z)e^{-i\omega_2t} + \text{c. c.} \quad (2.33)$$

The polarization components can be found from equations (2.30) and (2.30.2)

$$P_1(z) = 4\varepsilon_0 d_{\text{eff}} E_2 E_1^* = 2\varepsilon_0 d_{\text{eff}} A_2(z) A_1^*(z) e^{i(k_2 - k_1)z} \quad (2.34.1)$$

$$P_2(z) = 2\varepsilon_0 d_{\text{eff}} (A_1(z))^2 e^{2ik_1z}. \quad (2.34.2)$$

Substituting equations (2.32), (2.33), (2.34), and (2.34.2) into the wave equation (2.31) and using the slowly varying amplitude approximation where $|d^2 A_2/dz^2| \ll |k_2 dA_2/dz|$ result in

$$\frac{dA_1(z)}{dz} = \frac{2i\omega_1^2 d_{\text{eff}}}{k_1 c^2} A_2(z) A_1^*(z) e^{-i\Delta kz} \quad (2.35)$$

and

$$\frac{dA_2(z)}{dz} = \frac{i\omega_2^2 d_{\text{eff}}}{k_2 c^2} (A_1(z))^2 e^{i\Delta kz} \quad (2.36)$$

where $\Delta k = 2k_1 - k_2$ is called the wavevector mismatch.

The second harmonic wave can be generated by a single Gaussian beam of frequency ω , focused on a parallel slab of thickness L of a nonlinear crystal. After a distance L of the nonlinear medium, the intensity of the second harmonic field is given by integrating equation (2.36) from $z = 0$ to $z = L$ with the initial condition $A_2(0) = 0$:

$$A_2(L) = \frac{i\omega_2^2 d_{\text{eff}}}{k_2 c^2} A_1^2 \int_0^L e^{i\Delta kz} dz = \frac{i\omega_2^2 d_{\text{eff}}}{k_2 c^2} A_1^2 \frac{(e^{i\Delta kL} - 1)}{i\Delta k} \quad (2.37)$$

The intensity of a wave is the magnitude of the time-averaged Poynting vector¹¹

$$I_i = 2n_i \varepsilon_0 c |A_i|^2, \quad i = 1, 2 \quad (2.38)$$

Then the second harmonic intensity is given by⁸⁵

$$I_2 = \frac{2\omega_1^2}{\varepsilon_0 c^3 (n_1)^2 n_2} (d_{\text{eff}})^2 (L)^2 (I_1)^2 \text{sinc}^2\left(\frac{\Delta k L}{2}\right) \quad (2.39)$$

where $\text{sinc}(x) = \sin(x)/x$, d_{eff} = effective nonlinear optical susceptibility, c is the vacuum speed of light, and $\Delta k = |\vec{k}_2 - 2\vec{k}_1|$ is the phase mismatch between the fundamental and second harmonic. The wavevectors are $k_2 = \omega_2 n_2 / c$ and $k_1 = \omega_1 n_1 / c$, and refractive indices are n_2 and n_1 for frequency $\omega_2 = 2\omega$ and $\omega_1 = \omega$, respectively.

The intensity of the second harmonic wave is proportional to the square of the intensity of the fundamental wave and increases quadratically with the crystal length L when $\Delta k = 0$. In this case, when the phase-matching condition is achieved, all dipoles of the material are properly phased to emit an oscillating field which coherently adds in the forward direction. However, in general, due to the crystal dispersion, Δk is nonzero and the efficiency of the process decreases as $|\Delta k|L$ increases as shown in **Figure 2.5**.

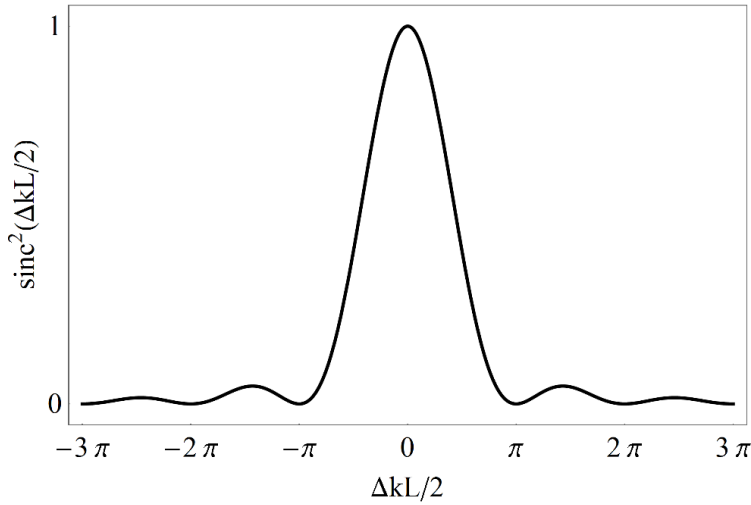


Figure 2.5 The phase mismatch factor of second harmonic generation

For the case of $\Delta k \neq 0$, the intensity of the second harmonic wave along the z direction is derived from equation (2.36) and (2.38) with the initial condition $A_2(0) = 0$ for an undepleted pump, i.e., $A_1(z) \approx A_1(0)$:

$$A_2(z) = \frac{\omega_2 d_{\text{eff}}}{n_2 c \Delta k} A_1^2 (e^{i\Delta k z} - 1) \quad (2.40)$$

and

$$\begin{aligned} I_2(z) &= 2n_2 \varepsilon_0 c |A_2(z)|^2 \\ &= \frac{\varepsilon_0 \omega_2^2 d_{\text{eff}}^2}{2n_1^2 n_2 c^3} I_1^2 \left(\frac{\sin\left(\frac{\Delta k z}{2}\right)}{\frac{\Delta k}{2}} \right)^2. \end{aligned} \quad (2.41)$$

The second harmonic propagating intensity is proportional to the square of the intensity of the incident fundamental wave and oscillates periodically as a function of the crystal length, L , with a period of $2\pi/\Delta k$ along the z axis for a fixed nonzero Δk as shown in **Figure 2.6**. When the phases of the second harmonic wave and its driving polarization waves are not matched, the energy from the fundamental wave cannot transfer to the second harmonic wave effectively. Therefore, the energy transferred by the SHG quickly oscillates back and forth between pump and second harmonic wave, instead of consistently moving in certain direction.

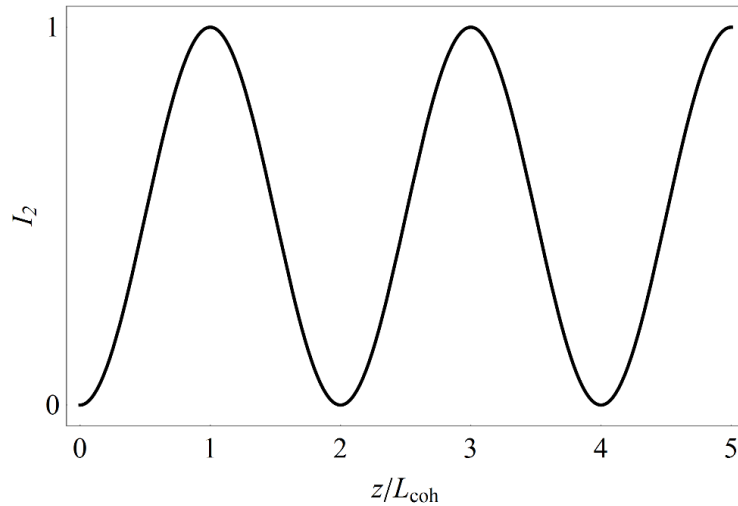


Figure 2.6 Normalized second harmonic intensity versus z for $\Delta k \neq 0$.

2.6 Nonlinear Optical Materials

The invention of the laser accelerated research exploration in nonlinear optics and it became necessary to develop materials for its applications. To achieve a nonlinear optical (NLO) interaction, the material must be well transmissive to the incident and generated radiation. It also needs to withstand the laser intensity without damaging and allow for phase-matching. Most importantly, for $\chi^{(2)}$ to be non-zero, the material must lack a center of inversion symmetry.

There are two types of materials studied in the past three decades. The first type is bulk materials such as inorganic crystals and nonlinearities in these materials come from electrons not associated with individual nuclei. The second type is molecular materials such as organic crystals and polymers and for these materials the nonlinearity comes from the molecular structure. Molecules that can be excited by absorption of light are called chromophores and the molecular origin of their optical nonlinearity comes from their electrical polarization which interacts with electromagnetic radiation. In noncentrosymmetric materials, asymmetric chromophores must have polar alignment in NLO materials.

2.6.1 Inorganic Materials for SHG

In early research into second-order nonlinear optics, the materials studied for second-order optical nonlinearity were inorganic single crystals, such as lithium niobate (LiNbO_3), β -barium borate (BBO) and potassium dihydrogen phosphate (KDP). These crystals exhibit sufficient magnitude of $\chi^{(2)}$ on the order of 10^{-14} to 10^{-12} m/V.⁸⁴ In order to achieve significant conversion efficiency, the crystals need to be greater than 1 mm in length (thousands of wavelengths long). The polarizability of inorganic crystals originates mostly from the interaction between the lattice components such as atoms and molecules. Therefore, the electronic characteristics of the bulk medium play a dominant role in nonlinear optical effects of inorganic materials. Therefore, in the inorganic materials system, higher-order nonlinear optical effects are resonant (absorptive) which limits the bandwidth of a modulator due to absorption and heat dissipation.

The majority of inorganic crystals are fabricated by growth from the liquid phase, which is a complicated, time-consuming, and highly sensitive process. It also requires post-processing such

as high temperature annealing and vapor treatment, as well as precise orientation, cutting, and surface smoothing by grinding, lapping, polishing, and finally coating. There are issues of moisture incorporation in raw chemicals, volatilization losses during heating and reaction, and infiltration of impurity species.⁸⁴ In addition, for a ferroelectric crystal which has domains within each of which the electric dipole orientation is uniform, it is necessary to perform the poling process to achieve a single consistent dipole orientation throughout the volume. Finally, process-dependent properties of the NLO materials tend to vary from one crystal to the next. Despite these issues, nearly all commercial frequency conversion and electro/optic devices utilize inorganic crystals.

2.6.2 Organic Molecules for SHG

The discovery of strong second harmonic generation in organic molecules by Davydov *et al.*⁹³ in 1970 introduced the approach of molecular engineering to synthesize new organic materials for the study of SHG. In this new concept, the second-order NLO effects in organic molecules come from a strong intramolecular interaction between electron donor and acceptor groups connected with a benzene ring. **Figure 2.7** shows an illustration of highly polarizable charge transfer molecules in terms of Mulliken resonance structures of the ground and excited states.⁹⁴

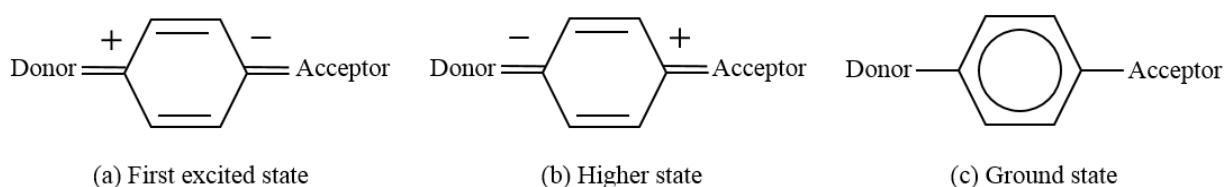


Figure 2.7 Illustration of donor-acceptor group connected with a benzene ring. (Mulliken resonance states) (a) First excited state where one electron is transferred from the donor to the acceptor which gives maximum charge transfer state. (b) Higher state where one electron is transfer from the acceptor to the donor. (c) Neutral state.

The nonlinear optical response of organic molecular crystals is predominantly due to the polarizability of the electrons in the π bonding orbitals. The π electrons tend to be delocalized and less tightly bound, and therefore they are more easily polarizable and can respond freely to an applied electric field producing large nonlinear optical responses.

When an oscillating electric field is applied to the π electrons of a donor-acceptor molecule, charge flow is preferential in one direction. The consequence is an asymmetric response to an applied electric field as shown in **Figure 2.8** in solid lines in contrast to the dotted lines that show a symmetric response. This distortion results in the harmonic frequencies in the field radiated by the molecular dipole oscillations. The large susceptibility of donor-acceptor conjugated systems typically comes from the large difference in dipole moment between the ground state and the first excited state.

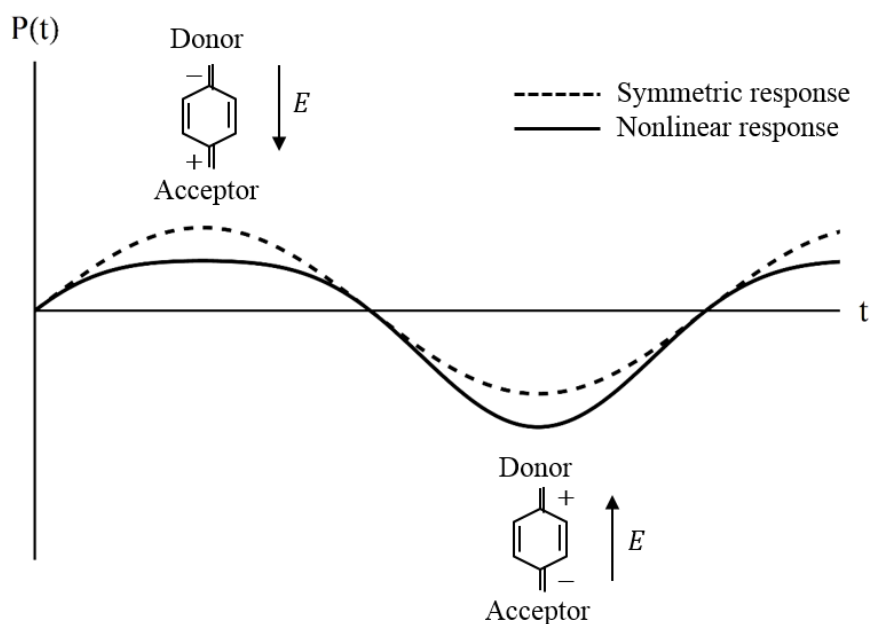


Figure 2.8 Illustration of an asymmetric electronic response of the polarization for molecules with donor-acceptor groups. The distortion in the nonlinear response is due to the preferred direction of the charge flow towards the acceptor.

Since the discovery of SHG effects in organic molecules, organic materials such as many organic crystals and polymers were increasingly investigated to optimize their molecular structures for maximum second-order nonlinear responses. In organic crystals, the molecules behave independently of each other due to the weak intermolecular interactions and therefore only the net orientations in the crystal lattice contribute to the macroscopic optical nonlinearity. This approach is known as the oriented gas model.⁹⁵ Almost all significant organic molecules in nonlinear optics have a π bond structure which has regions of delocalized electronic charge distribution above and below the intermolecular axis. This delocalized electronic charge distribution can be displaced by substituents. The dipole moment describes the amount of redistribution and the hyperpolarizability quantifies the ease of causing charge redistribution in response to an externally applied electric field. The net orientation of the molecules contributes to the macroscopic polarization P in equation (2.3).

Molecular Polarization and Hyperpolarizability

The polarization p of a molecule induced by an external field E can be described by

$$p_i = \mu_i + \epsilon_0 \left(\alpha_{ij}^{(1)} E_j + \beta_{ijk}^{(2)} E_j E_k + \gamma_{ijkl}^{(3)} E_j E_k E_l + \dots \right) \quad i, j, k, l = x, y, z \quad (2.41.1)$$

where (x, y, z) is the molecular coordinate system, μ_i is the ground state (permanent) dipole moment, α_{ij} is the polarizability tensor, β_{ijk} is the second-order polarizability or first-order hyperpolarizability tensor, and γ_{ijkl} is the second-order hyperpolarizability tensor. A quadratic nonlinear response results if the perturbation to the molecular electronic distribution induced by a strong optical field is asymmetric.

The second-order nonlinear optical polarizabilities of molecules can be determined experimentally by the EFISH (electric-field induced SHG) method⁹⁶ in which a DC field induces reorientation of chromophores in solution or by surface SHG⁹⁷ in which a monolayer of molecules are adsorbed on glass/water.

The bulk material's susceptibility can be calculated as a thermodynamic sum over the molecules.⁹⁸ A relationship between microscopic (β) and macroscopic (d_{IJK}) second-order nonlinear coefficient for organic molecules is as follows⁹⁹

$$d_{IJK}(-2\omega; \omega, \omega) = N f_I(2\omega) f_J(\omega) f_K(\omega) b_{IJK}(-2\omega; \omega, \omega) \quad (2.41.2)$$

where

$$b_{IJK}(-2\omega; \omega, \omega) = \frac{1}{n_g} \sum_{ijk} \left(\sum_{s=1}^{n_g} \cos(\theta_{Ii}^s) \cos(\theta_{Jj}^s) \cos(\theta_{Kk}^s) \right) \beta_{ijk}(-2\omega; \omega, \omega) \quad (2.41.3)$$

$$f_I(\omega) = \frac{(n^\omega)^2 + 2}{3}, \quad f_I(2\omega) = \frac{(n^{2\omega})^2 + 2}{3}. \quad (2.41.4)$$

N is the number of molecules per unit volume, n_g is the number of symmetry equivalent positions in the unit cell, θ_{Ii}^s are the angles between the macroscopic system axis I and the molecular system axis i in the unit cell, s is a site in the unit cell, $f_{J,K}(\omega)$ and $f_I(2\omega)$ are local field corrections and β_{ijk} is the molecular second-order polarizability.

As mentioned above, nonlinear optical effects in organic molecules arise from the intramolecular charge transfer between the two opposing groups possessing a permanent molecular dipole moment. The optical nonlinearity can be increased by either linking more conjugated bonds or increasing the strength of the donors and acceptors. The length of the conjugated molecular system can affect the second-order polarizability of the system dramatically up to three rings¹⁰⁰ due to large loss in the nonlinear optical susceptibilities which are proportional to the number of molecules per unit cell.⁹⁵ For strong second-order nonlinearities, the π -conjugated molecules with a donor and an acceptor must be highly asymmetric. The asymmetric electronic distribution can be enhanced by adding appropriate functionality at the ends of the π system.

Unlike inorganic materials where lattice vibrations are significant in their nonlinear responses, organic molecular materials, due to their unique chemical structure of π bonding, have large nonresonant (nonabsorptive) optical nonlinearities. Nonresonant electronic nonlinearities are very fast since they involve only virtual processes and thus organic materials are good for all-optical signal processing. In addition, organic materials have lower dielectric constants (of the order of 3) than those of inorganic crystals, which yields a low RC time constant that allows a large bandwidth

modulation over 10 GHz.¹⁰¹ Organic materials are easy to process and have great versatility in the synthesis to modify their molecular structures.

Although organic materials are relatively soft and have low melting points due to the weak intermolecular forces, they do not suffer optical damage easily and have high optical-damage thresholds.¹⁰² Organic materials for second-order nonlinearity include organic crystals, poled polymers, guest-host systems, Langmuir-Blodgett (LB) films, self-assembled systems, and ionic self-assembled multilayer (ISAM) technique.

2.6.3 Organic Crystals

Organic crystals are advantageous because of their high density in the crystalline state and highly specific and permanent molecular arrangements, which can result in the highest levels of bulk nonlinearity. The high packing density contributes to the magnitude of bulk nonlinearity because $\chi^{(2)}$ is proportional to the molecular density.¹⁰¹ Organic crystals are fabricated by various growth methods. Since the properties of organic compounds are diverse, a broad choice of growth methods are necessary to allow selection of the optimum crystal growth conditions for a given material. The growth methods are based on solution growth, melt growth, and vapor growth. In these methods, a nucleus is formed first and grows into a single crystal by organizing and congregating ions or molecules with specific interactions and bonding.⁹⁵ The driving force for crystallization is the chemical potential difference of the material in the vapor or liquid phase and in the solid.¹⁰³

Organic crystals can be cut, polished, and shaped into various useful devices. For example, they have been employed in thin-film waveguides, crystal-cored fiber (CCF), and organic channel waveguides for telecommunications. However, the crystal growth, especially from solution, of organic materials is not easy due to factors¹⁰³ including poor mechanical properties (soft and fragile), difficulty in large scale growth, thermal instability (thermal decomposition at or below the melting point), polymorphism (causing solid-state phase changes between the melting point and ambient temperature), and the highly polar nature of the organic nonlinear molecules where a large solute ground-state dipole moment enhances the solvent-solute interactions.

2.6.4 Poled Polymers

Polymers are promising for NLO applications because of their versatility in synthesis and processing. Polymers were first developed as a byproduct of the petrochemical industry¹⁰⁴ and then applied in chemical engineering to modify the structure of the polymer chains as desired. Polymers are macromolecules made up of many identical repeating units called monomers. Most polymers are semicrystalline which form combinations of crystalline domains and amorphous domains. A crystalline polymer exhibits a high degree of structural order by folding and stacking of the polymer chains. On the other hand, amorphous materials have no long range order and the chains are tangled but they can have order along the polymer backbone. Most technological NLO applications employ amorphous materials because it is possible to obtain a wide range of physical properties such as temperature stability, optical scattering, and processability by altering the structure unit of a polymer.⁹⁸ It has been shown that polymers can be engineered to yield electro-optic, insulating, semi-conducting, and photo-luminescent properties.^{105–108}

Nonlinear optical molecules can be incorporated in glassy polymers in three different ways: guest-host system in which a NLO chromophore is mixed in a polymeric matrix, covalent linking of the NLO molecules to a polymer backbone as a side chain, or incorporation of them in the main chain.⁹⁵ Then, the polymers can be easily formed into films. Polymer solutions can be spread as thin films on substrates by various methods including spin coating and dipping. Common nonlinear optical polymeric films are glassy polymers with asymmetric chromophores which point in the same direction, making the films asymmetrically polarizable. Electric-field poling can be utilized for aligning the chromophores and poled-polymers of guest-host systems yield typical d_{33} values of $10^{-12} \sim 10^{-10}$ m/V.²

Poling Technique

Most polymers are isotropic materials which lack a net permanent dipole moment and are incapable of exhibiting second-order nonlinear effects. This problem can be solved by using electric field poling to break the symmetry and provide overall polar orientation.

In the process of electric poling, a polymer film containing dipole molecules is heated slightly above its glass transition temperature. At the glass transition temperature, a polymer makes a transition from being glassy to becoming rubbery and the polymer chains become free to rotate resulting in maximum alignment. A strong applied electric field ($10^5 \sim 10^6$ V/m) then can cause the dipoles to rotate preferentially in the field direction. The film is cooled down below its transition temperature with the field still applied, effectively keeping the chromophore alignment. However, the nonlinear optical susceptibility decays with time^{109–113} when the field is turned off because of both relaxation motion of the polymer^{114,115} and thermally activated rotational motion of the chromophore in the polymer.^{110,116}

The poling procedure imposes an ∞_{mm} or $C_{\infty V}$ point group symmetry (a polar axis perpendicular to the film but isotropic in the plane of the film) on the polymer.¹¹⁷ In this symmetry, the susceptibility tensor for SHG has only three independent elements d_{33} , d_{31} and d_{15} in equation (2.28) where the 3-axis is along the poling field.¹¹⁸ If there is no absorption of materials, it is reduced to two independent components according to Kleinman symmetry ($d_{15} = d_{31}$). The second harmonic coefficients d_{IJK} of poled polymer films are typically measured via a Maker-fringe method^{119,120} and this will be discussed in detail in **Chapter 4**.

Guest-host Systems

A guest-host system is prepared for poled polymer by mixing a NLO dye that has large molecular polarizability with an amorphous polymer matrix. By coating, dipping, and lithography, a guest-host system can be easily processed into large area thin films on various substrates including optical fibers and semiconductor substrates. For SHG activity, the guest-host system is poled under an electric field at a raised temperature to induce polar orientation. Since a wide variety of centrosymmetric NLO chromophores can be used for SHG, this method provides an unlimited selection of desired NLO guest molecules. Many organic polymers can be used as a host matrix, but it is necessary to select an amorphous polymer of high optical transparency. Unfortunately, by relying on electric poling for SHG applications, the NLO activity decays on typical timescales of hours to days due to orientational relaxation. Moreover, guest and host molecules become separated at higher concentrations due to the limited solubility of NLO dye in the polymer matrix.²

The poling technique is advantageous due to great flexibility in the choice of molecular and polymeric constituents. Polymers dissolved in solvent can be fabricated in planar films so that they can be applied to waveguide and integrated optical devices. There are several drawbacks including the relatively complex and difficult control of the electric field poling process, the dilution of the nonlinear chromophore in the matrix, and temporal instability of the poled state.¹⁰¹ The problem of orientational relaxation of poled polymers causes the second-order nonlinearity to decrease over time both at room temperature and at high temperature. In order to overcome this issue, NLO chromophores can be incorporated in a polymer backbone with a high glass transition temperature. Since molecular motions of NLO chromophores are related to the glass transition temperature of an individual polymer, NLO chromophores with high glass transition temperature can improve temporal stability of SHG activity.² Dalton *et al.* reported a cross-linked polymer that exhibited greater than 95% retention of SHG for longer than 5000 hours.¹²¹ Other techniques such as Langmuir-Blodgett deposition and self-assembly method can achieve intrinsic structural asymmetry by aligning molecules by the deposition procedure itself without the need for poling. These techniques will be reviewed in the following sections.

2.6.5 Langmuir-Blodgett Film

The Langmuir-Blodgett (LB) technique overcomes some of the drawbacks of other material processing methods. Methods like spin coating and casting produce films with imprecise thickness and randomly oriented molecules on the substrate; while electric poling can align the chromophores, orientational relaxation is inevitable. The Langmuir-Blodgett (LB) technique creates monolayers and multilayers which are tightly packed and uniformly oriented with controlled thickness.

The LB deposition creates many successive single layers of molecules on glass or metal and it is based on organic molecules that can organize a monolayer spontaneously when they are in contact with an air/water interface between the gaseous and the liquid phase.^{122,123} The molecules are amphiphiles composed of a hydrophilic headgroup ('water loving', blue ovals in **Figure 2.9a**) soluble in water, and a hydrophobic tailgroup ('water hating', black lines in **Figure 2.9a**) soluble in nonpolar solvents of low surface tension.

This method involves three steps. (**Figure 2.9**)

- i. Molecule spreading (**Figure 2.9a**): molecules in a solution with a volatile solvent spread over a pure water surface of a trough where the evaporation of the solvent leaves the monolayer of one molecule thick with the heads immersed in water and the tails pointing towards the gaseous phase.
- ii. Monolayer compression (**Figure 2.9b**): after incubation for a few minutes the layer is compressed by two mobile barriers until the molecules are closely-packed and aligned.
- iii. Monolayer transfer (**Figure 2.9c**): a solid substrate is immersed vertically in the water through the monolayer and the monolayer is transferred from water onto the substrate at a particular deposition rate and at a defined surface pressure.

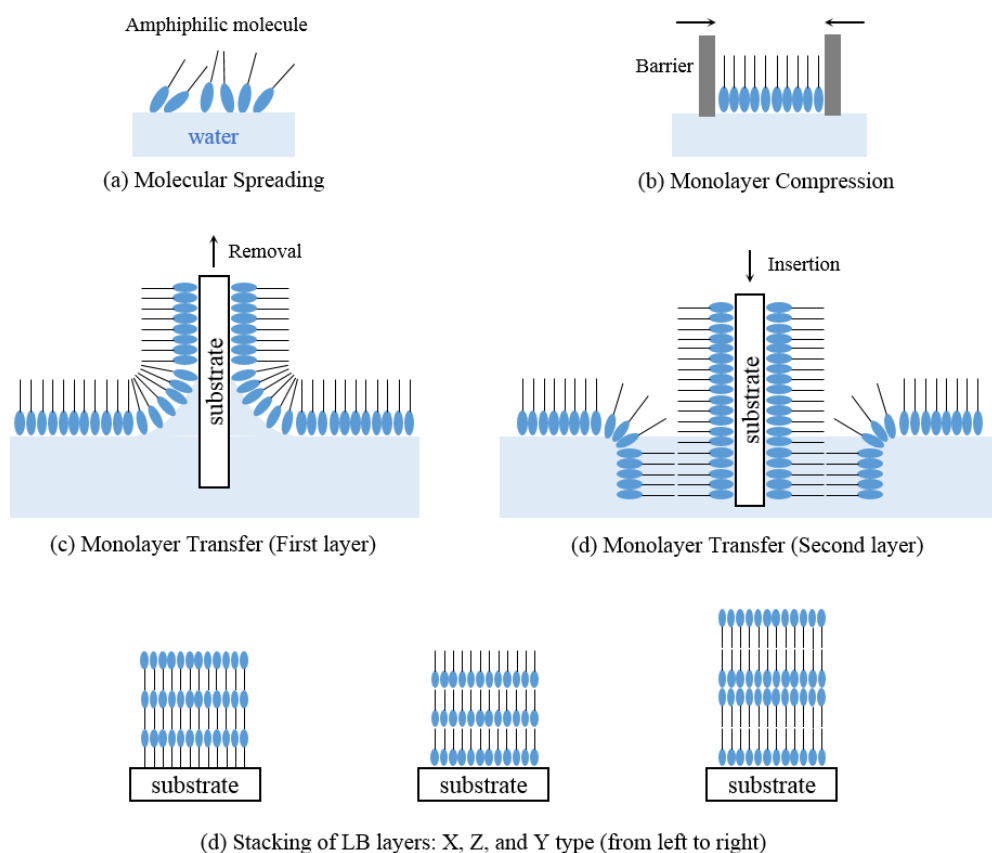


Figure 2.9 Langmuir-Blodgett Deposition. (a) Amphiphilic molecules (hydrophilic in blue ovals and hydrophobic in black lines) spread on water surface. (b) Monolayer compression by barriers. (c) Deposition of Langmuir-Blodgett molecules on a hydrophilic substrate of both sides. (d) Second layer deposition on top of the first layer.

Additional layers can be deposited on top of the existing layer by down and upstroke motion of the substrate. There are three different ways of LB deposition: X-type structure of tail-to-head and tail-to-head arrangement; Z-type structure of head-to-tail and head-to-tail arrangement; and Y-type structure of head-to-head and tail-to-tail arrangement. In most cases the Y-type structure is obtained. For X-type structure, layers are deposited during the downstroke of a hydrophobic substrate and for Z-type structure, layers are deposited during the upstroke of a hydrophilic substrate. Both X- and Z-type structures have an inherent structural asymmetry whereas the Y-type structure has an inherent structural symmetry.

To generate second harmonic light in an LB film, the film must contain SHG chromophores in such a way that the second-order hyperpolarizabilities of the molecules in one monolayer are not cancelled by those in the next layer. Therefore, the chromophore containing layers must be in X- or Z-type multilayers or in a Y-type of alternating layers with an inactive material. The Y-type films composed of hemicyanine dye have produced second-order nonlinear susceptibilities of 500~1,500 pm/V, and the Z-type films with quinolinium dye have produced 120 pm/V.^{124,125}

Langmuir-Blodgett deposition technique allows control at the molecular level and generates large second-order susceptibilities, but it is complicated and requires special equipment under clean room conditions to avoid contamination of dust particles. It is also time consuming compared to other material processing techniques like spin coating or dipping and LB films show poor mechanical and thermal stability due to the van Der Waals interactions between layers.

2.6.6 Covalent Self-Assembled Systems

The self-assembled monolayer (SAM) technique provides an attractive alternative to Langmuir-Blodgett films, which overcomes some of the drawbacks mentioned in **Section 2.6.5**. In this method, hydroxylated (containing an -OH group) substrates are immersed into an amphiphilic fluid containing molecules possessing a headgroup. The headgroups can covalently (chemisorption) anchor the molecules to the substrate. A single monolayer is created once the substrate is covered with closely packed molecules and becomes a thermodynamically stable film. The monolayer fills in tightly due to van der Waals interactions. Additional layers can be deposited by alternating steps creating highly organized multilayer structures. These films show excellent mechanical, chemical,

and electrical stability due to covalent monolayer-surface binding and interlayer crosslinking.¹²⁶⁻¹²⁸

For second-order nonlinear optics, Marks *et al.*^{2,4,129-134} introduced a new approach of building covalently linked chromophores containing self-assembled organic multilayer superlattice systems. This method provides higher chromophore density and greater net alignment than poled polymeric films and better structural control and stability than LB films. The superlattice films exhibited $\chi_{zzz}^{(2)}$ of 84 pm/V.⁴ In another study, siloxane-based self-assembled superlattice multilayer films showed large $\chi^{(2)}$ of 180 pm/V.¹³⁵ Self-assembled multilayers exhibited SHG activities as large as that of LB films and show improved performance regarding mechanical and chemical stability.

2.6.7 Ionic Self-Assembled Multilayer (ISAM) Technique

The technique of creating polymer layers with alternating charges by electrostatic attraction was first introduced by G. Decher and his colleagues in 1991.¹³⁶ It is simply done by immersing a charged substrate into an oppositely charged aqueous polyelectrolyte solution followed by rinsing with deionized water in order to remove unbounded polymer as in **Figure 2.10**. This method has many advantages over previous methods such as poled polymer films^{137,138} which do not have temporal stability, Langmuir-Blodgett films^{122,123} which needs constant pressure for deposition and requires delicate handling afterward, or covalently self-assembled films^{126,139} which is very time consuming (several hours to several days per layer) and needs high temperature. The ISAM method provides a quick and simple process and versatile structures. The deposition process of each layer typically takes 3 to 5 minutes and it is performed at ambient conditions without special facilities. The simple procedure can be repeated in the cyclic fashion of $(AB)_n$ or $(ABCB)_n$ structures¹⁴⁰ to allow different functionality.

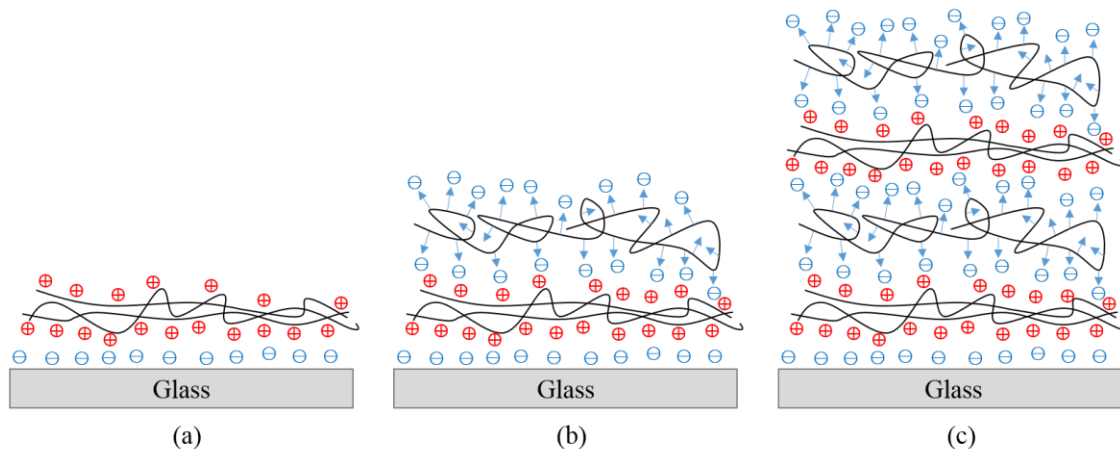


Figure 2.10 Illustration of ISAM film deposition. (a) A monolayer of polycation adsorbed onto the negatively charged microscope slide, (b) a bilayer of NLO-active anion adsorbed on the previous polycation where the arrows represent nonlinear chromophore dipoles, and (c) it can be repeated for as many as layers as desired.

From the late 90's to early 2000's, our team has conducted extensive studies on ISAM films that exhibit a second-order nonlinear optical (NLO) response. The rest of this section gives a summary of the work done by our team. One important study showed that when the sample thickness is much less than the coherence length ($\sim 10 \mu\text{m}$), the SHG grows quadratically with increased film thickness, which evidenced the preservation of a degree of polar orientation for each layer.⁷ Another important study showed that the ISAM NLO films exhibit remarkable thermal and temporal stability of the second order nonlinear susceptibility, $\chi^{(2)}$, which resisted decay over three years at room temperature and twenty hours at 150°C .¹⁴¹

Another interesting study explored the relationship between $\chi^{(2)}$ and the thickness of ISAM NLO films. The thickness of ISAM films was controlled by making changes in the pH and ionic strength of the polyelectrolyte solutions; the thickness was increased by lowering the anion pH and increasing the NaCl concentration.¹⁴² This was explained according to the relationship between the polymer conformation and layer thickness. The conformation of a polymer is determined by the Debye length, which is proportional to the inverse of the ionic strength. As the Debye length is reduced (at higher ionic strength), the polymer adsorbs with a greater number of loops, leading to thicker adsorbed layers. This was observed for lowered pH and increased NaCl

concentration. On the other hand, at lower ionic strength, polymer adsorbs mostly in train conformations, resulting in thinner layers. Although the SHG grew quadratically with increased film thickness for all of the films that were prepared at a fixed pH and NaCl concentration, it turned out that the $\chi^{(2)}$ values actually decreased as the NaCl concentration increased as shown in **Figure 2.11**.⁸ This is due to the random orientation of the anionic chromophore units which were incorporated into the bulk monolayer as the layer thickness increased. **Figure 2.10** shows the chromophores (in blue arrows) bound to the PAH (poly(allylamine hydrochloride) layers above and below, oriented both toward and away from the substrate. Consequently, chromophores in the bulk monolayer, not at the interfaces, possessed random orientations, resulting in a high degree of cancellation of $\chi^{(2)}$. Therefore, the greatest $\chi^{(2)}$ values were found in the thinnest films, indicating that the NLO response was determined mainly by the chromophores at the layer interfaces.

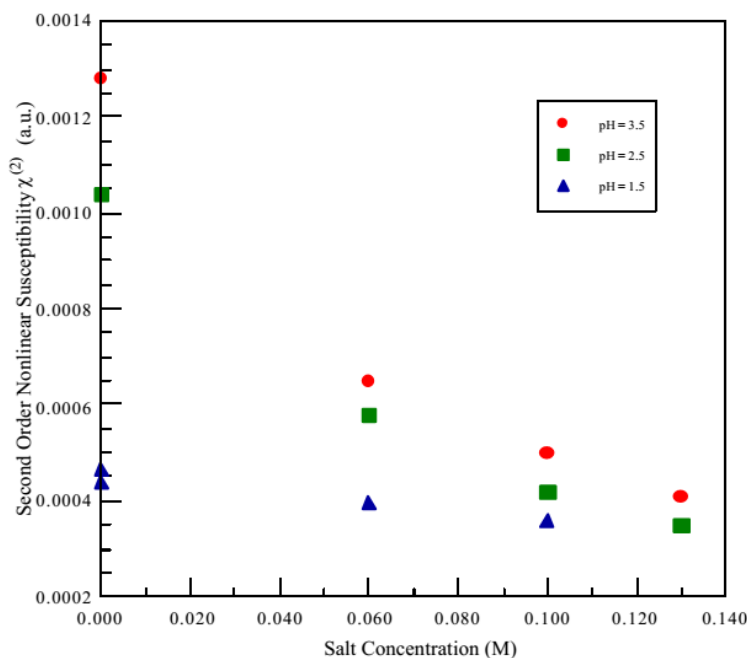


Figure 2.11 Second order susceptibility of Poly S-119/PAH ISAM films versus salt concentration for several pH values.⁶⁵

To overcome significant cancellation of the chromophore orientations, a different approach was developed to obtain enhanced $\chi^{(2)}$ by reducing the film thickness and incorporating dianionic molecules, Mordant Orange 10, into ISAM films to increase the polar order.¹⁴³ Mordant Orange 10 (**Figure 2.12**) has a sulfonate acid moiety ($pK_a \sim 0$) on one end and a carboxylic acid ($pK_a = 5$) on the opposite end. In this way, at pH 3, the chromophore was ionized on only one of the ends as it was adsorbed on the substrate, resulting in a preferential polar orientation. It was demonstrated that the ISAM films incorporated with Mordant Orange 10 exhibited an order of magnitude increase in $\chi^{(2)}$ compared to the ISAM films fabricated using polyelectrolytes with NLO sidechains.

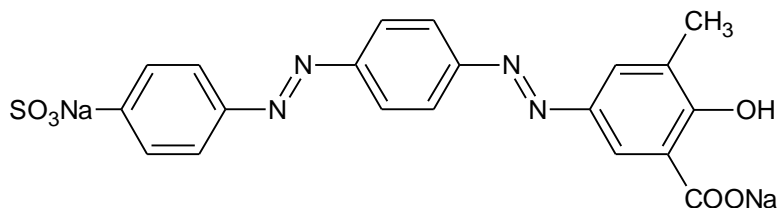


Figure 2.12 Molecular structure of Mordant Orange 10.

More recently, the ISAM method was applied in plasmonic enhancement of SHG. Chen *et al.*,⁷² in our team, incorporated silver nanotriangles on an NLO ISAM film by using nanosphere lithography. The ISAM films were fabricated using PAH as the polycation and PCBS (poly(carboxyhydroxyphenylazobenzenesulfonamidoethanediyl) sodium salt) as the NLO polyanion. Due to the localized surface plasmons of the silver nanotriangles, the incident electromagnetic field was concentrated at the sharp corners of the triangles, causing a significant enhancement in SHG from the PAH/PCBS ISAM films. The enhancement in the SHG efficiency was as much as 1600 times compared to the PAH/PCBS ISAM films without the nanotriangles.

2.6.8 Hybrid Covalent/Ionic Deposition

Hybrid covalent/ionic self-assembled multilayer (HCISAM) deposition is a novel technique introduced by our research group to overcome the random orientation of the chromophores in the bulk ISAM film and provide a high degree of polar ordering and $\chi^{(2)}$ of organic chromophores in thin films. This technique can reduce the random orientations of chromophores by a covalent bond of the chromophore at one of its ends and electrostatic attraction with the subsequent cationic layer.¹⁴⁴ In the early studies, a chromophore called Procion Red (PR) MX-5B (**Figure 2.13a**) was used to make ISAM films with the cation PAH. When a PAH layer is immersed in a Procion Red solution at pH 10.5 (above the pK_a of PAH), the triazine ring of PR can covalently react with an unprotonated amine group of PAH. When a PR layer is immersed in a PAH solution at pH 7, protonated PAH amines can electrostatically bind with the sulfonates of PR. Despite its very low hyperpolarizability, Procion Red exhibited a second-order susceptibility comparable to the reported ISAM films ($\chi^{(2)} = 11.3 \times 10^{-9}$ esu.).^{9,144}

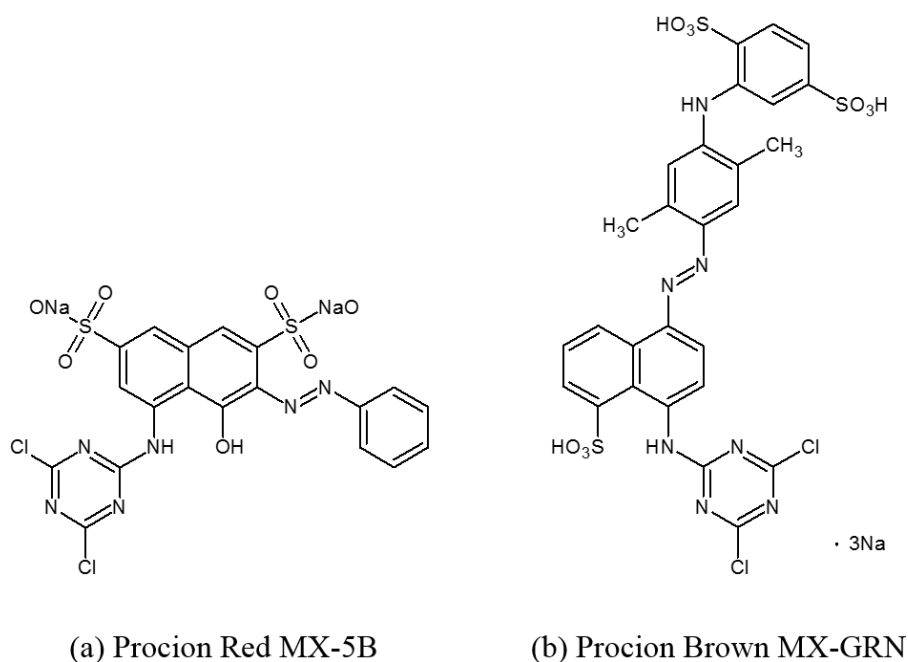


Figure 2.13 Molecular structures of (a) Procion Red and (b) Procion Brown.

In further attempts to improve the hybrid covalent-ionic self-assembled multilayer technique, Procion Brown (PB) was chosen for its excellent hyperpolarizability⁹ ($\beta = 300 \times 10^{-30}$ esu.). As shown in **Figure 2.13b**, unlike the Procion Red molecule, Procion Brown is conjugated along one axis. The PB films were reported to show linear growth of film absorbance as a function of bilayers above the initial adsorption effect compared to Procion Red.¹⁴⁵ It was also discovered that the addition of NaCl up to 0.5 ~ 1.0 M concentration resulted in improved polar ordering and packing of the chromophores. The PB films with 0.5 M NaCl demonstrated good temporal stability for more than 400 days and better thermal stability at 150 °C than Procion Red chromophores.¹⁴⁵

The ISAM method can not only be applied on a flat substrate as we have so far discussed, but also be used on a curved surface such as a silica optical fiber. Optical fibers have been historically applied in telecommunications and fiber optic sensors. More recently, optical fibers have been used as a platform for nonlinear optical effects as an alternative to bulk crystal.¹⁴⁶ However, due to the full inversion symmetry of silica glass, standard optical fibers do not possess second-order nonlinearity. In our research group, Daengngam *et al.*¹⁰ created 40 bilayers of PAH/PB HCISAM films on a silica fiber taper to achieve radial alignment of the NLO chromophores and demonstrated a thermodynamically stable $\chi^{(2)}$ from the silica optical fiber. However, due to phase-mismatching, the efficiency of the SHG by the nonlinear taper was very low. Therefore, to overcome this, Daengngam *et al.* established a method for quasi-phase matching, where a spatially periodic coating of ISAM film was fabricated on a silica fiber taper by a UV ablation technique.¹² The UV ablation was carried out using a custom aluminum photomask comprising an array of 25 μm wide slits with a spatial periodicity of 50 μm . The patterned aluminum layer of the photomask was designed to be 800 nm thick in order to block the UV light from an excimer laser with a wavelength of 248 nm. It was demonstrated that the taper with a periodic structure of a 10-bilayer PAH/PB film produced 15 times greater SHG signal than a fiber taper with a uniform coating at the pump wavelength of 1220 nm.

In the continuing work of plasmonically enhanced SHG using Ag nanoparticles, Chen *et al.*⁸³ from our group fabricated PAH/PB films combined with Ag nanoparticles to study the interface effects in SHG from ISAM films. The second harmonic signals from the PAH/PB films decorated with Ag nanoparticles were compared to those from the PAH/PCBS films also decorated with Ag

nanoparticles. Despite the fact that PB exhibits a stronger $\chi^{(2)}$ than PCBS due to its ability to achieve a high polar order by the hybrid covalent ISAM method, the PAH/PB films produced lower NLO efficiencies than the PAH/PCBS films. Also, the $\chi^{(2)}$ of the PAH/PB film surface had the opposite sign of the bulk. This seemed to indicate that the PAH/PB films were more susceptible to disruption at the interface by the nanoparticle deposition process and thus produced lower NLO efficiencies than the PAH/PCBS films combined with the nanoparticles.

2.7 Applications of Second Order Nonlinear Optics

Nonlinear optics has important applications in optical information processing, telecommunications, and integrated optics. Nonlinear optical materials can be utilized to build optical devices such as frequency mixers,¹⁴⁷ light modulators,^{111,148,149} optical switches,⁷⁷ optical information storage,⁷⁷ optical logic,⁷⁸ optical limiters,⁷⁹ and so on. As a widely investigated and highly applicable field in nonlinear optics, second harmonic generation (SHG) offers a number of technological applications discussed in this section.

As one example, second harmonic generation makes it possible to convert near-infrared light from a diode laser into deep blue light. Since the focused spot size of a laser is directly proportional to its wavelength, this halving of the wavelength is particularly useful where applications are performed on a small scale. In regards to optical information storage, the use of second harmonic generation to shrink the effective footprint of a laser beam can significantly increase the capacity of data storage on optical disks.

Surface nonlinear optics and nonlinear optical microscopy are other important applications of SHG.¹ In surface nonlinear optics, SHG can be used as a diagnostic tool to examine the surface properties of optical materials because the intensity and angular distribution of surface second harmonic generation depends on the morphology of a surface and on the impurities on the material surface. SHG is often used in nonlinear optical microscopy. It can provide enhanced transverse resolution⁸⁰ of 50 nm and high subwavelength resolution⁸¹ of 16 nm. SHG-based microscopy also provides a clean signal without unwanted background from incident light scattering. Furthermore, light at a long wavelength is useful for biological materials to achieve a resolution requiring a

shorter wavelength without damaging them. Harmonic-generation microscopy can be used for transparent objects because the phase matching condition depends on the refractive index variation within the imaging sample.⁸² A tomography based on SHG can characterize biological materials.⁸³ It has also been used for imaging live cells,⁸⁴ three-dimensional imaging with fs laser pulses,⁸⁵ and imaging membranes using styryl dyes as labels.⁸⁶

Separate from second harmonic generation, electro-optical devices employing the second-order nonlinear optical response have been investigated as one of the most significant technological applications of second-order NLO for its capability to alter optical properties of a material using an electric signal. An electro-optic modulator can change the phase, amplitude, frequency, or polarization of the incident beam. Fabrication of various types of optical modulators and switches for fiber optics communications and lasers is made possible by applying the electro-optic effect. For example, in the Pockels electro-optic effect an applied electric field induces birefringence. One important type is the Pockels cell in Q-switches for producing pulsed laser beams with high peak power. Organic thin films may be more suitable in the future for such applications than inorganic crystals due to the inexpensive fabrication cost and easier flexibility in organic thin films.⁸⁷

2.8 Plasmonics

Plasmonics is a relatively new discipline of nanophotonics that deals with the interaction between electromagnetic radiation and the conduction electrons at a metal/dielectric interface or a surface of metallic nanoparticles. When the light couples to electrons, waves called surface plasmons are formed that propagate on the metal surface. There are two types of electromagnetic excitations in plasmonics – surface plasmon polaritons and localized surface plasmons.

Surface plasmon polaritons (SPPs) are longitudinal waves that propagate along continuous metal-dielectric interfaces. Light is effectively confined to the interface because the SPP wavevector is greater than that in the dielectric. Therefore, the electromagnetic field decays exponentially from the interface on both sides as illustrated in **Figure 2.14**. Electric field components of the SPPs are perpendicular to the metal-dielectric interface and parallel to the

wavevector. Consequently, efficient excitation of SPPs requires that the incident light be transverse magnetic with its electric field lying in the plane of incidence.

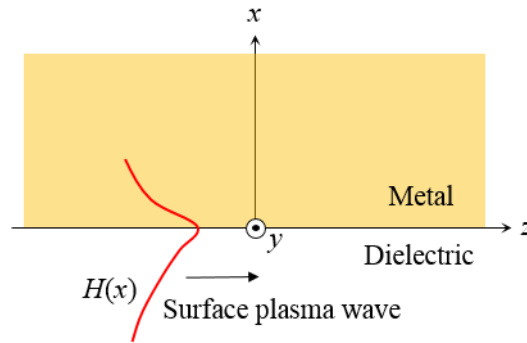


Figure 2.14 Illustration of traveling surface plasma wave at the metal-dielectric interface

On the other hand, localized surface plasmons (LSPs) are nonpropagating excitations of the conduction electrons coupled to the electromagnetic field induced in metallic nanostructures. This type of excitation comes from the scattering of a conductive nanoparticle in an oscillating electromagnetic field. Resonance of these modes can happen when an effective restoring force caused by the closed surface of the particle is exerted on the driven electrons, amplifying the fields both inside and in the near-field zone outside the particle. This excited resonance occurs at a particular frequency when the incident light frequency matches the resonant frequency of conduction electrons of the metallic nanoparticles. This process is called the localized surface plasmon resonance (LSPR) oscillation, and it results in a strong enhancement of absorption and scattering of the incident light.

The spectral positions of the LSPRs depend on the aspects of the nanoparticles including geometrical parameters such as size and shape, the metal composition, as well as the surrounding dielectric environment. Therefore, the absorption and scattering properties of the nanoparticles can be engineered by changing their host medium, size, and shape.⁸⁸⁻⁹⁰ For example, the resonance red-shifts as the dielectric constant increases,⁹¹ which makes metal nanoparticles attractive systems for optical sensing of changes in refractive index. In addition, gold and silver nanoparticles exhibit

bright colors in both their transmission and reflection spectra due to resonantly enhanced absorption and scattering in the visible region. This effect has been applied (somewhat unknowingly) for many centuries in artwork. A good example is the Lycurgus cup in the British Museum, a 4th century Roman goblet made of dichroic glass. It appears green by a reflected light and red by a transmitted light when lit from inside. This is due to plasmonic excitation of electrons in the metallic particle colloids dispersed throughout the glass. The cup absorbs and scatters short wavelengths like blue and green light but transmits longer wavelengths like red. Another example of the use of metallic nanoparticles is stained glass windows in medieval churches.⁹² When the stained glass is illuminated, the colloidal suspensions of gold and silver nanoparticles within the glass scatter at specific wavelengths depending on the size and shape of the particles.

Plasmonic excitations that occur when light interacts with metal nanostructures can give a significant enhancement to nonlinear optical effects in several ways. First, the light coupling to the surface plasmons can give rise to strong local electromagnetic fields and thus enhance nonlinear optical effects.⁹³ Surface-enhanced Raman scattering (SERS) provides a good example, where several orders of magnitude enhancement are given to the weak Raman process by plasmonic excitations at a rough metal surfaces. SERS has been demonstrated to allow even a single molecule detection.⁹⁴ Second, the localized surface plasmons demonstrate an extreme sensitivity to the dielectric properties of the metal and the embedding medium. This provides an enabling platform for plasmonic sensors⁹⁵ whose resonance wavelength shifts in response to minute environmental changes. Lastly, plasmonic excitation have quick response times on the timescale of a few femtoseconds,⁹⁶ which can be the basis of ultrafast optical signal processing.

2.9 Colloidal Gold

Colloidal gold nanoparticles have unusual optical properties dependent on size and shape. For instance, spherical colloidal gold nanoparticles with a diameter around 10 nm are red in aqueous dispersions, but a rod-like shape, with length 30 nm and diameter 10 nm, makes the colloidal dispersion appear blue. Due to their unusual optical properties and promising applications using local field enhancements, colloidal gold has been widely employed in nonlinear plasmonics. This

section starts with a brief historical background of colloidal gold, focusing on the past progress. Optical properties of gold nanorods and a review of the synthesis of gold nanorods will follow.

2.9.1 Historical Background

Colloidal gold has been used as a colorant for centuries especially in making ruby glass and providing red stains to ceramics. Studies on the synthesis by reduction of dilute gold chloride and size-dependent optical properties were presented by Michael Faraday⁹⁷ in 1857. Almost a half century later, Richard Zsigmondy combined Faraday's method with his own colloidal gold synthesis technique to develop a two-step nuclear method,⁹⁸ nowadays referred to as the seed-mediated method. By using his invention, the ultramicroscope, in which Brownian motion of colloidal particles was detected by light scattering from the particles, Zsigmondy was able to visualize the colloidal gold particles in their dispersed state.⁹⁹ Wilhelm Ostwald presented experimental and theoretical principles useful for the synthesis of gold sols in his textbook.¹⁰⁰ He described a process of obtaining colloidal gold in which an ionically dispersed gold chloride solution was neutralized by sodium bicarbonate and then reduced to metallic gold by organic substances. He also emphasized the importance of size in keeping particles dispersed and stressed the importance of pH in changing the color of the final dispersion from red to blue. Then, Theodor Svedberg reported in his textbook¹⁰¹ the use of all the possible reducing agents available to him to produce colloidal gold by reduction of chloroauric acid to gold. Later, he invented the ultracentrifuge for size separation of particles and investigating the influence of size and shape on the sedimentation equilibria.^{101–103}

In the meantime, theoretical studies on colloidal particles were carried out by Gustav Mie and Richard Gans. Mie explained, in 1908, the color of colloidal gold dispersions by developing a theory of light absorption and scattering from spherical particles. Mie theory solves Maxwell's equations for the case of an electromagnetic plane wave incident on a dielectric sphere. The results of his theory provided plots of the absorption and scattering spectra versus particle size.¹⁰⁴ Then, in 1912, Gans published an article¹⁰⁵ considering prolate and oblate spheroidal particles by extending Mie's theory. He showed that the absorption depends only on the aspect ratio (Length/Width) of the particles and not on the absolute dimensions. For gold nanorods, two

fundamental oscillation modes of conduction electrons exist: one longitudinal mode along the long axis of the rod and a transverse mode along the short axis perpendicular to the first. However, Gans theory only considers dipole oscillations.

2.9.2 Optical Properties of Gold Nanorods

When an optical beam passes through a colloidal dispersion of metallic nanoparticles, light gets attenuated due to absorption and scattering as given by

$$I(z) = I_0 e^{-n_0 C_{ext} z}, \quad (2.42)$$

where I_0 is the intensity of the incident light, $I(z)$ is the intensity of the light after travelling path length z inside the sample, n_0 is the number density of particles, and $C_{ext} = C_{abs} + C_{sca}$ is the extinction cross section of a single particle, which is a sum of absorption and scattering cross sections. The extinction coefficient, γ is the product of $n_0 C_{ext}$ and has units of $M^{-1}cm^{-1}$.

The optical properties of noble metal particles come from localized surface plasmons. Localized surface plasmons are nonpropagating excitations of conduction electrons and arise when metal particles are illuminated by light. For these metal particles placed in an oscillating electric field, the electron cloud is driven into oscillations as shown in **Figure 2.15**. At the plasmon resonant frequency, electric fields are amplified both inside and outside of the particles. The resonance occurs due to the confinement of the conduction electrons to the small particle volume. For nanoparticles with a diameter $d \ll \lambda$, the conduction electrons oscillate in phase when excited by a planewave with a wavelength λ , which leads to the accumulation of polarization charges on the particle surface. These charges behave as an effective restoring force, causing a resonance at the particle plasmon frequency. A resonantly enhanced field builds up to create a dipolar field outside the particle, which leads to larger absorption and scattering cross sections for electromagnetic waves. The resonantly enhanced near field is then created in the vicinity of the particle surface, which enables a number of applications using metallic nanoparticles.

Gold nanorods have two modes: a strong longitudinal mode (longitudinal surface plasmon resonance, LSPR) in the near-infrared region and a weak transverse mode (transverse surface

plasmon resonance TSPR) in the visible region at around 520 nm. The transverse mode is insensitive to aspect ratio, but the LSPR mode is redshifted from the visible to near-infrared region with increasing aspect ratio. The aspect ratio can be precisely controlled by changing the catalyst of silver ions in the seed-mediated growth method, to be discussed in detail in **Chapter 3**.

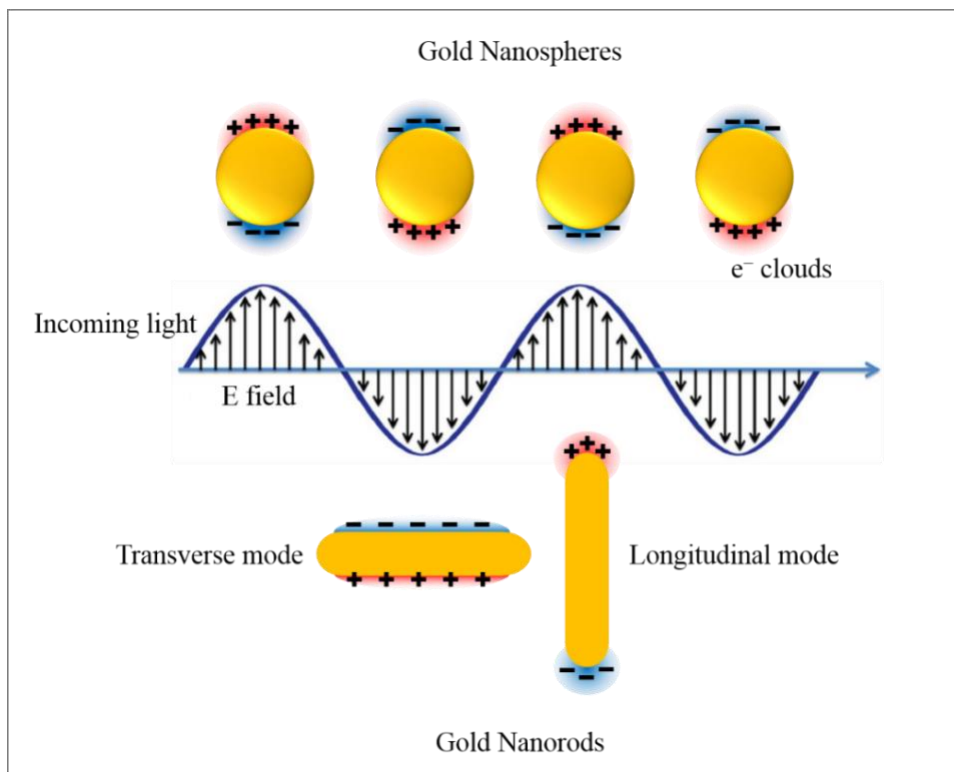


Figure 2.15 Localized plasmon resonance in gold nanospheres and gold nanorods.

According to Gans theory (an extension of Mie theory), the extinction coefficient for randomly oriented elongated ellipsoids in the dipole approximation can be written as^{91,105}

$$\gamma = \frac{2\pi NV(\epsilon_m)^{\frac{3}{2}}}{3\lambda} \sum_j \frac{(1/P_j^2)\epsilon_2}{\left(\epsilon_1 + \frac{1-P_j}{P_j}\epsilon_m\right)^2 + \epsilon_2^2} \quad (2.43)$$

- N Number of particles per unit volume
- V Volume of each particle
- λ Wavelength of the incident light
- ϵ_m Dielectric constant of the surrounding medium
- ϵ_1, ϵ_2 Real and complex parts of the material dielectric function
- P_j Depolarization factors for the three axes A, B , and C of the rod with $A > B = C$
- R Aspect ratio, A/B

$$P_A = \frac{1-e^2}{e^2} \left[\frac{1}{2e} \ln \left(\frac{1+e}{1-e} \right) - 1 \right] \quad (2.44)$$

$$P_B = P_C = \frac{1-P_A}{2} \quad (2.45)$$

$$e = \sqrt{1 - \left(\frac{B}{A}\right)^2} \quad (2.46)$$

From equation (2.43) the derived relationship between the absorption maximum of the LSPR mode λ_{max} as a function of R and ϵ_m is given as⁹¹

$$\lambda_{max}[\text{nm}] = (53.71 * R - 42.29)\epsilon_m + 495.14. \quad (2.47)$$

Simulated extinction spectra are plotted in **Figure 2.16** for various aspect ratios, 2.6, 2.9, 3.1, 3.3, and 3.6. The transverse resonance peak around 520 nm is not affected by the change in aspect ratios. However, the longitudinal resonance peak is shifted toward the near-infrared region with increasing aspect ratio.

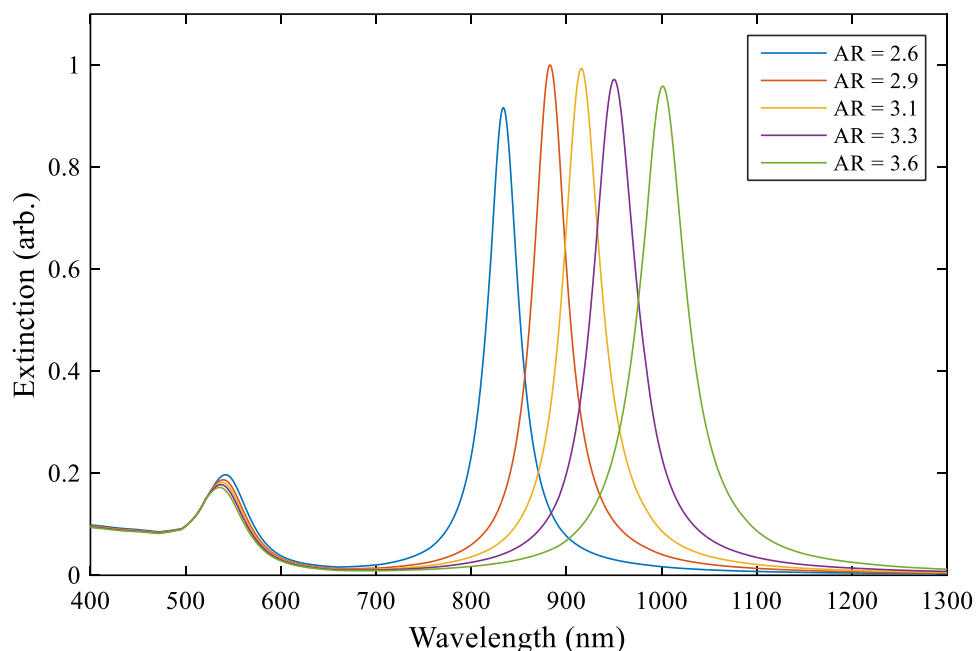


Figure 2.16 Simulated extinction spectra of gold nanorod suspension in water with different aspect ratios. The longitudinal resonance peak is shifted toward the near-infrared region with increasing aspect ratio. The transverse resonance peak is not affected by aspect ratio. This is plotted using the equation (1.2). The medium dielectric constant, ϵ_m was fixed at 4.

2.9.3 Synthesis of Gold Nanorods

The synthesis of gold nanorods typically involves the reduction of an aqueous solution of oxidized Au(III) derivatives-chloroaurate (AuCl_4^-) to neutral gold atoms.¹⁰⁶ These gold atoms are essentially insoluble in liquid and aggregate into clusters called embryos. Once embryos reach a critical size containing a certain number (“magic number”) of atoms they become stable and separate from the solution as sub-nanometer solid particles called nuclei. The nuclei can grow to nanosized primary particles through the addition of more gold atoms. These primary particles are unstable due to their large free energy and can continue to grow by diffusion or aggregate to form the final gold particles. To stabilize the nanoparticles, the aggregation process must be stopped in the early stages of particle formation by vigorous stirring and addition of stabilizing agents.¹⁰⁷ The

kinetics of nucleation and growth is controlled by oxidation/reduction agents, the concentration of reactants, temperature, and pH. And therefore the size, shape and structure of the colloidal gold nanoparticles can be tailored.

Reduction potential measures the tendency of a chemical species to gain electrons and then be reduced. The reduction is driven by the difference between the redox potentials of the two half-cell reactions, ΔE , of gold ions and oxidation of the reducing agent.^{106,107} For an allowed reduction reaction, the redox potential of the reducing agent must have a more negative value than that of the metallic species. An increase in the value of ΔE allows a reaction to be more spontaneous, creating smaller sized gold particles due to the generation of a larger number of nuclei. Thus, the size of the final gold particles decreases as ΔE of the reaction increases.¹⁰⁶ Although having a large ΔE can result small particles, other parameters such as ionic strength, particle charge, and the surfactants are also important in the final dispersion.

In the synthesis of gold nanorods, several reduction methods have been developed in the past two decades. The electrochemical method¹⁰⁸ was applied to make gold nanorods via electrochemical oxidation/reduction in the presence of cetyltrimethylammonium bromide (CTAB) solution by Yu *et al.*¹⁰⁹ Then Jana *et al.*¹¹⁰ used the seed-mediated method in an aqueous micellar template (CTAB) to produce high aspect ratio gold nanorods by reducing gold salts with borohydride. They were able to control the aspect ratio by varying the concentration of surfactant, CTAB, and adding AgNO₃. Nikoobakht and El-Sayed modified the seed-mediated method by using a binary surfactant (mixture of CTAB and benzyldimethylhexadecylammonium chloride (BDAC)) and produced higher yield with fewer byproducts.¹¹¹ Many other reports of gold nanorod synthesis¹¹⁰⁻¹¹⁹ focused on the seed-mediated method producing with high yield and high quality. Therefore, the gold nanorods were prepared using the seed-mediated method in this dissertation, which is discussed in detail in **Chapter 3 Section 3.2**. An illustration of the seed-mediated method with CTAB as the surfactant and hydroquinone as the reducing agent is shown in **Figure 2.17**. In the first step, gold seeds are prepared by reduction with sodium borohydride. In the second step, gold salts experience the first reduction by hydroquinone and the second reduction by the gold seeds. Aspect ratios can be tuned by adding different amounts of silver nitride. As shown in the illustration, gold nanorods are physisorbed by CTAB bilayers.

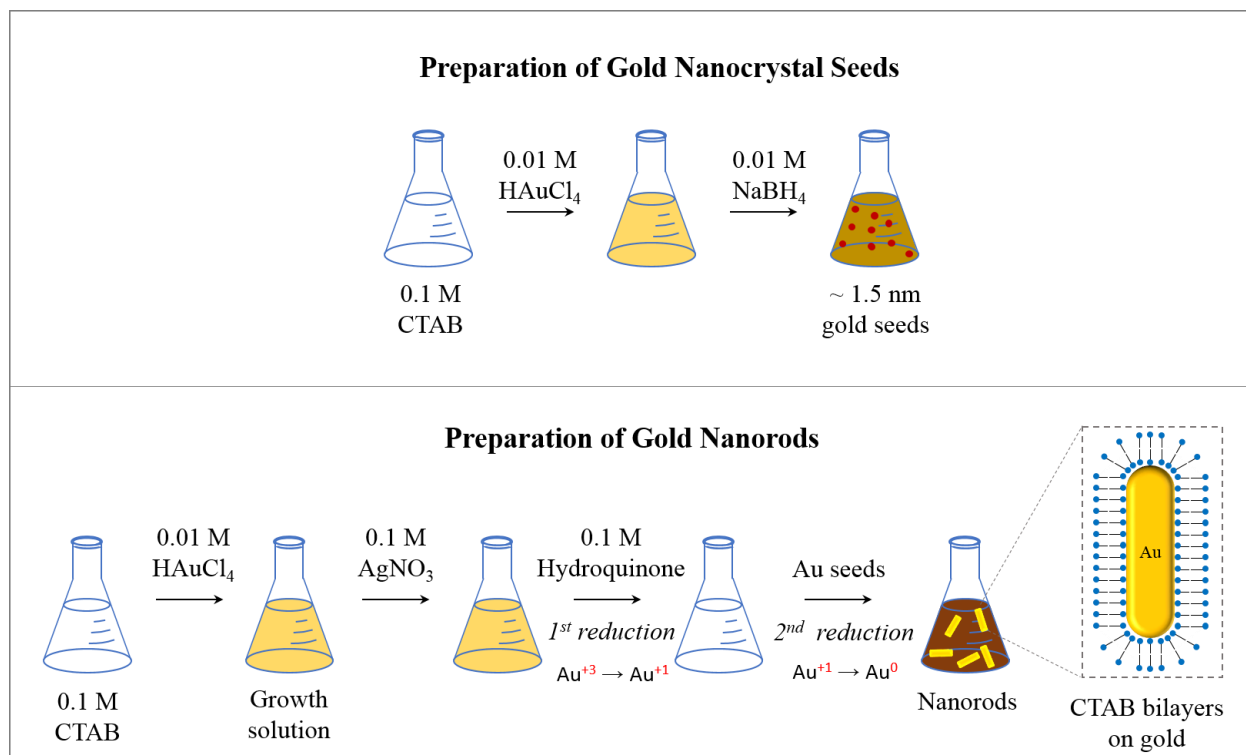


Figure 2.17 Illustration of the seed-mediated method with CTAB as surfactant and hydroquinone as the reducing agent.

2.10 Applications of Nanoparticles in Plasmonics

Plasmonic nanoparticles have been investigated for a variety of applications, such as biological/chemical sensors, nanomedicine, all-optical devices, and nonlinear optics. The peak wavelength of the LSPR band depends on the nanoparticle size, shape, composition, orientation, interparticle distance, and surrounding dielectric media.¹²⁰ Thus the wavelength position of LSPR can be tuned by optimizing these parameters during synthesis. For example, by using nanoparticles, changes in the bulk refractive index of their environment can be detected via shifts in the LSPR peak wavelength. Mayer *et al.* fabricated gold nanorod substrates for refractive index sensing and showed a substrate sensitivity of 170 nm/RIU (refractive index unit).¹²¹

Since most organic molecules have a higher refractive index than the buffer solution, when the nanoparticles are coated with such molecules, the extinction and scattering spectra shift toward the near infrared region. Because field enhancements by the LSPR decay rapidly with distance from the nanoparticle surface, molecular binding can be monitored with high sensitivity via optical spectroscopy.¹²² For instance, absorption-based colorimetric sensors are developed using the shift in the LSPR band of gold nanorods.¹²³ Chai *et al.* detected Pb^{2+} by monitoring the colorimetric response of glutathione functionalized gold nanoparticles from a UV-Vis spectrometer or even with the naked eye (red to blue).¹²⁴ Haes *et al.* measured the LSPR shift from a silver nanotriangle self-assembled monolayer (SAM) as the monolayer length increased one CH_2 group at a time.¹²⁵ When successive SAM layers were deposited alternately with copper ions, the LSPR shift per added layer began to level off when the film thickness was around 20 nm. This indicates that the thickness of the capture layers must be less than 20 nm, so that the LSPR shift due to target binding is detectable.

Gold nanoparticles can also be applied to cancer research due to their easy synthesis, surface modification, and strongly enhanced tunable optical properties.¹²⁶ Huang *et al.*¹²⁷ distinguished cancer cells from normal cells via SERS by gold nanorods. The surface enhanced plasmon of the antibody-functionalized gold nanorods on the cancer cell surface was found in a Raman spectrum due to the aggregated nanorod assembly. In addition, gold nanoparticles can be used for photothermal therapy due to their strong light absorption.¹²⁷ They can convert the absorbed light into heat via their nonradiative properties. Therefore, photon energy can be converted to heat sufficient enough to induce cellular damage via thermal effects, such as hyperthermia and evaporation.¹²⁸ Strong light absorption and scattering of gold nanorods are also useful in imaging techniques, such as dark-field microscopy. In dark-field microscopy, transmitted white light is blocked by a dark field condenser to collect only the scattered light.^{129,130} El-Sayed *et al.* showed that the gold nanorods conjugated to anti-EGFR scattered light differently after binding to cancerous and noncancerous cells.¹²⁹

Near-field coupling between nanoparticles in ordered arrays can overcome the diffraction limit. In these arrays, each nanoparticle with a diameter much smaller than the wavelength of the excitation light behaves like an electric dipole. Exciting light sets the array of the dipoles into coherent oscillation, which results in a propagating wave of alternating positive and negative

charges that is guided with a mode width below the diffraction limit.¹³¹ In addition, since optical frequencies are so much higher than electrical frequencies, plasmonic nanoparticle arrays can transfer data more efficiently than electronic waveguides.¹³² It has been shown that ordered nanoparticle arrays can carry signals over distances of a few hundred nanometers.¹³¹ Reducing absorption loss by an appropriate choice of surrounding dielectric is one way to improve the propagation length.¹³² These array structures can potentially be used in nanoscale all-optical networks, providing a new class of optical devices that operate below the diffraction limit.^{133,134}

For nonlinear applications, the local-field near the metal surface should be maximized so that the higher-order nonlinear optical processes are correspondingly maximized. The local-field enhancement factor is written as $L(\omega) = |\mathbf{E}_{\text{loc}}(\omega)|/|\mathbf{E}_0|$, where $|\mathbf{E}_{\text{loc}}(\omega)|$ is the local-field amplitude and \mathbf{E}_0 is the amplitude of the incoming field with frequency ω .¹³⁵ For a single nanoparticle, the two possible enhancement processes are the surface plasmon resonance (L_{SP}) and the lightning rod effect (L_{LR}), and the enhancement factor can be written as $L(\omega) = L_{SP}(\omega)L_{LR}$.¹³⁵ The plasmon resonance (L_{SP}) describes the field enhancement averaged over the particle surface, whereas the lightning rod effect (L_{LR}) describes the field enhancement due to a geometric phenomenon of electric field lines crowding at pointed metallic surfaces. For a nanosphere in the Rayleigh limit, only the dipole surface-plasmon resonance gives enhancement. However, for a nanorod, the lightning rod effect also contributes to the enhancement.

For second harmonic generation, two different contributions exist, one from the intrinsic nonlinear susceptibility of the metal nanostructure and one from a nonlinear surrounding host medium. Metals are organized in the cubic symmetry lattice, which is centrosymmetric and thus second harmonic radiation is forbidden. However, due to the symmetry breaking at the surface, the nanoscale second-order nonlinearity is possible on the metal surface.^{136–138} This process was first demonstrated on flat silver films experimentally and theoretically.¹³⁹ Later, an enhancement of second harmonic generation was found by a factor of 36 from silver gratings of various groove depths compared to the flat silver case.¹⁴⁰ The significant enhancement of SHG was also observed on rough metal surfaces and explained by the local-field model, where the SH power was scaled as $P_{SH} \propto |L(2\omega)|^2|L^2(\omega)|^2$.¹⁴¹ Enhanced SHG from rough metal films were investigated by using laser scanning optical microscopy. It was revealed that the origin of the enhancement was due to hot spots with high fields caused by localized modes.¹⁴² Thus far, the highest enhancement of a

nonlinear optical process on a rough metal surface is surface-enhanced Raman scattering (SERS). It was reported that the Raman scattering by single molecules on chemically roughened silver surfaces was enhanced by factors up to 10^{14} .^{143,144}

For metal nanoparticles, the nonlinear susceptibilities were observed from nanoparticle arrays,^{145–149} gold nanoparticles of different geometry,¹⁵⁰ and nanoantennas.^{151–153} For gold nanorods, the SHG was measured from gold nanorods with different aspect ratios using harmonic light scattering (HLS). It was shown that the dipolar hyperpolarizability (β) increased from the sphere to the rod shape and continued to increase with an increase in the aspect ratio of the nanorods.¹⁵⁴ Another study showed that the surface area of the gold nanorods increased linearly with β per particle.¹⁵⁵ However, researchers in this study reported decreased β values for an increase in aspect ratio of the gold nanorods. This was due to the decrease in the nanorod surface area as the aspect ratio increased. Therefore, the nanorod surface area was emphasized as influencing the β values. Another interesting study showed that the SHG from gold nanorods depends on the polarization and wavelength of the fundamental light.¹⁵⁶ In this study, the maximum intensity of SHG was obtained when the incident light polarization was directed parallel to the nanorod's long axis, whereas no SHG signal was detected from the light polarization along the short axis. In addition, the enhancement of SHG was maximized when the fundamental wavelength was tuned towards the extinction peak of the nanorods.

The local-field enhancement around the nanoparticles can also lead to the enhancement of second harmonic generation. The SHG enhancements have been observed in both far-field^{157–159} and near-field^{160,161} spectroscopic techniques. The SHG/two-photon excited fluorescence (TPEF) imaging of gold nanoparticles coated with nonlinear dye (JPW4041) in aqueous solution showed a lower bound of 100-fold enhancement.¹⁶² Nonlinear frequency mixing was efficiently modulated by using a gold nanoparticle dimer attached to the end of a pointed optical pipette.¹⁶³ A different study measured SHG from the smallest inorganic NLO-active nanoparticles in a two-photon microscopy setup.¹⁶⁴ The particles used were 10-15 nm diameter core/shell CdTe/CdS nanoparticles and showed a maximum SHG response at 970 nm.

Other than the applications in spectroscopy, several studies demonstrated local-field enhancement in SHG from nanoparticles. Our research group measured SHG from NLO ISAM

films and demonstrated that the surface plasmon enhancement by silver nanotriangles was 1600 times the SHG from bare ISAM film.⁶⁶ Another study demonstrated enhanced SHG from hybrid polymer nanoassemblies consisting of NLO polymer nanosheets with gold nanoparticles.¹⁶⁵ The distance between the NLO Langmuir-Blodgett polymer nanosheet and the gold nanoparticle monolayer was controlled by spacer pDDA nanosheets between the nanosheet and the gold nanoparticle monolayer. The second harmonic light from the two layers of hybrid NLO nanosheet with nanoparticle monolayer separated by pDDA spacers showed an enhancement factor of 288 compared to a pristine single layer NLO polymer nanosheet. It was observed that the SHG intensity from the NLO polymer nanosheet decreased exponentially with increasing spacer distance between the nanosheet and the gold nanoparticle monolayer. This study also showed the decay length dependence on the gold nanoparticle size.

References

1. Boyd, R. W. *Nonlinear optics*. (Academic Press, 2008).
2. P F Bordui & Fejer, and M. M. Inorganic Crystals for Nonlinear Optical Frequency Conversion. *Annu. Rev. Mater. Sci.* **23**, 321–379 (1993).
3. Armstrong, J. A., Bloembergen, N., Ducuing, J. & Pershan, P. S. Interactions between Light Waves in a Nonlinear Dielectric. *Phys. Rev.* **127**, 1918–1939 (1962).
4. Sauter, E. G. *Nonlinear optics*. (Wiley, 1996).
5. Lotspeich, J. F. Electrooptic light-beam deflection. *IEEE Spectr.* **5**, 45–52 (1968).
6. Mimoun, E., De Sarlo, L., Zondy, J.-J., Dalibard, J. & Gerbier, F. Sum-frequency generation of 589 nm light with near-unit efficiency. *Opt. Express* **16**, 18684 (2008).
7. Ricciardi, I. *et al.* Sum-frequency generation of cw ultraviolet radiation in periodically poled LiTaO₃. *Opt. Lett.* **34**, 1348 (2009).
8. Bass, M., Franken, P. A., Ward, J. F. & Weinreich, G. Optical Rectification. *Phys. Rev. Lett.* **9**, 446–448 (1962).
9. He, G. & Liu, S. H. *Physics of nonlinear optics*. (World Scientific, 1999).
10. Kleinman, D. A. Nonlinear Dielectric Polarization in Optical Media. *Phys. Rev.* **126**, 1977–1979 (1962).
11. Davydov, B. L. *et al.* Connection between charge transfer and laser second harmonic generation. *JEPT Lett* **12**, 16 (1970).
12. *Nonlinear optical properties of organic molecules and crystals*. (Academic Press, 1987).
13. Bosshard, C. *et al.* *Organic nonlinear optical materials*. (Gordon and Breach, 1995).
14. Levine, B. F. & Bethea, C. G. Second and third order hyperpolarizabilities of organic molecules. *J. Chem. Phys.* **63**, 2666–2682 (1975).

15. Marowsky, G. *et al.* Efficiency studies of second-harmonic-active organic dye coverages. *J. Opt. Soc. Am. B* **4**, 956 (1987).
16. *Molecular nonlinear optics: materials, physics, and devices.* (Academic Press, 1994).
17. Zyss, J. & Oudar, J. L. Relations between microscopic and macroscopic lowest-order optical nonlinearities of molecular crystals with one- or two-dimensional units. *Phys. Rev. A* **26**, 2028–2048 (1982).
18. Ledoux, I., Zyss, J., Jutand, A. & Amatore, C. Nonlinear optical properties of asymmetric polyphenyls: Efficiency versus transparency trade-off. *Chem. Phys.* **150**, 117–123 (1991).
19. Prasad, P. N. & Williams, D. J. *Introduction to nonlinear optical effects in molecules and polymers.* (Wiley, 1991).
20. Bailey, R. T., Cruickshank, F. R., Pugh, D. & McLeod, A. Quantitative Measurement Of Energy Deposited In Optical Coatings. in (eds. Colles, M. J. & Swift, D. W.) 88–89 (1983). doi:10.1117/12.934351
21. *Principles and applications of nonlinear optical materials.* (Blackie Academic & Professional ; Published in the USA and Canada by CRC Press, 1993).
22. Wood, R. M. *Optical materials.* (Inst. of Materials, 1993).
23. Meredith, G. R. Appraisal of Nonlinear Organic Optical Materials. in *SPIE* (eds. Mentzer, M. A. & Sriram, S.) **704**, 234–239 (1987).
24. Nayar, B. K. & Winter, C. S. Organic second-order non-linear optical materials and devices. *Opt. Quantum Electron.* **22**, 297–318 (1990).
25. Donald, A. M., Windle, A. H. & Hanna, S. *Liquid crystalline polymers.* (Cambridge Univ. Press, 2006).
26. Burroughes, J. H. *et al.* Light-emitting diodes based on conjugated polymers. *Nature* **347**, 539–541 (1990).
27. *Nonlinear optics of organic molecules and polymers.* (CRC Press, 1997).
28. Ye, C., Marks, T. J., Yang, J. & Wong, G. K. Synthesis of molecular arrays with nonlinear optical properties: second-harmonic generation by covalently functionalized glassy polymers. *Macromolecules* **20**, 2322–2324 (1987).

29. Singer, K. D. & King, L. A. Relaxation phenomena in polymer nonlinear optical materials. *J. Appl. Phys.* **70**, 3251–3255 (1991).
30. Singer, K. D. *et al.* Electro-optic phase modulation and optical second-harmonic generation in corona-poled polymer films. *Appl. Phys. Lett.* **53**, 1800–1802 (1988).
31. Reck, B. *et al.* Crosslinked Epoxy Polymers With Large And Stable Nonlinear Optical Susceptibilities. in (ed. Khanarian, G.) 74–83 (1990). doi:10.1117/12.962109
32. Eich, M. *et al.* Second-harmonic generation in poled organic monomeric glasses. *J. Opt. Soc. Am. B* **6**, 1590 (1989).
33. Eich, M. *et al.* Corona poling and real-time second-harmonic generation study of a novel covalently functionalized amorphous nonlinear optical polymer. *J. Appl. Phys.* **66**, 2559–2567 (1989).
34. Köhler, W., Robello, D. R., Dao, P. T., Willand, C. S. & Williams, D. J. Second harmonic generation and thermally stimulated current measurements: A study of some novel polymers for nonlinear optics. *J. Chem. Phys.* **93**, 9157–9166 (1990).
35. Wu, J. W. Birefringent and electro-optic effects in poled polymer films: steady-state and transient properties. *J. Opt. Soc. Am. B* **8**, 142 (1991).
36. Mortazavi, M. A., Higgins, B. G., Dienes, A., Knoesen, A. & Kowel, S. T. Second-harmonic generation and absorption studies of polymer–dye films oriented by corona-onset poling at elevated temperatures. *J. Opt. Soc. Am. B* **6**, 733 (1989).
37. Nye, J. F. *Physical properties of crystals: their representation by tensors and matrices.* (Clarendon Press ; Oxford University Press, 1984).
38. Maker, P. D., Terhune, R. W., Nisenoff, M. & Savage, C. M. Effects of Dispersion and Focusing on the Production of Optical Harmonics. *Phys. Rev. Lett.* **8**, 21–22 (1962).
39. Jerphagnon, J. & Kurtz, S. K. Maker Fringes: A Detailed Comparison of Theory and Experiment for Isotropic and Uniaxial Crystals. *J. Appl. Phys.* **41**, 1667–1681 (1970).
40. Dalton, L. R., Yu, L. P., Chen, M., Sapochak, L. S. & Xu, C. Recent advances in the synthesis and characterization of nonlinear optical materials: second-order materials. *Synth. Met.* **54**, 155–160 (1993).

41. Blodgett, K. B. Films Built by Depositing Successive Monomolecular Layers on a Solid Surface. *J. Am. Chem. Soc.* **57**, 1007–1022 (1935).
42. Blodgett, K. B. & Langmuir, I. Built-Up Films of Barium Stearate and Their Optical Properties. *Phys. Rev.* **51**, 964–982 (1937).
43. Ashwell, G. J., Hargreaves, R. C., Baldwin, C. E., Bahra, G. S. & Brown, C. R. Improved second-harmonic generation from Langmuir–Blodgett films of hemicyanine dyes. *Nature* **357**, 393–395 (1992).
44. Ashwell, G. J., Jackson, P. D. & Crossland, W. A. Non-centrosymmetry and second-harmonic generation in Z-type Langmuir–Blodgett films. *Nature* **368**, 438–440 (1994).
45. Netzer, L. & Sagiv, J. A new approach to construction of artificial monolayer assemblies. *J. Am. Chem. Soc.* **105**, 674–676 (1983).
46. Sagiv, J. Organized monolayers by adsorption. 1. Formation and structure of oleophobic mixed monolayers on solid surfaces. *J. Am. Chem. Soc.* **102**, 92–98 (1980).
47. Polymeropoulos, E. E. & Sagiv, J. Electrical conduction through adsorbed monolayers. *J. Chem. Phys.* **69**, 1836–1847 (1978).
48. Marks, T. J. & Ratner, M. A. Design, Synthesis, and Properties of Molecule-Based Assemblies with Large Second-Order Optical Nonlinearities. *Angew. Chem. Int. Ed. Engl.* **34**, 155–173 (1995).
49. Li, D. *et al.* Chromophoric self-assembled multilayers. Organic superlattice approaches to thin-film nonlinear optical materials. *J. Am. Chem. Soc.* **112**, 7389–7390 (1990).
50. Yitzchaik, S. *et al.* Chromophoric self-assembled NLO multilayer materials: real time observation of monolayer growth and microstructural evolution by in situ second harmonic generation techniques. *J. Phys. Chem.* **97**, 6958–6960 (1993).
51. Kakkar, A. K. *et al.* Chromophoric self-assembled nonlinear optical multilayer materials. Synthesis, properties, and structural interconversions of assemblies with rodlike alkynyl chromophores. *Langmuir* **9**, 388–390 (1993).
52. Lundquist, P. M. *et al.* Dispersion of second-order optical nonlinearity in chromophoric self-assembled films by optical parametric amplification: Experiment and theory. *Appl. Phys. Lett.* **64**, 2194 (1994).

53. Yitzchaik, S., Lundquist, P. M., Lin, W., Marks, T. J. & Wong, G. K. X(2) dispersion and waveguiding measurements in acentric chromophoric self-assembled NLO materials. in (ed. Moehlmann, G. R.) 282–289 (1994). doi:10.1117/12.187523
54. Roscoe, S. B. *et al.* Ion Exchange Processes and Environmental Effects in Chromophoric Self-Assembled Superlattices. Manipulation of Microstructure and Large Enhancements in Nonlinear Optical Response. *Langmuir* **10**, 1337–1339 (1994).
55. Zhu, P. *et al.* Realization of Expeditious Layer-by-Layer Siloxane-Based Self-assembly as an Efficient Route to Structurally Regular Acentric Superlattices with Large Electro-optic Responses. *Chem. Mater.* **14**, 4982–4989 (2002).
56. Decher, G., Hong, J. D. & Schmitt, J. Buildup of ultrathin multilayer films by a self-assembly process: III. Consecutively alternating adsorption of anionic and cationic polyelectrolytes on charged surfaces. *Thin Solid Films* **210–211**, 831–835 (1992).
57. Singer, K. D., Sohn, J. E. & Lalama, S. J. Second harmonic generation in poled polymer films. *Appl. Phys. Lett.* **49**, 248–250 (1986).
58. Singer, K. D., Kuzyk, M. G. & Sohn, J. E. Second-order nonlinear-optical processes in orientationally ordered materials: relationship between molecular and macroscopic properties. *J. Opt. Soc. Am. B* **4**, 968 (1987).
59. Lin, W., Lin, W., Wong, G. K. & Marks, T. J. Supramolecular Approaches to Second-Order Nonlinear Optical Materials. Self-Assembly and Microstructural Characterization of Intrinsically Acentric [(Aminophenyl)azo]pyridinium Superlattices. *J. Am. Chem. Soc.* **118**, 8034–8042 (1996).
60. Decher, G., Lvov, Y. & Schmitt, J. Proof of multilayer structural organization in self-assembled polycation-polyanion molecular films. *Thin Solid Films* **244**, 772–777 (1994).
61. Heflin, J. R., Figura, C., Marciu, D., Liu, Y. & Claus, R. O. Thickness dependence of second-harmonic generation in thin films fabricated from ionically self-assembled monolayers. *Appl. Phys. Lett.* **74**, 495–497 (1999).
62. Figura, C. *et al.* Thermal stability and immersion solution dependence of second-order nonlinear optical ionically self-assembled films. in **3939**, 214–222 (2000).
63. Figura, C. Second Order Nonlinear Optics in Ionically Self-Assembled Thin Films. (2000).

64. Figura, C. *et al.* Control of Second-Order Nonlinear Optical Susceptibility in Ionically Self-Assembled Films by pH and Ionic Strength. *MRS Proc.* **598**, (1999).
65. Neyman, P. J. *et al.* Enhanced Second Order Nonlinear Optical Susceptibilities in Ionically Self-Assembled Films Incorporating Dianionic Molecules. in *Mater. Res. Soc. Proc.* **660**, (2001).
66. Chen, K., Durak, C., Heflin, J. R. & Robinson, H. D. Plasmon-Enhanced Second-Harmonic Generation from Ionic Self-Assembled Multilayer Films. *Nano Lett.* **7**, 254–258 (2007).
67. Van Cott, K. E. *et al.* Layer-By-Layer Deposition and Ordering of Low-Molecular-Weight Dye Molecules for Second-Order Nonlinear Optics. *Angew. Chem. Int. Ed.* **41**, 3236–3238 (2002).
68. Heflin, J. R. *et al.* Efficient, Thermally Stable, Second Order Nonlinear Optical Response in Organic Hybrid Covalent/Ionic Self-Assembled Films. *Langmuir* **22**, 5723–5727 (2006).
69. Neyman, P. J. Second-Order Nonlinear Optical Characteristics of Nanoscale Self-Assembled Multilayer Organic Films. (Virginia Tech, 2004).
70. Agrawal, G. P. *Nonlinear fiber optics.* (Elsevier / Academic Press, 2007).
71. Daengngam, C. *et al.* Demonstration of a cylindrically symmetric second-order nonlinear fiber with self-assembled organic surface layers. *Opt. Express* **19**, 10326 (2011).
72. Daengngam, C. *et al.* Fabrication and characterization of periodically patterned silica fiber structures for enhanced second-order nonlinearity. *Opt. Express* **23**, 8113 (2015).
73. Chen, K. *et al.* Interface effects in plasmon-enhanced second-harmonic generation from self-assembled multilayer films. *J. Opt. Soc. Am. B* **27**, 92 (2010).
74. Kimura, K. & Asazawa, H. Frequency mixer with a frequency doubler for integrated circuits. *IEEE J. Solid-State Circuits* **29**, 1133–1137 (1994).
75. Chen, Q. & Zhang, X.-C. Polarization modulation in optoelectronic generation and detection of terahertz beams. *Appl. Phys. Lett.* **74**, 3435–3437 (1999).
76. Lu, Y., Xiao, M. & Salamo, G. J. Wide-bandwidth high-frequency electro-optic modulator based on periodically poled LiNbO₃. *Appl. Phys. Lett.* **78**, 1035 (2001).

77. Cotter, D. *et al.* Nonlinear Optics for High-Speed Digital Information Processing. *Science* **286**, 1523–1528 (1999).
78. Wu, Y.-D., Shih, T.-T. & Chen, M.-H. New all-optical logic gates based on the local nonlinear Mach-Zehnder interferometer. *Opt. Express* **16**, 248 (2008).
79. Perry, J. W., Mansour, K., Lee, I.-Y. S., Wu, X.-L. & al, et. Organic optical limiter with a strong nonlinear absorptive response. *Science* **273**, 1533 (1996).
80. Gustafsson, M. G. L. Nonlinear structured-illumination microscopy: Wide-field fluorescence imaging with theoretically unlimited resolution. *Proc. Natl. Acad. Sci. U. S. A.* **102**, 13081–13086 (2005).
81. Westphal, V. & Hell, S. W. Nanoscale Resolution in the Focal Plane of an Optical Microscope. *Phys. Rev. Lett.* **94**, 143903 (2005).
82. Müller, Squier, Wilson & Brakenhoff. 3D microscopy of transparent objects using third-harmonic generation. *J. Microsc.* **191**, 266–274 (1998).
83. Guo, Y. *et al.* Second-harmonic tomography of tissues. *Opt. Lett.* **22**, 1323 (1997).
84. Campagnola, P. J., Wei, M. D., Lewis, A. & Loew, L. M. High-resolution nonlinear optical imaging of live cells by second harmonic generation. *Biophys. J.* **77**, 3341–3349 (1999).
85. Gauderon, R., Lukins, P. B. & Sheppard, C. J. R. Three-dimensional second-harmonic generation imaging with femtosecond laser pulses. *Opt. Lett.* **23**, 1209 (1998).
86. Moreaux, L., Sandre, O. & Mertz, J. Membrane imaging by second-harmonic generation microscopy. *J. Opt. Soc. Am. B* **17**, 1685 (2000).
87. Ma, H., Jen, A. k.-Y. & Dalton, L. r. Polymer-Based Optical Waveguides: Materials, Processing, and Devices. *Adv. Mater.* **14**, 1339–1365 (2002).
88. Mulvaney, P. Surface Plasmon Spectroscopy of Nanosized Metal Particles. *Langmuir* **12**, 788–800 (1996).
89. Lee, K.-S. & El-Sayed, M. A. Gold and Silver Nanoparticles in Sensing and Imaging: Sensitivity of Plasmon Response to Size, Shape, and Metal Composition. *J. Phys. Chem. B* **110**, 19220–19225 (2006).

90. Jensen, T. R. *et al.* Nanosphere Lithography: Effect of the External Dielectric Medium on the Surface Plasmon Resonance Spectrum of a Periodic Array of Silver Nanoparticles. *J. Phys. Chem. B* **103**, 9846–9853 (1999).
91. Link, S., Mohamed, M. B. & El-Sayed, M. A. Simulation of the Optical Absorption Spectra of Gold Nanorods as a Function of Their Aspect Ratio and the Effect of the Medium Dielectric Constant. *J. Phys. Chem. B* **103**, 3073–3077 (1999).
92. Kerker, M. The optics of colloidal silver: something old and something new. *J. Colloid Interface Sci.* **105**, 297–314 (1985).
93. Novotny, L. & van Hulst, N. Antennas for light. *Nat. Photonics* **5**, 83–90 (2011).
94. Sharma, B., Frontiera, R. R., Henry, A.-I., Ringe, E. & Van Duyne, R. P. SERS: Materials, applications, and the future. *Mater. Today* **15**, 16–25 (2012).
95. Homola, J. Surface Plasmon Resonance Sensors for Detection of Chemical and Biological Species. *Chem. Rev.* **108**, 462–493 (2008).
96. Stockman, M. I. Nanoplasmonics: past, present, and glimpse into future. *Opt. Express* **19**, 22029 (2011).
97. Faraday, M. The Bakerian Lecture: Experimental Relations of Gold (and Other Metals) to Light. *Philos. Trans. R. Soc. Lond.* **147**, 145–181 (1857).
98. Zsigmondy, R. *The Chemistry of Colloids*. (John Wiley & Sons, Inc., New York, 1917).
99. Zsigmondy, R. & Alexander, J. *Colloids and the ultramicroscope: a manual of colloid chemistry and ultramicroscopy*. (John Wiley & Sons, Inc., New York, 1909).
100. Ostwald, C. W. W. *An Introduction to Theoretical and Applied Colloid Chemistry, 'the World of Neglected Dimensions.'* (John Wiley & Sons, Inc., New York, 1917).
101. Svedberg, T. *The Formation of Colloids*. (D. Van Nostrand Company, Inc., New York, 1921).
102. Svedberg, T. & Tiselius, A. *Colloid chemistry*. (The Chemical Catalog Company, Inc., New York, 1928).
103. Svedberg, T. & Pedersen, K. O. *The ultracentrifuge*. (Oxford University Press, Oxford, 1940).

104. Mie, G. Beiträge zur Optik trüber Medien, speziell kolloidaler Metallösungen. *Ann. Phys.* **330**, 377–445 (1908).
105. Gans, R. Über die Form ultramikroskopischer Goldteilchen. *Ann. Phys.* **342**, 881–900 (1912).
106. Goia, D. V. & Matijević, E. Preparation of monodispersed metal particles. *New J. Chem.* **22**, 1203–1215 (1998).
107. Sharma, V., Park, K. & Srinivasarao, M. Colloidal dispersion of gold nanorods: Historical background, optical properties, seed-mediated synthesis, shape separation and self-assembly. *Mater. Sci. Eng. R Rep.* **65**, 1–38 (2009).
108. Reetz, M. T. & Helbig, W. Size-Selective Synthesis of Nanostructured Transition Metal Clusters. *J. Am. Chem. Soc.* **116**, 7401–7402 (1994).
109. Yu, Chang, S.-S., Lee, C.-L. & Wang, C. R. C. Gold Nanorods: Electrochemical Synthesis and Optical Properties. *J. Phys. Chem. B* **101**, 6661–6664 (1997).
110. Jana, N. R., Gearheart, L. & Murphy, C. J. Wet Chemical Synthesis of High Aspect Ratio Cylindrical Gold Nanorods. *J. Phys. Chem. B* **105**, 4065–4067 (2001).
111. Nikoobakht, B. & El-Sayed, M. A. Preparation and Growth Mechanism of Gold Nanorods (NRs) Using Seed-Mediated Growth Method. *Chem. Mater.* **15**, 1957–1962 (2003).
112. Johnson, C. J., Dujardin, E., Davis, S. A., Murphy, C. J. & Mann, S. Growth and form of gold nanorods prepared by seed-mediated, surfactant-directed synthesis. *J. Mater. Chem.* **12**, 1765–1770 (2002).
113. Gao, J., Bender, C. M. & Murphy, C. J. Dependence of the gold nanorod aspect ratio on the nature of the directing surfactant in aqueous solution. *Langmuir* **19**, 9065–9070 (2003).
114. Cao, L., Zhu, T. & Liu, Z. Formation mechanism of nonspherical gold nanoparticles during seeding growth: Roles of anion adsorption and reduction rate. *J. Colloid Interface Sci.* **293**, 69–76 (2006).
115. Gole, A. & Murphy, C. J. Seed-Mediated Synthesis of Gold Nanorods: Role of the Size and Nature of the Seed. *Chem. Mater.* **16**, 3633–3640 (2004).
116. Jana, N. R., Gearheart, L. & Murphy, C. J. Seed-Mediated Growth Approach for Shape-Controlled Synthesis of Spheroidal and Rod-like Gold Nanoparticles Using a Surfactant Template. *Adv. Mater.* **13**, 1389–1393 (2001).

117. Gou, L. & Murphy, C. J. Fine-Tuning the Shape of Gold Nanorods. *Chem. Mater.* **17**, 3668–3672 (2005).
118. Jana, N. R., Gearheart, L. & Murphy, C. J. Evidence for Seed-Mediated Nucleation in the Chemical Reduction of Gold Salts to Gold Nanoparticles. *Chem. Mater.* **13**, 2313–2322 (2001).
119. Murphy, C. J., Jana, N. R. & others. Controlling the aspect ratio of inorganic nanorods and nanowires. *Adv. Mater.* **14**, 80 (2002).
120. Anker, J. N. *et al.* Biosensing with plasmonic nanosensors. *Nat. Mater.* **7**, 442–453 (2008).
121. Mayer, K. M. *et al.* A Label-Free Immunoassay Based Upon Localized Surface Plasmon Resonance of Gold Nanorods. *ACS Nano* **2**, 687–692 (2008).
122. Willets, K. A. & Van Duyne, R. P. Localized Surface Plasmon Resonance Spectroscopy and Sensing. *Annu. Rev. Phys. Chem.* **58**, 267–297 (2007).
123. Jayabal, S. *et al.* A gold nanorod-based localized surface plasmon resonance platform for the detection of environmentally toxic metal ions. *The Analyst* **140**, 2540–2555 (2015).
124. Chai, F., Wang, C., Wang, T., Li, L. & Su, Z. Colorimetric Detection of Pb²⁺ Using Glutathione Functionalized Gold Nanoparticles. *ACS Appl. Mater. Interfaces* **2**, 1466–1470 (2010).
125. Haes, A. J., Zou, S., Schatz, G. C. & Van Duyne, R. P. A Nanoscale Optical Biosensor: The Long Range Distance Dependence of the Localized Surface Plasmon Resonance of Noble Metal Nanoparticles. *J. Phys. Chem. B* **108**, 109–116 (2004).
126. Huang, X., Neretina, S. & El-Sayed, M. A. Gold Nanorods: From Synthesis and Properties to Biological and Biomedical Applications. *Adv. Mater.* **21**, 4880–4910 (2009).
127. Huang, X. & El-Sayed, M. A. Gold nanoparticles: Optical properties and implementations in cancer diagnosis and photothermal therapy. *J. Adv. Res.* **1**, 13–28 (2010).
128. Svaasand, L. O., Gomer, C. J. & Morinelli, E. On the physical rationale of laser induced hyperthermia. *Lasers Med. Sci.* **5**, 121–128 (1990).
129. El-Sayed, I. H., Huang, X. & El-Sayed, M. A. Surface Plasmon Resonance Scattering and Absorption of anti-EGFR Antibody Conjugated Gold Nanoparticles in Cancer Diagnostics: Applications in Oral Cancer. *Nano Lett.* **5**, 829–834 (2005).

130. Murphy, C. J. *et al.* Gold Nanoparticles in Biology: Beyond Toxicity to Cellular Imaging. *Acc. Chem. Res.* **41**, 1721–1730 (2008).
131. Maier, S. A. & Atwater, H. A. Plasmonics: Localization and guiding of electromagnetic energy in metal/dielectric structures. *J. Appl. Phys.* **98**, 011101 (2005).
132. Atwater, H. A. The Promise of Plasmonics. *Sci. Am.* **296**, 56–62 (2007).
133. Dobrzynski, L. *et al.* Simple nanometric plasmon multiplexer. *Phys. Rev. E* **69**, (2004).
134. Barnes, W. L., Dereux, A. & Ebbesen, T. W. Surface plasmon subwavelength optics. *Nature* **424**, 824–830 (2003).
135. Maier, S. A. *Plasmonics: fundamentals and applications*. (Springer, 2007).
136. Bloembergen, N., Chang, R. K., Jha, S. S. & Lee, C. H. Optical Second-Harmonic Generation in Reflection from Media with Inversion Symmetry. *Phys. Rev.* **174**, 813–822 (1968).
137. Rudnick, J. & Stern, E. A. Second-Harmonic Radiation from Metal Surfaces. *Phys. Rev. B* **4**, 4274–4290 (1971).
138. Sipe, J. E., So, V. C. Y., Fukui, M. & Stegeman, G. I. Analysis of second-harmonic generation at metal surfaces. *Phys. Rev. B* **21**, 4389–4402 (1980).
139. Simon, H. J., Mitchell, D. E. & Watson, J. G. Optical Second-Harmonic Generation with Surface Plasmons in Silver Films. *Phys. Rev. Lett.* **33**, 1531–1534 (1974).
140. Coutaz, J. L., Neviere, M., Pic, E. & Reinisch, R. Experimental study of surface-enhanced second-harmonic generation on silver gratings. *Phys. Rev. B* **32**, 2227–2232 (1985).
141. Chen, C. K., Heinz, T. F., Ricard, D. & Shen, Y. R. Surface-enhanced second-harmonic generation and Raman scattering. *Phys. Rev. B* **27**, 1965–1979 (1983).
142. Bozhevolnyi, S. I., Beermann, J. & Coello, V. Direct Observation of Localized Second-Harmonic Enhancement in Random Metal Nanostructures. *Phys. Rev. Lett.* **90**, 197403 (2003).
143. Kneipp, K. *et al.* Single Molecule Detection Using Surface-Enhanced Raman Scattering (SERS). *Phys. Rev. Lett.* **78**, 1667–1670 (1997).
144. Nie, S. & Emory, S. R. Probing Single Molecules and Single Nanoparticles by Surface-Enhanced Raman Scattering. *Science* **275**, 1102–1106 (1997).

145. McMahon, M. D., Lopez, R., Haglund, R. F., Ray, E. A. & Bunton, P. H. Second-harmonic generation from arrays of symmetric gold nanoparticles. *Phys. Rev. B* **73**, 041401 (2006).
146. Moran, A. M., Sung, J., Hicks, E. M., Van Duyne, R. P. & Spears, K. G. Second Harmonic Excitation Spectroscopy of Silver Nanoparticle Arrays. *J. Phys. Chem. B* **109**, 4501–4506 (2005).
147. Canfield, B. K. *et al.* Local Field Asymmetry Drives Second-Harmonic Generation in Noncentrosymmetric Nanodimers. *Nano Lett.* **7**, 1251–1255 (2007).
148. Metzger, B. *et al.* Strong Enhancement of Second Harmonic Emission by Plasmonic Resonances at the Second Harmonic Wavelength. *Nano Lett.* **15**, 3917–3922 (2015).
149. Yang, M. *et al.* Plasmon-enhanced second-harmonic generation from hybrid ZnO-covered silver-bowl array. *J. Phys. Condens. Matter* **28**, 214003 (2016).
150. Czaplicki, R. *et al.* Second-Harmonic Generation from Metal Nanoparticles: Resonance Enhancement versus Particle Geometry. *Nano Lett.* **15**, 530–534 (2015).
151. Chen, P.-Y., Argyropoulos, C. & Alù, A. Enhanced nonlinearities using plasmonic nanoantennas. *Nanophotonics* **1**, 221–233 (2012).
152. Linnenbank, H., Grynko, Y., Förstner, J. & Linden, S. Second harmonic generation spectroscopy on hybrid plasmonic/dielectric nanoantennas. *Light Sci. Appl.* **5**, e16013 (2016).
153. Celebrano, M. *et al.* Mode matching in multiresonant plasmonic nanoantennas for enhanced second harmonic generation. *Nat. Nanotechnol.* **10**, 412–417 (2015).
154. Singh, A., Lehoux, A., Remita, H., Zyss, J. & Ledoux-Rak, I. Second Harmonic Response of Gold Nanorods: A Strong Enhancement with the Aspect Ratio. *J. Phys. Chem. Lett.* **4**, 3958–3961 (2013).
155. Ngo, H. M., Nguyen, P. P. & Ledoux-Rak, I. Optimization of second harmonic generation of gold nanospheres and nanorods in aqueous solution: the dominant role of surface area. *Phys. Chem. Chem. Phys.* **18**, 3352–3356 (2016).
156. Hubert, C. *et al.* Role of surface plasmon in second harmonic generation from gold nanorods. *Appl. Phys. Lett.* **90**, 181105 (2007).

157. Boyd, G. T., Rasing, T., Leite, J. R. R. & Shen, Y. R. Local-field enhancement on rough surfaces of metals, semimetals, and semiconductors with the use of optical second-harmonic generation. *Phys. Rev. B* **30**, 519–526 (1984).
158. Podlipensky, A., Lange, J., Seifert, G., Graener, H. & Cravetchi, I. Second-harmonic generation from ellipsoidal silver nanoparticles embedded in silica glass. *Opt. Lett.* **28**, 716 (2003).
159. Kim, E. *et al.* Second-Harmonic Generation of Single BaTiO₃ Nanoparticles down to 22 nm Diameter. *ACS Nano* **7**, 5343–5349 (2013).
160. Zayats, A. V., Kalkbrenner, T., Sandoghdar, V. & Mlynek, J. Second-harmonic generation from individual surface defects under local excitation. *Phys. Rev. B* **61**, 4545–4548 (2000).
161. Mauser, N. & Hartschuh, A. Tip-enhanced near-field optical microscopy. *Chem Soc Rev* **43**, 1248–1262 (2014).
162. Clark, H. A., Campagnola, P. J., Wuskell, J. P., Lewis, A. & Loew, L. M. Second Harmonic Generation Properties of Fluorescent Polymer-Encapsulated Gold Nanoparticles. *J. Am. Chem. Soc.* **122**, 10234–10235 (2000).
163. Palomba, S., Danckwerts, M. & Novotny, L. Nonlinear plasmonics with gold nanoparticle antennas. *J. Opt. Pure Appl. Opt.* **11**, 114030 (2009).
164. Zielinski, M., Oron, D., Chauvat, D. & Zyss, J. Second-Harmonic Generation from a Single Core/Shell Quantum Dot. *Small* **5**, 2835–2840 (2009).
165. Ishifuji, M., Mitsuishi, M. & Miyashita, T. Bottom-up Design of Hybrid Polymer Nanoassemblies Elucidates Plasmon-Enhanced Second Harmonic Generation from Nonlinear Optical Dyes. *J. Am. Chem. Soc.* **131**, 4418–4424 (2009).

Chapter 3

Sample Fabrication Methods

This chapter will discuss sample fabrication methods including ISAM film fabrication and gold nanorod synthesis. First, the procedure of ISAM film deposition on a glass substrate will be discussed. Then, gold nanorod synthesis by seed-mediated growth method will be discussed in detail. In this study, hydroquinone was used as a reducing agent instead of ascorbic acid, which is more commonly used for different applications. The aspect ratio of gold nanorod was controlled by the amount of silver ions, and the role of silver ions in gold nanorod synthesis will be explained. Gold nanorods were characterized via UV-Vis-NIR spectral measurement and zeta potential measurement. The former identified the wavelength location of the longitudinal surface plasmon resonance (LSPR) peak and the latter confirmed the charge of the particles.

In our early studies of functionalized nanorods on ISAM films, PSS-coated nanorods were received from the Murphy group at UIUC. However, PSS-coated nanorods deposited on PAH/PCBS film did not demonstrate any enhancement in the SHG signal even when the density of nanorods were high. This may be attributed to the thick layer of PSS polymer and CTAB bilayer surrounding each nanorod, making it difficult for the LSPR mode to reach the PCBS film. Therefore, functionalizing gold nanorods with PCBS was pursued to bring the NLO film (PCBS) closer to nanorods. A method of replacing the CTAB bilayer and a procedure of coating PAH/PCBS layers onto nanorods will be presented, followed by deposition of the functionalized gold nanorods on ISAM films. To observe how gold nanorods deposited on ISAM films, the samples were imaged by Field Emission Scanning Electron Microscopy (FESEM).

3.1 Second-order NLO ISAM Film Deposition Process

The standard ISAM fabrication procedure was done as following. Glass microscope slides (Fisher Scientific) were used as substrates and cleaned by the RCA cleaning process¹ which involved two steps. First, the slides were placed in a 1:1:5 by volume NH_4OH : 30 % H_2O_2 : H_2O solution at 70 - 75 °C for 20 minutes. Rinsed thoroughly with purified deionized (DI) water, the slides were then placed in a 1:1:6 by volume HCl : 30 % H_2O_2 : H_2O solution at 70 - 75 °C for 20 minutes, followed by rinsing in DI water and drying with nitrogen gas. After the cleaning process, the slides were immersed into the initial cationic solution and stirred for 3 minutes. After rinsing in DI water for 2 minutes to remove excess polymer, the slides were immersed into the NLO-active anionic solution and stirred for 3 minutes, followed by rinsing in DI water for 2 minutes. This process was automated by a StratoSequenceTM Mark VI robotic deposition system (nanoStrata Inc.) which can be programmed to perform dipping and stirring motions in a beaker placed on a rotation stage.

For the ISAM film deposition, poly(allylamine hydrochloride) known as PAH ($[\text{C}_3\text{H}_7\text{N}]_n \text{HCl}$, $M_w \sim 15000$ g/mol, Aldrich 283215) was used for the NLO-inactive cation layer. For the anion layer, two types were used in this study; PSS and PCBS. Poly(sodium 4-styrenesulfonate) known as PSS ($[\text{C}_8\text{H}_7\text{NaO}_3\text{S}]_n$, $M_w \sim 70000$ g/mol, Aldrich 243051) is an NLO-inactive anion, and (poly[carboxyhydroxyphenylazobenzenesulfonamidoethanediyl] sodium salt) known as PCBS ($[-\text{CH}_2\text{CH}[\text{NH}\text{SO}_2\text{C}_6\text{H}_4\text{N}=\text{NC}_6\text{H}_3(\text{OH})\text{CO}_2\text{Na}]-]_n$, Aldrich 346411) is an NLO-active anion. PCBS contains pendant azobenzene chromophores that have a high hyperpolarizability generating high SHG signal. The molecular structures of these polymers are shown in **Figure 3.1**.

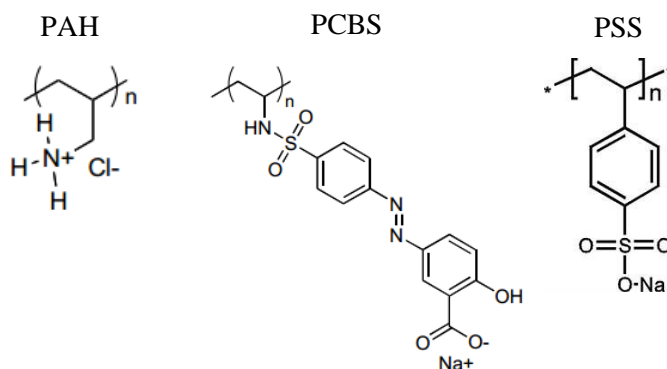


Figure 3.1 Molecular structures of the polymers used in ISAM NLO film fabrication. PAH is the cation and either PCBS or PSS is the anion.

All of the polymers mentioned above were dissolved in water to make 10 mM concentration and stirred overnight before use. In solution, PAH was colorless, PSS was pale yellow, and PCBS was orange-yellow. The original pH values of PAH, PSS, and PCBS were around 4, 5, and 10, respectively, and all were adjusted to pH 7.0 by adding NaOH (for PAH and PSS) or HCl (for PCBS).

The pK_a values of PAH, PSS, and PCBS are 8.7,²⁻⁴ 1,^{5,6} and 3,⁷ respectively. The relationship between pK_a and pH is described by the Henderson-Hasselbalch equation which is obtained by rearranging the acid dissociation constant equation, $K_a = [H^+][A^-]/[HA]$.

$$pH = pK_a + \log_{10} \left(\frac{[A^-]}{[HA^+]}\right) \quad (3.1)$$

The acid dissociation constant, K_a , expresses how easily the acid releases a proton to become more acidic. In equation (3.1), $pH = pK_a$ when $[A^-] = [HA^+]$. Therefore, when the pH is equal to the pK_a exactly half of the acid is dissociated and there are equal amounts of protonated and deprotonated acid molecules.

Polyelectrolytes can be separated into strong and weak types. A strong polyelectrolyte, such as PSS, is completely dissociated in solution for most reasonable pH values. However, a weak polyelectrolyte, like PAH, is partially dissociated, not fully charged, in solution at intermediate pH values because its dissociation constant (pK_a) is in the range of 2 to 10. Consequently, the charge of PAH can be modified by changing the pH, counterion concentration, or ionic strength of the solution. At around pH 7, the PAH polyelectrolytes are fully charged in the flat, train-like conformations.^{2,8,9} The structure of polymer conformation consisting of tails, loops, and trains is illustrated in **Figure 3.2**. The resulting layers are optically homogeneous and very thin with about 1.2 nm thick bilayers.¹⁰ The PCBS/PAH ISAM films deposited on glass at pH 7 exhibit long-range polar ordering of the PCBS chromophore for films of more than 600 bilayers.¹¹

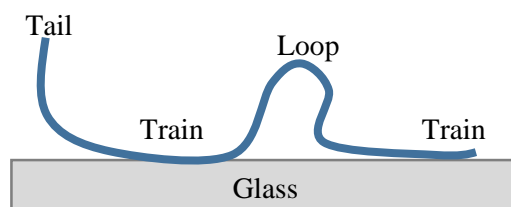


Figure 3.2 Polymer conformation: tails, loops, and trains.

The ISAM films for this study contained three or three and a half bilayers of cation (PAH) and NLO-inactive or NLO-active anions (PSS or PCBS, respectively). The number of layers were chosen based on a previous study done by Chen et al. at Virginia Tech, where plasmon-enhanced SHG from silver triangular nanoparticles was reported.¹² In this report, the SHG signal from the ISAM film incorporated with the silver nanoparticles increased very quickly for the first few bilayers and then leveled off after three bilayers (3 - 4 nm thick) due to the decay length of the LSPR (localized surface plasmon resonance) mode. The upper most layer of the ISAM film must be oppositely charged to that of the functionalized nanorods in order to bind (negatively/positively charged) gold nanorods on to the ISAM film.

3.2 Gold Nanorod Synthesis: Seed-mediated Growth Method

Gold nanorods were synthesized using the silver-assisted seed-mediated growth method using two different reducing agents for different applications. The seed-mediated growth method is the most popular method for the synthesis of gold nanorods due to several advantages: it is simple to execute, the growth rate is fast due to increased overall reaction rate, it is easy to control the size of particles by varying the ratio of gold salt to seed, and it provides high quality and yield of nanorods.

The shape-controlled seed-mediated gold nanorod growth synthesis involves two steps. First, the small size spherical gold nanoparticles (seed solution) was prepared. Second, in the growth solution containing a weak reducing agent (such as ascorbic acid or hydroquinone), the growth of nanorods was controlled by the amount of seed and silver ions. Because the reducing agent in growth solution is too weak to reduce gold ions to gold atoms at low pH, it is necessary to follow

two reduction steps. In the first reduction, Au^{3+} is reduced to Au^+ by a weak reducing agent and in the second reduction, Au^+ is reduced to Au^0 by seed solution. Seed particles act as nucleation sites catalyzing the reduction of Au^+ to Au^0 on their surfaces.¹³

The first seed-mediated growth method was developed by Jana et al.¹⁴ in 2001 and modified by Nikoobakht et al.¹⁵ in 2003. In the original method by Jana et al., the seed was prepared by citrate-capped small gold nanospheres (3 - 4 nm) and gold nanorods were prepared by adding the seed to HAuCl_4 growth solution containing gold salt, CTAB, ascorbic acid (Vitamin C) as the reducing agent, and silver ions for shape selection. In this method, the aspect ratio (Length/Width) was controlled by varying the seed-to-gold salt ratio in the presence of silver ions. The role of silver ions to change the aspect ratio of the gold nanorods was already observed in the electrochemical synthesis of gold nanorods by Yu et al.¹⁶ and Mohamed et al.¹⁷ One of the limitations of this method is poor yield of gold conversion. It requires a half-dozen rounds of centrifugation and washings to separate nanorods from spherical and plate-like gold nanoparticle byproducts.¹⁸ In order to overcome this drawback, Nikoobakht and El-Sayed made two modifications to this method by replacing sodium citrate with CTAB in the seed formation process and adjusting silver contents in the growth solution to control the aspect ratios. This method produced gold nanorods with high yield without repetitive centrifugations for sphere separation. However, later it was observed by Liu et al. and others that the nanorods can further grow into a dumbbell shape causing the LSPR to blue-shift by up to 100 nm over the first few hours.¹⁹⁻²² Liu et al. reported that controlling the pH by adding hydrochloric acid (HCl) could improve the method and stability of the nanorods.¹⁹

Recently, Vigdeman and Zubarev reported the synthesis of gold nanorods using hydroquinone yielding nanorods with LSPR up to 1250 nm.²³ Hydroquinone is a novel reducing agent and has been used in the synthesis of silver²⁴ and gold^{25,26} nanoparticles. Hydroquinone is a weaker reducing agent than ascorbic acid and thus the growth occurs at a much slower rate (up to 12 hours) than in the standard procedure using ascorbic acid (30 minutes). Since the LSPR of the nanorods for this research needs to be around 1064 nm and the gold nanorod synthesis by reduction of ascorbic acid produces nanorods of LSPR peaks less than 850 nm, the hydroquinone reduction method was considered for this study.

3.3 Hydroquinone Reduction of the Growth Solution

Glasswares (500 mL and 1 L Erlenmeyer flasks) was cleaned prior to each use with aqua regia (3 parts hydrochloric acid (HCl) and 1 part nitric acid (HNO₃), yellow-orange fuming liquid) in the fume hood for 30 minutes and rinsed copiously with DI water. It is important to remove any residual gold nanoparticles to avoid contamination and gold nanoparticles can only be dissolved in aqua regia. The 500 mL flask is for CTAB solution and 1 L flask is for gold nanorod solution. For the solutions of gold, silver, sodium hydroxide, sodium borohydride, and hydroquinone, it is possible to use glass flasks (25 mL Erlenmeyer flask) after being thoroughly cleaned. However, if available, it is more convenient to use sterile disposable centrifuge tubes (15 mL and 45 mL).

In order to determine the desired LSPR of gold nanorods, various samples of 10 mL nanorod solution with differing amounts of silver were first synthesized. After that, a scaled-up batch can be synthesized with the correct amount of silver based on the first trial.

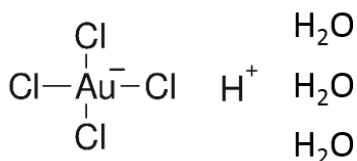
3.3.1 Materials

All materials used for gold nanorod synthesis are listed in the **Table 3.1** and their chemical structures are shown in **Figure 3.3**. All solutions were dissolved in ultrapure (18M Ω) DI water. All chemicals were prepared fresh each time, but CTAB can be prepared in advance. In order to prevent contamination, all chemicals were weighed using disposable spatulas and weighing boats. If necessary, solvent was squirted into the weighing boats to remove all of the powders.

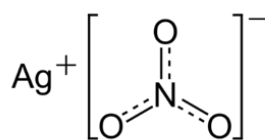
It is known that CTAB from different suppliers and different catalog numbers affect both the aspect ratio of the nanorods and the yield due to the impurities.²⁷ In this research, we obtained CTAB (for molecular biology, > 99%) from Sigma with a product code H6269.

Table 3.1 Materials for gold nanorod synthesis

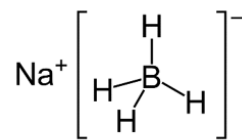
Materials
Gold (III) chloride trihydrate ($\text{HAuCl}_4 \cdot 3\text{H}_2\text{O}$; 99%, Aldrich 254169)
Silver nitrate (AgNO_3 ; 99%, Aldrich 204390)
Cetyltrimethylammonium bromide (CTAB, $\text{CH}_3(\text{CH}_2)_{15}\text{N}(\text{Br})(\text{CH}_3)_3$, Sigma H6269)
Sodium hydroxide (NaOH ; >98%, Sigma-Aldrich S5881)
Sodium borohydride (NaBH_4 ; >96%, Aldrich 452882)
Hydroquinone ($\text{C}_6\text{H}_6\text{O}_2$; 99%, Alfa Aesar A11411)



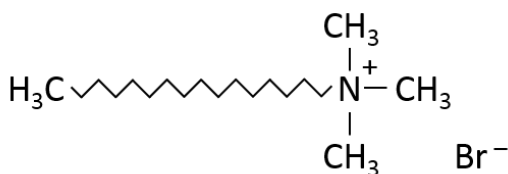
(a) $\text{HAuCl}_4 \cdot 3\text{H}_2\text{O}$ (chloroauric acid)



(b) AgNO_3 (silver nitrate)



(c) NaBH_4 (sodium borohydride)



(d) CTAB (cetyltrimethylammonium)



(e) $\text{C}_6\text{H}_4(\text{OH})_2$ (Hydroquinone)

Figure 3.3 The structures of the materials for gold nanorod synthesis.

3.3.2 Solution Preparation

Gold (chloroauric acid) and silver (silver nitrate) salt solutions are light sensitive, and therefore, they should be prepared in the dark and covered with aluminum foil for storage. It is best to prepare them fresh for each use as they become unstable after a week. Gold salts rapidly absorb moisture from the air and become sticky, and thus it is best to weigh them out under nitrogen or argon and store them in a desiccator.

All other chemicals can be prepared in light under a fume hood. CTAB can be prepared in advance, but it crystallizes at room temperature and needs to be heated to 28 - 30 °C to dissolve before mixing into gold salt solution. It is useful to keep CTAB solution in an oven with temperature set at 28 °C or in a warm water bath.

Sodium borohydride (NaBH_4) is a strong reducing agent used for gold seeds. Just like gold salts, sodium borohydride quickly absorbs moisture from the air and becomes wet and clumps together. Therefore, the weighed powder should not be returned to the container to avoid contamination. In aqueous solutions, it is hydrolyzed to Na_3BO_3 and H_2 and the hydrolysis slows down in alkaline solutions. Therefore, in a strongly basic solution (at or above pH 10), sodium borohydride is stabilized against reaction with water. Since NaBH_4 strongly reacts with water at room temperature, the solvent is cooled with ice. In this study, it was dissolved in ice cold 0.01 M sodium hydroxide (NaOH). NaOH is often available as small pellets, it is easier to prepare 0.1M NaOH first and dilute to make 0.01 M NaOH . Likewise, for NaBH_4 solution preparation, an easy way is to prepare 0.1 M NaBH_4 in 0.01 M NaOH and dilute to prepare the final concentration. A solution of NaBH_4 should be prepared freshly just before its use.

A list of solution preparation conditions is shown in **Table 3.2**. The volume of gold solution and/or CTAB solution can vary depending on the particular size of the scaled-up batch. Hydroquinone solution is best to be prepared just before its use in the growth synthesis (step 2).

Table 3.2 Solution Preparation for Gold Nanorod Synthesis

Solution Preparation	
0.01 M Gold solution	0.118 g of (HAuCl ₄ · 3H ₂ O) dissolved in 30 mL of H ₂ O
0.1 M CTAB solution	3.6445 g of CTAB dissolved in 100 mL of H ₂ O (at 28 - 30 °C)
0.1 M Silver solution	0.1699 g of AgNO ₃ dissolved in 10 mL of H ₂ O
0.1 M NaOH solution	0.12 g of NaOH dissolved in 30 mL of H ₂ O
0.1 M NaBH ₄ solution	0.045 g of NaBH ₄ dissolved in 10 mL of 0.01 M NaOH (on ice)
0.1 M Hydroquinone solution	0.110 g of hydroquinone dissolved in 10 mL of H ₂ O

3.3.3 Gold Nanorod Synthesis Procedure

The synthesis of gold nanorods by reduction of hydroquinone was slightly modified from the procedure given by Vidgerman and Zubarev.²³ The procedure was developed and passed down by a graduate student of Prof. Murphy at the University of Illinois at Urbana-Champaign (UIUC). As mentioned earlier, this procedure is typically done twice: the test trial to determine the desired LSPR wavelength of gold nanorods and the main trial for making a scaled-up batch.

In the first trial, five different samples (10 mL each) with various amounts of silver were prepared, followed by spectral measurement using a UV-Vis-NIR spectrometer or a reflectometer. Once the desired amount of silver was determined, a large batch (~ 500 mL) was prepared. Since CTAB molecules crystallize at room temperature (21 °C), the entire process was done in an oven at 28 - 29 °C with a magnetic stirrer placed inside for stirring with a stir bar. It can also be done in a warm water bath at the said temperature. The protocol involved two steps as follows.

Step 1: Gold seeds preparation

Seeds were prepared by reduction of a gold salt with a strong reducing agent, sodium borohydride. After preparing gold, silver, CTAB, and NaOH solutions, the gold seeds were prepared by the following instruction.

- i. If using an oven, set temperature at 28 °C and put a magnetic stirrer inside. If using a warm water bath, place a big dish containing water on a magnetic stirrer with hot plate at 28 °C.
- ii. Prepare 9.5 mL of 0.1 M CTAB solution in a 20 mL glass vial with a tiny stir bar and place them in the oven (or in a warm water bath) to dissolve CTAB.
- iii. Cool two 15 mL centrifuge tubes on ice until very cold but not frozen. One tube contains 10 mL of 0.01 M NaOH and the other tube contains 9 mL of 0.01 M NaOH.
- iv. Add 0.5 mL of 0.01 M chloroauric acid solution (gold solution) into the CTAB solution in the vial. Set to stir vigorously with a stir bar inside the oven.
- v. Weigh out 0.045 g of NaBH₄ and add it to the 10 mL tube of 0.01 M NaOH and shake vigorously to dissolve.
- vi. Transfer 1 mL of the NaBH₄ solution to the other tube containing 9 mL of 0.01 M NaOH and shake to mix.
- vii. Quickly add 0.46 mL of the final solution (0.01 M NaBH₄ in 0.01 M NaOH) into the rapid stirring gold and CTAB solution.
- viii. Let stir for 10 minutes without the cap on and then let sit for 1 hour, loosely capped, before using. The solution should change to brown after the addition of NaBH₄.

It is important to note that the gold solution mixture (chloroauric acid and CTAB) should be stirred vigorously, creating a vortex, before adding sodium borohydride. The seeds need to be stored at temperature 28 - 29 °C in order to prevent CTAB crystallization and can be used within 24 hours.

Step 2: Synthesis of Gold Nanorods

Gold nanorods are synthesized by hydroquinone reduction of gold ions and second reduction by gold seeds. The aspect ratio of the nanorods are controlled by changing the amounts of silver ions in the gold growth solution. In a typical test trial, five different amounts of silver between 10 and 50 μL were used. Prepare gold, CTAB, silver, hydroquinone, and seed solutions.

- i. Add 9.5 mL of 0.1 M CTAB to a 15 mL centrifuge tube. Prepare 5 of them and label them.
- ii. Add 0.5 mL of 0.01 M HAuCl_4 (gold solution) and to each one invert to mix.
- iii. Add 10, 20, 30, 40, and 50 μL of 0.1 M AgNO_3 (silver solution) to the different tubes and invert to mix.
- iv. Add 0.5 mL of 0.1 M hydroquinone to each one and invert to mix. Solution should turn completely transparent. This indicates that Au(III) is reduced to Au(I).
- v. Add 0.160 mL of seeds to each one and invert to mix.
- vi. Store them overnight.
- vii. Centrifuge at 6,000 rcf for 40 minutes to remove the supernatant and redisperse in DI water. Repeat the centrifugation to remove as much excess CTAB as possible.

The final products are red to brown color depending on the amounts of silver solution. It varies red through brown with increasing silver amounts resulting in increasing the aspect ratios of gold nanorods. The centrifugation parameters may depend on the sample volume and concentration. Settling time can be estimated from the Stokes equation and optimized by trial and error. If temperature setting is available in the centrifuge, set it to 28 $^{\circ}\text{C}$ to avoid crystallization of excess CTAB in the gold nanorod solution.

For a scaled-up batch, the same seed solution can be used within a day. A 1 L flask was used to make ~ 500 mL nanorod solution. The volume can be scaled up linearly. Once everything including the seeds was added to the growth solution, it was stirred moderately overnight in the oven (or in a warm bath). After 12 plus hours later, the nanorod solution was centrifuged once to remove excess CTAB and redispersed in DI water. For convenience in storage, the nanorod solution was concentrated about 13 times and kept at room temperature in darkness.

3.3.4 Characterization of Gold Nanorods

In order to investigate the LSPR peaks of the test trial samples, samples can be characterized by a UV-Vis-NIR spectrometer that has a wavelength range from 150 nm to over 1 μm because the LSPRs of the gold nanorods are expected to be in the near infrared range (around 1100 nm). Since such equipment was not available for our use, we used a reflectometer, Filmetrics (F10-VC), which measures reflectance and transmittance simultaneously. Water was used as a baseline and the as-synthesized nanorods were inserted into a flat glass cell (1 mm thick, 1mL volume) for spectral measurement. The absorbance was calculated from the reflectance and transmittance using the Beer-Lambert law.

$$A = \log_{10} \left(\frac{I_0}{I} \right) = \log_{10} \left(\frac{1}{T} \right) = 2 - \log_{10}(\%T) \quad (3.2.1)$$

$$A = \epsilon CL \quad (3.2.2)$$

where the parameters are as follows.

A optical density (also called extinction or absorbance)

T transmittance

I_0 incident light intensity

I transmitted light intensity

ϵ extinction coefficient, in $\text{M}^{-1}\text{cm}^{-1}$

C molar concentration of the nanoparticles/molecules, in mole/L or M

L absorption path length (distance the light travels through the sample), in cm

The Beer-Lambert law relates the optical density to the properties of a material through which light is traveling. The optical density of a sample is linearly related to the molar concentration, path length, and the extinction coefficient. The extinction coefficient measures how strongly a material absorbs light of a certain wavelength. According to the Beer-Lambert law, the transmitted light intensity decreases exponentially as any one of the three parameters increases.

The extinction spectra of the gold nanorod solutions with various amounts of silver are plotted in **Figure 3.4**. It is well known that the longitudinal resonance is red-shifted as the aspect ratio

increases^{16,18,28,29} and that increasing silver concentration increases the aspect ratio of the nanorods.^{15,19} In **Figure 3.4**, the longitudinal resonance band was red-shifted with silver amounts up to 30 μL (a, b, and c in **Figure 3.4**), hitting a maximum at about 1130 nm. Further increasing of the silver amounts resulted in blue-shift (d and e in **Figure 3.4**).

The role of silver ions in controlling the aspect ratio was initially explained by Jana and Murphy that the large amounts of Ag^+ and Br^- (from the CTAB) precipitate and may adsorb at the nanorod surface in the form of AgBr, restricting the particle growth.¹⁴ This was based on the fact that silver ions cannot be reduced to silver atoms at low pH because ascorbic acid is a weak reducing agent. Later Liu and Guyot-Sionnest described how Ag^+ can be reduced to Ag^0 in the form of monolayers at the gold nanorod surface at a potential lower than its standard reduction potential, known as underpotential deposition (UPD).¹⁹ They proposed that the deposition of silver on the sides of the nanorods is faster than the ends due to the lower reduction potential, inhibiting the nanorod growth on the sides and leading to preferential growth at the ends. Consequently, increasing Ag^+ results in more catalyzed growth and increases the aspect ratio of the nanorods. The reverse effect of Ag^+ at higher concentration (above 35 μL in **Figure 3.4**) is possibly due to the interaction between silver and the bromide ion of CTAB.^{13,30} Small peaks visible at around 600 nm may correspond to cube-like impurities.²³

The concentration of gold nanorod solution can be estimated from the Beer-Lambert law (3.2.2), the extinction coefficient of nanorods, and using the following equation linearly fitted to experimental data³¹

$$\epsilon \times 10^9 = 0.0123 * \lambda_{\text{max}} - 5.0192, \quad (3.3)$$

where ϵ is the extinction coefficient in $\text{M}^{-1}\text{cm}^{-1}$ and λ_{max} is the plasmon peak maximum (LSPR maximum) in nm. The LSPR maximum near 1060 nm was estimated as $20 \times 10^9 \text{ M}^{-1}\text{cm}^{-1}$ from preliminary ICP-AES results and TEM images done by the Murphy group at UIUC. The equation (3.3) may not directly apply to LSPR of gold nanorods above 850 nm, however, the concentration of as-synthesized CTAB-GNR was roughly estimated as 0.2 - 0.3 nM.

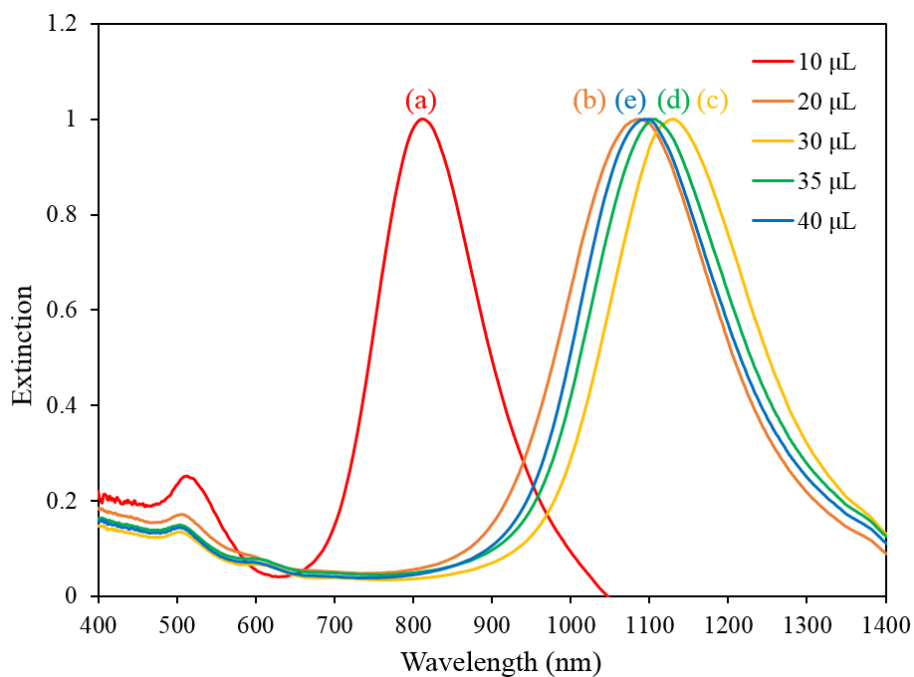
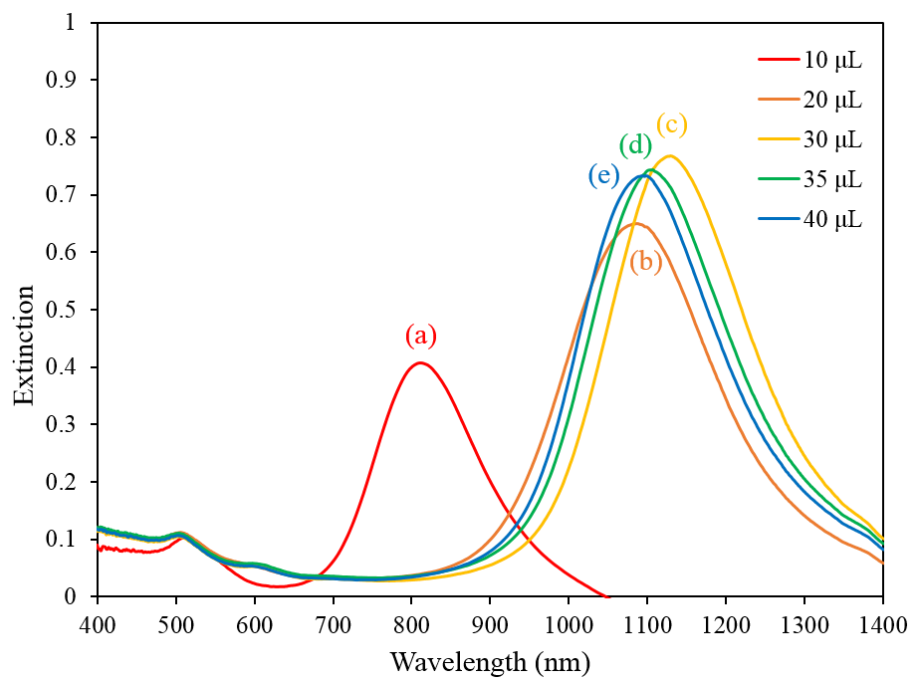


Figure 3.4 Extinction spectra of hydroquinone reduced gold nanorods with various silver amounts: (a) 10, (b) 20, (c) 30, (d) 35, (e) 40 μL . The top figure shows as-synthesized spectra and the bottom figure shows normalized spectra.

3.4 Functionalized Gold Nanorod Synthesis

The gold nanorods were functionalized with the NLO-active polymer, PCBS, and the polycation PAH via the layer-by-layer method. The procedure was modified from the layer-by-layer deposition by Schneider and Decher who described how to consecutively coat concentrated colloidal gold with PAH and PSS up to 20 layers.³²

The as-synthesized gold nanorods are noncovalently coated with CTAB, a cationic surfactant with a long tail comprising 16 carbon atoms as shown in Figure 3.3d. that forms bilayers.³³ For several reasons it is necessary to modify the surface of nanorods. Although this bilayer prevents nanorods from aggregating by steric and charge repulsion, having CTAB is not ideal for further NLO or biological applications. Also, CTAB is physisorbed on gold surfaces and is in equilibrium with excess CTAB in the solution, and thus decreasing CTAB concentration in the solution will lead to aggregation of nanorods. This excess CTAB limits the biological applications of nanorods because free CTAB is highly cytotoxic.³⁴ Lastly, the thick CTAB bilayer (3.4 nm)³⁵ can inhibit enhancement of the SHG signal because the maximum SHG intensity from silver nanoparticles reaches a plateau after 3 bilayers of ISAM film as mentioned in **Section 3.1**.

For this study poly(allylamine hydrochloride)-dithiocarbamate (PAH-DTC) was used to replace CTAB via dialysis and PAH and PCBS were chosen to functionalize the nanorods. The number of bilayers of PAH and PCBS was chosen to be three for the same reason as mentioned above. The functionalized gold nanorods were characterized by optical spectrum measurement and zeta potential measurement to confirm successful coating of each polymer layer.

3.4.1 PAH-DTC Preparation

PAH-DTC is a dithiocarbamate-anchored PAH which is formed by transforming 10 % of the primary amine groups in PAH into DTC groups by condensation with carbon disulfide.³⁶ DTC can bind to gold with much greater binding energy than thiol groups. By converting 10 % of the amine groups in a PAH chain into DTC, PAH-DTC can be robustly attached to a gold surface.

Since PAH is a weak polyelectrolyte, its net charge varies for different pH values of the solution. At pH 8.8, the pK_a value of PAH, half of the amine groups on PAH are uncharged. This

allows deprotonated amine groups to react with carbon disulfide (CS_2), producing dithiocarbamate (DTC) moieties across the polymer chain.³⁷ When functionalized onto gold nanoparticles, the thickness of the layer is only 1.5 - 2 nm.³⁶ The standard procedure of PAH-DTC preparation follows as below.

- i. Prepare 100 mM PAH and raise its pH to 8.8 by adding NaOH.
- ii. Transfer 1 - 4 mL of 100 mM PAH at pH 8.8 into a 4 mL vial (capped with a resealable septum and including a tiny magnetic stir bar) and de-gas with argon for 5 - 10 minutes.
- iii. Prepare 1 M CS_2 in ethanol and inject one-tenth equivalent 1 M CS_2 (10 - 40 μL).
- iv. Quickly combine the mixture with a vortex mixer for 30 seconds and incubate for 4 hours on a magnetic stirrer before use.

Characterization can be done via UV-Vis spectroscopy to confirm successful preparation. **Figure 3.5** shows the absorption spectrum of 1 mM PAH-DTC after 4 hours measured by a miniature fiber optic spectrometer (Ocean Optics, HR2000) using a deuterium lamp. It shows the two characteristic peaks at 254 and 286 nm which confirms successful formation of PAH-DTC. It is best to use freshly made PAH-DTC, however, it is stable for several days when sealed and protected from air.

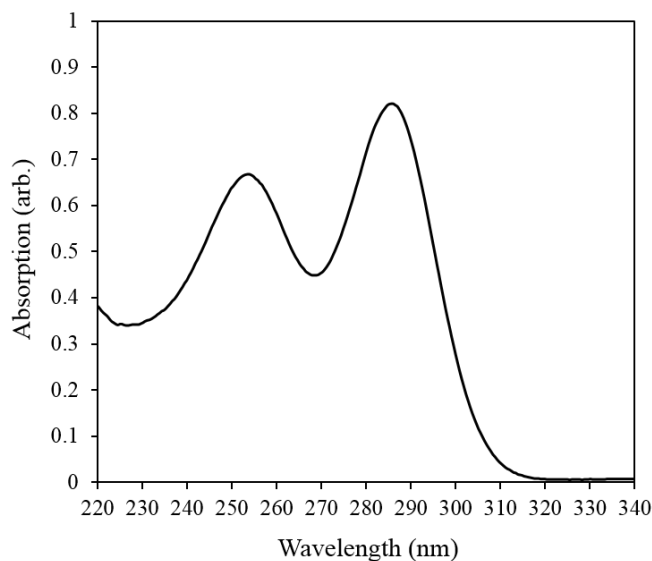


Figure 3.5 Absorption spectrum of 1 mM PAH-DTC. The two peaks at 254 and 286 nm are characteristic of DTC formation.

3.4.2 CTAB Replacement with PAH-DTC via Dialysis

In order to replace a CTAB surfactant bilayer on the nanorods with a thin tightly bound positively-charged polymer layer of PAH-DTC, the CTAB-coated gold nanorod (CTAB-GNR) solution was dialyzed against DI water (buffer) whose volume was 100 times greater than that of the sample. Dialysis is a common practice in biochemistry for separating molecules in solution by differential diffusion across a semipermeable membrane (dialysis tubing). Since the molecular weight of CTAB is 364.45 g/mol and the molecular weight of PAH is around 15000 g/mol, the molecular weight cut off (MWCO) was chosen to be 2000 Da (1 Da = 1 g/mol) and the dialysis membrane (Spectra/Por 6) was purchased from Spectrum Labs. When CTAB-GNR solution is placed in a dialysis tubing, the CTAB molecules diffuse into the buffer (water) until they reach equilibrium, while PAH remains in the dialysis tubing.

Before attempting to replace CTAB with PAH-DTC, the dialysis process of CTAB-GNR was monitored and their extinction spectrum was measured at various times. For this dialysis study, short GNRs (LSPR around 780 nm) were used because the LSPR of the long GNRs are over 1000 nm and thus they are not in the wavelength range of the UV-Vis spectrometer (Ocean Optics HR 2000). As the CTAB molecules diffuse into the buffer over time, the nanorods start to flocculate. The decrease in nanorod concentration is shown in **Figure 3.6** (top) where each extinction spectrum was obtained from 1mL of CTAB-GNR in suspension at various times during dialysis. The strength of the plasmon extinction peak can be used as a measure of the number of nanorods remaining in suspension. It is clearly shown that without PAH-DTC the number of nanorods decreases as dialysis progresses. The time evolution of the extinction spectrum integration is plotted in **Figure 3.6** (bottom). After 15 minutes of dialysis the nanorod concentration is reduced to 78 % and it continued to reduce to 27 % of its initial value after 2 hours of dialysis. This confirms that the CTAB molecules can be removed from CTAB via dialysis, however, it is important to functionalize the nanorod surface with PAH-DTC to prevent flocculation.

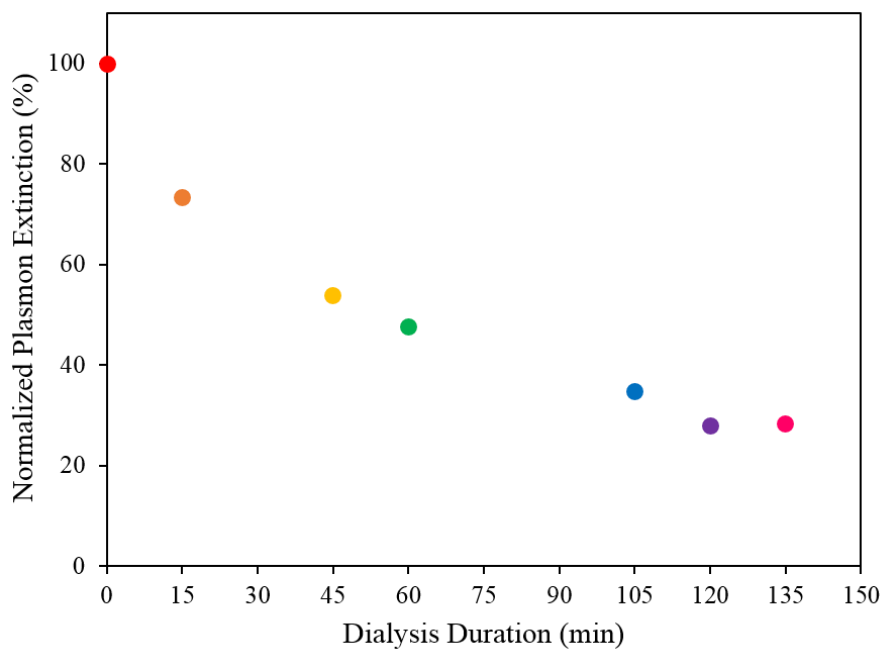
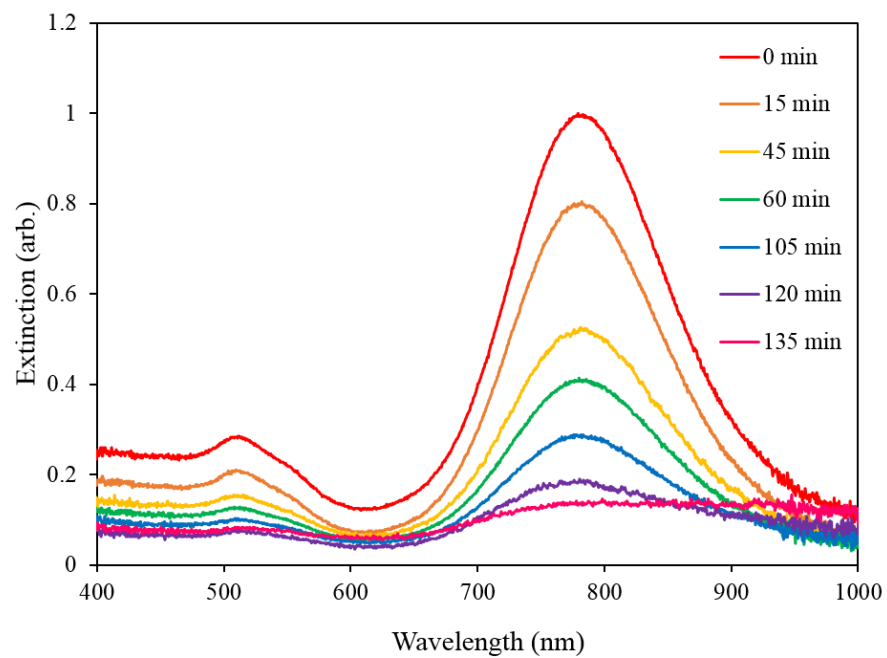


Figure 3.6 Extinction spectra of gold nanorod solution prior to and during dialysis (top). Normalized plasmon extinction of various dialysis times (bottom).

The effectiveness of the PAH-DTC functionalization was verified by periodically measuring the extinction spectrum of the nanorod suspension after PAH-DTC was added to the solution. Dialysis was stopped just before the nanorods aggregate irreversibly when the CTAB layers begin to dissolve, and then the nanorods were exposed to PAH-DTC. The experiment proceeded as follows. First, 2 mL of CTAB-GNR was centrifuged at 4500 rcf for 10 minutes and 95 % of the supernatant was replaced with DI water. Additional centrifugation was done at 2500 rcf for 10 minutes to remove as much excess CTAB as possible. Then, the nanorod solution was transferred to a dialysis tubing and dialyzed for 20 minutes which is when about 70 % of the original plasmon peak remains. Finally, the nanorod solution was stirred into a small beaker containing 400 μ L of the 100 mM PAH-DTC.

The absorptivity was measured via UV-Vis spectrometer before dialysis, after dialysis for 20 minutes, and after 3, 6, and 30 hours of stirring in PAH-DTC as shown in **Figure 3.7** (top). A small red-shift of the LSPRs is attributed to the change of refractive index at the nanorod ends (hotspots) because of a PAH-DTC layer bound to the gold surface. The bottom graph of **Figure 3.7** shows that the plasmon peak remains at 80 % of the original strength up to 30 hour of dialysis, and thus we can conclude that the PAH-DTC is successfully coated on the gold nanorods. Some of the reduction observed in the extinction spectra may be due to osmosis of water into the dialysis bag or due to some flocculation of nanorods.

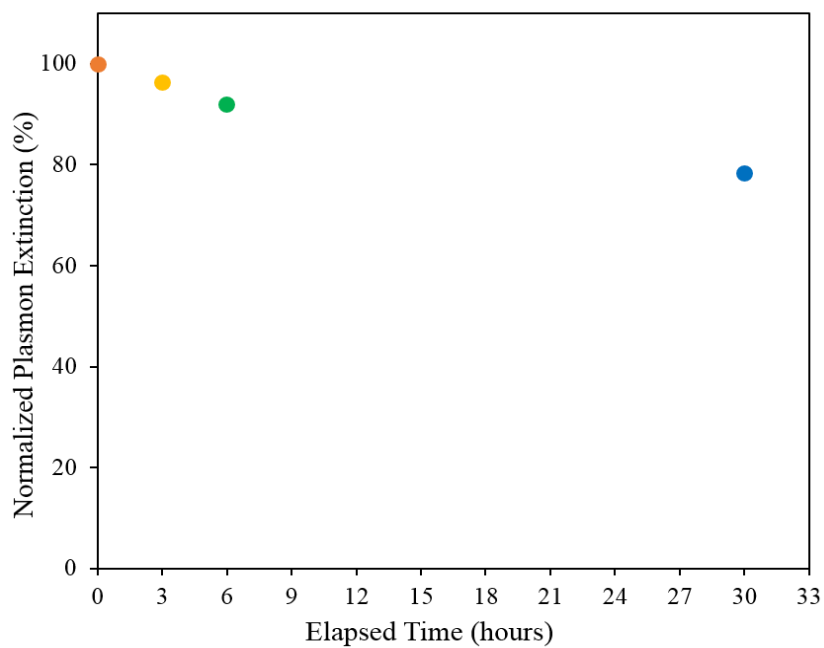
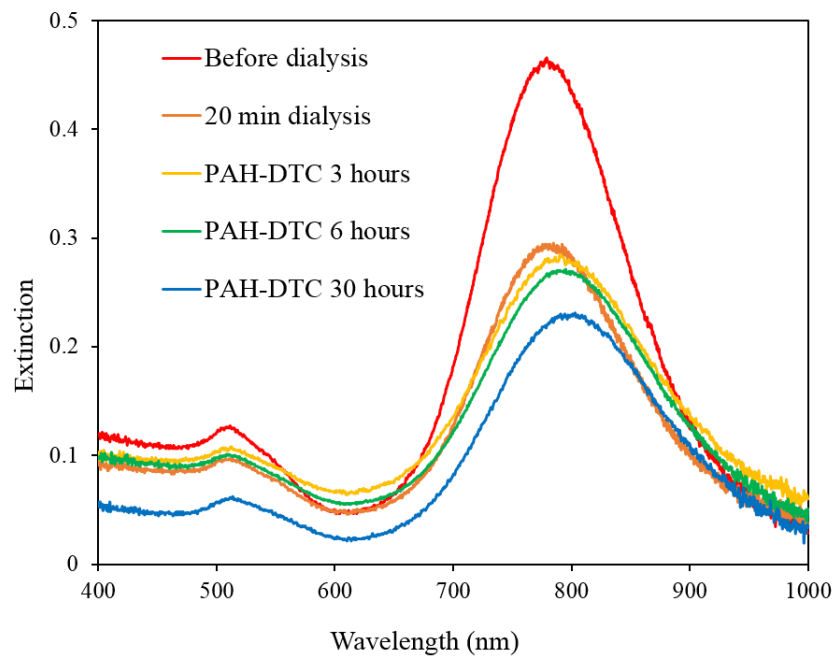


Figure 3.7 Extinction spectra of gold nanorod solution measured before dialysis, 20 minutes after dialysis, and after stirring in PAH-DTC for 3, 6, and 30 hours. (top) Time evolution of the normalized plasmon extinction of gold nanorod suspension after dialysis (orange dot) and after stirring in PAH-DTC. (bottom)

The long gold nanorods with a longitudinal surface plasmon resonance peak near 1080 nm were received from the Murphy group at the University of Illinois, Urbana Champaign, and the extinction spectrum is shown in **Figure 3.8**. The concentration of the nanorod suspension was estimated to be 201 nM from the absorbance of the UV-Vis spectrum measurement. The inset of **Figure 3.8** shows an FESEM (Field-Emission Scanning Electron Microscopy, LEO (Zeiss) 1550) image of PAH-DTC coated gold nanorods deposited on a 3 bilayer PAH/PCBS ISAM film. The dimensions of the nanorod are roughly 108×30 nm.

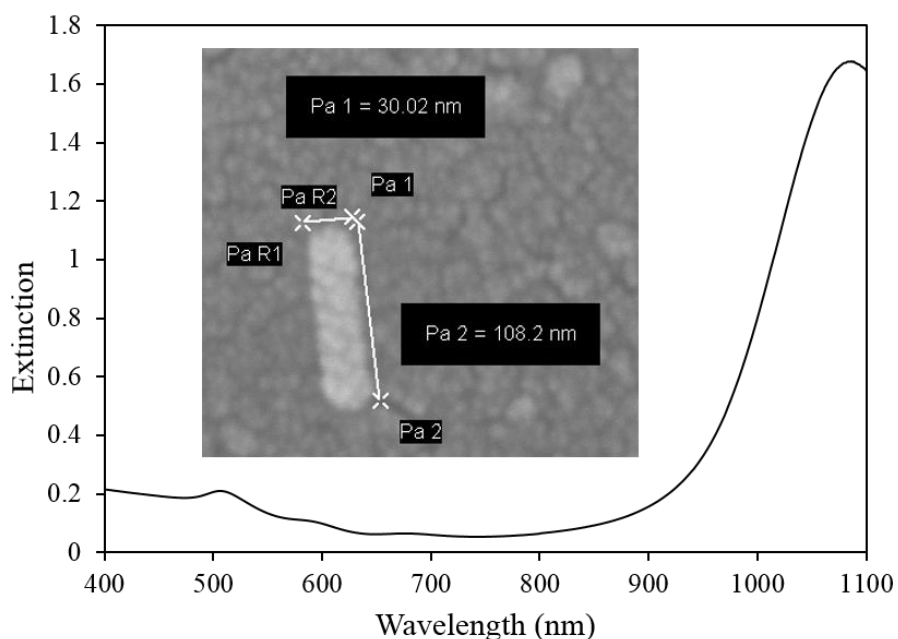


Figure 3.8 Extinction spectrum of CTAB-coated long gold nanorod measured by a UV-Vis spectrometer. The longitudinal resonance peak is around 1080 nm. The inset is an FESEM image of PAH-DTC coated GNR deposited on 3 bilayer PAH/PCBS ISAM film. (The nanorod solution and its spectrum data was provided by the Murphy group at the University of Illinois at Urbana Champaign.)

The long nanorods were diluted 50 times and dialyzed to remove excess CTAB and the absorptivity was measured to observe the nanorod suspension concentration during dialysis. Due to the upper wavelength limit of the UV-Vis spectrometer (Perkin-Elmer Lambda 25), the spectra

was measured up to 1100 nm. As can be seen from the extinction spectra in **Figure 3.9**, the long nanorods started to aggregate rapidly which led to the loss of suspended particles. This can be due to lower initial CTAB concentration in the suspension compared to that of short nanorods in **Figure 3.6**. Therefore, it was determined that PAH-DTC should be added to the nanorod suspension immediately at the start of the dialysis.

As with the shorter nanorods, 200 μL of the 100 mM PAH-DTC solution was added to 1 mL of 50 times diluted gold nanorods. However, the nanorods were found to be stuck to the wall of the centrifuge tube and could not be redispersed with ultrasonication. This could be due to incomplete wrapping of some polymer chains, leaving dangling polymer chains that cause irreversible bridging flocculation of PAH-DTC in the nanorod suspension. In order to prevent bridging flocculation, it is necessary to determine an optimum PAH-DTC concentration for the long nanorods.

The long nanorod solution was supplied at 201 nM concentration, or $2.01 \times 10^{-4} \text{ mol/m}^3$ from the Murphy group in UIUC. The gold nanorod concentration is $1.21 \times 10^{20} \text{ m}^{-3}$ as found by multiplying the given concentration with the Avogadro's number. By including the dilution both from the original GNR solution (50X, in this case) and from the addition of PAH polymer (0.2 mL in 1mL GNR solution), the diluted gold nanorod concentration is $2.02 \times 10^{18} \text{ m}^{-3}$. The total surface area of long gold nanorod can be roughly calculated from the SEM image of a nanorod in **Figure 3.8**. Taking the nanorod length to be 108 nm and the diameter 30 nm, the total surface area is $1.3 \times 10^{-14} \text{ m}^2$ (the side of a cylinder and two hemispheres). Then, we can calculate the GNR surface area per unit volume by multiplying the diluted nanorod concentration with the surface area, or $2.03 \times 10^4 \text{ m}^2/\text{m}^3$. Roughly 1 mg/m^2 is required to obtain a monolayer coverage of a polymer.³⁸ The molecular formula weight of PAH ($\text{C}_3\text{H}_7\text{N HCl}$) is 93.6 g/mol, and thus PAH monolayer coverage per mole is $93600 \text{ m}^2/\text{mol}$. By dividing it from the GNR surface area per volume, we can find the concentration for PAH monolayer coverage to be 217 μM . This is the minimum required concentration of PAH-DTC in the given nanorod suspension. Therefore, the excess amount of PAH in PAH-DTC coated GNR solution (16700 μM) is about 77 times the minimum concentration. It was reported that an increase of a non-ionic polymer can cause interparticle bridging and entanglement of the adsorbed polymer chains.³⁹ Since PAH is a weak polyelectrolyte, adding an

excess amount into the nanorod solution can cause bridging flocculation, decreasing the value of the zeta potential of the nanorods.

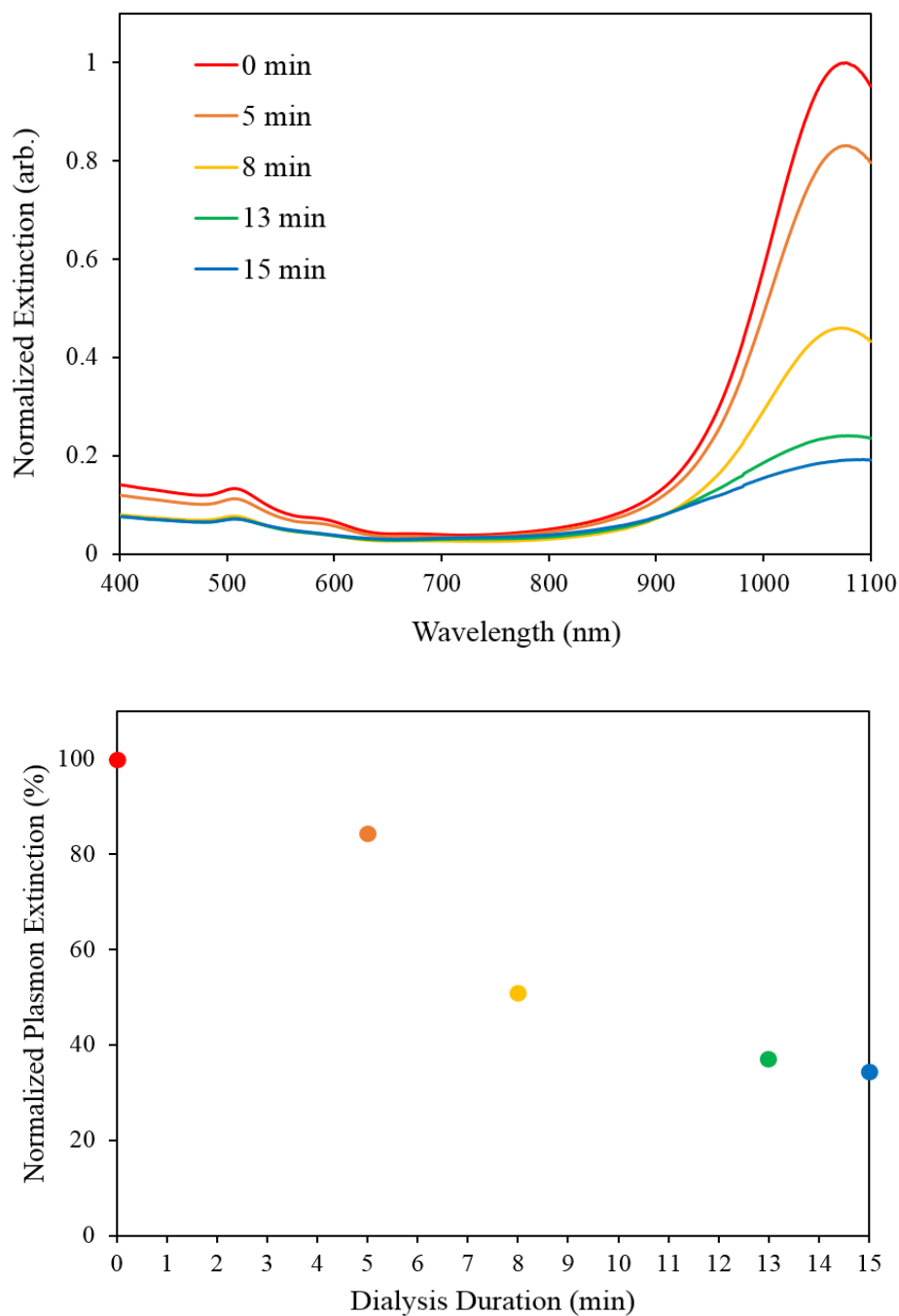


Figure 3.9 Normalized extinction spectra of CTAB-coated long gold nanorods during dialysis (top) and plasmon extinction of various dialysis times (bottom).

Zeta potential is a prime indicator of the stability of colloidal dispersions. **Figure 3.10** is an illustration of liquid layers surrounding a negatively charged gold nanoparticle. There are two identifiable layers in the electric double layer: the Stern layer where the oppositely charged ions are strongly bound and the diffuse layer where they are loosely associated. Within the diffuse layer, there is a boundary called the slipping plane inside which the ions are stable. The slipping plane moves with the particle in suspension and zeta potential is measured on that surface typically in mV.

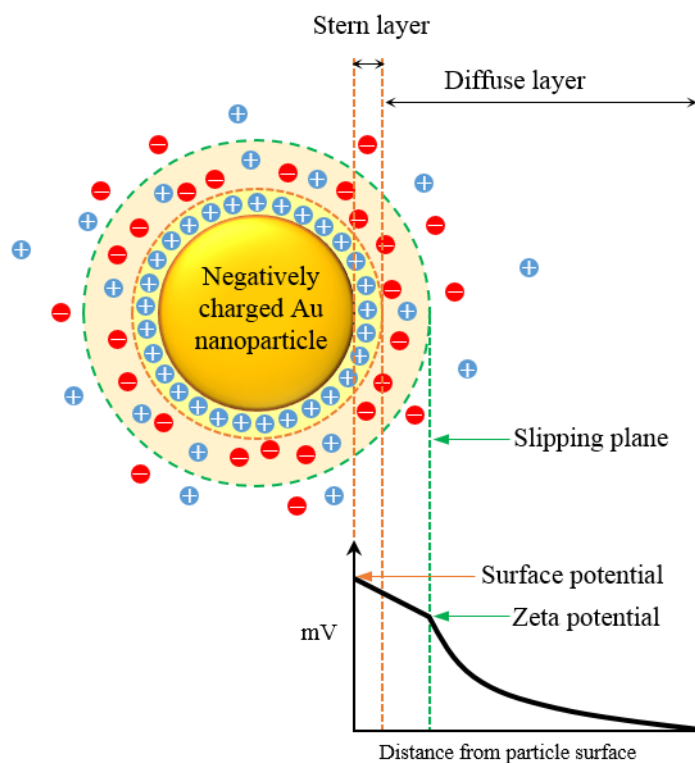


Figure 3.10 Illustration of the liquid layers surrounding a negatively charged gold nanoparticle.

3.4.3 PCBS/PAH Functionalized Gold Nanorods

In this section, the method of functionalizing gold nanorods with PAH and PCBS will be discussed. After the replacement of CTAB with PAH-DTC via dialysis, PCBS and PAH are coated alternately up to 3 bilayers on the nanorod surface.

PAH-DTC concentration test

To study the stability of nanorods in suspension, CTAB-GNRs with various amounts of PAH-DTC were dialyzed for a day and centrifuged to remove excess PAH-DTC. The concentration of GNR solution was estimated to be 0.9 - 1.3 nM. Spectral data of PAH-DTC functionalized nanorods were taken with the Filmetrics as shown in **Figure 3.11**. Each spectrum was normalized to the LSPR of CTAB-GNR. As seen with the short nanorods coated with PAH-DTC (**Figure 3.7**, top), it was also observed that LSPRs of the PAH-DTC coated long GNRs were red-shifted due to the change of refractive index at the nanorod hotspots where a dense PAH layer was deposited. The nanorods seemed to aggregate for lower PAH-DTC concentrations (2 & 4 mM) because of an insufficient amount of polymer to wrap the particles. Nanorods with higher PAH-DTC concentrations, from 16 to 36 mM, did not appear to aggregate.

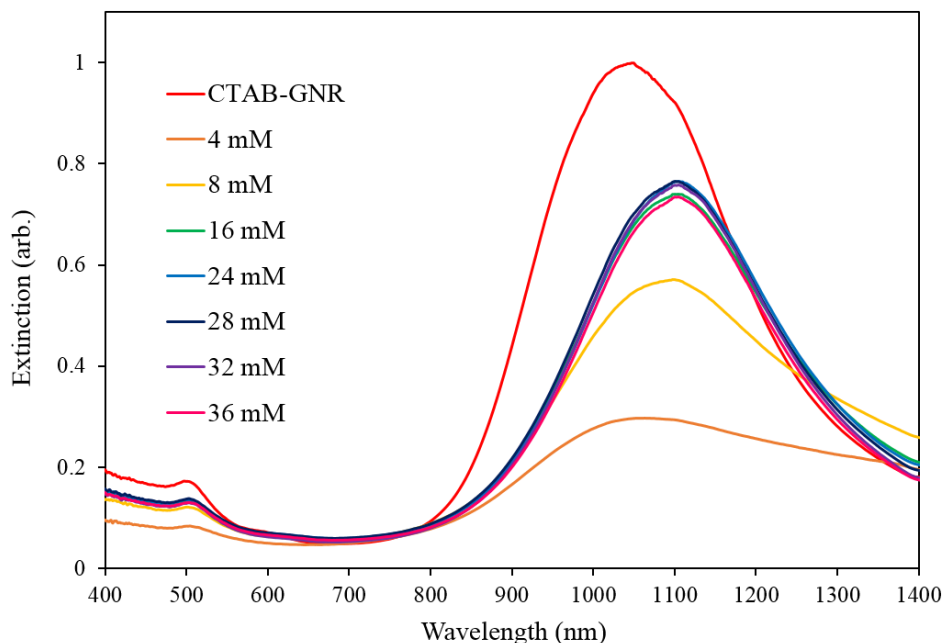


Figure 3.11 Extinction spectra of GNR with various PAH-DTC concentrations. The LSPR red-shifts indicates that PAH-DTC is bound to the gold nanorods.

To observe the stability of the PAH-DTC coated nanorods, we also measured the zeta potential with the Zetasizer Nano ZS (Malvern). It is generally accepted that nanoparticles with zeta potential values greater than +30 mV or less than -30 mV generally have high stability.⁴⁰ The stability of a colloidal suspension is explained by the DLVO theory (Dejarguin, Landau, Verwey, and Overbeek) which describes the balance between the van der Waals attraction and the electrostatic repulsion due to the double layer. A small zeta potential causes particles to eventually flocculate because the repulsive force is insufficient to overcome the van der Waals attraction. As seen in **Figure 3.12**, addition of PAH-DTC increased the zeta potential as a result of PAH-DTC beyond 32 mM adsorption on the particle surface. However, further addition of PAH-DTC decreased the zeta potential, which indicated aggregation of the nanorods. Hence, the optimum concentration of PAH-DTC required to stabilize the nanorods was determined as 28 mM.

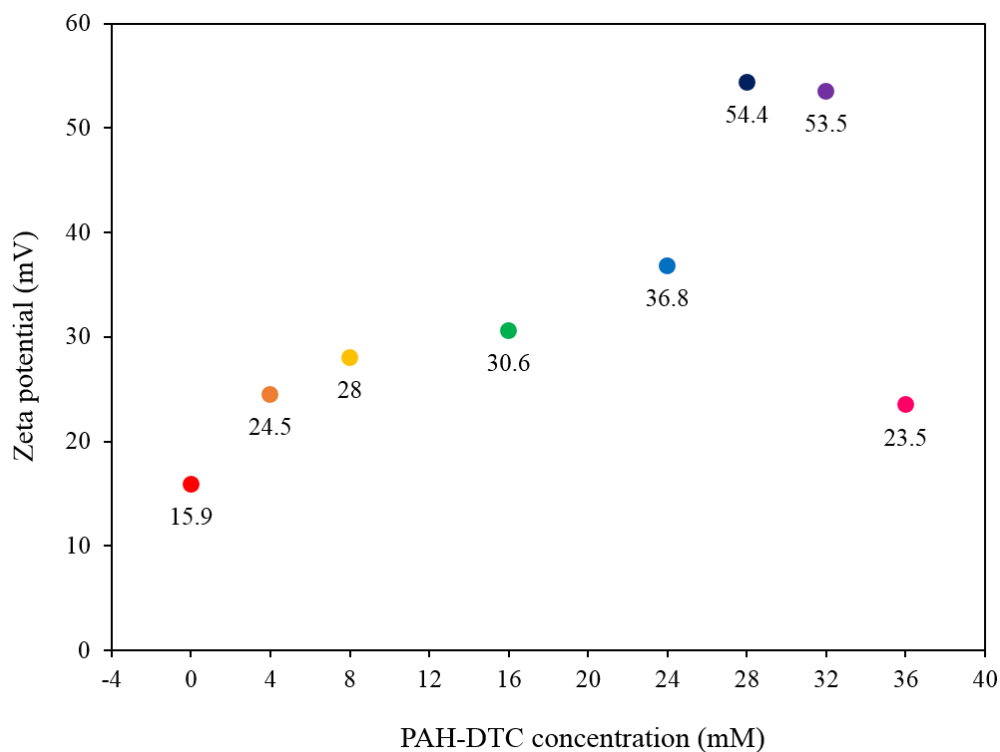


Figure 3.12 Zeta potential of various PAH-DTC concentration for GNR functionalization.

PCBS concentration test

After the CTAB surfactant was replaced with 28 mM PAH-DTC via dialysis, the nanorods were stirred in a solution containing the negatively-charged NLO-active polymer, PCBS, with various concentrations. Each time the nanorods were dialyzed (stirred) in a PAH-DTC (or PCBS) solution, centrifugation was done at 4500 rcf for 20 minutes to remove excess polymer. The extinction spectra of the nanorods with different PCBS concentrations were measured by the Filmetrics as shown in **Figure 3.13**. To compare the concentration of various nanorod solutions with the original CTAB-GNR concentration, all spectra were normalized to the LSPR of CTAB-GNR. The resonance peak of the PAH-DTC coated GNR was red-shifted from that of CTAB-GNR as expected. The PAH-DTC/PCBS coated nanorods aggregated at the low PCBS concentration, 2 mM, due to insufficient amount of PCBS. For the higher PCBS concentrations (45, 50, 55, and 60 mM) the LSPR extinction was comparable to that of PAH-DTC coated nanorods.

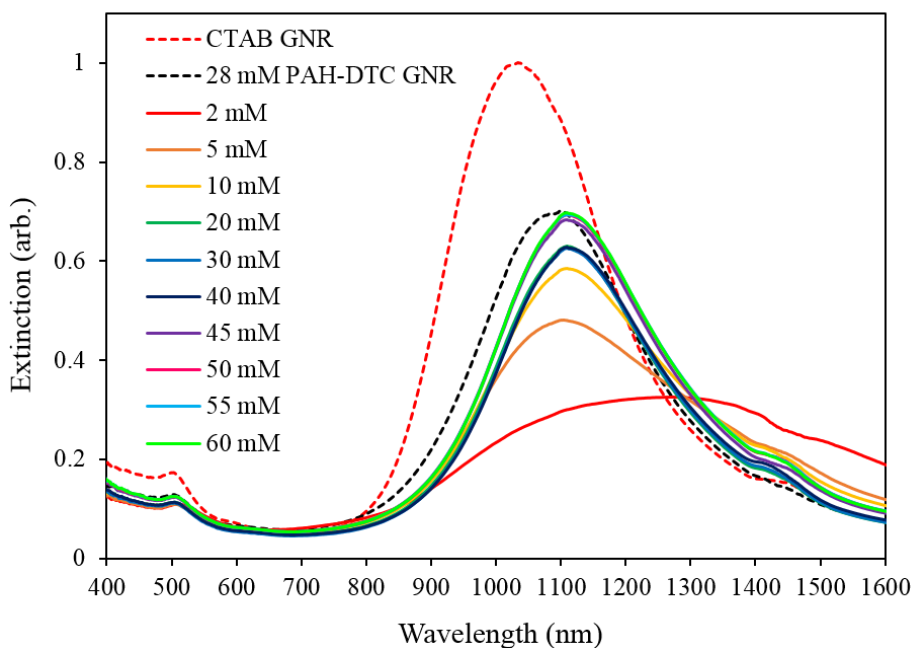


Figure 3.13 Extinction spectra of GNR with various PCBS concentrations. The LSPR red-shifts indicates that PCBS is bound to the PAH-DTC coated GNRs.

Figure 3.14 shows zeta potential of CTAB coated GNR, PAH-DTC coated GNR, and PAH-DTC/PCBS coated GNR made with various PCBS concentrations. It should be noted that the zeta potential measurement took place after the PAH-DTC coated nanorods were stirred in PCBS solutions for a day. Since PAH is a weak polyelectrolyte, PAH-DTC coated nanorods become unstable after a couple of days, which is why its zeta potential was lower than expected (below +30 mV). The negative zeta potential of PAH-DTC/PCBS coated GNRs supported the hypothesis of successful adsorption of PCBS on PAH-DTC. Increased concentration of the PCBS solution increased the value of zeta potential. In consideration of the extinction spectra, zeta potential and centrifugation for excess PCBS removal, the optimum concentration of PCBS solution required to stabilize the nanorods was chosen to be 45 mM.

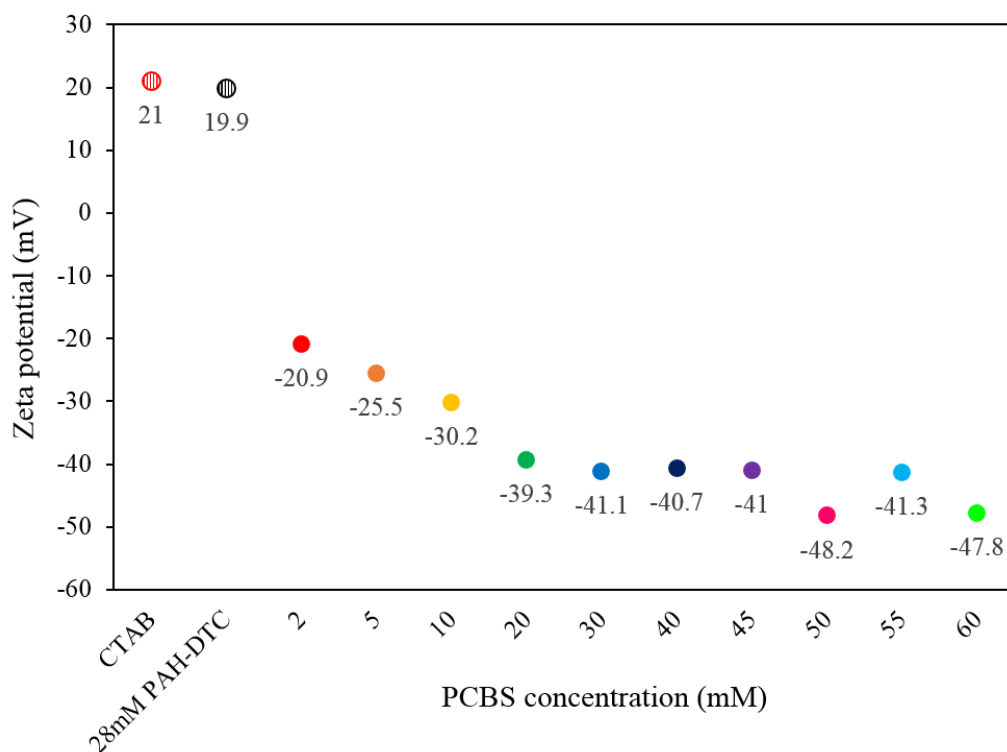


Figure 3.14 Zeta potential of CTAB-GNR, PAH-DTC coated GNR, and PAH-DTC/PCBS coated GNR with various PCBS concentrations.

Figure 3.15 shows typical positive (top) and negative (bottom) zeta potential distribution graphs taken by the Zetasizer (Malvern) of Prof. Davis group at Virginia Tech. The top one shows a positive zeta potential (+54.4 mV) of PAH-DTC coated GNRs for PAH-DTC concentration 28 mM. The bottom one shows a negative zeta potential (-42.2 mV) of PAH-DTC/PCBS coated GNRs for PCBS concentration of 45 mM.

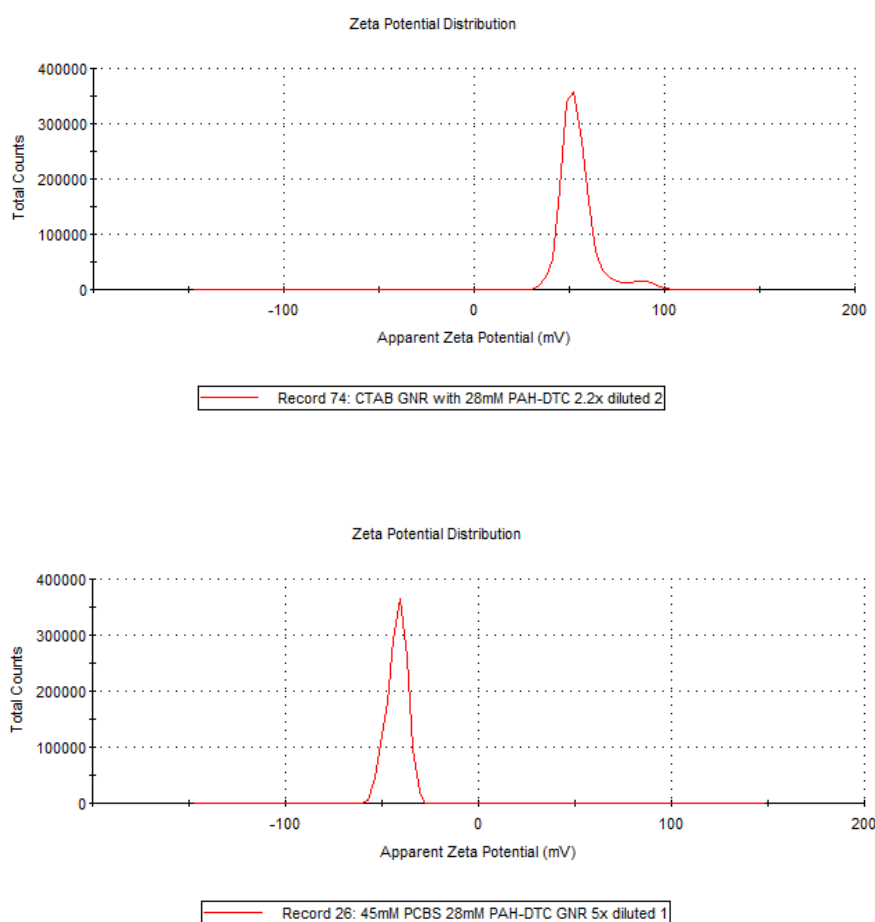


Figure 3.15 Zeta potential graphs taken by Zetasizer (Malvern). 28mM PAH-DTC (top) and 45 mM PCBS (bottom).

Functionalized GNR via Layer-by-Layer

Gold nanorods were coated with PAH and PCBS using Layer-by-Layer (LbL) deposition. The following is modified from the procedure by Schneider and Decher.³² In this procedure, to ensure a constant quantity of gold nanorod colloids, an equal volume of nanorod solution and polymer solution were mixed together and the centrifuged colloidal suspension was redispersed by DI water with half the volume of the mixture. **Figure 3.16** is an illustration of the procedure.

- i. Prepare 100 mM PAH-DTC (**Section 3.4.1**) and confirm its double peaks at 254 & 286 nm.
- ii. To remove excess CTAB in the CTAB-GNR solution, centrifuge the nanorod suspension at 4500 rcf for 20 minutes once and replace the supernatant with DI water to redisperse. To remove as much supernatant as possible, two pipettes with different sizes: about 90% of the supernatant was first removed using a 1000 μ L pipette and the rest was carefully removed using a 200 μ L pipette for fine control.
- iii. Dilute the CTAB-GNR 3X with DI water. (Concentrated 4.3X the as-synthesized GNRs.)
- iv. Prepare for dialysis: Cut a piece of dialysis tubing (Spectra/Por 6) to an appropriate size and soak it in DI water for 15 minutes to remove the preservative. Fill a large beaker with DI water (100 times the CTAB-GNR volume). Put a magnetic stir bar in the large beaker.
- v. Prepare 28 mM PAH-DTC (with a volume equal to that of the nanorod solution) in a beaker by diluting 100 mM PAH-DTC with DI water. Put a small magnetic stir bar in the beaker.
- vi. Add the diluted CTAB-GNR drop-by-drop into the beaker containing 28 mM PAH-DTC solution while stirring vigorously.
- vii. Put the mixture of CTAB-GNR and PAH-DTC into the dialysis bag and carefully close the open ends with clips. Immerse the bag into the large beaker with DI water. Cover it with parafilm and place it on a magnetic stirrer inside an oven (28 - 29 °C) for 24 hours. Change the buffer solution (water) two or three times during dialysis.
- viii. To remove excess PAH-DTC, place the PAH-DTC coated GNR into 1.5 mL microcentrifuge tubes, centrifuge the nanorod suspension at 4500 rcf for 20 minutes, and replace the supernatant with DI water. Repeat centrifugation and redisperse the precipitate with 0.75 mL DI water to preserve the nanorod concentration.
- ix. Prepare 45 mM PCBS (with a volume equal to that of the PAH-DTC coated GNR solution) in a beaker and adjust its pH to 7 by adding 1M HCl.

- x. Add the PAH-DTC coated GNR dropwise into the 45 mM PCBS solution while stirring vigorously. Cover with parafilm and stir for 12 hours.
- xi. To remove excess PCBS, use 1.5 mL microcentrifuge tubes and centrifuge at 4500 rcf for 20 minutes. Remove the supernatant (which has the color of PCBS (brown-orange)) and add DI water to redisperse. Repeat centrifugation and replace the supernatant (pale yellow) with 0.75 mL DI water.
- xii. Prepare 28 mM PAH solution (pH 7) in a beaker.
- xiii. Add the PAH-DTC/PCBS coated GNR in drops into the 28 mM PAH solution while stirring vigorously. Cover with parafilm and stir for 12 hours.
- xiv. To remove excess PAH, follow the same centrifugation procedure as in step viii.
- xv. For further deposition of each polymer layer, repeat steps ix-xi for PCBS, and steps xii-xiv for PAH. In this research 3 bilayers of PAH/PCBS were coated on the nanorods.

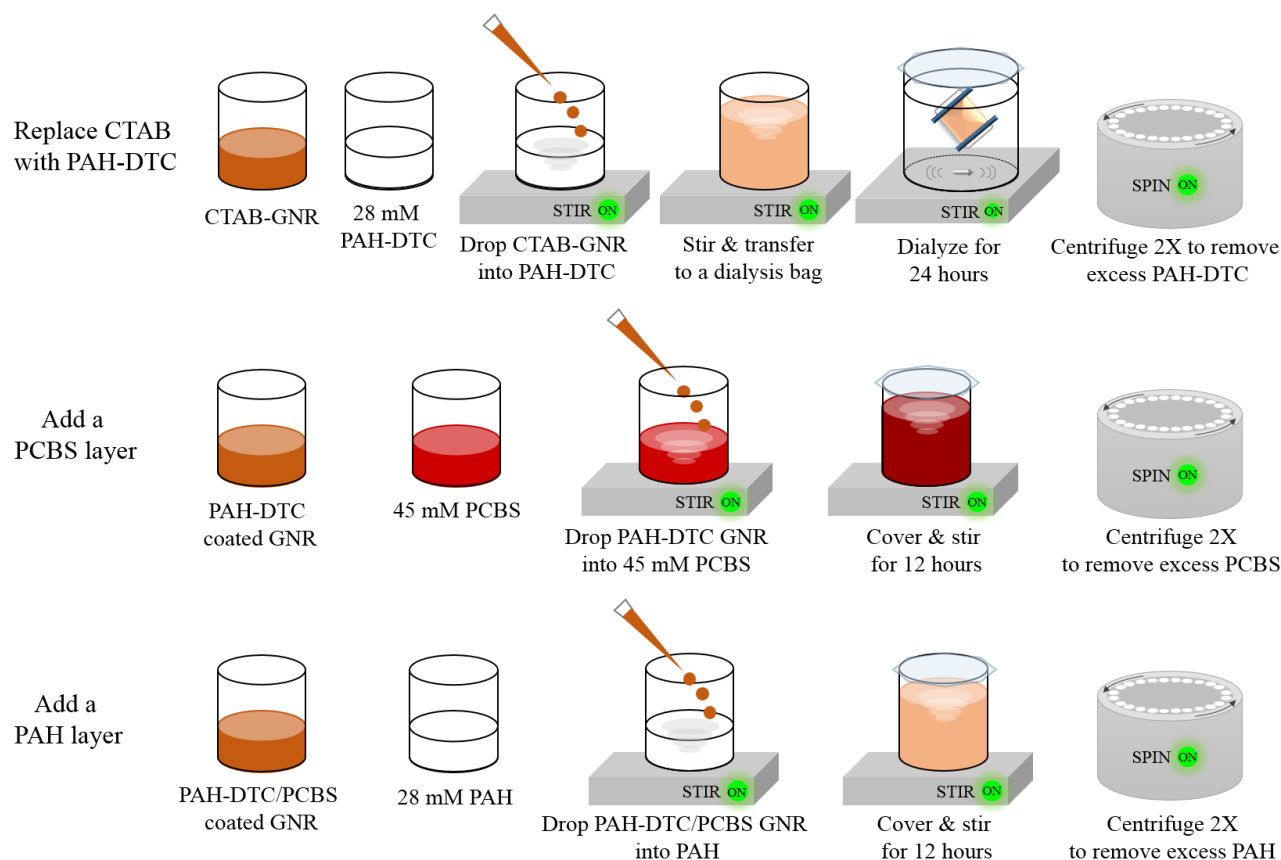


Figure 3.16 Illustration of the PAH/PCBS functionalized GNR procedure.

The PAH/PCBS functionalized GNRs were prepared as described above and characterized by extinction spectral measurement via Filmetrics and zeta potential measurement via Zetasizer. **Figure 3.17** shows normalized spectral data obtained from GNR dispersions coated with an increasing number of polymer layers. The longitudinal plasmon bands are extremely sensitive to the changes in the surrounding dielectric: LSPR peaks generally red-shift with an increasing refractive index of the surrounding environment. Therefore, as seen in **Figure 3.17**, LSPRs of the nanorods red-shifted as more polymer layers were added. The amounts of LSPR red-shift from the CTAB coated GNRs to the one, two, and three bilayers of PAH/PCBS coated GNRs are 50, 82, and 108 nm, respectively.

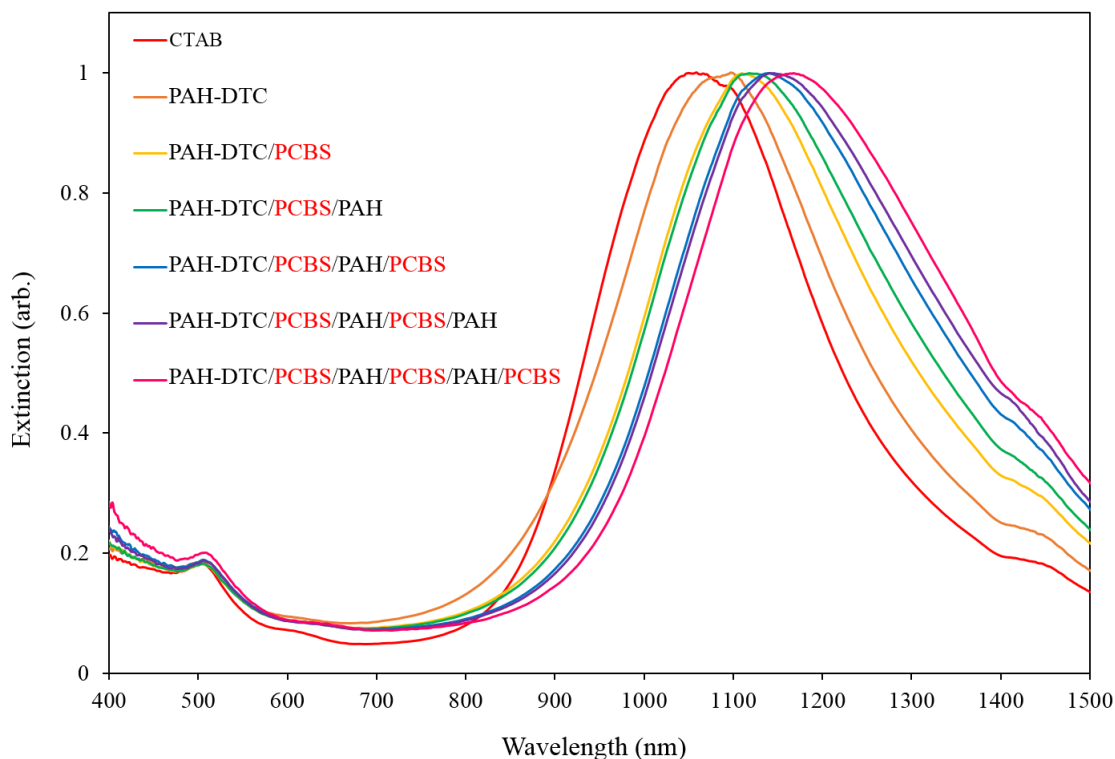


Figure 3.17 Normalized extinction spectra of PAH/PCBS functionalized GNR. The most left spectrum was CTAB coated GNR and the spectrum red shifted as each additional polymer layer was added.

Along with the spectral data, zeta potential is a key indicator to determine successful coating of polymers on gold nanorods. **Figure 3.18** is a zeta potential plot for each functionalized gold nanorod sample. The zeta potentials of CTAB-GNR and PAH-DTC coated GNR were both positive. After PCBS, a negatively-charged NLO-active polymer, was adsorbed onto PAH-DTC, the zeta potential became negative. Therefore, the zeta potential measurement confirmed successful functionalization of the nanorods up to 6 polymer layers.

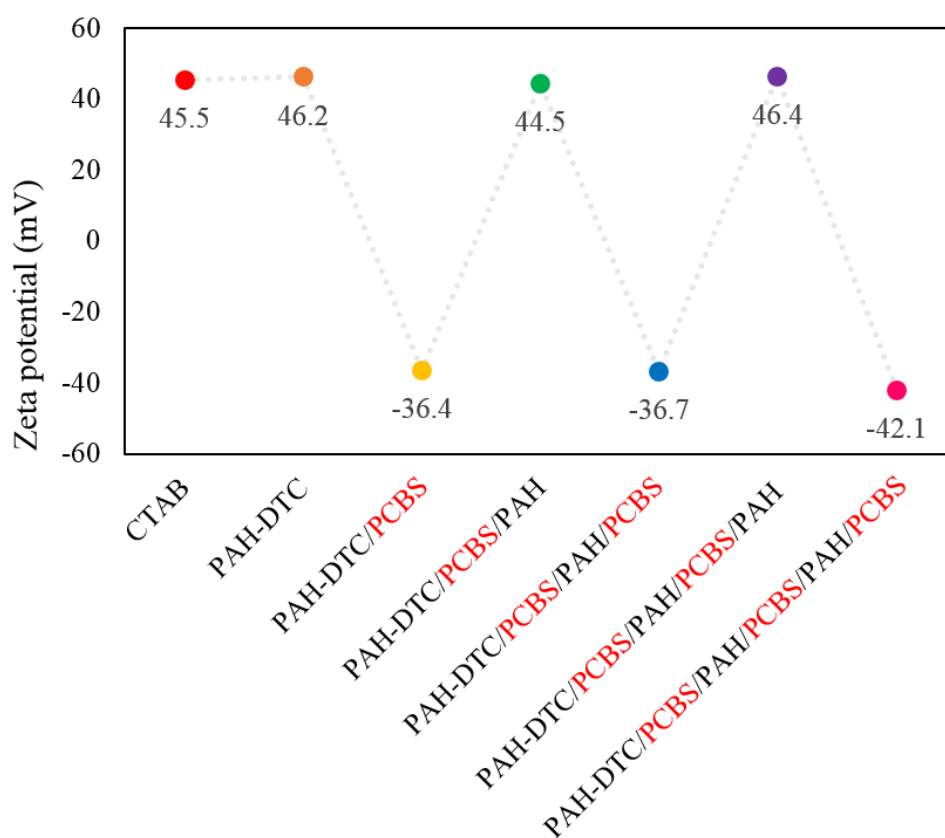


Figure 3.18 Zeta potential of PAH/PCBS functionalized GNR.

3.5 Functionalized Gold Nanorods on ISAM Film

In the beginning of this research, PSS-coated GNRs were prepared and sent from the Murphy group at UIUC and deposited by us onto NLO ISAM films to measure SHG from the ISAM-nanorod samples. To achieve high SHG signal, it is important to have a high density of nanorods on ISAM film. At first approximation, the nanorod deposition density is proportional to the concentration of nanorod solution. Therefore, a high nanorod density should be achieved more quickly with a highly concentrated nanorod solution than a less concentrated solution. However, this is only valid in the low surface density regime because particles slowly saturate the surface during deposition, causing the rod density to asymptotically approach an upper limit. In fact, it was observed that, for a given period of time, a high nanorod density was attained by a diluted nanorod solution rather than by a highly concentrated one. This can probably be attributed to the limit of high deposition density (jamming) where previously deposited particles decrease the probability of subsequent particle deposition due to coulomb repulsion between particles.

In the following subsections, a study of nanorod density in relation to the nanorod concentration is discussed. Based on the study of PAH/PCBS functionalized nanorod density, an appropriate dilution factor was chosen to deposit GNRs onto ISAM films.

3.5.1 Nanorod Density of PSS-coated GNRs on ISAM film

To investigate where the high deposition density limit occurs for the PSS-coated nanorods, nanorods from highly diluted solution were deposited by the “dropcast method.” In the dropcast method, as shown in **Figure 3.19**, a droplet of nanorod solution is dropped onto a horizontally placed substrate. By contrast, in the “immersion method”, as shown in **Figure 3.24**, a substrate is immersed vertically into a large quantity of nanorod suspension. In general, the immersion method is preferable because it yields more uniform deposition and is easy to control without causing “coffee-ring” effects or effects due to evaporation. Therefore, in the later phase of the study, PAH/PCBS functionalized GNRs were deposited onto ISAM film by the immersion method. Moreover, it was necessary to have nanorods on both side of the substrate in order for the SHG minima to reach zero, which is greatly preferred for measurement analysis.

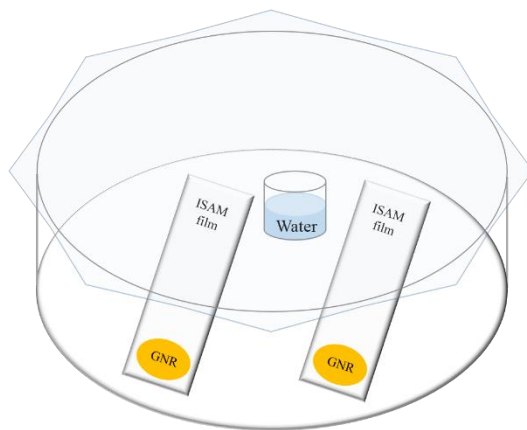


Figure 3.19 GNR deposition by the dropcast method. The incubation dish includes samples laying on the bottom and a beaker of water to raise the humidity and minimize evaporation. It was covered with parafilm to seal.

An Extinction spectrum of PSS-coated GNR suspended in water is shown in **Figure 3.20a** with an inset showing the same data measured by the Murphy group at UIUC. The wavelength detection limit of the spectrometer (Perkin Elmer) we used here was 1100 nm. According to the inset the LSPR was at $\lambda = 1132$ nm. These nanorods were diluted by factors of 30, 40, and 50 from the as-received suspensions whose concentration was given as 2.5 nM. By using the dropcast method, a droplet of each diluted nanorod solution was dropped onto a PAH (pH 7) substrate, placed horizontally at the bottom of the incubation dish. A small beaker of water was placed inside the dish to reduce evaporation of nanorod droplets. After 16 hours, samples were rinsed in DI water and dried with N_2 gas. The extinction spectrum of the nanorods deposited on (PAH/PCBS)₃PAH film was blue-shifted about 120 nm as shown in **Figure 3.20b**. Corresponding FESEM images and nanorod densities are shown in **Figure 3.21** and in **Table 3.3**, respectively. In the table, the product of the dilution and the nanorod density is approximately the same for each dilution. Since the dilution factor is proportional to the inverse of the particle concentration, i.e. $n = n_0/d$, where n_0 is the concentration of the nanorod solution, this trend is expected in the linear deposition regime where jamming is not significant. The FESEM images also confirmed that nanorod density increased as the dilution factor decreased (more concentrated).

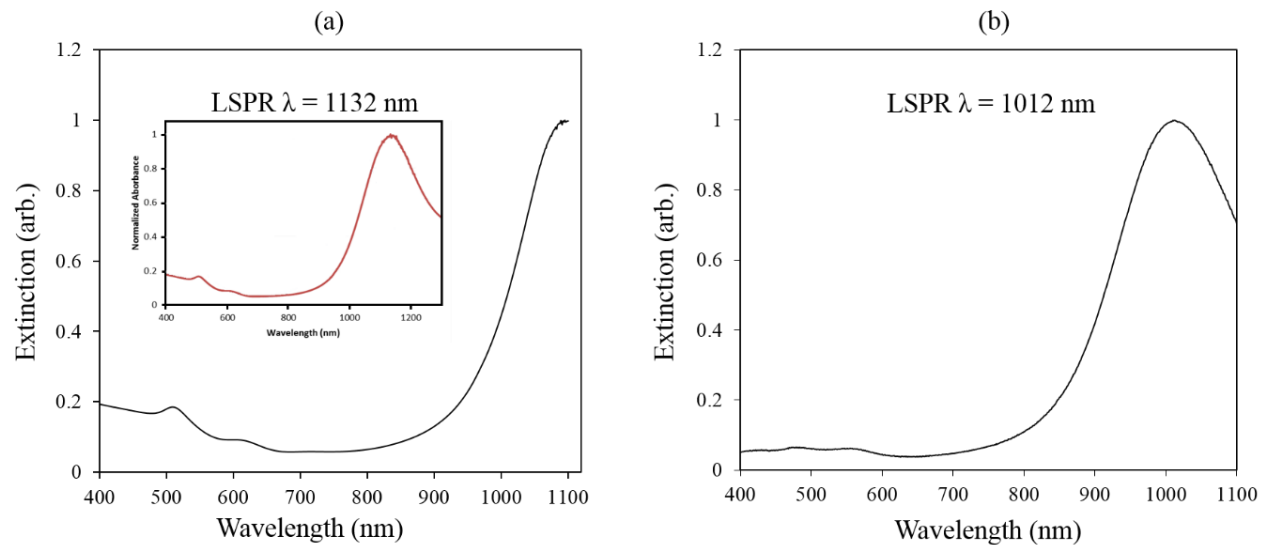


Figure 3.20 Extinction spectra of PSS-coated nanorods: (a) in suspension and (b) on (PAH/PCBS)₃PAH film. The inset of (a) is provided by the Murphy group at UIUC.

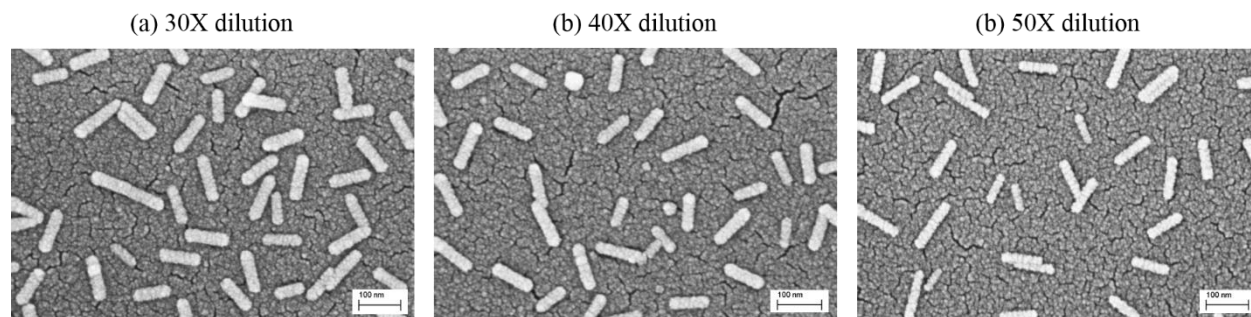


Figure 3.21 FESEM images of PSS-coated GNRs deposited on a PAH film by dropcasting. Nanorods were diluted by 30, 40, and 50 times from the as-received suspensions and deposited for 16 hours.

Table 3.3 PSS-coated GNR density on PAH film.

Dilution (d) [times]	Nanorod density (ρ) [# of GNRs / μm^2]	$d \cdot \rho$
30	73	2220
40	52	2080
50	43	2150

As will be discussed in **Chapter 4**, PSS-coated GNRs deposited on PAH/PCBS film did not demonstrated any enhancement in the SHG signal even when the density of nanorods were high. This may be attributed to the thick layer of PSS polymer and CTAB bilayer surrounding each nanorod, making it difficult for the LSPR mode of nanorod to interact with the PCBS film.

3.5.2 Nanorod Density of PAH/PCBS Functionalized GNRs on ISAM Film

To investigate the relationship between nanorod densities and nanorod solution concentration for PAH/PCBS functionalized GNRs, PAH-DTC/PCBS GNR solution was diluted by factors of 1, 1.5, 3, 4, and 5 and deposited on ISAM films by the immersion method. ISAM films were prepared on glass slides with PAH and PCBS and they were immersed into a beaker containing PAH-DTC/PCBS solutions of various concentrations for two days.

The extinction spectra of nanorods deposited on PAH/PCBS ISAM film is shown in **Figure 3.22** and corresponding FESEM images are shown in **Figure 3.23**. The extinction of nanorods on the ISAM film increased as the GNR solution was more diluted. Beyond 3X dilution (i.e., 4X and 5X dilution), the rods seemed to stack or aggregate as suggested by of the resonance peak broadening in their extinction spectra. This was also confirmed in **Figure 3.23d-e** which clearly showed stacking of nanorods.

From **Figure 3.23a-c**, we can assume that the nanorod density increases as the absorbance of nanorods on the film increases. The density of nanorods is greater when the ISAM film was immersed in a more diluted solution. This is most likely due to high deposition density jamming. An alternative explanation is that this can also be due to excess PCBS polymer in the functionalized nanorod solution which can be quickly adsorbed to the PAH layer of ISAM film, limiting the binding of nanorods to the PAH layer of ISAM film. Although centrifugation was performed twice to replace excess PCBS with DI water as discussed in **Figure 3.16**, small amount of PCBS might still remain. This was unavoidable because the nanorods started to aggregate after the third centrifugation. However, when the functionalized nanorod solutions were diluted, the hindrance of nanorod deposition due to excess PCBS in the nanorod solution was less, which could result in a higher nanorod density on the ISAM film.

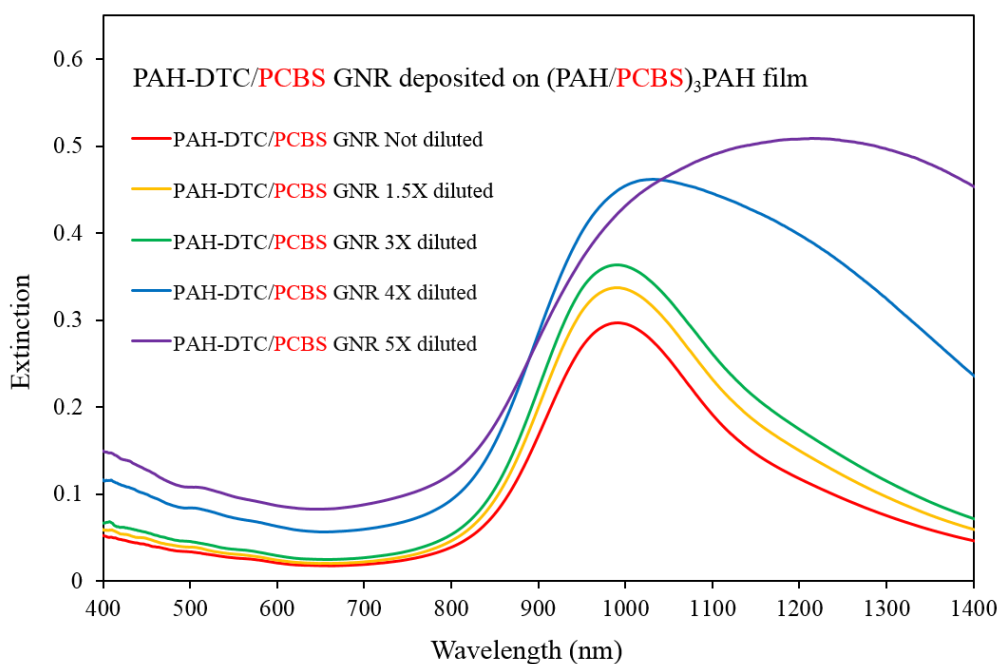


Figure 3.22 Extinction spectra of PAH-DTC/PCBS GNR of varying concentration deposited on $(\text{PAH}/\text{PCBS})_3\text{PAH}$ films. The ISAM films were immersed into various concentrations of nanorod solutions.

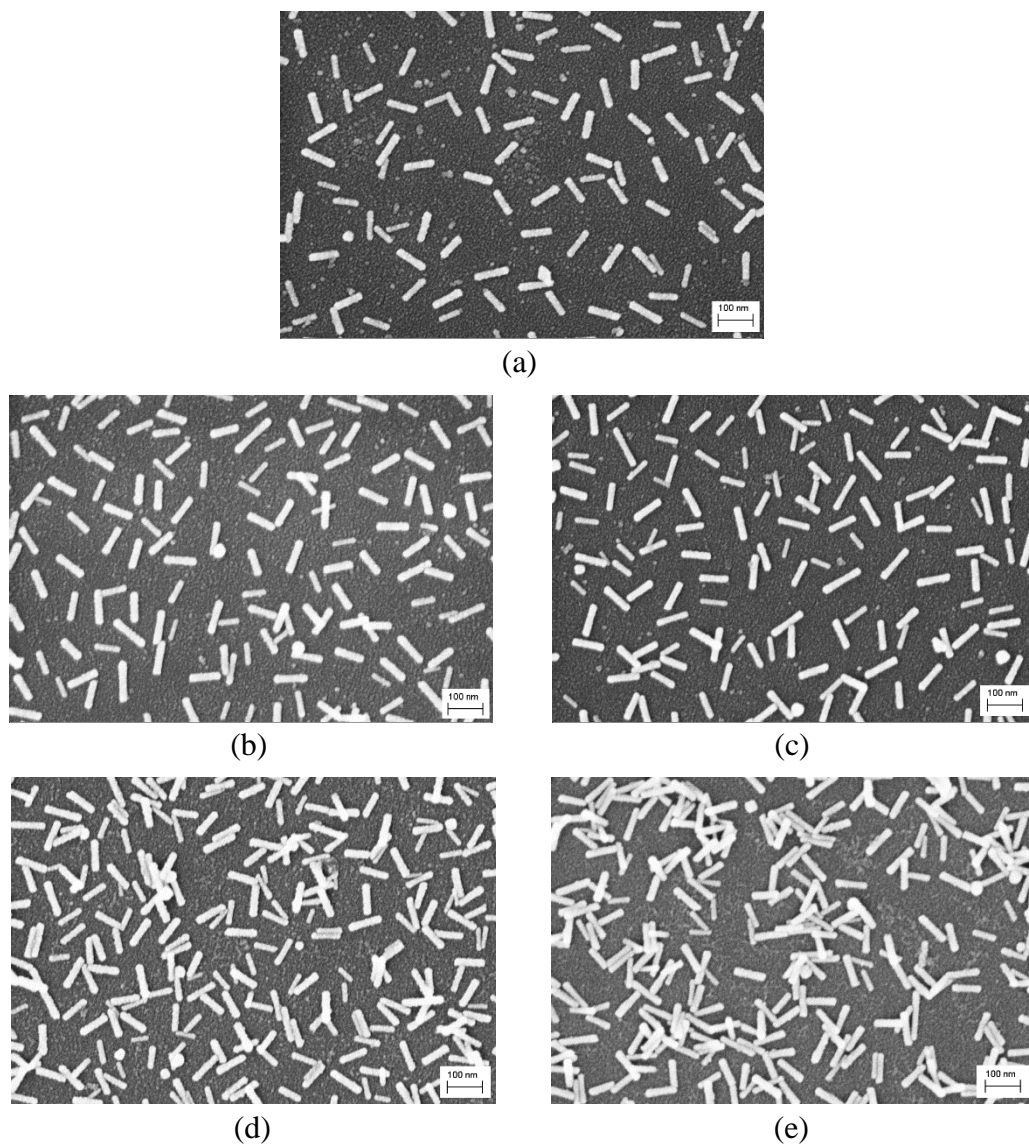


Figure 3.23 FESEM images of (PAH-DTC/PCBS) functionalized gold nanorods deposited on (PAH/PCBS)₃PAH ISAM films. The nanorod solutions were diluted and an ISAM film was immersed vertically into a beaker containing diluted nanorod solutions for 2 days: (a) not diluted, (b) 1.5X, (c) 3X, (d) 4X, and (e) 5X diluted.

3.5.3 PAH/PCBS Functionalized Gold Nanorods on ISAM Film

PAH/PCBS functionalized gold nanorods were deposited on ISAM films. There were two types of ISAM films: 3 bilayers of PAH/PSS film and 3 bilayers of PAH/PCBS film. The uppermost polymer layer was chosen so that its charge was opposite to the charge of the nanorods. Since there were four different functionalized GNR solutions and two different types of ISAM film, there were 8 samples total as listed in **Table 3.4**.

Table 3.4 Functionalized GNR on ISAM films.

Functionalized gold nanorods		ISAM film
PAH-DTC GNRs	deposited on	(PAH/PCBS) ₃
		(PAH/PSS) ₃
PAH-DTC/PCBS GNRs		(PAH/PCBS) ₃ PAH
		(PAH/PSS) ₃ PAH
PAH-DTC/PCBS/PAH/PCBS GNRs		(PAH/PCBS) ₃ PAH
		(PAH/PSS) ₃ PAH
PAH-DTC/PCBS/PAH/PCBS/PAH/PCBS GNRs		(PAH/PCBS) ₃ PAH
		(PAH/PSS) ₃ PAH

First, ISAM films were prepared on glass slides by following the procedure described in **Section 3.1**. The films contained 3 bilayers of PAH and PCBS (or PAH and PSS) for the deposition of PAH-DTC nanorods. For the remaining of nanorod solutions where PCBS was the uppermost layer, a PAH layer was added to provide a properly charged surface to the nanorods. Then, a pair of ISAM films (one containing PCBS and one containing PSS) were vertically immersed into a beaker containing a functionalized GNR solution of certain concentration. This process is illustrated in **Figure 3.24**. To achieve a high nanorod density on the film, the samples were incubated for a couple of days.

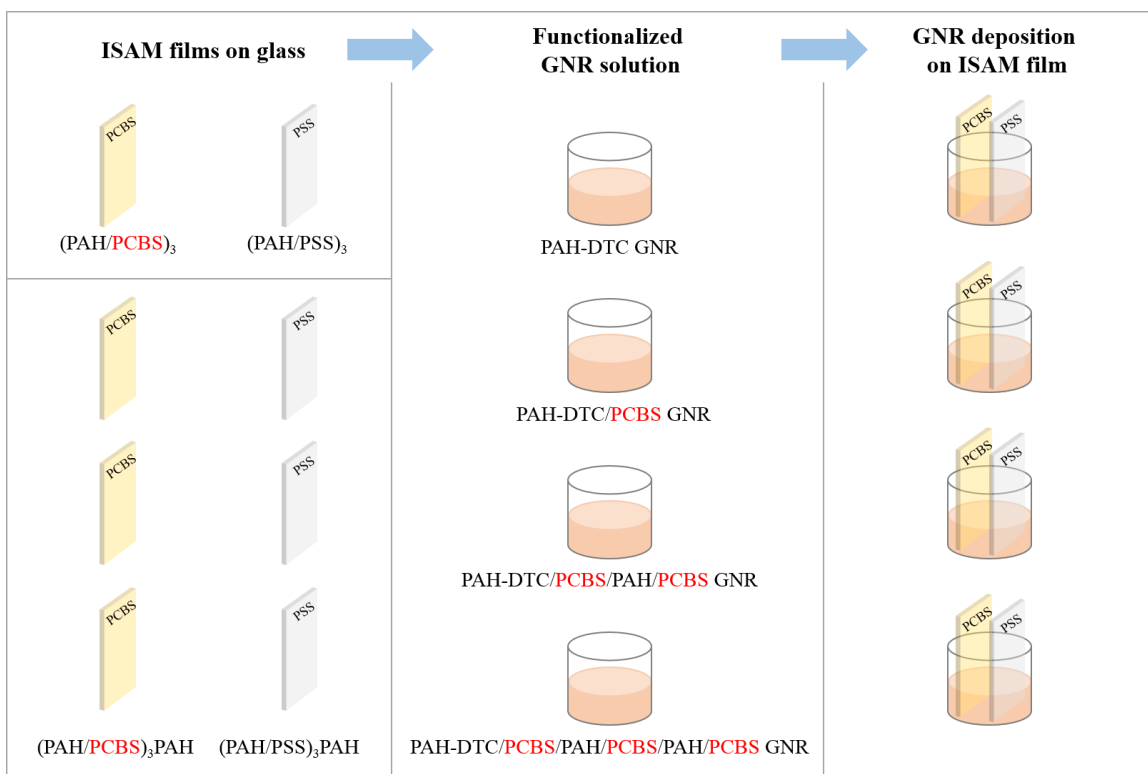


Figure 3.24 ISAM films (3 or 3.5 bilayers of PAH/PCBS or PAH/PSS on glass slides) vertically immersed into the functionalized GNR solutions. Gold nanorods were deposited on both sides of the film with an immersion depth of about 2.5 cm. Each GNR solution was 3.5 times diluted from the original concentration, based on the results of **Section 3.5.2**.

PAH/PCBS Functionalized GNRs deposited on ISAM film

The functionalized gold nanorods were deposited on the NLO-active and NLO-inactive ISAM films following the procedure described in **Figure 3.24**. Based on the results of **Figure 3.22** and **Figure 3.23**, the functionalized nanorod solution was diluted 3.5 times and the films were incubated for 20 to 40 hours to ensure good nanorod coverage.

The normalized extinction spectra of the functionalized gold nanorods are shown in **Figure 3.25**. As expected, the resonance peaks of each nanorod solution showed a red-shift with an additional adsorbed polymer layer. The longitudinal resonance peak started from 1075 nm for CTAB-coated nanorods and then an additional PAH-DTC layer resulted in a 34 nm red-shift while an additional PCBS layer caused a red-shift of 10 nm from PAH-DTC coated nanorods. Adding subsequent bilayers of PAH/PCBS to the PAH-DTC functionalized nanorods resulted in red-shifts of 25 nm and 9 nm from PAH-DTC/PCBS nanorods and PAH-DTC/PCBS/PAH/PCBS nanorods, respectively.

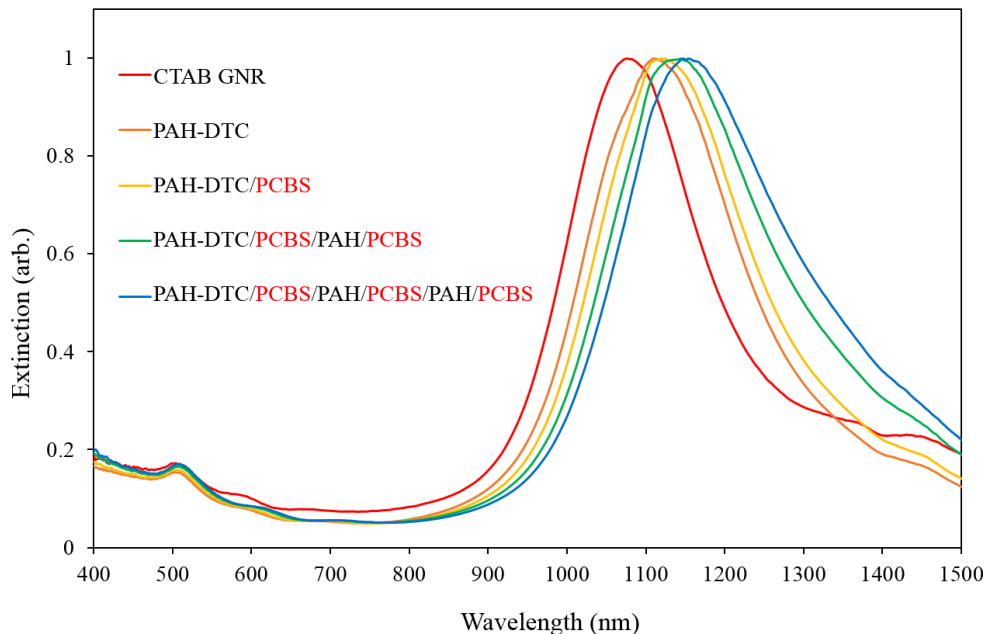


Figure 3.25 Extinction spectra of PAH/PCBS Functionalized GNR suspension. The LSPR peaks are 1075, 1109, 1119, 1144, and 1153 nm from CTAB coated GNR to 3 bilayers of PCBS coated GNR.

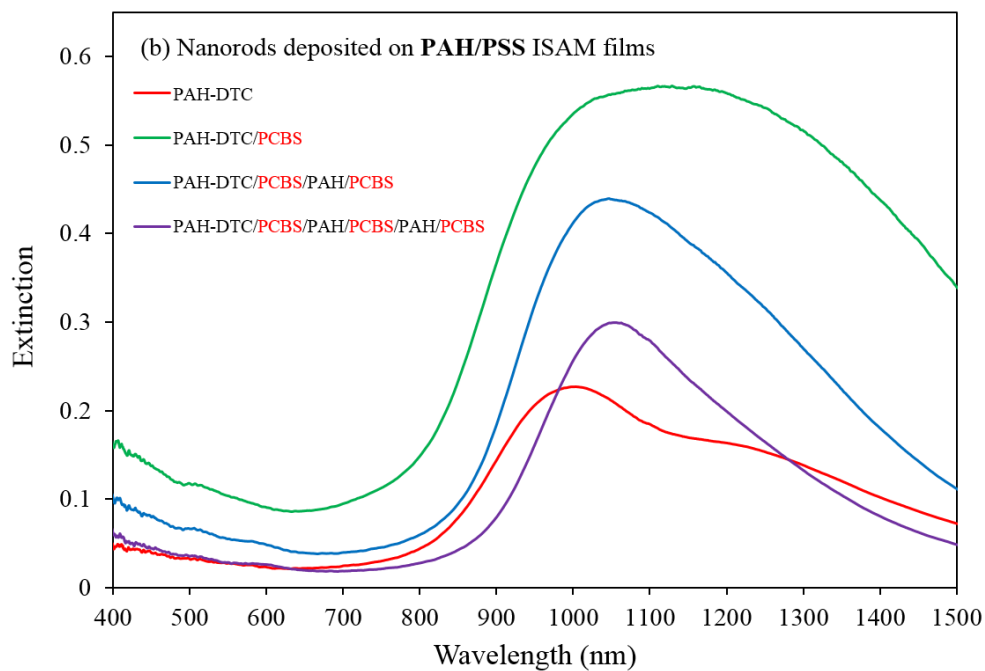
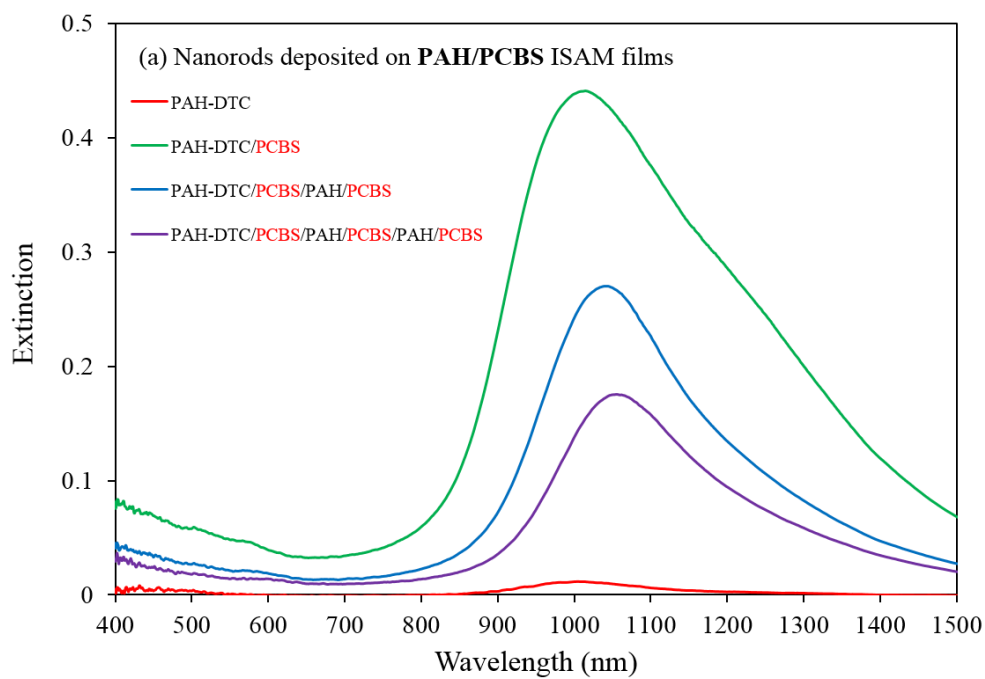


Figure 3.26 Functionalized GNR deposited on 3 or 3.5 bilayer PAH/PCBS (top) and PAH/PSS (bottom) films.

The extinction spectra of functionalized nanorods deposited on (PAH/PCBS)₃PAH and (PAH/PSS)₃PAH films are shown in **Figure 3.26**. The nanorod deposition on (PAH/PCBS)₃PAH and (PAH/PSS)₃PAH films are shown in **Figure 3.27** and **Figure 3.28**, respectively. It was observed that PAH-DTC/PCBS coated GNRs deposited on both ISAM films quicker than other GNRs. In addition, the coverage of these nanorods on (PAH/PSS)₃PAH film was denser than on (PAH/PCBS)₃PAH film. This may be a result of different pK_a values of PCBS ($pK_a = 3$)⁷ and PSS ($pK_a = 1$)^{5,6}. Since the samples were prepared on glass substrates, FESEM required the samples to be sputter-coated with gold for conductivity. Therefore, the images were taken after the SHG measurement of the samples was complete.

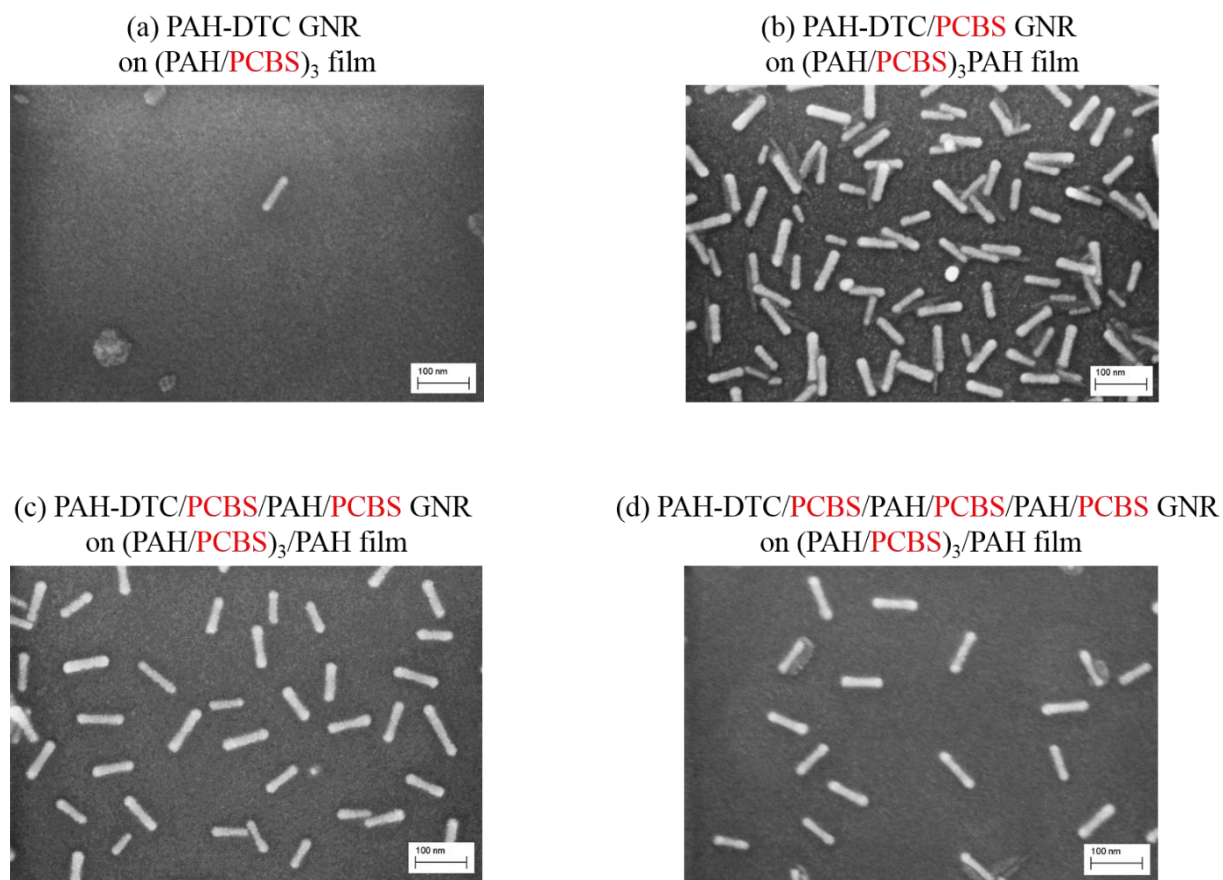
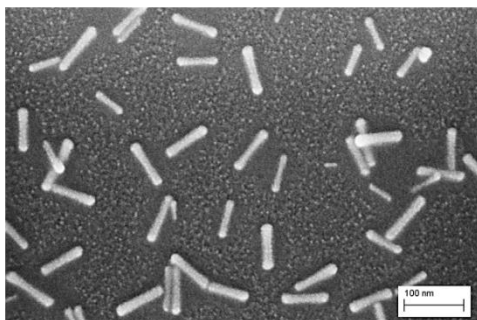
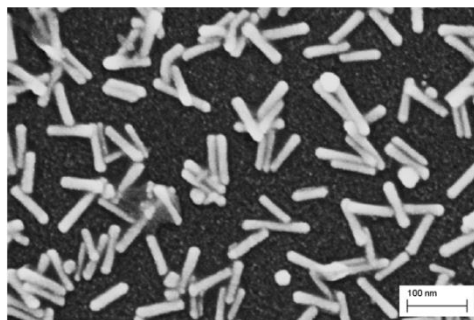


Figure 3.27 SEM images of functionalized GNRs deposited on (PAH/PCBS)₃ and (PAH/PCBS)₃PAH films.

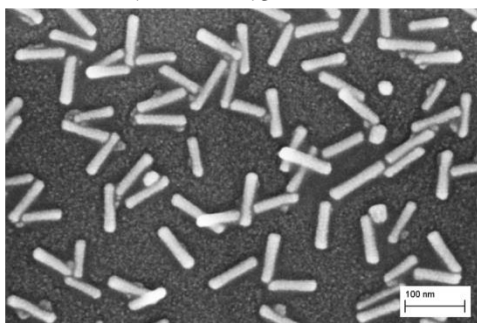
(a) PAH-DTC GNR
on $(\text{PAH/PSS})_3$ film



(b) PAH-DTC/PCBS GNR
on $(\text{PAH/PSS})_3/\text{PAH}$ film



(c) PAH-DTC/PCBS/PAH/PCBS GNR
on $(\text{PAH/PSS})_3/\text{PAH}$ film



(d) PAH-DTC/PCBS/PAH/PCBS/PAH/PCBS GNR
on $(\text{PAH/PSS})_3/\text{PAH}$ film

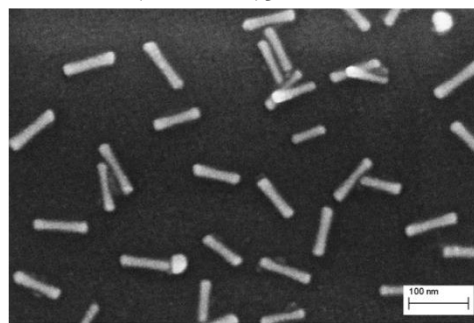


Figure 3.28 SEM images of functionalized GNRs deposited on $(\text{PAH/PSS})_3$ and $(\text{PAH/PSS})_3\text{PAH}$ films.

For convenience, the functionalized GNRs will be referred to as follows from now on.

Functionalized GNRs	referred to as
PAH-DTC GNR	PCBS0 GNR
PAH-DTC/ PCBS GNR	PCBS1 GNR
PAH-DTC/ PCBS /PAH/ PCBS GNR	PCBS2 GNR
PAH-DTC/ PCBS /PAH/ PCBS /PAH/ PCBS GNR	PCBS3 GNR

The shortened names represent the number of PCBS polymer layers coated on the nanorod surface. For example, the nanorods coated with zero, 1, 2, and 3 layers of PCBS are called PCBS0, PCBS1, PCBS2, and PCBS3 GNR, respectively.

A quantitative comparison of the nanorod coverage on the ISAM films is shown in **Table 3.5**. Maximum extinction strength and area under the extinction curve were calculated from the extinction spectra in **Figure 3.26**. The nanorod densities were obtained from the FESEM images in **Figure 3.27** and **Figure 3.28**. The ratios of each column were normalized to PCBS0 GNRs deposited on (PAH/PCBS)₃ film. As confirmed in the extinction spectra in **Figure 3.26**, the nanorod density on both ISAM films was highest for PCBS1 GNRs and lowest for PCBS0 GNRs. The maximum extinction peak and the area under the extinction curve are both indicators of the number of nanorods deposited on an ISAM film. The ratio of nanorod density shows closer agreement between ratios given by the area under the extinction curve and the FESEM images. Since the FESEM images are the most accurate indicator of the nanorod density, it is concluded that the area under the extinction curve is a valid estimation for comparison of nanorod density between samples. After using the FESEM, the samples become forfeit due to the sputter coating of gold needed for conductivity. Therefore, an estimation of the nanorod density via extinction spectrum is convenient because the FESEM images can only be taken after the SHG measurement has already been performed.

Table 3.5 Quantitative results of the functionalized GNRs on two different ISAM films. Max extinction strength and area under the extinction curve were calculated from the extinction spectra in **Figure 3.26** and the nanorod density was obtained from the FESEM images in **Figure 3.27** and **Figure 3.28**.

Functionalized GNR	Deposited on ISAM film	Max extinction		Area under the extinction curve		Nanorod density	
		--	ratio	--	ratio	# of GNRs per μm^2	ratio
PCBS0	(PAH/PCBS) ₃	0.01367	1	2.5	1	1.9	1
PCBS1	(PAH/PCBS) ₃ PAH	0.44102	32.3	163.4	65.5	156.7	83
PCBS2		0.27055	19.8	75.3	30.2	73.6	39
PCBS3		0.17545	12.8	48.2	19.3	32.1	17
PCBS0	(PAH/PSS) ₃	0.22736	16.6	104.2	41.7	103.8	55
PCBS1	(PAH/PSS) ₃ PAH	0.56641	41.4	345.3	138.3	277.5	147
PCBS2		0.43930	32.1	185.3	74.2	178.6	95
PCBS3		0.29937	21.9	99.2	39.7	79.6	42

References

1. Kern, W. & Puotinen, D. A. Cleaning Solutions Based on Hydrogen Peroxide for Use in Silicon Semiconductor Technology. *RCA Rev.* **31**, 187–206 (1970).
2. Burke, S. E. & Barrett, C. J. Acid–Base Equilibria of Weak Polyelectrolytes in Multilayer Thin Films. *Langmuir* **19**, 3297–3303 (2003).
3. Petrov, A. I., Antipov, A. A. & Sukhorukov, G. B. Base–Acid Equilibria in Polyelectrolyte Systems: From Weak Polyelectrolytes to Interpolyelectrolyte Complexes and Multilayered Polyelectrolyte Shells. *Macromolecules* **36**, 10079–10086 (2003).
4. Fang, M. *et al.* Layer-by-Layer Growth and Condensation Reactions of Niobate and Titanoniobate Thin Films. *Chem. Mater.* **11**, 1526–1532 (1999).
5. *CRC handbook of chemistry and physics: a ready-reference book of chemical and physical data.* (CRC Press, 1976).
6. Kharlampieva, E. *et al.* Bioenabled Surface-Mediated Growth of Titania Nanoparticles. *Adv. Mater.* **20**, 3274–3279 (2008).
7. Neyman, P. J. Second-Order Nonlinear Optical Characteristics of Nanoscale Self-Assembled Multilayer Organic Films. (Virginia Tech, 2004).
8. Shiratori, S. S. & Rubner, M. F. pH-Dependent Thickness Behavior of Sequentially Adsorbed Layers of Weak Polyelectrolytes. *Macromolecules* **33**, 4213–4219 (2000).
9. Garg, A., Heflin, J. R., Gibson, H. W. & Davis, R. M. Study of Film Structure and Adsorption Kinetics of Polyelectrolyte Multilayer Films: Effect of pH and Polymer Concentration. *Langmuir* **24**, 10887–10894 (2008).
10. Heflin, J. R., Figura, C., Marciu, D., Liu, Y. & Claus, R. O. Thickness dependence of second-harmonic generation in thin films fabricated from ionically self-assembled monolayers. *Appl. Phys. Lett.* **74**, 495–497 (1999).
11. Garg, A., Davis, R. M., Durak, C., Heflin, J. R. & Gibson, H. W. Polar orientation of a pendant anionic chromophore in thick layer-by-layer self-assembled polymeric films. *J. Appl. Phys.* **104**, 053116 (2008).

12. Chen, K., Durak, C., Heflin, J. R. & Robinson, H. D. Plasmon-Enhanced Second-Harmonic Generation from Ionic Self-Assembled Multilayer Films. *Nano Lett.* **7**, 254–258 (2007).
13. Sharma, V., Park, K. & Srinivasarao, M. Colloidal dispersion of gold nanorods: Historical background, optical properties, seed-mediated synthesis, shape separation and self-assembly. *Mater. Sci. Eng. R Rep.* **65**, 1–38 (2009).
14. Jana, N. R., Gearheart, L. & Murphy, C. J. Seed-Mediated Growth Approach for Shape-Controlled Synthesis of Spheroidal and Rod-like Gold Nanoparticles Using a Surfactant Template. *Adv. Mater.* **13**, 1389–1393 (2001).
15. Nikoobakht, B. & El-Sayed, M. A. Preparation and Growth Mechanism of Gold Nanorods (NRs) Using Seed-Mediated Growth Method. *Chem. Mater.* **15**, 1957–1962 (2003).
16. Yu, Chang, S.-S., Lee, C.-L. & Wang, C. R. C. Gold Nanorods: Electrochemical Synthesis and Optical Properties. *J. Phys. Chem. B* **101**, 6661–6664 (1997).
17. Mohamed, M. B., Ismail, K. Z., Link, S. & El-Sayed, M. A. Thermal Reshaping of Gold Nanorods in Micelles. *J. Phys. Chem. B* **102**, 9370–9374 (1998).
18. Jana, N. R., Gearheart, L. & Murphy, C. J. Wet Chemical Synthesis of High Aspect Ratio Cylindrical Gold Nanorods. *J. Phys. Chem. B* **105**, 4065–4067 (2001).
19. Liu & Guyot-Sionnest, P. Mechanism of Silver(I)-Assisted Growth of Gold Nanorods and Bipyramids. *J. Phys. Chem. B* **109**, 22192–22200 (2005).
20. Sau, T. K. & Murphy, C. J. Seeded High Yield Synthesis of Short Au Nanorods in Aqueous Solution. *Langmuir* **20**, 6414–6420 (2004).
21. Liu & Guyot-Sionnest, P. Synthesis and Optical Characterization of Au/Ag Core/Shell Nanorods. *J. Phys. Chem. B* **108**, 5882–5888 (2004).
22. Zweifel, D. A. & Wei, A. Sulfide-Arrested Growth of Gold Nanorods. *Chem. Mater.* **17**, 4256–4261 (2005).
23. Vigderman, L. & Zubarev, E. R. High-Yield Synthesis of Gold Nanorods with Longitudinal SPR Peak Greater than 1200 nm Using Hydroquinone as a Reducing Agent. *Chem. Mater.* **25**, 1450–1457 (2013).

24. Gentry, S. T., Fredericks, S. J. & Krchnavek, R. Controlled Particle Growth of Silver Sols through the Use of Hydroquinone as a Selective Reducing Agent. *Langmuir* **25**, 2613–2621 (2009).
25. Sirajuddin *et al.* The formation of gold nanoparticles using hydroquinone as a reducing agent through a localized pH change upon addition of NaOH to a solution of H₂AuCl₄. *Colloids Surf. Physicochem. Eng. Asp.* **370**, 35–41 (2010).
26. Li, J. *et al.* Controllable Synthesis of Stable Urchin-like Gold Nanoparticles Using Hydroquinone to Tune the Reactivity of Gold Chloride. *J. Phys. Chem. C* **115**, 3630–3637 (2011).
27. Smith, D. K. & Korgel, B. A. The Importance of the CTAB Surfactant on the Colloidal Seed-Mediated Synthesis of Gold Nanorods. *Langmuir* **24**, 644–649 (2008).
28. El-Sayed, M. A. Some Interesting Properties of Metals Confined in Time and Nanometer Space of Different Shapes. *Acc. Chem. Res.* **34**, 257–264 (2001).
29. Link, S., Mohamed, M. B. & El-Sayed, M. A. Simulation of the Optical Absorption Spectra of Gold Nanorods as a Function of Their Aspect Ratio and the Effect of the Medium Dielectric Constant. *J. Phys. Chem. B* **103**, 3073–3077 (1999).
30. Smitha, S. L., Gopchandran, K. G., Smijesh, N. & Philip, R. Size-dependent optical properties of Au nanorods. *Prog. Nat. Sci. Mater. Int.* **23**, 36–43 (2013).
31. Orendorff and Murphy - 2006 - Quantitation of Metal Content in the Silver-Assist.pdf.
32. Schneider, G. & Decher, G. From Functional Core/Shell Nanoparticles Prepared via Layer-by-Layer Deposition to Empty Nanospheres. *Nano Lett.* **4**, 1833–1839 (2004).
33. Nikoobakht, B. & El-Sayed, M. A. Evidence for Bilayer Assembly of Cationic Surfactants on the Surface of Gold Nanorods. *Langmuir* **17**, 6368–6374 (2001).
34. Takahashi, H. *et al.* Modification of Gold Nanorods Using Phosphatidylcholine to Reduce Cytotoxicity. *Langmuir* **22**, 2–5 (2006).
35. Gómez-Graña, S. *et al.* Surfactant (Bi)Layers on Gold Nanorods. *Langmuir* **28**, 1453–1459 (2012).
36. Chen, K. & Robinson, H. D. Robust dithiocarbamate-anchored amine functionalization of Au nanoparticles. *J. Nanoparticle Res.* **13**, 751–761 (2011).

37. Zhu, H. *et al.* Assembly of Dithiocarbamate-Anchored Monolayers on Gold Surfaces in Aqueous Solutions. *Langmuir* **24**, 8660–8666 (2008).
38. Auguste, D. T., Kirkwood, J., Kohn, J., Fuller, G. G. & Prud'homme, R. K. Surface Rheology of Hydrophobically Modified PEG Polymers Associating with a Phospholipid Monolayer at the Air–Water Interface. *Langmuir* **24**, 4056–4064 (2008).
39. Shimabayashi, S., Nishino, K. & Nakagaki, M. Aggregation/dispersion of amorphous silica particles by simultaneous adsorption of two polymers in an aqueous phase. *Colloids Surf.* **63**, 121–129 (1992).
40. Malvern Instruments Ltd, Zetasizer Nano series technical note, MRK654-01.

Chapter 4

Experimental Techniques and Measurements

This chapter discusses the SHG measurement technique and results. The Maker fringe method was utilized for SHG measurement. The second harmonic generation experimental apparatus was designed to measure SHG interference fringes. In this setup, the fundamental beam was directed, linearly polarized, filtered, and focused onto a sample mounted on a rotation stage. A Q-switched Nd:YAG (neodymium-doped yttrium aluminum garnet) laser provided fundamental light at the wavelength of 1064 nm with a 10 ns pulsewidth at 10 Hz . Lenses and mirrors were used to direct or shape the fundamental beam, and polarizers and waveplates were used to ensure vertical polarization and to control the incident beam power. The fundamental input signal was measured by a photodiode and the weak SHG signal was collected by a photomultiplier tube (PMT). Both signals were read by an oscilloscope and recorded by LabVIEW software. The SHG measurement was done in darkness to prevent ambient light entering the PMT. Noise reduction techniques were employed as well.

To avoid optical damage of the nanorods, various pump energies were tested to determine the threshold for incident beam fluence. SHG measurements were done on both functionalized nanorods and ISAM films for comparison. Polarization of the incoming pump energy was varied to investigate the corresponding polarization of outgoing SHG signals from either ISAM films or ISAM-nanorod films.

4.1 Maker Fringe Method for ISAM Film

The Maker fringe method was introduced in 1962 by Maker *et al.*¹ In this method, a parallel plane sample is rotated around an axis perpendicular to the incoming laser light. It is widely used for determining relative nonlinear optical coefficients of organic materials. It especially works best for thin plates and thus it is the standard method for characterizing organic crystals possessing parallel faces and thin films on substrates.

Consider a well-collimated pump beam that passes through a continuous slab of lossless, nonlinear material of thickness L . If the slab is rotated, then the fundamental beam intercepts the slab at a variable angle θ and generates SHG power that oscillates according to the basic Maker fringe pattern expressed as

$$P_{2\omega}(\theta) = P_{\text{env}}(\theta) \sin^2 \left[\frac{\pi L}{2l_c(\theta)} \right] \quad (4.1)$$

$P_{\text{env}}(\theta)$ is the Maker fringe envelope, proportional to P_{ω}^2 , which incorporates the Fresnel transmission coefficients. The Maker fringe period depends on the ratio of the slab thickness L and the coherence length $l_c(\theta)$. The coherence length parameterizes frequency dispersion in the nonlinear medium and has typical values between 10-100 μm . For a pump wavelength, λ , the coherence length is given by

$$l_c(\theta) = \frac{\pi}{\Delta k} = \frac{\lambda}{4 |n_{\omega} \cos \theta_{\omega}' - n_{2\omega} \cos \theta_{2\omega}'|} \quad (4.2)$$

where n_{ω} ($n_{2\omega}$) and θ_{ω}' ($\theta_{2\omega}'$) is the refractive index and transmission angle, respectively, inside the nonlinear slab at the fundamental (second harmonic) frequency. Due to dispersion of the refractive index, the fundamental and second harmonic waves travel at different velocities. This creates a phase mismatch between SHG generated at the front of the sample and SHG generated inside the sample at intermediate points. The superposed SHG signal cycles through maxima and minima as the sample rotates and the number of coherence lengths changes through integer values.

A detailed comparison of theory and experiment for optically isotropic and uniaxial crystals was discussed by Jerphagnon and Kurtz in 1970.² The complete theory for optically biaxial crystals was developed by Bechthold in 1976.³ For single-sided thin polymeric films, Herman and Hayden presented a new derivation of the Maker fringes in parallel-surface films in 1995. They discussed a general framework for SHG analysis of materials that are isotropic (non-absorbing), absorbing, or birefringent, using complete boundary conditions for the second harmonic waves.⁴ **Figure 4.1** shows Maker fringe plots for a 9 μm thick poled polymer film and 1000 μm thick X-cut quartz. They were plotted using the derivation Herman and Hayden provided. In 2008, Abe *et al.* included the effects of multiple reflections and interferences of the fundamental and SH waves in anisotropic plane-parallel plates.⁵ More recently, Park and Herman reported new closed-form Maker fringe expressions for anisotropic and absorbing poled polymer thin films in multilayer structures including back reflections of both fundamental and SH waves.⁶

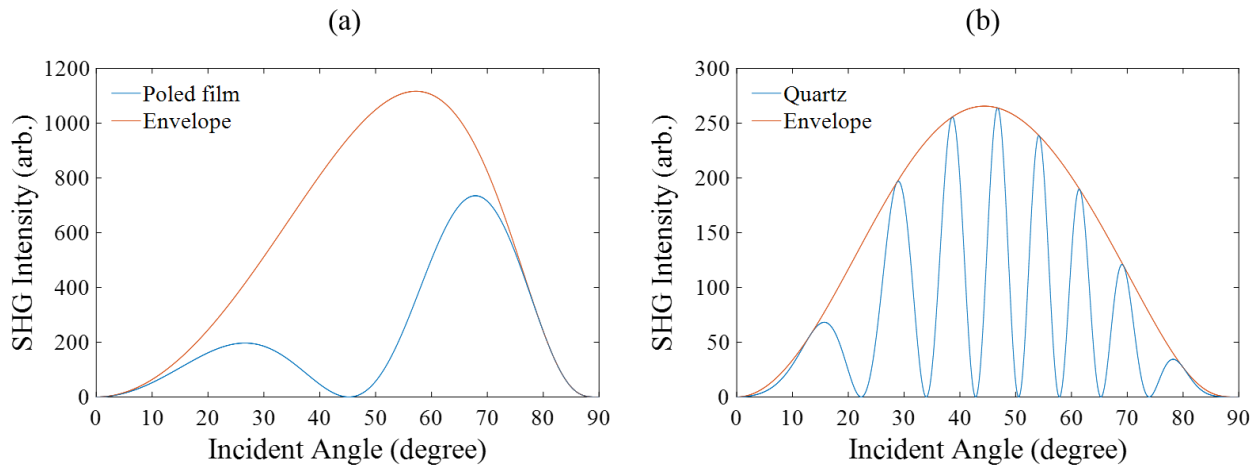


Figure 4.1 Maker fringe plots for (a) 9 μm thick NLO poled polymer film and (b) 1000 μm thick X-cut quartz. They were plotted following the derivation given by Herman and Hayden.

For the case in which NLO-active films are coated on both sides of the substrate, interference fringes of the SHG intensity are created as a function of incident angle. Each film is thin enough that it acts as a single coherent source of SHG. Since the path length inside the substrate varies with incident angle, the SHG from the two films interfere constructively and destructively creating maxima and minima along the fringe. These interference fringes oscillate within an envelope shaped by transmissions and reflections at the air-film interfaces, the path length inside the substrate, and coupling between the polarization and the $\chi^{(2)}$ tensor.² As a result, the SHG signal increases as the sample rotation angle increases up to 60° and decreases afterwards. The increased SHG signal is due to low reflection of the p-polarized pump beam, increased path length, and increased polarization coupling to the $\chi^{(2)}$ tensor. However, as the incident angles become larger than Brewster's angle, the SHG signal decreases due to higher reflectance for p-polarized pump light. **Figure 4.2** shows a common example of an interference fringe pattern from a double sided (PAH/PCBS)₃PAH film. The orange line indicates an interference fringe pattern of 3.5 bilayer PAH/PCBS film and the black dotted line follows the envelope of the fringe.

Due to dispersion, fundamental light and second harmonic light from the front side propagate at different velocities inside the glass, which causes constructive and destructive interference of the second harmonic signals depending on the distance traveled by the second harmonic from the front film before it reaches the rear film. Interference fringe maxima (minima) occur when the second harmonic signal from the rear side of the sample is in (out of) phase with the second harmonic signal from the front side which travels through the substrate.

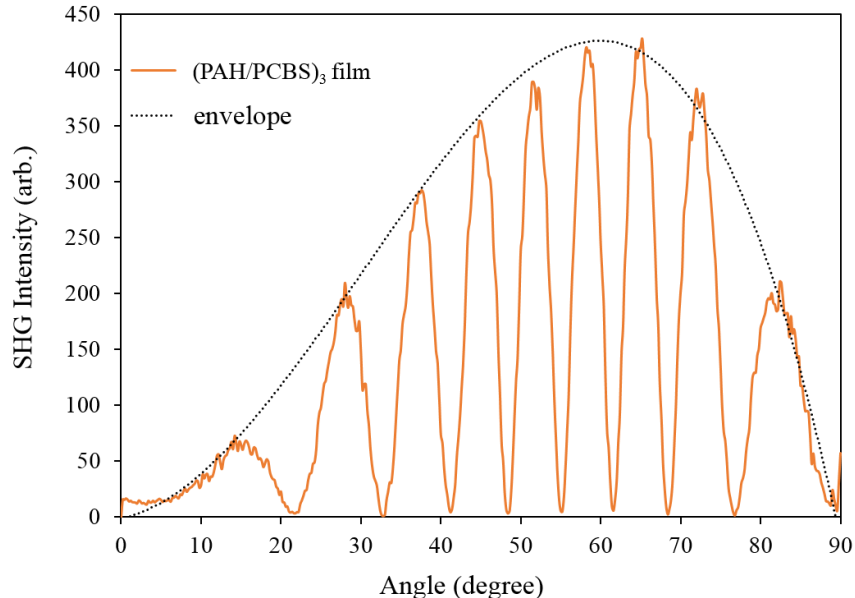


Figure 4.2 Interference fringe pattern from a double-sided (PAH/PCBS)₃PAH sample. The SHG signal envelope increases with rotation angle up to 60° because of low reflection of the p-polarized pump light, increased path length, and increased polarization coupling to the $\chi^{(2)}$ tensor. The SHG signal decreases afterwards due to increased reflection of the p-polarized pump light at incident angles larger than Brewster's angle.

4.2 SHG Measurement Apparatus

The experimental apparatus for SHG measurement is illustrated in **Figure 4.3**. The fundamental beam was provided by a Spectra Physics Quanta-Ray INDI Q-switched high-powered 10 Hz pulsed laser, Nd:YAG, operating at 1064 nm. The pulse width of the fundamental beam is 11 ns and the average pulse energy is 350 mJ. The laser includes a harmonic generator which can emit a light of wavelength 532 nm. To block this light, the SHG crystal was turned to create a phase mismatch. However, faint green light still came out of the laser that reached the sample stage and was detected by the PMT. To block this green stray light, a screen was placed in front of the laser.

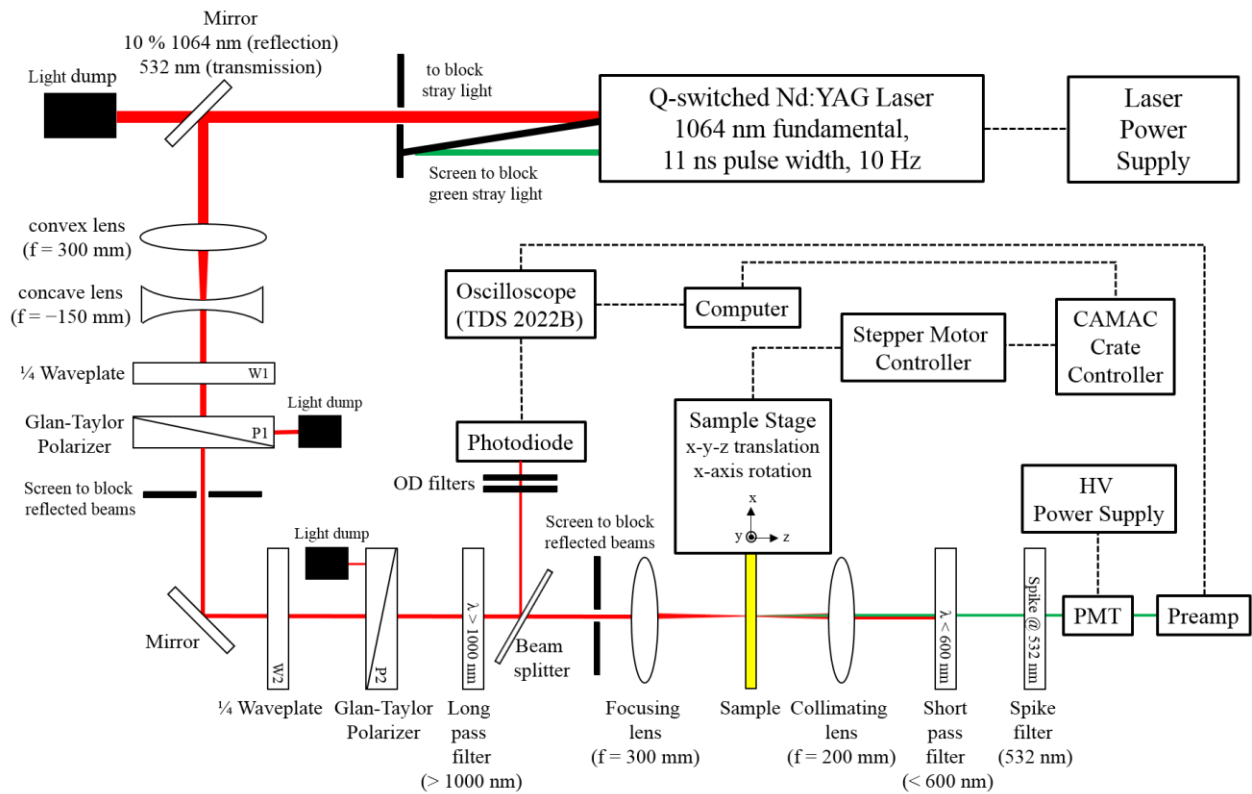


Figure 4.3 Experimental apparatus for second-harmonic generation measurement. A Q-switched Nd:YAG pulsed laser provides the 1064 nm fundamental light. A reference optical power is collected by a photodiode and the SHG signal (at 532 nm) is detected by a PMT, amplified by a preamp and read by an oscilloscope.

The fundamental beam was reflected by a mirror that reflects approximately 10% at 1064 nm (~ 30 mJ) and transmits at 532 nm. A beam dump (Blackhole Model 510) was put behind the mirror to absorb the transmitted 1064 nm light. The weak secondary reflections were blocked by a screen with an opening of 2 cm diameter placed between the laser and the 10% mirror. The beam diameter was about 10 mm which was slightly bigger than the face of a polarizer prism. Therefore, the beam size was reduced by half using a Galilean telescope which has a set of convex ($f = 300$ mm) and concave ($f = -150$ mm) lenses.

To avoid any laser-induced damage effects on the sample, the fundamental energy was reduced using a quarter waveplate and a Glan-Taylor polarizer. In general, a half waveplate and a linear polarizer may be used together to completely reduce the light intensity. However, a quarter waveplate together with a polarizer (analyzer) can be used to incompletely reduce the light intensity if this is acceptable for the application. This was the case for the apparatus here. To verify how these waveplates behave, a waveplate and a polarizer (fixed for vertical polarization) were placed after the Galilean telescope and power was measured at different rotation angles of the waveplate. As shown in **Figure 4.4**, both of the waveplates showed power variation between some maximum value and non-zero minimum value.

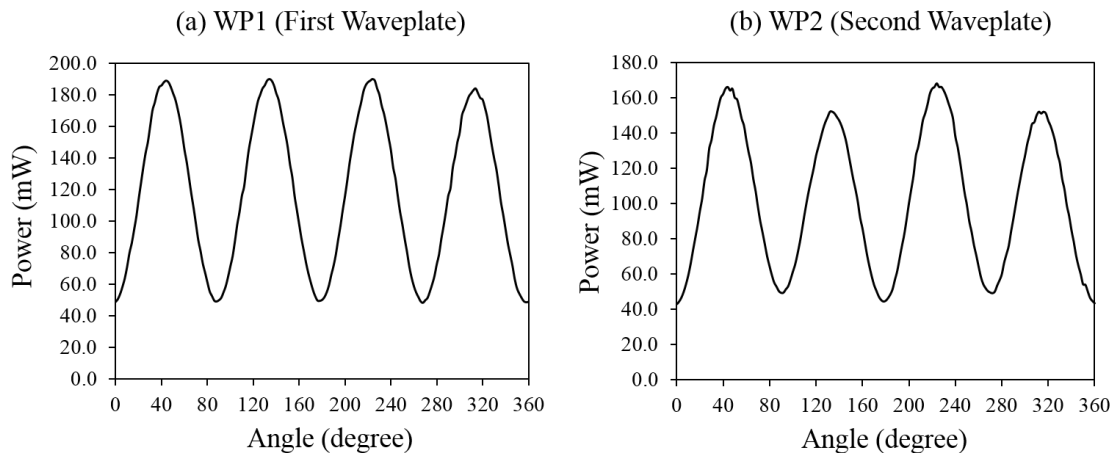


Figure 4.4 Power measurement vs. angle rotation of waveplates. A polarizer for vertically polarized light was placed after the waveplate. Power was measured after the polarizer. (a) WP1 was the first waveplate and (b) WP2 was the second waveplate in **Figure 4.3**.

Next, a mirror (BB1-EO3, Thorlabs) reflected the beam toward the path along the sample stage. Another set of a quarter waveplate and a Glan-Taylor polarizer was used to provide an option to adjust the incident energy and to ensure vertical polarization, respectively. Because the waveplates and the polarizers are made of birefringent materials, it is very important to remove

the SHG signal generated in these optical components in the input light with a band-pass filter that only transmits wavelengths above 1000 nm as shown in **Figure 4.5** (top left).

Using a glass slide, a small portion of the fundamental laser beam was split to a reference channel to monitor the input fundamental power detected by a photodiode (PIN10D BIAS Box 45V, built in the physics electronics shop at Virginia Tech). The purpose of the reference channel was to generate a signal from which to normalize the sample SHG signal and to eliminate any fluctuation effect in the laser power during the experiment. The photodiode was connected to the oscilloscope which then read the pump signal on channel 1. An additional screen was placed between the glass slide and a focusing lens to block any stray light generated from the polarizers and waveplates.

The fundamental beam was then focused onto the sample using a convex lens with focal length 300 mm. The sample stage consisted of three Aerotech (50SMC2N-HMK) stepper-motor linear translational stages and one Aerotech stepper-motor rotation stage attached to the linear stages. The linear stages afford 2- μm resolution and the rotational stage provides $1/27^\circ$ rotational resolution about the x-axis indicated in the sample stage of **Figure 4.3**. The stepper-motors were controlled by a Joerger SMC-R motor controller which allowed simultaneous control of two motors. The stepper-motor controller was operated by a KineticSystems 1510-P2C CAMAC (computer automated measurement and control) minicrate controlled by a LabVIEW program.

After the fundamental beam passed through the sample, both fundamental and SH beams were collimated by a convex lens with focal length 200 mm. It is known that the shape of the generated beam matches that of the incident beam.⁷ To eliminate the fundamental beam, a short-pass filter ($380 \text{ nm} < \lambda < 600 \text{ nm}$) was placed after the collimating lens. Finally, a spike filter centered at approximately 532 nm was placed after the short-pass filter. This allowed only the second harmonic light to pass and enter the photomultiplier tube (PMT). The transmittance of these filters are shown in **Figure 4.5**.

Since the conversion efficiencies are usually extremely low, on the order of 10^{-9} % or lower⁸, a PMT was used to detect the second harmonic light. The PMT (Hamamatsu R1924) was powered by a Bertran 230-03-R high voltage power supply operating at 1.2 kV. Although the pump energy used to generate SH signal from an NLO film was as high as 1 mJ, it was necessary to reduce the

pump energy for SHG measurement of nanorods to prevent optical damage. With a low pump energy, the weak SHG signal was buried under the electrical noise generated by the laser power supply. Therefore, a variable-gain high speed current amplifier (Femto DHP-100) was used to amplify the SHG signal which was then sent to the oscilloscope (Tektronix TDS 2022B). Finally, SHG data was collected from the oscilloscope and processed via LabVIEW.

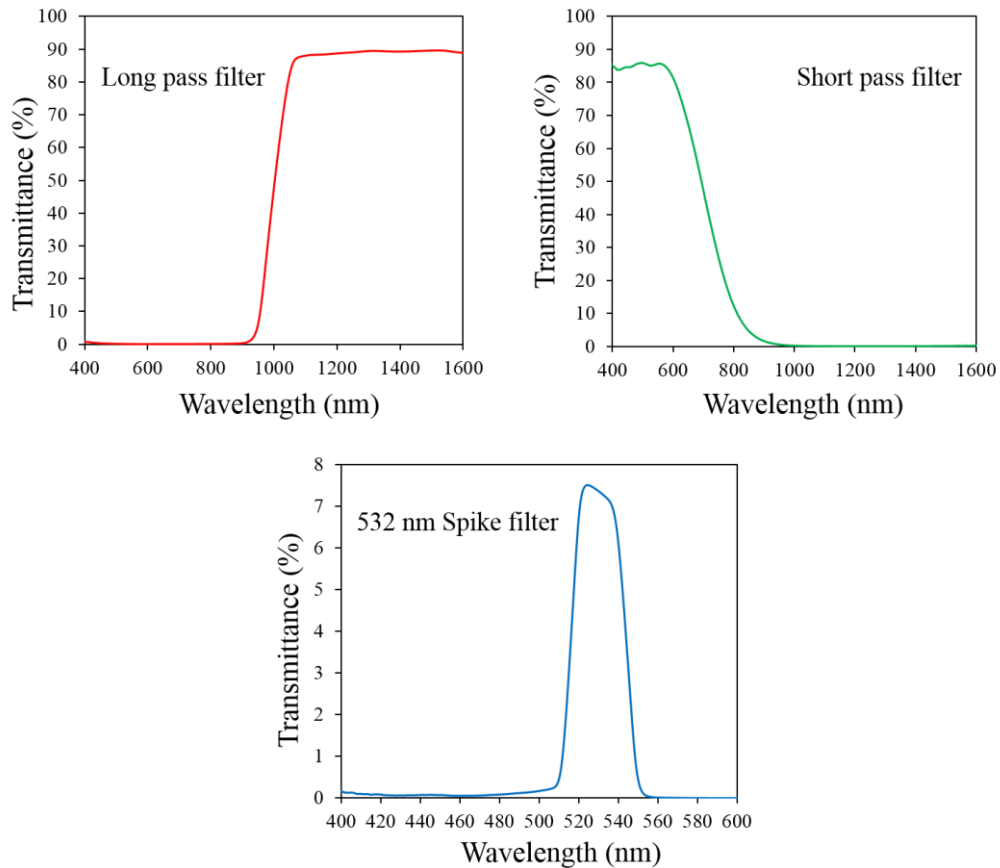


Figure 4.5 Transmittance spectra of filters: a long pass filter for $\lambda > 1000$ nm, a short pass filter for $380 \text{ nm} < \lambda < 600$ nm, and a spike filter at 532 nm.

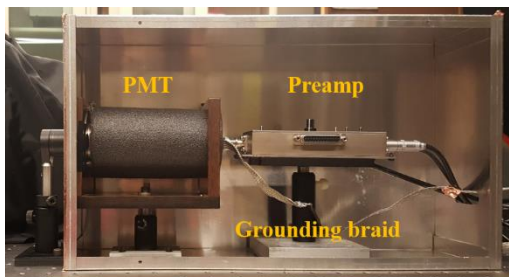
4.3 Electrical Noise Reduction Methods

Electrical noise from the power electronics driving the laser was so significant that the weak SHG signal from the nanorods was not easily identified from the oscilloscope using the peak detection mode. Therefore, several methods were pursued to reduce the electrical noise and extract the signal of interest.

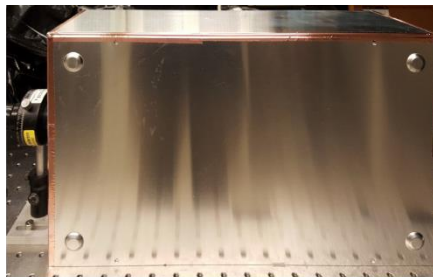
Grounding & Shielding

Grounding was done by attaching a ground braid (**Figure 4.6a**) to the chassis of the PMT and the preamp (current amplifier). The grounding braid connected to the ground of a surge protector for power plugs which included all electronic instruments such as the oscilloscope, current amplifier, HV power supply, and stepper-motor controller.

Ferrite rings and clips (**Figure 4.6c**) were utilized to shield the wires whose lengths were minimized by choosing shorter length BNC cables to connect the laser power supply and the oscilloscope. For better shielding of PMT and preamp, a purpose-built Faraday cage (**Figure 4.6a-b**) was fabricated with help of the Physics Department machine shop at Virginia Tech. This was not only for shielding but also for providing a dark environment for the PMT.



(a) Inside of Faraday cage



(b) Outside of Faraday cage



(c) Ferrite rings and clip

Figure 4.6 Faraday cage (enclosing PMT and preamp) and ferrite rings and clip.

Amplifier and low pass filter

A current amplifier (**Figure 4.6a**) was connected to the PMT for signal amplification. Unfortunately, it amplified both the signal of interest and the noise, which was still problematic. However, it was possible to obtain a detailed noise pattern which was used for ensemble averaging. The gain was set to 10000.

A low pass filter allows slow moving signals with low frequency to pass but stops signals with high frequency (jiggling noise). In the oscilloscope, the frequency bandwidth was set to 20 MHz. In other words, the cutoff frequency of the low pass filter was set to 20 MHz so that higher frequency noise was rejected.

Software method: Ensemble averaging

Ensemble averaging adds signals obtained from identical runs together. For this, it was required to repeat SHG measurements for a fixed angle between sample and pump light. Ensemble averaging was performed via a LabVIEW program in which a total waveform was created by adding the previous instances of the waveforms, and the total waveform was divided by the number of waveforms added together to achieve an average waveform. The number of SHG waveforms per rotation angle was typically 50 for nanorods deposited on ISAM film and 30 for ISAM films. After the average waveform for a fixed angle was obtained, it was integrated (summed) over some range that includes the SHG signal, which represented the SHG signal at the angular position of the sample. This method made it possible to extract SHG signal buried under the noise.

For ensemble averaging, it is important to add waveforms in phase from one iteration to the next. However, it was observed that the waveform displayed in the oscilloscope shifted vertically over time, which resulted in different integrated values for identical waveforms. Therefore, to make the baselines of all waveforms align, a DC bias was subtracted from each waveform before taking the ensemble average. **Figure 4.7** shows an image of the oscilloscope showing both pump (in yellow) and SHG (in blue) real time signals. Integration of the average waveform was performed within the region indicated in **Figure 4.7** as ‘Noise + SHG’ in red.

To stabilize the waveforms read from the oscilloscope, average mode was chosen for acquisition. In average mode, the oscilloscope averages waveform points from consecutive acquisitions and displays the final waveform.

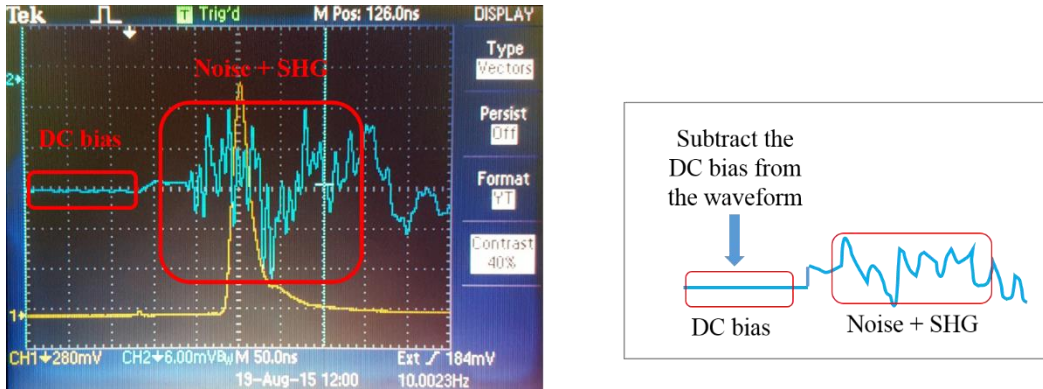


Figure 4.7 Oscilloscope screenshot of waveforms of channel 1 (pump, yellow) and channel 2 (SHG, blue). To the right is an illustration of the DC bias and the SHG waveform buried in the electrical noise.

4.4 LabVIEW Programming for SHG Measurement

The SHG data was collected and processed by software written in LabVIEW. The program has three stages: (1) initialization, (2) data processing and display, and (3) data recording. **Figure 4.8** shows the front panel of the LabVIEW program.

The initialization stage receives the initial inputs for the stepper-motor rotation stage (initial and final rotation angles, angle step), the number of ensemble averages, the CAMAC setup parameters, and the USB address for the oscilloscope. The number of ensemble averages is the number of measurements at each angle, averaged to create a single data point. The data processing and display stage reads and processes the pump and SHG signals from the oscilloscope to display graphs on the front panel. Finally, the data recording stage saves the collected data from the data processing stage.

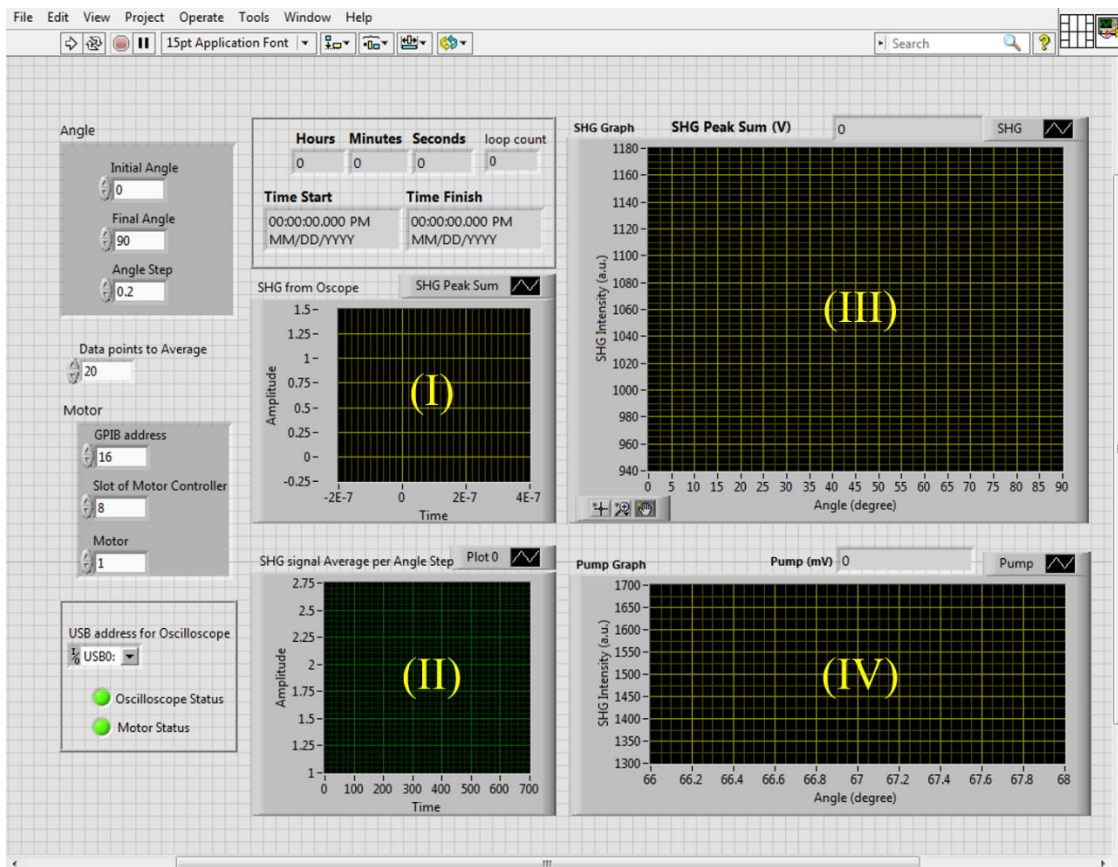
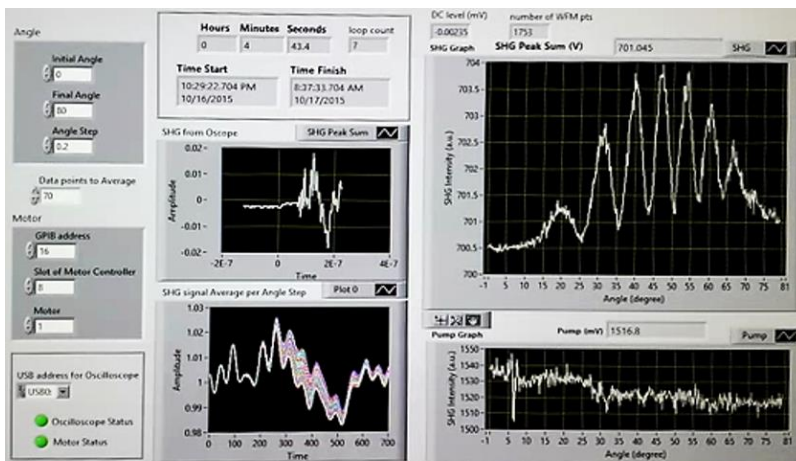
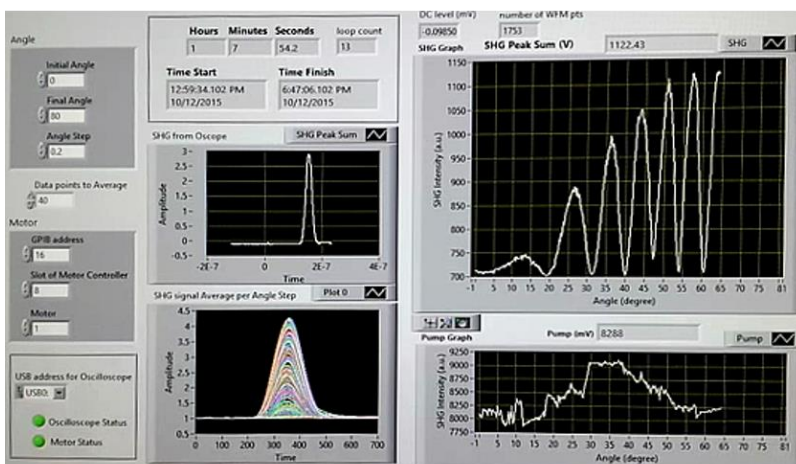


Figure 4.8 Front panel of the LabVIEW program shows the initialization values (left column) and the display graphs for processed data (labeled I, II, III, and IV).

Two examples of the front panel of the LabVIEW program of real time SHG measurement are shown in **Figure 4.9**. SHG measurements are shown in the top figure (a) for nanorods deposited on $(\text{PAH/PCBS})_3\text{PAH}$ film and in the bottom figure (b) for $(\text{PAH/PCBS})_3\text{PAH}$ ISAM film. Each figure displayed four graphs as labeled as I, II, III, and IV in **Figure 4.8**: (I) is a graph of the real time SHG signal from the oscilloscope channel 2 (as seen in **Figure 4.7**), (II) is a persistent graph of the average of each signal in (I) after the DC bias removal, (III) is a plot of the summed data of (II) for each angle, and (IV) is a graph of the averaged pump signal from the oscilloscope channel 1.



(a) SHG measurement of GNRs



(b) SHG measurement of $(\text{PAH/PCBS})_3\text{PAH}$ film

Figure 4.9 Front panel of the LabVIEW program for SHG measurement of (a) GNRs and (b) $(\text{PAH/PCBS})_3\text{PAH}$ film.

The LabVIEW plots of PCBS1 GNR deposited on $(\text{PAH/PSS})_3\text{PAH}$ film are shown in **Figure 4.10**. The top figure (a) shows all waveforms measured at angles between 30° and 80° and appears in (II) in **Figure 4.8**. The middle figure (b) is the waveforms in (a) subtracted with the background waveform which was measured without the sample. It is seen that the SHG signals are in the data points between 300 and 500. Finally, the bottom figure (c) is the summed waveforms of the waveforms in figure (a), plotted for various rotation angles.

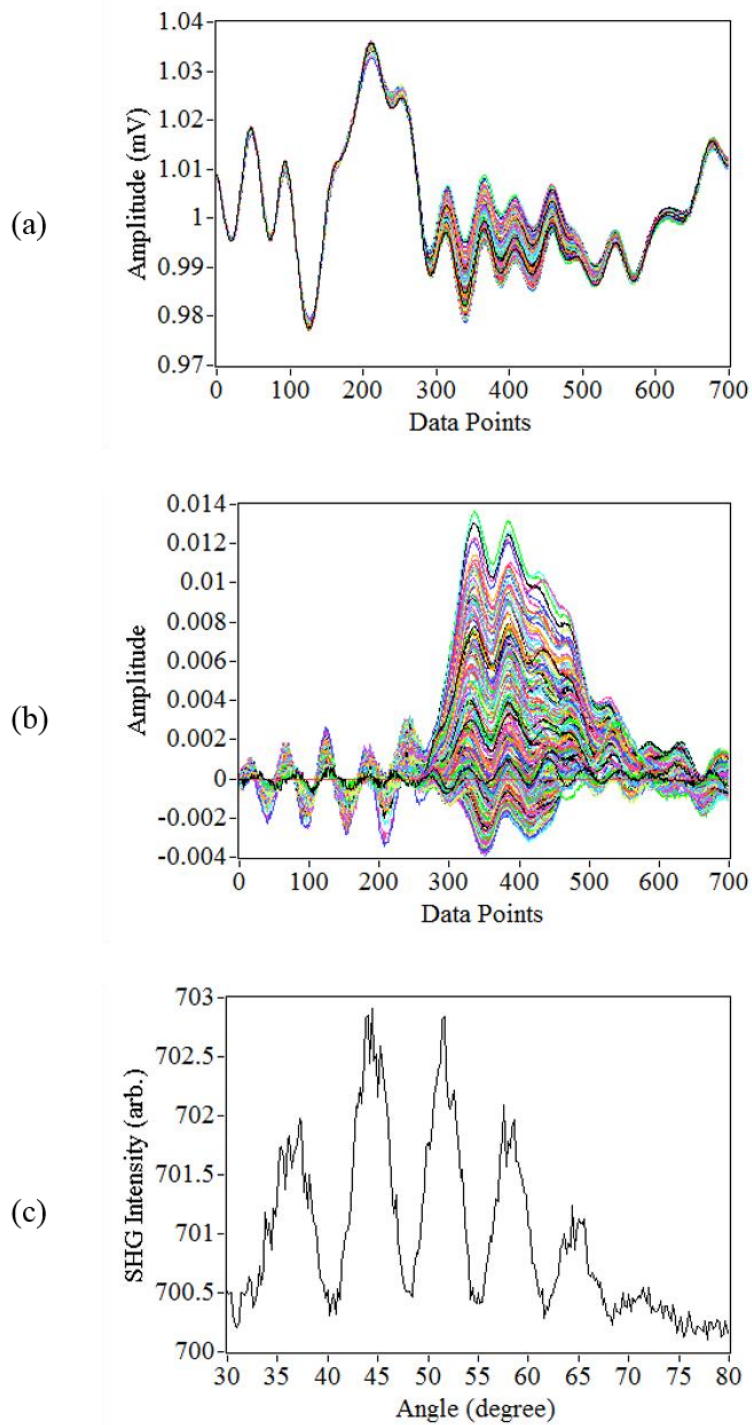


Figure 4.10 LabVIEW plots of SHG waveforms. (a) SHG waveforms subtracted from the DC bias. (b) SHG waveforms subtracted from a background waveform. (c) SHG intensity vs. rotation angles 30° to 80°.

4.5 Pump Energy Threshold for Gold Nanorods

As mentioned in **Section 4.2**, when the same pump energy (400 μJ) was used to generate SH signal as was used for a bare NLO film, the nanorods underwent optical damage as shown in **Figure 4.13** where the nanorods started to become dogbone-shaped. To investigate the pump energy threshold for SHG measurement of nanorods, a sample of PCBS1 GNRs deposited on $(\text{PAH}/\text{PCBS})_3\text{PAH}$ film was set at a fixed angle for max SHG intensity (between 40° and 60°) and the SHG intensity was measured at various pump energies between 0 and 150 μJ .

The results are shown in **Figure 4.11** where the red and blue markers indicate measured and calculated SHG measurement, respectively. The SHG signal should vary as the square of the power as discussed in **Chapter 2 Section 2.5**, and thus the calculated data points were quadratically scaled by the increase in pump energy. The fitting equations are displayed in the graphs for their respective pump energy ranges. According to the results, the SHG intensity failed to grow quadratically when the pump energy was increased above 50 μJ . This is attributed to optical damage of the nanorods in excess of this threshold. For this measurement, the sample was placed about an inch away from focus to keep the same fluence with more pump energy.

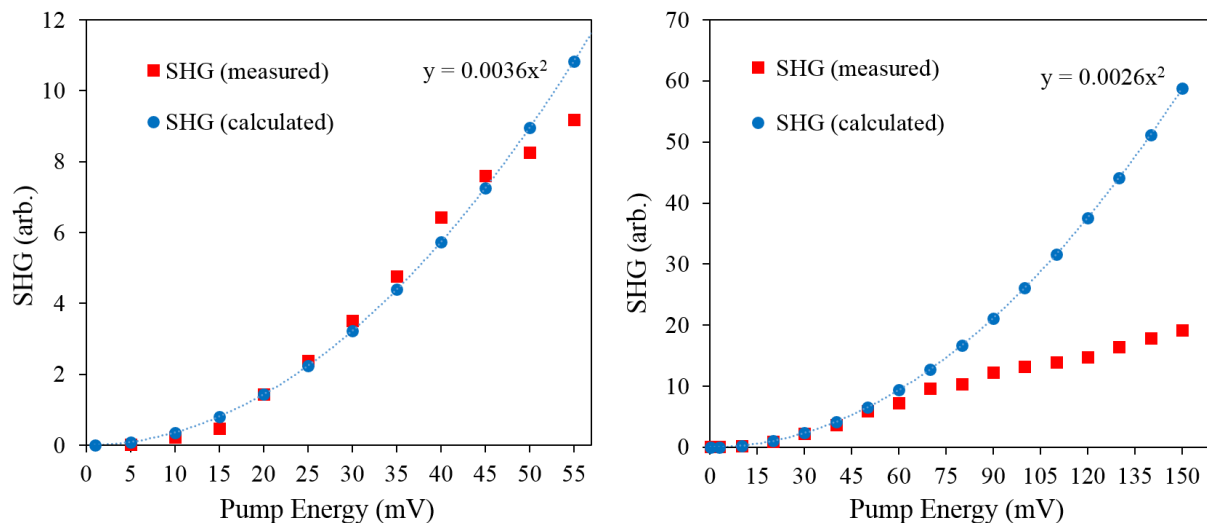


Figure 4.11 SHG vs. Pump energy measurement. The sample used for the test was PCBS1 GNRs deposited on $(\text{PAH}/\text{PCBS})_3\text{PAH}$ film. The graph on the right shows a wider range of pump energy than that of the graph on the left. The blue markers and the dotted fit indicate calculated SHG data points and the red markers indicate measured data points.

Fluence is the optical energy delivered per unit area and can be found from laser pulse energy divided by effective Gaussian beam spot area, $(\pi \times w^2)/2$, where w is the Gaussian beam radius. The collimated beam radius before the focusing lens was in the range of 4 - 5 mm. The beam waist radius w_0 is the beam spot radius at $z = 0$ (at the focal point) and is related to the beam radius at arbitrary z by

$$w(z) = w_0 \sqrt{1 + \left(\frac{z}{z_R}\right)^2} \quad (4.3)$$

where $z_R = \pi w_0^2 / \lambda$ is the Rayleigh range that determines the length over which the beam can propagate without diverging significantly. This is plotted in **Figure 4.12** for a collimated Gaussian beam of radius 2.5 mm passing through a focusing lens with a focal length of 30 cm.

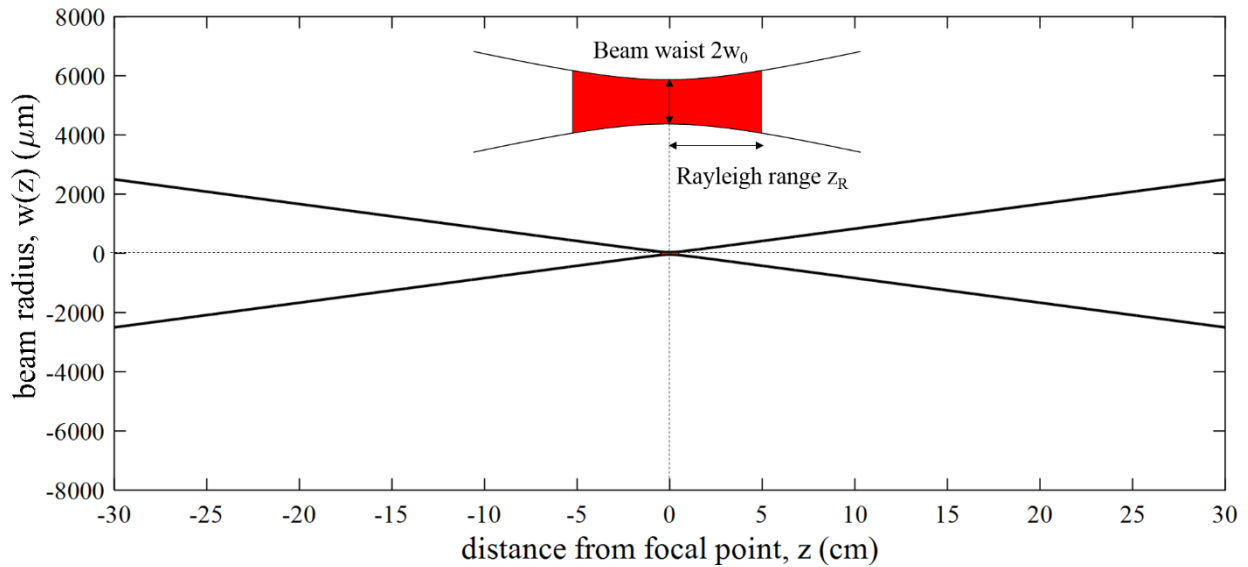


Figure 4.12 Illustration of a focused Gaussian beam. It was plotted for the collimated Gaussian beam (radius of 2.5 mm) passing through a convex lens with a focal length of 30 cm. The inset is the Rayleigh range (red filled) of z_0 and a beam waist $2w_0$.

Figure 4.13 is an FESEM image of PCBS3 GNRs deposited on (PAH/PSS)₃PAH film. It was placed about 2.5 cm away from the focus and was exposed to a pump energy of 0.4 mJ. The beam radius at this spot was 212 μm , calculated from the plot in **Figure 4.12**. Therefore, the corresponding fluence was found to be about 0.57 J/cm^2 at which the laser exposed gold nanorods were observed to become dogbone-shaped as shown in **Figure 4.13**. This is likely a stage in shape transformation from a rod to a sphere due to laser irradiation according to studies on laser-induced shape changes of nanoparticles. Link *et al.*⁹ reported that nanosecond pulses can fragment gold nanorods into smaller spherical particles. Moreover, Chang *et al.*¹⁰ reported that a high amount of ϕ -shaped nanorods were produced after exposure with low power nanosecond pulses with an average laser fluence of 18.5 mJ/cm^2 . The ϕ -shaped nanorods were suggested to be an early stage of transformation of the shape from a rod to a sphere.

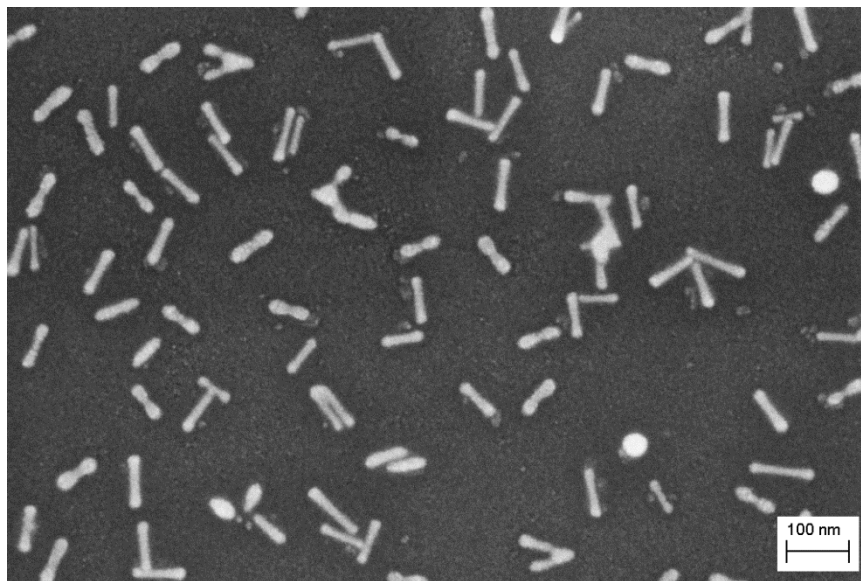


Figure 4.13 FESEM image of PCBS3 GNRs deposited on (PAH/PSS)₃ film. Nanorods are forming dogbone-like structures due to optical damage by laser irradiation. The pump energy was 0.4 mJ and the fluence was 0.7 J/cm^2 when the sample was placed 2.5 cm away from the focal point.

From the plots in **Figure 4.11**, a pump energy of 50 μJ was chosen as a threshold and the laser fluence was calculated. In consideration of the sample's position, 2.5 cm away from the focal point, the laser fluence threshold at 50 μJ was about 0.071 J/cm^2 . For a pump energy of 35 μJ , laser fluences at various positions between the focus and 10 cm from the focus were plotted in **Figure 4.14**. The dashed line represents the laser fluence threshold (0.07 $\mu\text{J}/\text{cm}^2$), which requires the sample be at least 2 cm away from the focus to prevent optical damage.

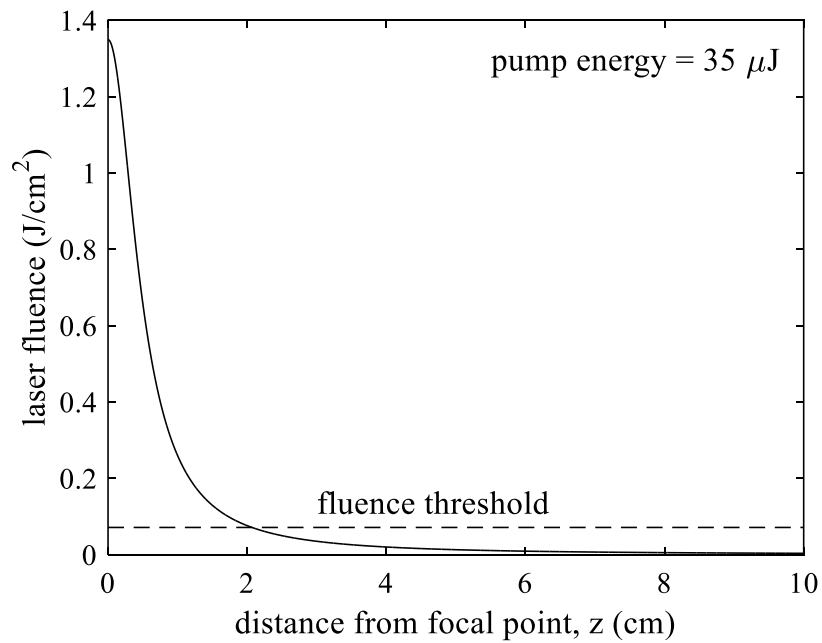


Figure 4.14 Laser fluences at various positions from focal point for pump energy 35 μJ . The laser fluence threshold was 0.071 J/cm^2 , represented by the dashed line in the plot.

4.6 Preliminary SHG Measurement of PSS-coated Gold Nanorods

In the beginning of our study of the plasmonically enhanced SHG response from gold nanorods, PSS-coated nanorods were obtained from the Murphy group at UIUC. CTAB gold nanorods were fabricated using the hydroquinone reduction method and then wrapped with poly(sodium 4-styrenesulfonate) (PSS) to make the surface charge negative. The extinction spectrum of the PSS-coated nanorods is shown in **Figure 3.20a**.

The PSS-coated GNRs were deposited on 3.5 bilayer PAH/PCBS ISAM films by the immersion method. Two different nanorod solutions were prepared for each ISAM film. One was diluted by a factor of 2 and the other was used as-received. After 7 hours of deposition, the samples were rinsed in DI water and blow-dried with N₂ gas. **Figure 4.15** shows the SHG intensity plots of these samples with their corresponding FESEM images above. SHG was measured between 30° and 60° for the nanorod-ISAM hybrid film and bare PAH/PCBS film. The comparison between the SHG signal from PSS-coated nanorods on PCBS film (red solid line) and that from the PCBS film (blue solid line) showed no enhancement in the SHG efficiency. This was possibly due to the low nanorod density as shown in the FESEM images in the figure.

In order to increase the nanorod density, the nanorod solution was diluted further by factors of 4 and 10 to prevent high density jamming. The same type of ISAM films was prepared and vertically immersed in the diluted nanorod solution for 16 hours, which was longer than the previous case of 7 hours. As shown in the FESEM images in **Figure 4.16**, the nanorod density increased significantly. However, the comparison between the SHG signal from PSS-coated nanorods on PCBS film (red solid line) and that from the bare PCBS film (blue solid line) showed that the SHG efficiency decreased slightly with the addition of nanorods.

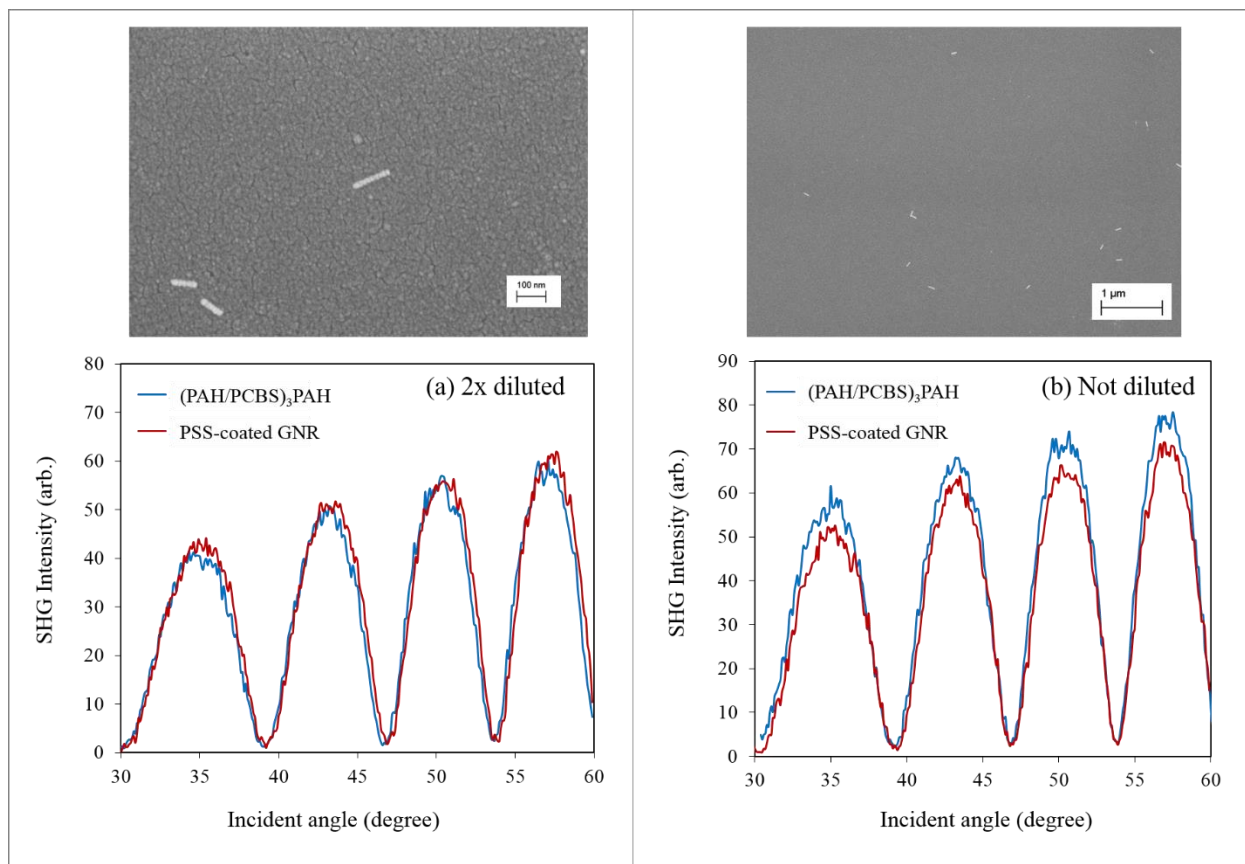


Figure 4.15 SHG intensity of 3.5 bilayer PAH/PCBS films with and without PSS-coated GNRs. The deposition of PSS-coated GNRs were done by immersing the ISAM films vertically into the nanorod solutions. (a) The nanorod solution was diluted by a factor of 2. (b) The nanorod solution was used as-received. The deposition duration was 7 hours. The SHG signals from these samples did not show any enhancement in SHG. The nanorod density was very low as shown in the corresponding FESEM images shown above each plot.

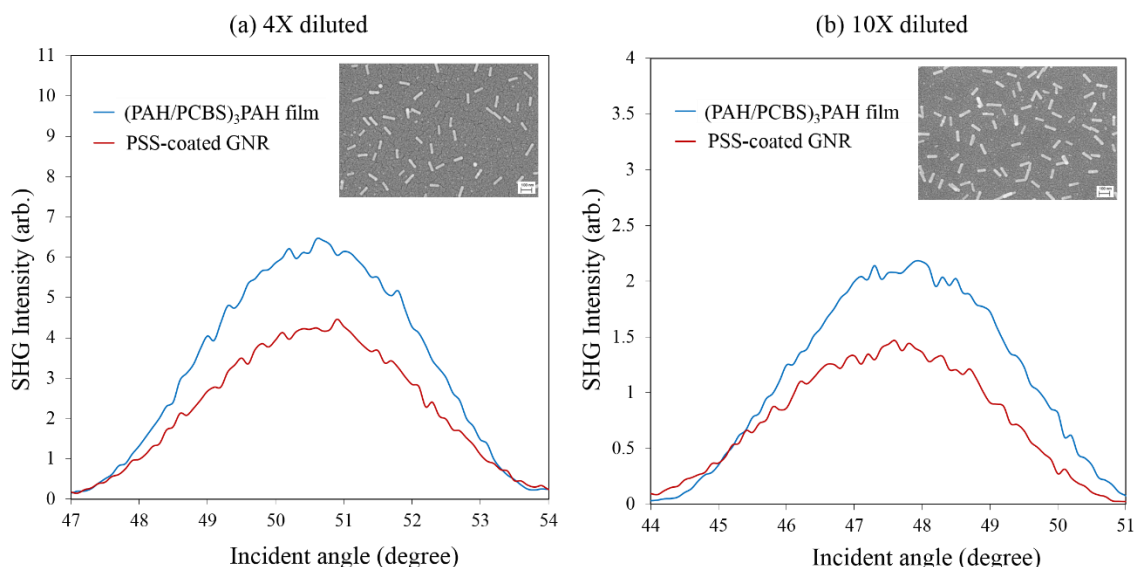


Figure 4.16 SHG intensity plots for PSS-coated GNRs deposited on (PAH/PCBS)₃PAH film with insets showing FESEM images. ISAM films were immersed vertically into the 4X diluted and 10X diluted PSS-coated GNR solutions for 16 hours.

In the next attempt, the PSS-coated nanorods were deposited on 3.5 bilayers of PAH/PCBS ISAM films by immersion and dropcasting. The nanorod solution was diluted by a factor of 20 and the deposition lasted for 16 hours. The nanorod density was higher in the sample prepared by dropcasting than the sample prepared by immersion. Unfortunately, in both cases, the SHG efficiency was decreased with the addition of nanorods as shown in **Figure 4.17**. Therefore, from these early measurements, the variation in nanorod density demonstrated no observable enhancement of the SHG signal.

The pump energy used here was around 0.35 mJ with a collimated Gaussian beam diameter of 10 mm. The fluence at the sample position (about 1 cm from focus) was estimated as 0.79 J/cm² which later turned out to be quite high for the nanorods as discussed in **Section 4.5**. This preliminary study was carried out before we completed the study of the pump energy threshold to avoid optical damage of the nanorods. Although it was suspected that the pump energy

used in this measurement might be high enough to damage the nanorods, it was not seriously considered problematic until the evidence of damage was provided via FESEM images such as the dogbone-shaped nanorods in **Figure 4.13**.

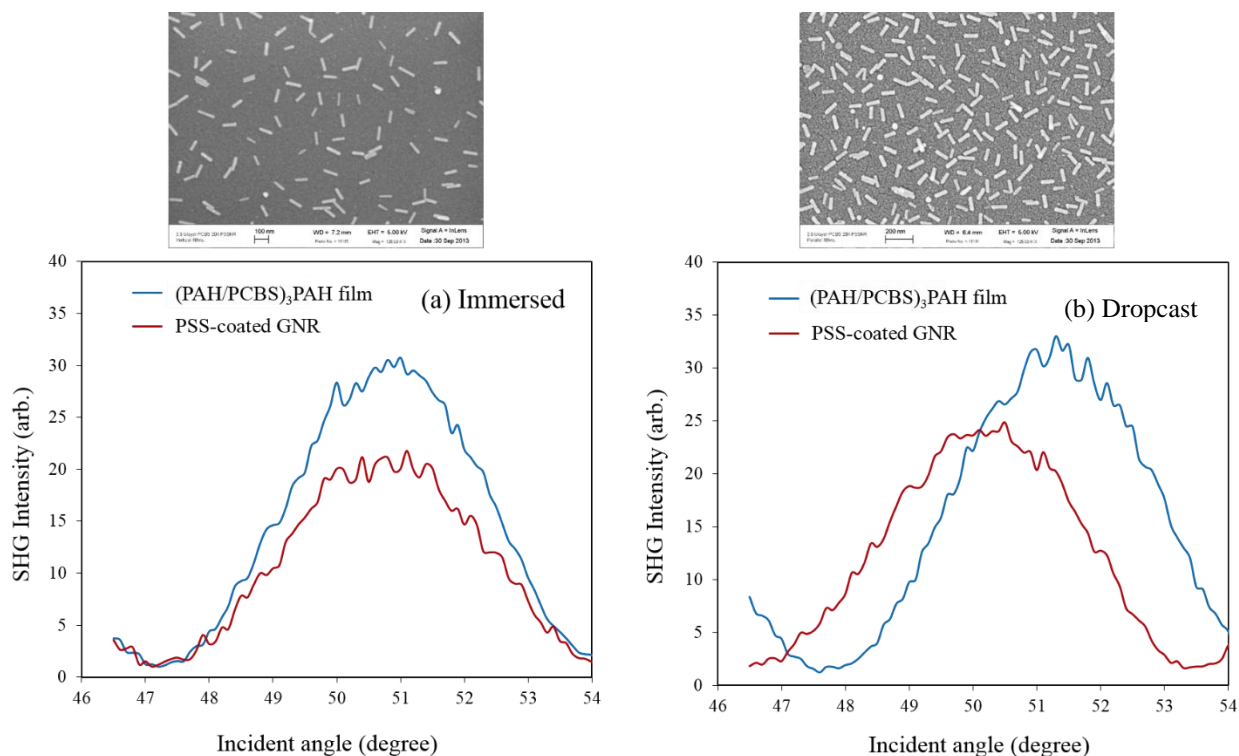


Figure 4.17 SHG intensity from 3.5bi layer PAH/PCBS films with (red solid lines) and without (blue solid lines) PSS-coated GNRs. (a) The substrate was vertically immersed in the nanorod solution, having nanorods on both sides of the substrate. (b) The nanorod solution was dropcast on the film, having nanorods on one side of the substrate.

In consideration of the possibility that the hotspots of field enhancement of the nanorods might not be within the ISAM film due to the large diameter of nanorods (~ 10 nm) compared to the thickness of 3.5 bilayer ISAM films (~ 4 nm), an adjustment was made to the sample fabrication. To ensure the proximity of ISAM film to the nanorod hotspots, three additional bilayers of PAH/PCBS film were added after the deposition of nanorods as illustrated in **Figure 4.18**.

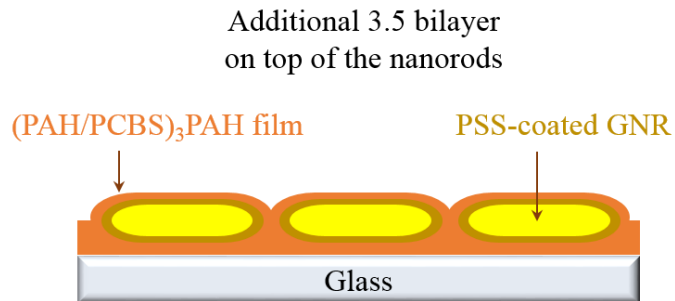


Figure 4.18 Illustration of PSS-coated nanorods deposited on $(\text{PAH/PCBS})_3\text{PAH}$ film with an additional 3.5 bilayer PAH/PCBS film deposited on top.

SHG intensity was measured for NLO ISAM film without PSS-coated nanorods and for nanorods deposited on $(\text{PAH/PCBS})_3\text{PAH}$ film with an additional 3.5 bilayer of (PAH/PCBS) film on top. The pump energy was 0.15 mJ, about half the previous pump energy, to avoid possible optical damage and laser fluence at the sample position (about 1 cm from focus) was 0.33 J/cm^2 . The result is shown in **Figure 4.19** where each SHG intensity was normalized to that of nanorods for comparison. There are two distinctive aspects shown in this plot. One is the enhancement of SHG from the nanorods and another is a phase difference of the fringes between NLO film and nanorods deposited on NLO film. Although the fluence, 0.33 J/cm^2 , was less than the previous measurement, this was still higher than the pump energy damage threshold (0.07 J/cm^2) as discovered later. Nonetheless, the enhanced SHG efficiency may owe to extra polymer layers on top of nanorods. Another aspect of the result was the angular distance between the fringe peaks which was about 2 degrees. This was not an error of manual angular positioning of the sample.

These features were more apparent in the SHG intensity of NLO polymer functionalized nanorods as will be discussed in **Section 4.7**.

Although the result was somewhat promising, our Nd:YAG laser unfortunately stopped working around this time, and we could not move forward with SHG measurement until it was repaired. In the meantime, we decided to pursue a different approach to bring nanorod hotspots closer to NLO polymer, i.e. functionalization of the nanorod surface with PCBS. Therefore, in the next section the results of SHG measurement from PAH/PCBS functionalized nanorods will be presented.

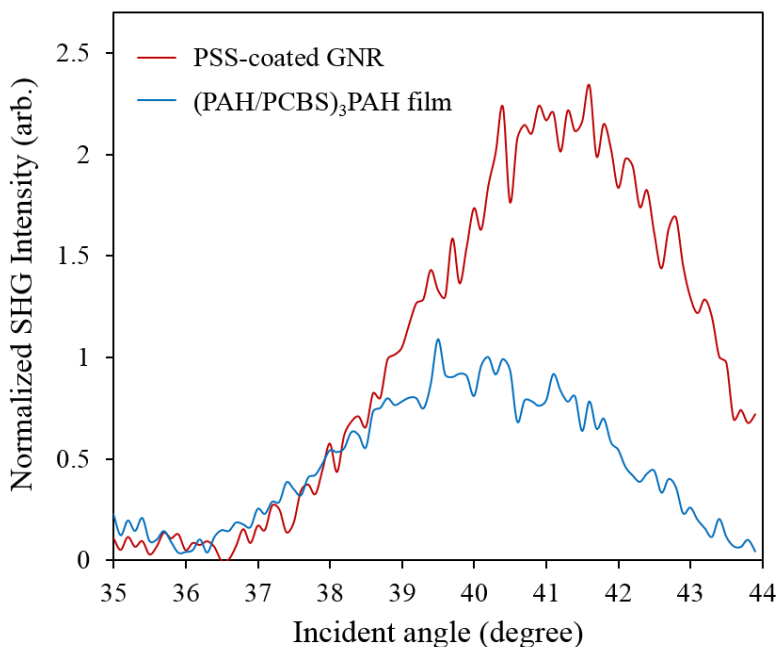


Figure 4.19 Normalized SHG intensity of PSS-coated GNRs deposited on (PAH/PCBS)₃PAH film with an additional 3.5 bilayer (PAH/PCBS) film.

4.7 SHG Measurements of PAH/PCBS Functionalized GNRs on ISAM Film

Second harmonic generation measurements were carried out using the optical setup described in **Section 4.2** for functionalized GNRs deposited on NLO-active or NLO-inactive ISAM films as described in **Table 3.4**. Incident angles were stepped 0.2° between 30° and 70° . The voltage supplying the PMT was 1.2 kV and the gain by the current amplifier was 10000. Since the electrical noise generated by the power supply of the laser was significant, each SHG data point was acquired by ensemble averaging. Typically, the number of data was chosen around 100 for nanorods and 50 for ISAM films. Due to the large number of data points, each measurement took about 10 hours.

After each sample measurement, the background signal was measured for no sample and it was subtracted from the raw data. Then, SHG measurement of the GNR samples were compared with those of the ISAM films alone by normalizing each SHG intensity by its pump energy. In theory, the second harmonic intensity is proportional to the square of pump intensity. Thus, to normalize the SHG intensity, it was divided by the square of the pump intensity as measured from the photodiode and read from oscilloscope channel 1. Since SHG interference fringes are very sensitive to even a slight modification (a few micrometers) of the thickness of the substrate, the comparison was made for SHG intensities measured on the same substrate (microscope slide) but from different spots; one was within the ISAM film and the other was within the functionalized nanorods deposited on the ISAM film.

Initial SHG measurements of functionalized nanorods (PCBS0, PCBS1, PCBS2, and PCBS3 GNRs) deposited on NLO-active (PCBS) and NLO-inactive (PSS) films were first performed before we noticed any optical damage on nanorods due to the high pump energy. Therefore, in this earlier measurement, the pump energy was $150 \mu\text{J}$ and its corresponding fluence was 0.054 J/cm^2 . After completing the pump power threshold study, the pump energy was lowered to $35 \mu\text{J}$ which had a corresponding fluence of 0.012 J/cm^2 for SHG measurement of nanorods. However, for SHG measurement of the bare ISAM films, it was necessary to increase the pump energy to $350 \mu\text{J}$ to obtain measurable SHG signals. Samples were placed 2.5 cm away from the focus to keep the laser fluence below the threshold for nanorods. All measurements were done in darkness to avoid any ambient light entering the PMT.

4.7.1 Laser Warm-up

It is important to warm up the laser so that the pump power is stable during the measurement. **Figure 4.20** shows the pump power reading measured by the photodiode and output to oscilloscope channel 1 over a period of time. The pump intensity oscillated for about 10 minutes in the beginning and then decreased until stabilizing 2 hours after the start. For laser warm-up, the long pulse mode is recommended instead of the Q-switched mode for safety reasons since the pulse peak power is lower for the former. However, in order to record the pump reading, the laser must be triggered by the oscilloscope which is only available in the Q-switched mode.

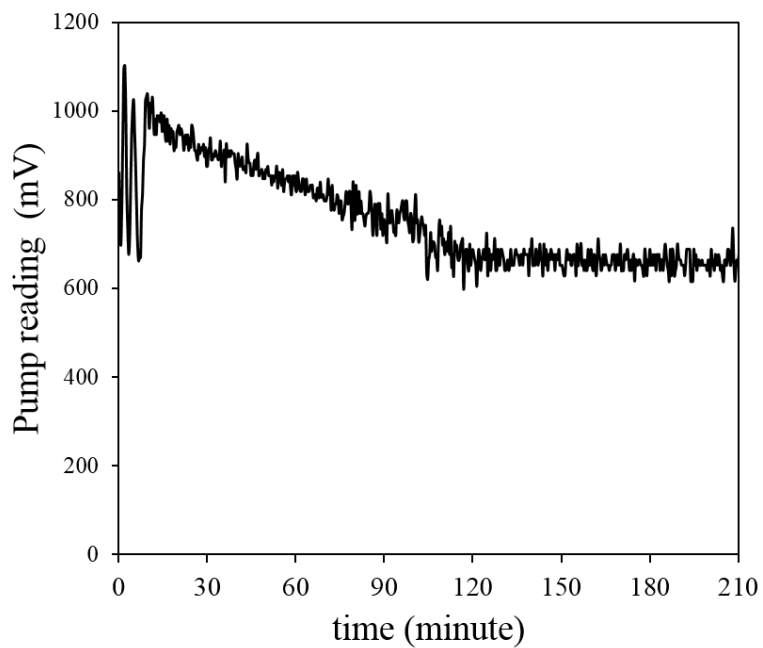


Figure 4.20 Laser pump reading of the photodiode from the oscilloscope over time. It stabilized after 2 hours. It was measured in the sample mode of the oscilloscope.

4.7.2 GNRs on PCBS ISAM Film (Pump Energy: 150 μ J)

Figure 4.21 and **Figure 4.22** display SHG intensities of functionalized nanorods deposited on the NLO-active (PCBS) films. Blue lines represent the SHG intensity from functionalized nanorods deposited on (PAH/PCBS)₃ or (PAH/PCBS)₃PAH films. Orange dashed lines represent SHG intensity from the bare ISAM films. Each plot is normalized to the maximum SHG peak of the corresponding PCBS film for comparison. The pump energy was 150 μ J for both nanorod-ISAM samples and bare ISAM films and samples were 2.5 cm away from the focus.

As can be seen in the upper plot of **Figure 4.21**, SHG signals from the PAH-DTC GNR (PCBS0 GNR) sample was less than (about half) the SHG signals from the (PAH/PCBS)₃ film. This is possibly due to the relatively high fluence, 0.054 J/cm² but more likely due to low nanorod density as revealed in the spectrum in **Figure 3.26** and the FESEM image in **Figure 3.27a**. However, for PCBS1, PCBS2, and PCBS3 GNRs on (PAH/PCBS)₃PAH film, there was small enhancement of the SHG signals from the nanorod samples, which was 7, 2.5, and 1.2 times the SHG signals from the PCBS film. The nanorod densities of PCBS1, PCBS2, and PCBS3 GNRs on (PAH/PCBS)₃PAH films were found in **Table 3.5** as 156.7, 73.6, and 32.1 per μ m², respectively. It should be emphasized that the enhancements observed here are likely lower than maximum possible enhancements with the GNRs since the pump energy was above the damage threshold of the GNRs.

Regarding the angular position of the SHG maxima, there was a noticeable phase shift of SHG peaks between the PCBS1 nanorods and (PAH/PCBS)₃PAH film. For PCBS2 and PCBS3 nanorods on (PAH/PCBS)₃PAH film (shown in **Figure 4.22**), there was a phase shift only between 40° and 65°. The origin of the SHG signal shift was explained by Zdanowicz *et al.*¹¹ in their Maker fringe measurement of multilayer silica-metal nanocomposites. In their study, the SHG signal maxima of one layer of nanocomposite on a substrate were shifted in the same way as in the bottom plot of **Figure 4.21**, and they continued to shift with increasing nanocomposite layers. They suggested that the shift originates from the difference in values of the susceptibility components for the active layers and the bottom surface of the substrate. In the case of functionalized GNRs on NLO film, the shift of the fringe may come from the different values of susceptibility ($\chi_{zzx}^{(2)}$, $\chi_{zzz}^{(2)}$, and $\chi_{xxz}^{(2)}$) between the NLO film coated on GNRs and the NLO film itself.

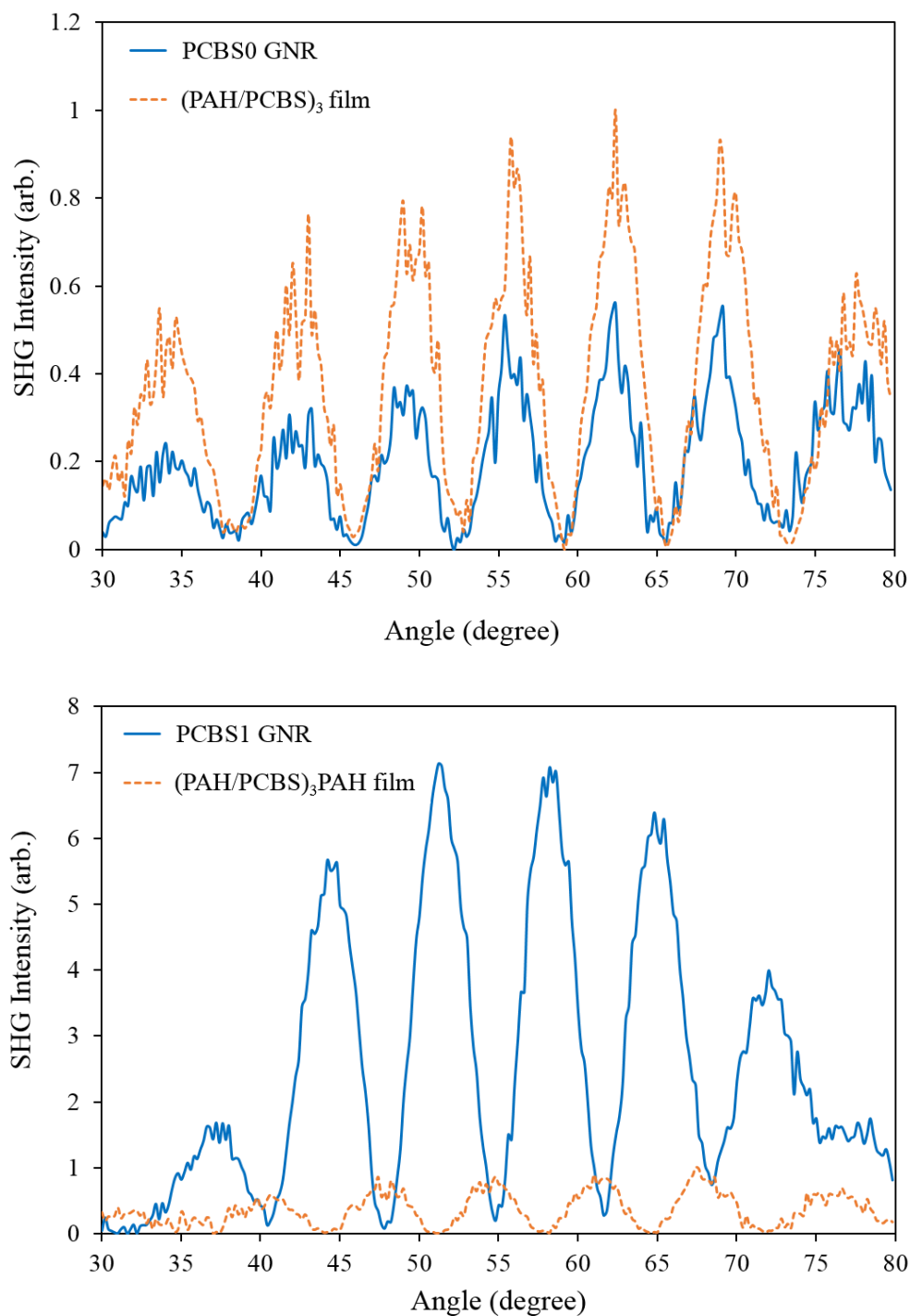


Figure 4.21 Normalized SHG intensity of 3 or 3.5 bilayer PCBS film with and without nanorods (pump energy 150 μ J). (Top) PAH-DTC GNRs (PCBS0 GNRs) deposited on (PAH/PCBS)₃ film. (Bottom) PCBS1 GNRs deposited on (PAH/PCBS)₃PAH film.

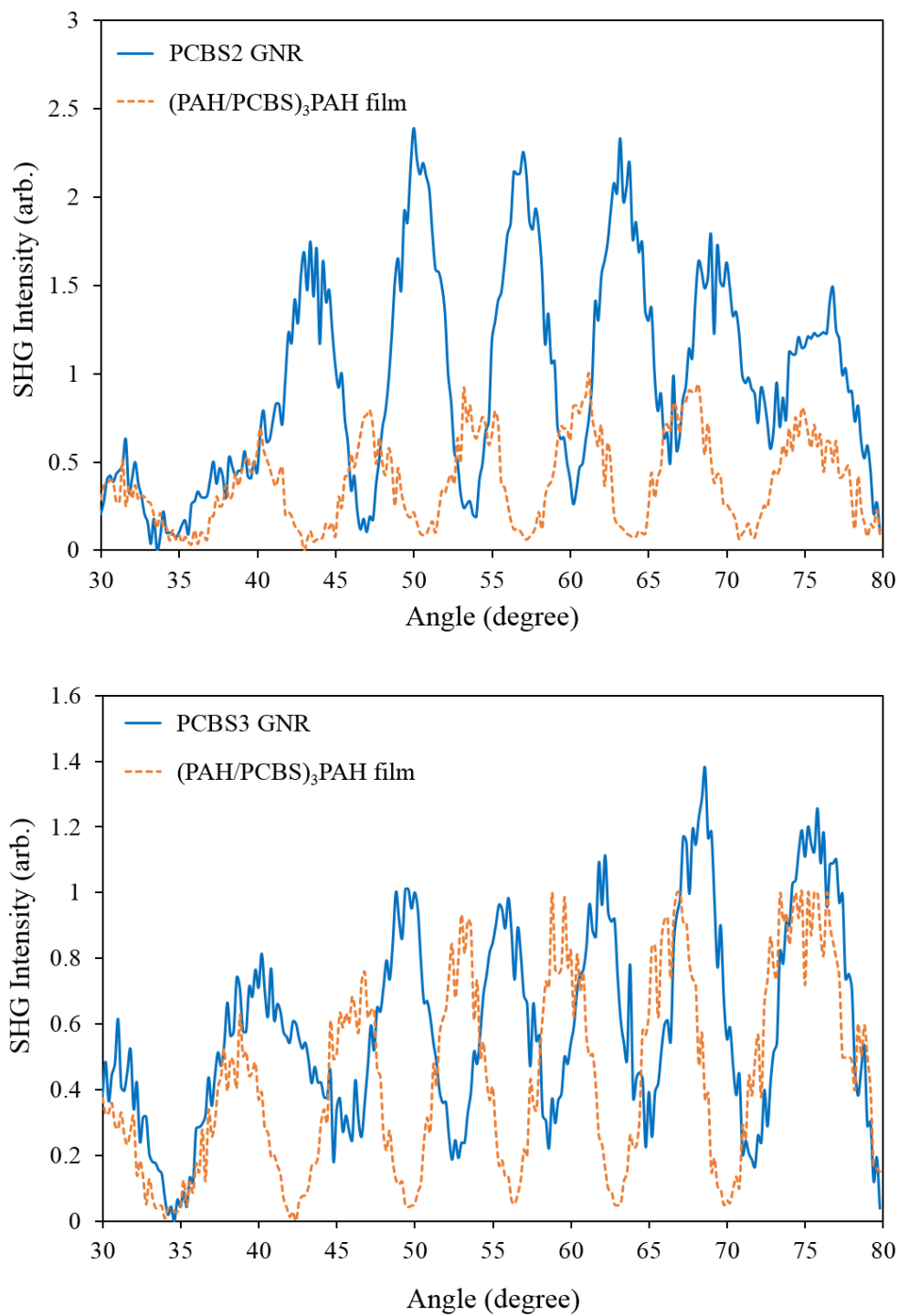


Figure 4.22 Normalized SHG intensity of 3.5 bilayer PAH/PCBS film with and without nanorods (pump energy 150 μ J). (Top) PCBS2 GNRs deposited on (PAH/PCBS)₃PAH film. (Bottom) PCBS3 GNRs deposited on (PAH/PCBS)₃PAH film.

4.7.3 GNRs on PSS ISAM Film (Pump Energy: 150 μ J)

Figure 4.23 and **Figure 4.24** show SHG intensities of functionalized nanorods (PCBS0, PCBS1, PCBS2, and PCBS3 GNRs) deposited on the NLO-inactive (PSS) films. Blue lines represent the SHG intensity from functionalized nanorods deposited on (PAH/PSS)₃ or (PAH/PSS)₃PAH films. Brown dashed lines represent the PMT signal for the SHG measurement from the PSS ISAM films.

PSS is a NLO-inactive polymer and cannot possess a bulk $\chi^{(2)}$. However, the second-order optical nonlinearity exists near the interface in a thin region between air and polymer film because the inversion symmetry is broken at the interface, and thus a weak SH wave can be emitted from this thin region.⁷ The SHG intensity at this surface layer depends on the structural properties of the surface and the presence of molecules on the surface. In order to observe the SHG at the interface, a high fundamental intensity is required. The pump energy used here was 150 μ J for PSS films and was not high enough to acquire detectable SHG signals from the bare PSS film. Therefore, the SHG signals from the PSS film showed no interference fringes in both **Figure 4.23** and **Figure 4.24**.

It is likely that the SHG signals from the PSS films were below the noise floor of the PMT. Therefore, the brown dashed lines in these plots represent the cumulative noise of the system. The noise was post-averaged over the time of the total measurement period. Using this average noise, the maximum signal-to-noise ratios (SNR) were 19, 24, 28, and 14 for PCBS0, PCBS1, PCBS2, and PCBS3, respectively. If the noise floor could be sufficiently suppressed to reveal the SHG signal from the PSS film, then it is expected that the relative enhancement from the PCBS-functionalized GNRs would be much greater than the observed SNRs.

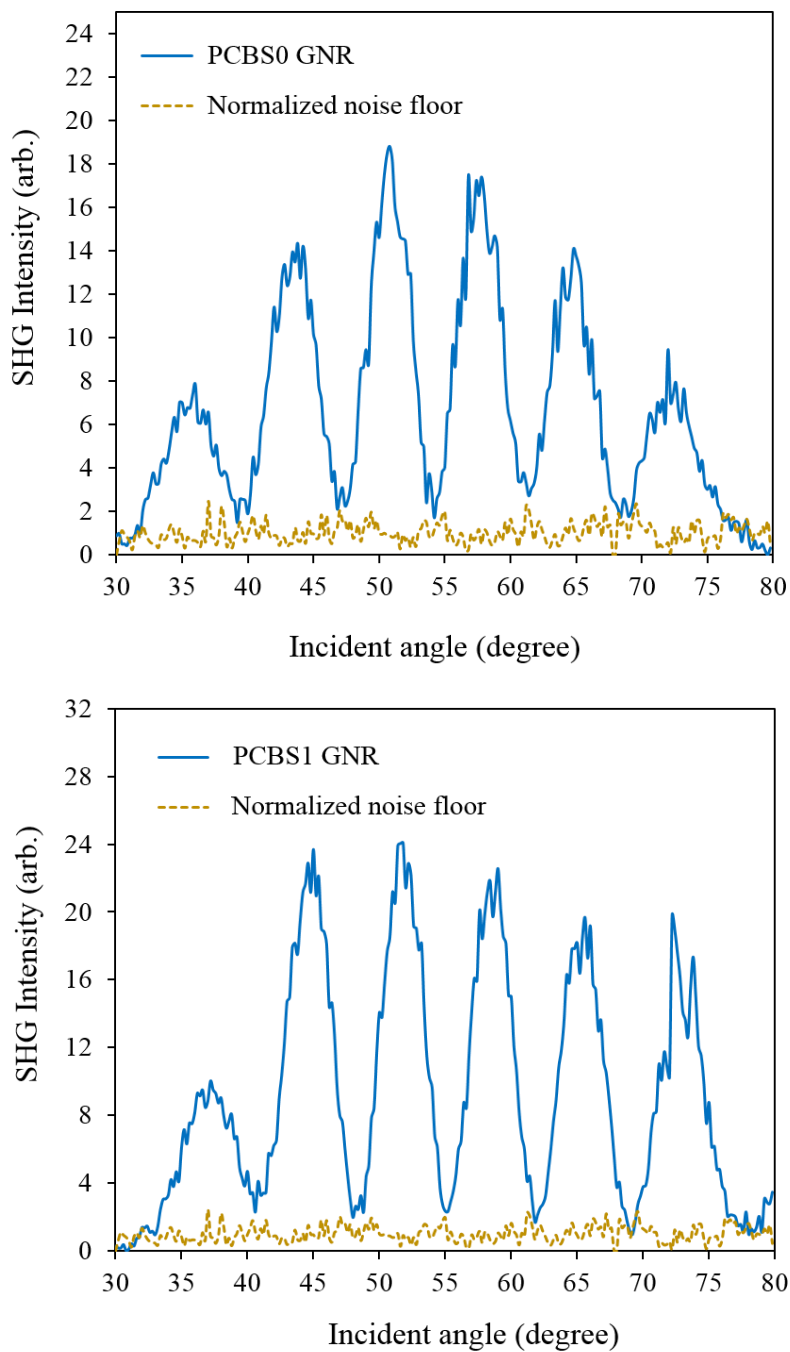


Figure 4.23 Signal-to-noise ratio for the SHG intensity of 3 or 3.5 bilayer PAH/PSS film with nanorods (pump energy 150 μJ). (Top) PAH-DTC GNRs (PCBS0 GNRs) deposited on $(\text{PAH/PSS})_3$ film. (Bottom) PCBS1 GNRs deposited on $(\text{PAH/PSS})_3\text{PAH}$ film.

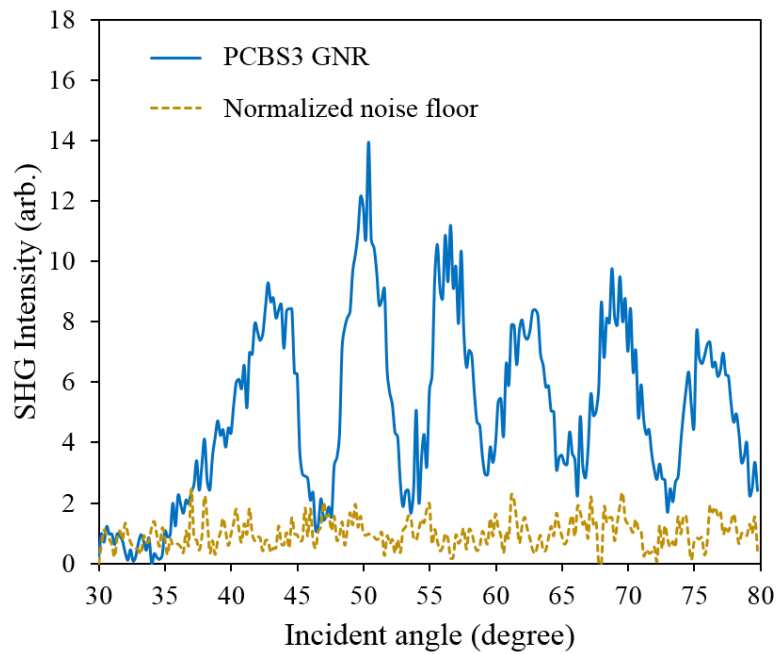
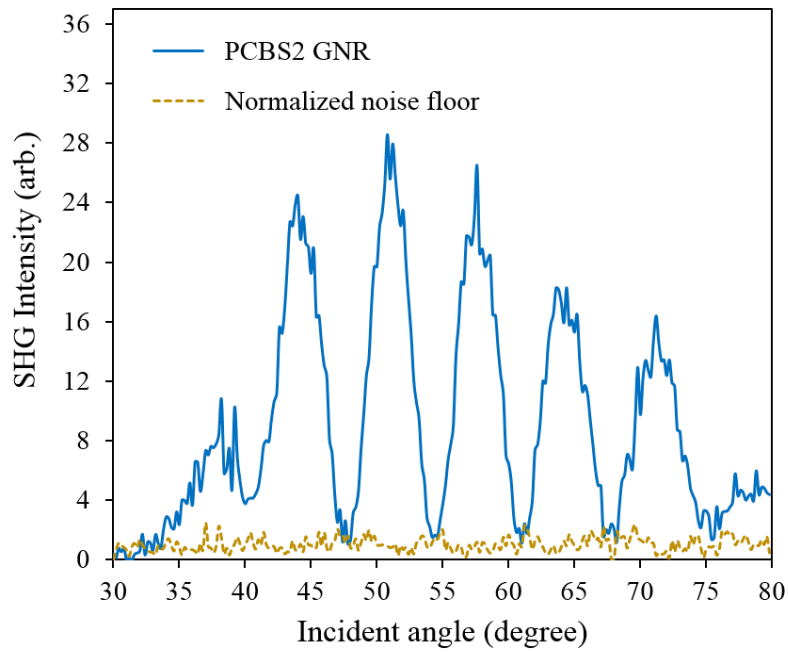


Figure 4.24 Signal-to-noise ratio for the SHG intensity of 3.5 bilayer PAH/PSS film with nanorods (pump energy 150 μJ). (Top) PCBS2 GNRs deposited on $(\text{PAH/PSS})_3\text{PAH}$ film. (Bottom) PCBS3 GNRs deposited on $(\text{PAH/PSS})_3\text{PAH}$ film.

4.7.4 GNRs on PCBS ISAM Film (Pump Energy: 35 μJ)

After the pump energy damage threshold for GNR samples was determined, the exact same samples were tested by SHG measurements at lower pump energy. For gold nanorods, it was 35 μJ for a fluence of 0.012 J/cm^2 . For ISAM films, the SHG signals are not visible at such a low energy, and thus it was chosen 10 times greater than that for the gold nanorod samples. This measurement was done at different spots on the same sample to avoid any damaged spots from the previous measurement at 150 μJ pump energy.

Due to the low nanorod density on PCBS0 GNRs on $(\text{PAH}/\text{PCBS})_3$ film, at such a low pump energy, the SHG signal was too small to detect above the electrical noise. The plot on top in **Figure 4.25** shows the signal collected from the PMT when SHG measurement was attempted on the sample containing PCBS0 GNRs on a 3 bilayer PAH/PCBS film. Since the nanorod density was very low, it is unlikely that there is any SHG signal from the nanorods. In addition, pump energy of 35 μJ was not sufficient to detect any SHG from the 3 bilayer PAH/PCBS film. To be able to measure SHG power from this type of sample, it is necessary to increase the density of nanorods on the film. There are two possible ways to do this. One is to increase the density of the PCBS0 GNR solution to increase the deposition rate. But it was revealed in **Section 3.5** that when the nanoparticle solution is too dense, the jamming effect prevents particles to deposit on a surface at high density. Therefore, another way is to increase the deposition time without changing the concentration of the solution. However, in numerous cases, the PAH-DTC GNRs solution was the least stable among other types of functionalized GNR solutions (PCBS1, PCBS2, and PCBS3 GNR solutions), such that the nanorods started to aggregate after a day or so. Consequently, it is best to find a way to stabilize the nanorod solution.

For PCBS1 GNRs deposited on $(\text{PAH}/\text{PCBS})_3\text{PAH}$ film, the SHG enhancement was much more promising. The bottom plot in **Figure 4.25** displays SHG intensities from PCBS1 GNRs (blue solid line) and from the bare 3.5 bilayer PAH/PCBS film (orange dashed line). All SHG signals were normalized by the squared pump intensity. This allows a comparison of how much SHG the two samples would generate if they had the same pump energy. The plots were also normalized to the average of two adjacent SHG fringe peaks (around 47° and 55°) of the 3.5 bilayer PAH/PCBS film for comparison. The results show that the enhancement of the SHG efficiency by

the PCBS1 GNRs is about 100 times. Similar to the case when the pump energy was 150 μJ (the bottom plot of **Figure 4.21**), the SHG fringe of the PCBS1 GNR sample here shifted 180° from the SHG fringe of the 3.5 bilayer PAH/PCBS film.

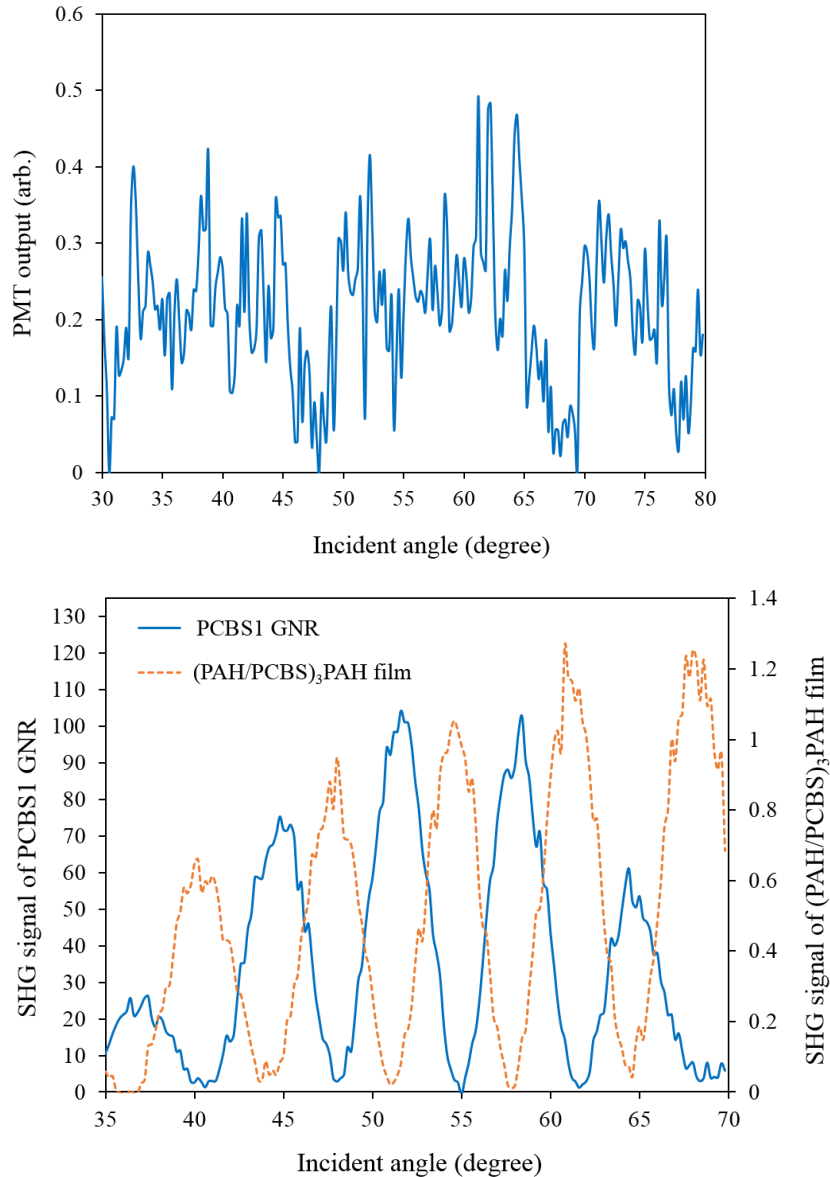


Figure 4.25 (Top) Signal from the PMT when SHG measurement was conducted on PAH-DTC GNRs on $(\text{PAH}/\text{PCBS})_3$ film. The post-measurement FESEM image in **Figure 3.27(a)** showed this sample's GNR density was extremely low, so the displayed signal is most likely random noise. (Bottom) Normalized SHG intensity of 3 bilayer PCBS film with and without nanorods (pump energy 35 μJ for nanorods, 350 μJ for bare film).

Similar to the case of PCBS1 GNRs on 3.5 bilayer PAH/PCBS film, the plots shown in **Figure 4.26** were normalized by the average of two adjacent SHG fringe peaks for the (PAH/PCBS)₃PAH film as well as to the square of the pump energy. As before, the blue solid line represents the SHG signal from the nanorod sample and the orange dashed line represents the SHG signal from the bare PAH/PCBS film. From the above plot, the peak angles of the SHG intensity from the (PAH/PCBS)₃PAH film was around 47° and 54° and from the below plot, they were around 46° and 53°. The SHG efficiency was enhanced 65 and 8 times from the PCBS2 GNRs and the PCBS3 GNRs, respectively. Likewise, the 180° fringe shift between the nanorod sample and bare film was also observed in accordance with the previous case shown in **Figure 4.25**.

To summarize, the SHG efficiency was enhanced by 100, 65, and 8 times from PCBS1, PCBS2, and PCBS3 GNRs on (PAH/PCBS)₃PAH film. Unfortunately, it was not possible to detect any measureable SHG signal from PAH-DTC coated GNRs on (PAH/PCBS)₃ film due to its extremely low nanorod density. From the SHG intensity plots of the other samples, a phase shift was observed between the SHG fringe patterns from the nanorods and the ISAM film. Also, the envelope of the SHG fringe of the nanorods was different from that of the ISAM film. As suggested by Zdanovicz *et al.*¹¹ this may be due to the different values of susceptibility components, $\chi_{xxz}^{(2)}$, $\chi_{zxx}^{(2)}$, and $\chi_{zzz}^{(2)}$ for the PCBS functionalized nanorod sample and bare PCBS film.

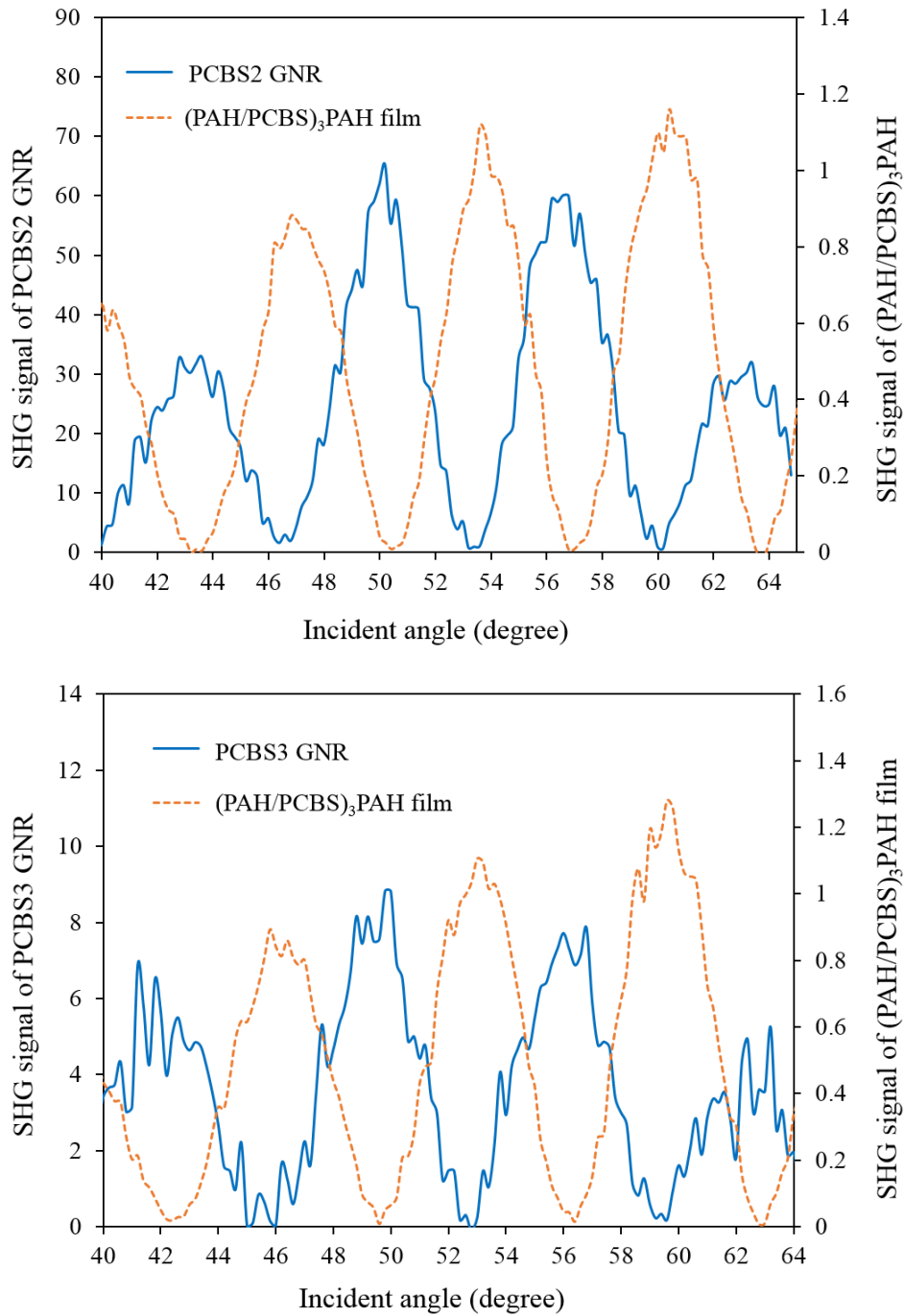


Figure 4.26 Normalized SHG intensity of 3.5 bilayer PCBS film with (left axis) and without (right axis) nanorods (pump energy 35 μJ for nanorods, 350 μJ for film). (Top) PCBS2 GNRs deposited on $(\text{PAH}/\text{PCBS})_3\text{PAH}$ film. (Bottom) PCBS3 GNRs deposited on $(\text{PAH}/\text{PCBS})_3\text{PAH}$ film.

4.7.5 GNRs on PSS ISAM Film (Pump Energy: 35 μ J)

Next, SHG was measured from PCBS0 GNRs on (PAH/PSS)₃ film and PCBS1, PCBS2, and PCBS3 GNRs on (PAH/PSS)₃PAH films. The measured SHG intensities are shown in **Figure 4.27** and **Figure 4.28**. Again, the SHG intensities were normalized by the average of two adjacent SHG fringe peaks for 3 or 3.5 bilayer PAH/PSS film and the square of the pump power. The SHG signal from the nanorod samples is the blue solid line and the SHG signal from the (PAH/PSS)₃ or (PAH/PSS)₃PAH films is the brown dashed line. In most cases, the maximum SHG fringe of the nanorod samples was around 50°, and thus the SHG fringe maxima of the PAH/PSS film were chosen from left and right of the maximum peak of nanorod samples around 50°.

Regarding the interference fringes from the nanorods (blue solid lines), a similar fringe envelope and phase shift were observed. These characteristics were consistent with the interference fringes from nanorods on PAH/PCBS film shown in **Figure 4.25** and **Figure 4.26**. However, the SHG efficiency from gold nanorods on PAH/PSS film was relatively greater than in the case of PAH/PCBS film because the SHG contribution from PAH/PSS film was minute compared to that from PAH/PCBS film. For PCBS0, PCBS1, PCBS2, and PCBS3 GNRs on 3 or 3.5 bilayer PAH/PSS film, the enhancement factors were about 450, 600, 500, and 220, respectively.

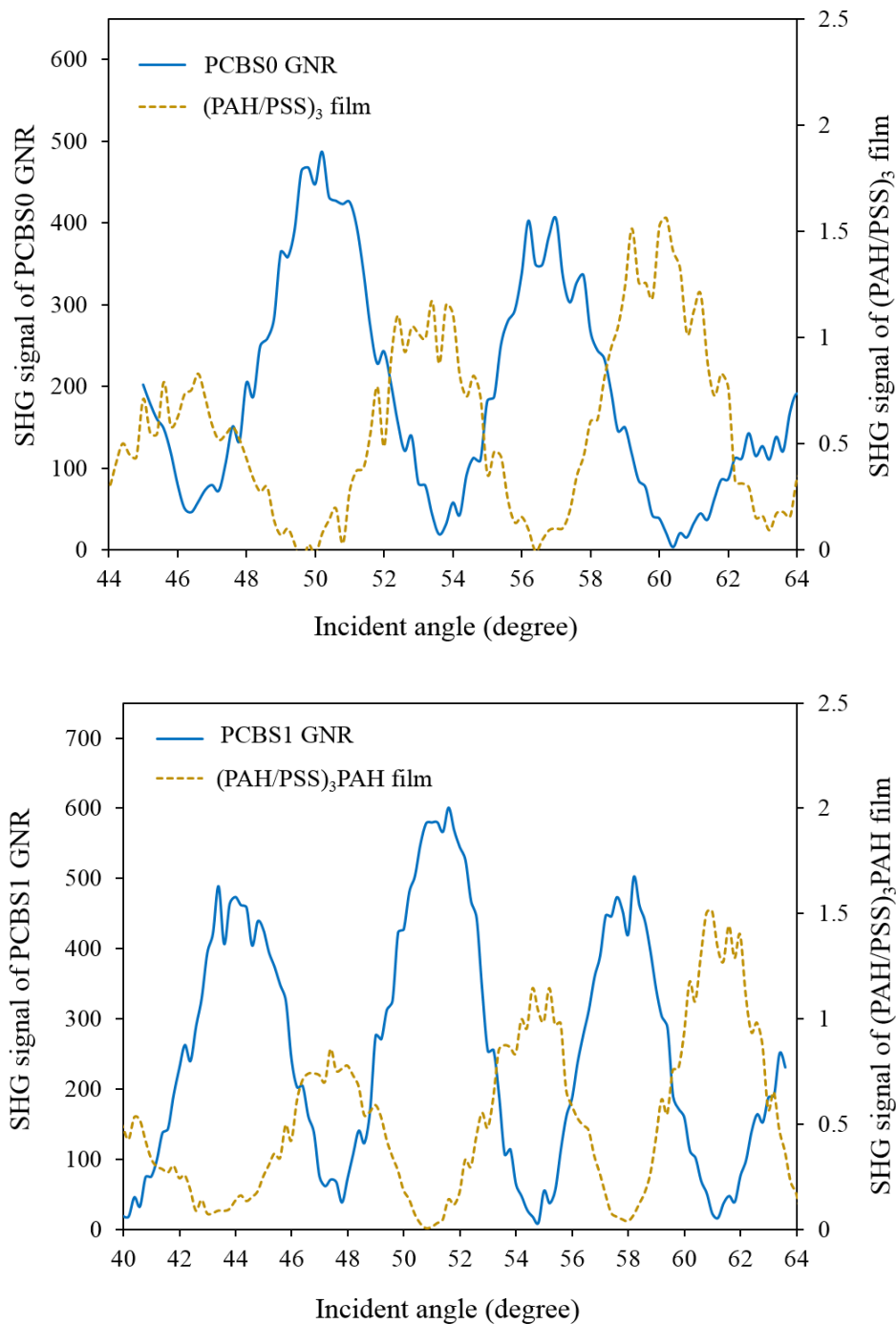


Figure 4.27 Normalized SHG intensity of 3 or 3.5 bilayer PCBS film with (left axis) and without (right axis) nanorods (pump energy 35 μJ for nanorods, 350 μJ for film). (Top) PAH-DTC GNRs (PCBS0 GNRs) deposited on (PAH/PSS)₃ film. (Bottom) PCBS1 GNRs deposited on (PAH/PSS)₃PAH film.

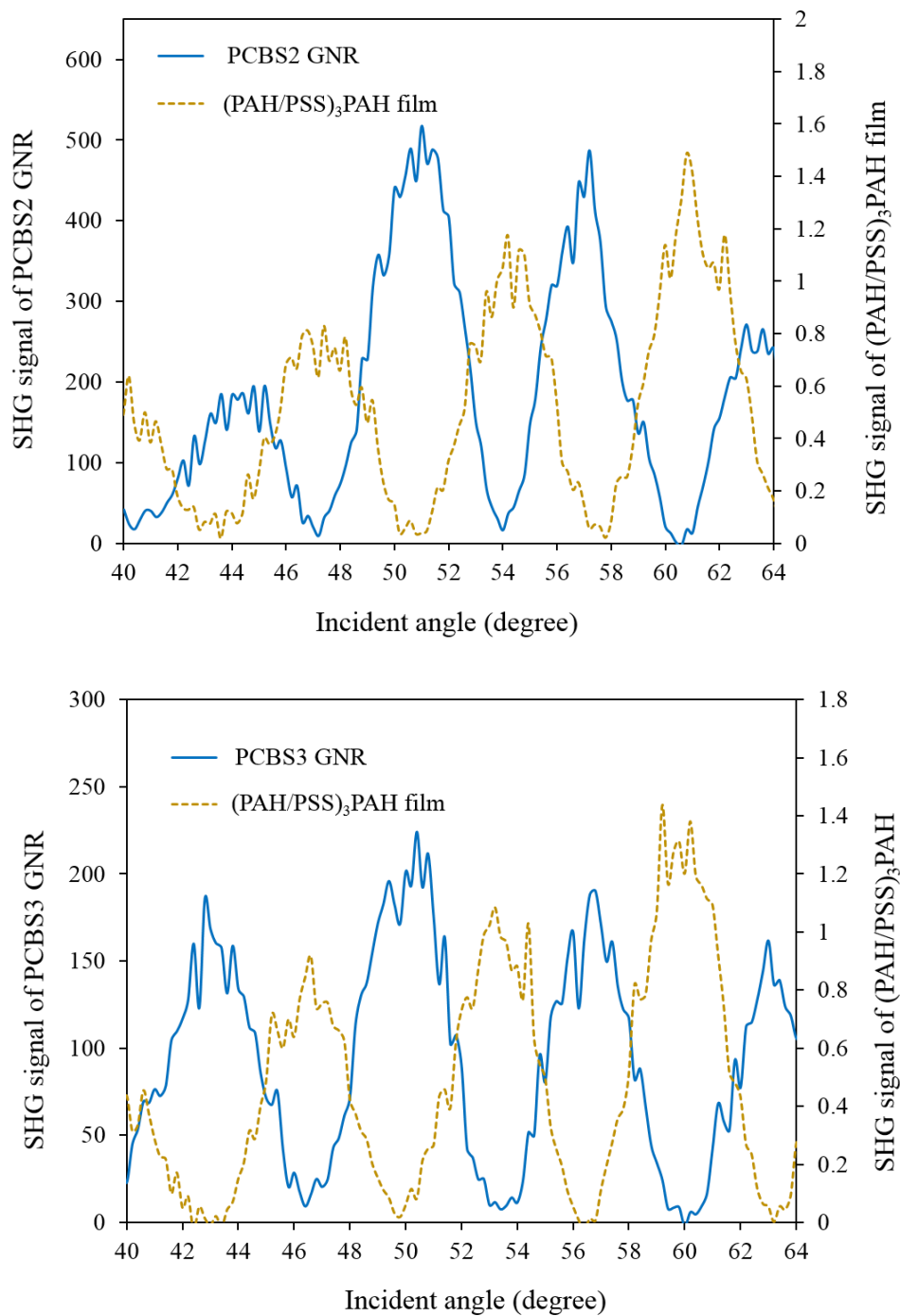


Figure 4.28 Normalized SHG intensity of 3.5 bilayer PCBS film with (left axis) and without (right axis) nanorods (pump energy 35 μJ for nanorods, 350 μJ for film). (Top) PCBS2 GNRs deposited on (PAH/PSS)₃PAH film. (Bottom) PCBS3 GNRs deposited on (PAH/PSS)₃PAH film.

4.7.6 Summary of SHG Measurement

The enhancement of SHG from functionalized nanorods on PAH/PCBS or PAH/PSS film are summarized in **Table 4.1**. The enhancement factors are calculated by normalizing the SHG intensity from gold nanorod samples to the squared pump intensity. According to this data set, functionalized gold nanorods deposited on 3.5 bilayer PAH/PSS film produced greater enhancements in all cases, except for the case of PCBS0 GNRs where a comparison could not be made. This is because neither PCBS-functionalized nanorod sample nor the 3.5 bilayer PAH/PCBS film could generate SHG. The enhancement by the addition of nanorods to PCBS films is smaller than that for PSS films. This is because PCBS films generate quite a bit more SHG than PSS films since PSS is NLO-inactive. However, in all cases, the enhancement by adding PCBS-coated GNRs is substantial.

Table 4.1 Summary of SHG enhancement from functionazlied gold nanorods

Functionalized GNRs	Normalized SHG signal from GNRs ($I_{\text{PCBS}\# \text{ GNR}}/I_{\text{ISAM film}}$), where # = 1,2, or 3	
	on (PAH/PCBS) ₃ PAH film	on (PAH/PSS) ₃ PAH film
PCBS0	Not detectable (low GNR density)	450
PCBS1	105	600
PCBS2	65	500
PCBS3	8	220

Because the nanorod density on the surfaces showed significant variation as determined by extinction and FESEM imaging, a comparison of the enhancement should account for this as well. Since the SHG increases as the square of the nanorod density, the SHG signals from PCBS1, PCBS2, and PCBS3 GNRs on each ISAM film were normalized by the square of the nanorod density in addition to the square of the pump energy.

The multilayer factor $\alpha_{\#}$ is defined by

$$\alpha_{\#} = \left(\frac{I_{\text{PCBS}\# \text{ GNR}}}{I_{\text{PCBS1 GNR}}} \right), \text{ where } \# = 1, 2, \text{ and } 3, \quad (4.4)$$

and indicates the ratio of the SHG enhancement of additional PCBS layers on the nanorods over that of the PCBS1 GNRs. For instance, the multilayer factor α_2 (where $\# = 2$) is the ratio of the SHG of the PCBS2 GNRs to the PCBS1 GNRs. **Table 4.2** summarizes the SHG multilayer factor, $\alpha_{\#}$, of the PCBS-functionalized GNRs on 3.5 bilayer PAH/PCBS or PAH/PSS film, normalized to that of PCBS1 GNRs on either film.

Table 4.2 SHG multilayer factor normalized by the nanorod density

Functionalized GNRs	SHG enhancement, $\alpha_{\#} = \left(\frac{I_{\text{PCBS}\# \text{ GNR}}}{I_{\text{PCBS1 GNR}}} \right)$ and $\# = 1, 2, \text{ or } 3$	
	on (PAH/PCBS) ₃ PAH film	on (PAH/PSS) ₃ PAH film
PCBS1	1	1
PCBS2	3.4	2.2
PCBS3	8	5.4

Figure 4.29a shows the SHG multilayer factor, α , of the PCBS-functionalized GNRs on (PAH/PCBS)₃PAH films. **Figure 4.29b** shows the fitted SHG signals between 47° and 53° using a sum-of-sines fitting in gray solid lines. For the PCBS-functionalized GNRs on 3.5 bilayer PAH/PCBS films, α_2 and α_3 were 3.4 and 8, respectively.

Figure 4.30a shows the SHG multilayer factor, α , of the PCBS-functionalized GNRs on (PAH/PSS)₃PAH films. **Figure 4.30b** shows the fitted SHG signals between 48° and 53° using a sum-of-sines fitting in gray solid lines. For the PCBS-functionalized GNRs on 3.5 bilayer PAH/PSS films, α_2 and α_3 were 2.2 and 5.4, respectively.

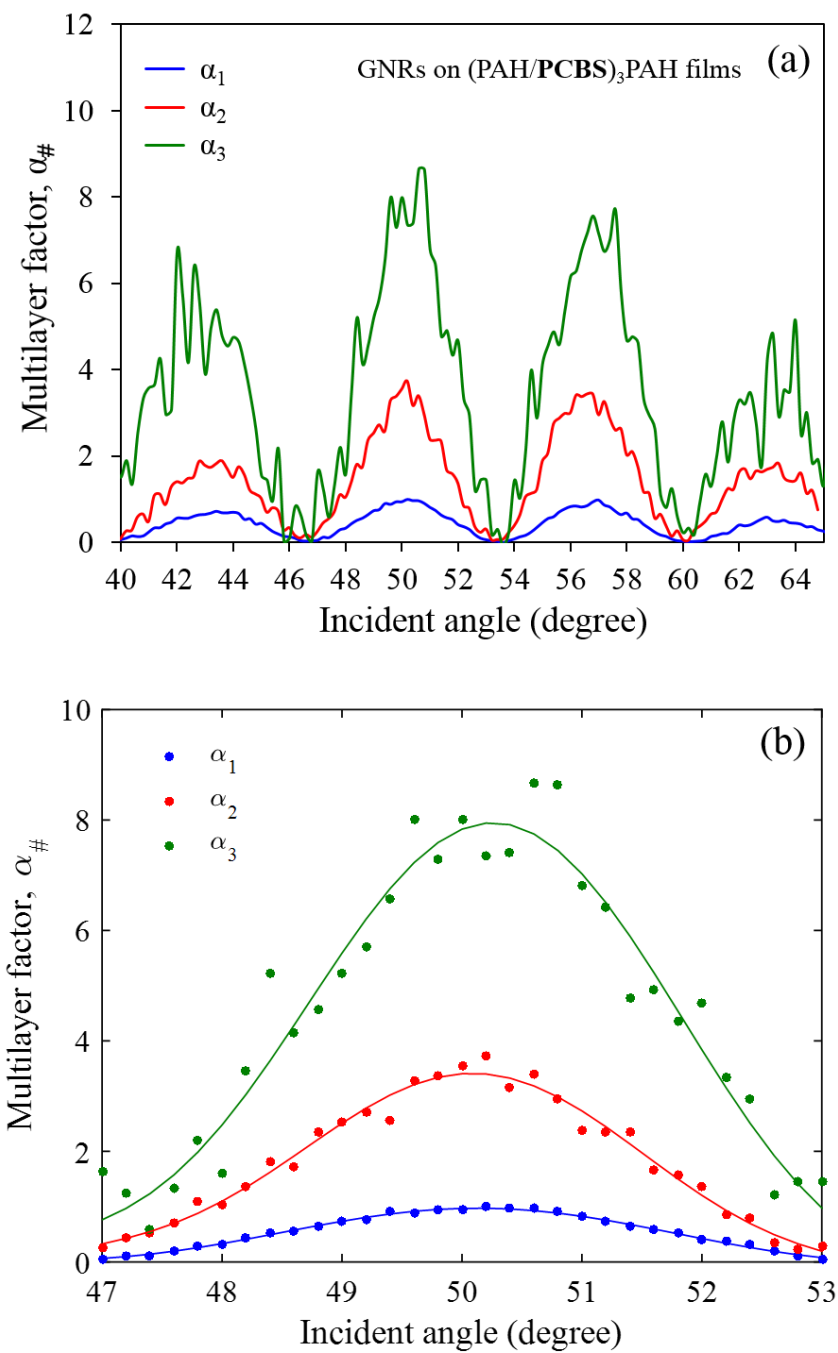


Figure 4.29 SHG intensity of PCBS-functionalized GNRs on 3.5 bilayer PAH/PCBS films. Plot (a) shows the SHG signals from PCBS1, PCBS2, and PCBS3 GNRs on PCBS films, normalized by both square of the pump energy and the nanorod density. Plot (b) shows the SHG data between 47° and 53° with a sum-of-sines fitting in solid lines.

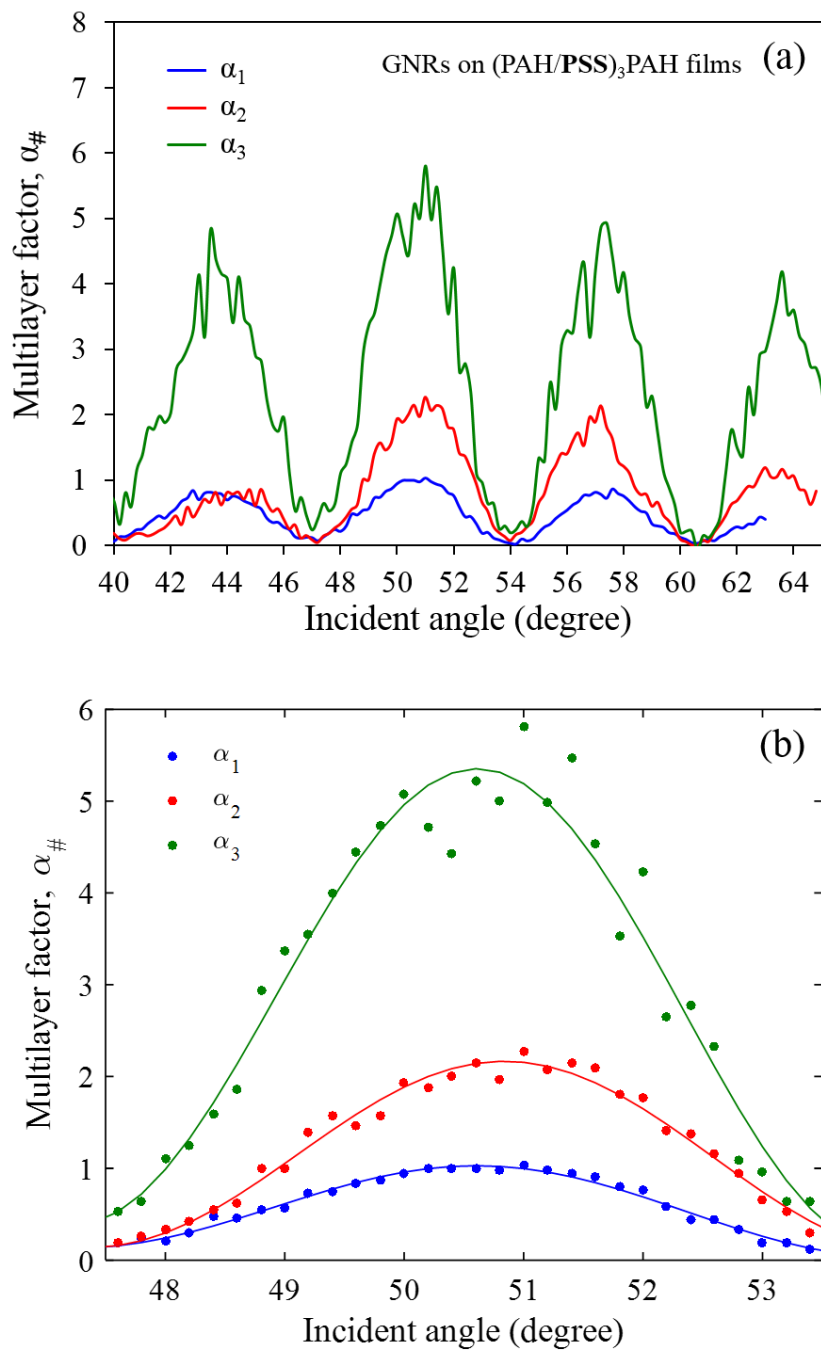


Figure 4.30 SHG intensity of PCBS-functionalized GNRs on 3.5 bilayer PAH/PSS films. Plot (a) shows the SHG signals from PCBS1, PCBS2, and PCBS3 GNRs on PSS films, normalized by both square of the pump energy and the nanorod density. Plot (b) shows the SHG data between 48° and 53° with a sum-of-sines fitting in solid lines.

Table 4.3 summarizes the SHG enhancement factors for the PCBS-functionalized GNRs on (PAH/PCBS)₃PAH or (PAH/PSS)₃PAH films normalized by nanorod density. In other words, the SHG enhancement here is calculated assuming the nanorod densities of PCBS2, and PCBS3 GNRs on either PCBS or PSS ISAM films are equal to that of PCBS1 GNRs on the same type of ISAM films. The subscript of the SHG intensity of the functionalized GNRs on ISAM films, $I_{\text{PCBS}\# \text{ GNR}}$, indicates the number of PCBS layers on the nanorod. Since the enhancement factor of the PCBS1 GNRs on 3.5 bilayer PAH/PCBS film was 105, the SHG enhancement from the PCBS2 and PCBS3 GNRs on 3.5 bilayer PAH/PCBS film were calculated to be 357 and 840, respectively,

Table 4.3 SHG enhancement comparison from functionalized gold nanorods.

Functionalized GNRs	SHG enhancement, $\alpha_{\#} \cdot \left(\frac{I_{\text{PCBS}\# \text{ GNR}}}{I_{\text{ISAM film}}} \right)$, where $\alpha_{\#} = \left(\frac{I_{\text{PCBS}\# \text{ GNR}}}{I_{\text{PCBS1 GNR}}} \right)$ and # = 1,2, or 3	
	on (PAH/PCBS) ₃ PAH film	on (PAH/PSS) ₃ PAH film
PCBS1	105	600
PCBS2	357	1320
PCBS3	840	3240

In order to determine the SHG contribution from the ISAM film, the SHG signals from the PCBS-functionalized GNRs on 3.5 bilayer PAH/PCBS were compared to those on 3.5 bilayer PAH/PSS films. Each SHG intensity was normalized by the square of the pump energy and the square of the nanorod density obtained from the FESEM images. For comparison, they were normalized to the maximum intensity of PCBS1 GNRs on (PAH/PSS)₃PAH film around 50° and fitted using a sum-of-sines as shown in **Figure 4.31**. The result is summarized in **Table 4.4**. The SHG signals from the PCBS-functionalized GNRs on (PAH/PCBS)₃PAH films samples showed larger values compared to those on (PAH/PSS)₃PAH films due to the SHG contribution from the ISAM film. These results indicate that in addition the large SHG from the ISAM film that is wrapped around the GNRs, there is also a contribution from the ISAM film that was deposited directly onto the substrate and which is likely also enhanced by the plasmonic field. The SHG

signals from the bare PCBS film were compared to that from the bare PSS film in **Figure 4.32**. The SHG signals from both PCBS and PSS films were normalized to the maximum SHG intensity from the bare PSS film around 55°. The SHG from the PCBS film was about 10 times greater than that from the PSS film.

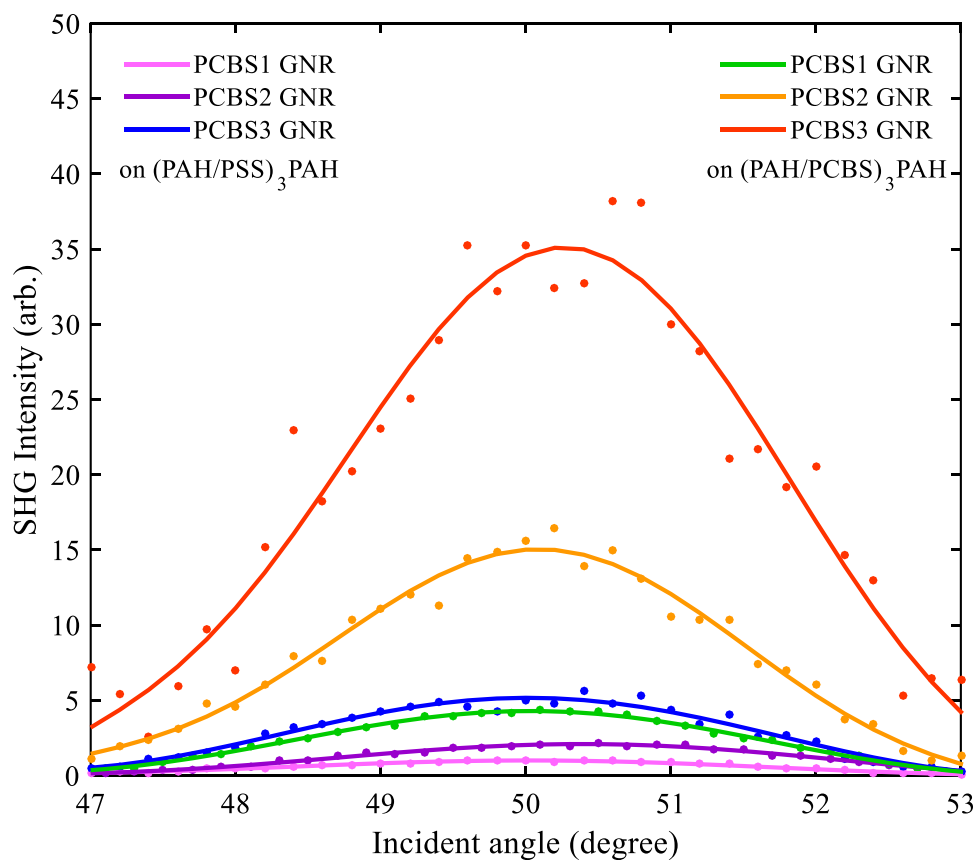


Figure 4.31 SHG intensity of PCBS-functionalized GNRs on (PAH/PSS)₃PAH and (PAH/PCBS)₃PAH films. The SHG signals from each sample was normalized to the SHG signal from PCBS1 GNR on (PAH/PSS)₃PAH film.

Table 4.4 Comparison of the SHG intensity from the PCBS-functionalized GNRs on ISAM films.

GNRs	PCBS1	PCBS2	PCBS3	PCBS1	PCBS2	PCBS3
on ISAM film	(PAH/PSS) ₃ PAH			(PAH/PCBS) ₃ PAH		
$\frac{I_{PCBS\#onISAMfilm}}{I_{PCBS1onPSSfilm}}$	1	2.1	5.2	4.3	15	35.1

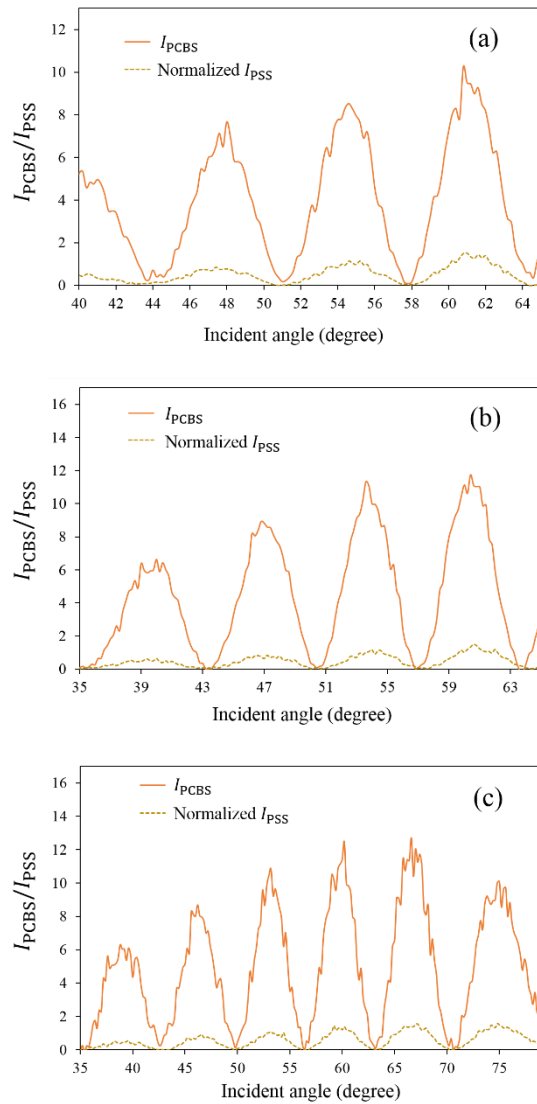


Figure 4.32 SHG intensity of the bare PCBS films compared to the SHG of the bare PSS films. The samples were (a) PCBS1 GNRs, (b) PCBS2 GNRs, and (c) PCBS3 GNRs, on PCBS films (orange solid lines) and on PSS films (brown dashed lines). The SHG signals were measured from the sample area of each ISAM film without the GNRs.

4.8 Polarization Dependent SHG Measurement

To further investigate the SHG fringes generated from functionalized nanorods deposited on ISAM films, polarization dependent SHG measurements were conducted by controlling the polarization of the incoming fundamental light and the second-harmonic light entering the PMT. The polarization of fundamental light was adjusted by the polarizer (labeled as P1 in **Figure 4.3**) placed before the long-pass filter. The waveplate (W2) and polarizer (P2) were removed and the pump power was adjusted by the first waveplate (W1). The polarization of the second harmonic light entering the PMT was selected by an additional polarizer placed between the filters (short-pass filter and spike filter in a lens tube) and the PMT inside the Faraday cage. The top and side views of the SHG detection apparatus are shown in **Figure 4.33**.



Figure 4.33 Top view and side view of the new SHG detection apparatus. An additional polarizer was included between the filters (short-pass filter and spike filter in a lens tube) and the PMT (inside the Faraday cage) to select a certain polarization of second-harmonic light.

In this experiment, two samples were tested; PCBS1 GNRs deposited on (PAH/PCBS)₃PAH film and PCBS1 GNRs deposited on (PAH/PSS)₃PAH film. These samples were chosen because the enhancement of SHG signal from the nanorods was highest among the samples as discussed in **Section 4.7**. The pump energies for SHG measurement were 700 μJ for ISAM films and 70 μJ for nanorods, and corresponding fluence was 0.25 J/cm^2 and 0.025 J/cm^2 . The fundamental beam was either p- or s-polarized and the SHG beam was either p- or s-polarized for each case of the fundamental polarization. Therefore, four different combinations of SHG intensity were measured between 0° and 80° incident angles. The SHG intensities were not normalized by pump intensity detected by the photodiode because of the significant difference in pump power readings in the oscilloscope for p- and s-polarized beams.

4.8.1 GNRs on PAH/PCBS ISAM Film

The results for the bare $(\text{PAH/PCBS})_3\text{PAH}$ film and the sample containing PCBS1 GNRs deposited on $(\text{PAH/PCBS})_3\text{PAH}$ are shown in **Figure 4.34** and **Figure 4.35**, respectively. For the bare PCBS film, as shown in the plot (a), only p-polarized incoming pump light interacted with PCBS chromophores to generate p-polarized SHG light.

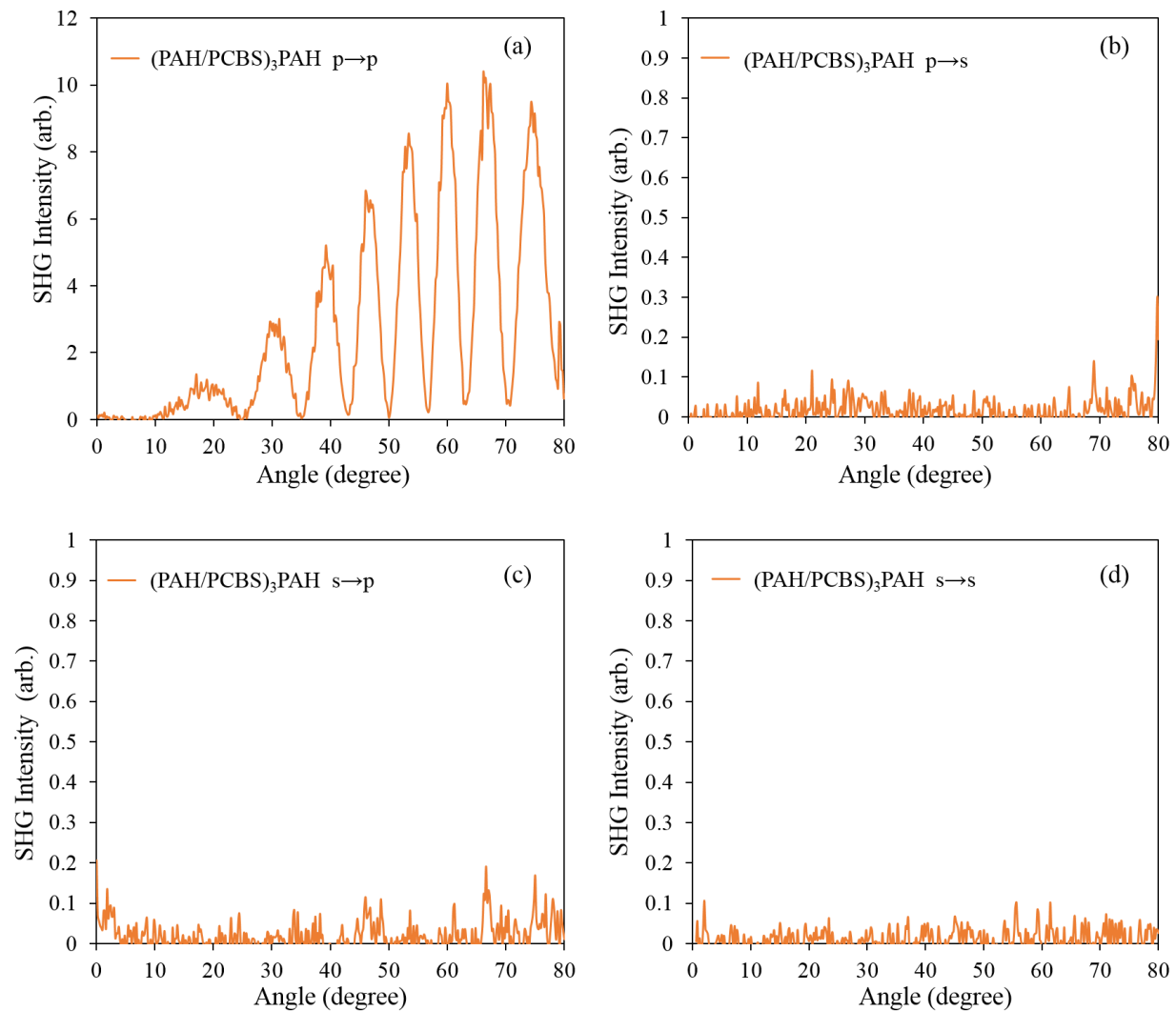


Figure 4.34 SHG intensity of $(\text{PAH/PCBS})_3\text{PAH}$ film for different fundamental and second-harmonic polarizations. (a) p-polarized fundamental light and p-polarized SH light, (b) p-polarized fundamental light and s-polarized SH light, (c) s-polarized fundamental light and p-polarized SH light, and (d) s-polarized fundamental light and s-polarized SH light.

For PCBS1 GNRs deposited on (PAH/PCBS)₃PAH film, both p- and s-polarized pump beams generated p-polarized SHG light. The results are displayed in **Figure 4.35a** and **Figure 4.35c** which show the SHG intensity generated from nanorods by p-polarized pump light and s-polarized pump light, respectively.

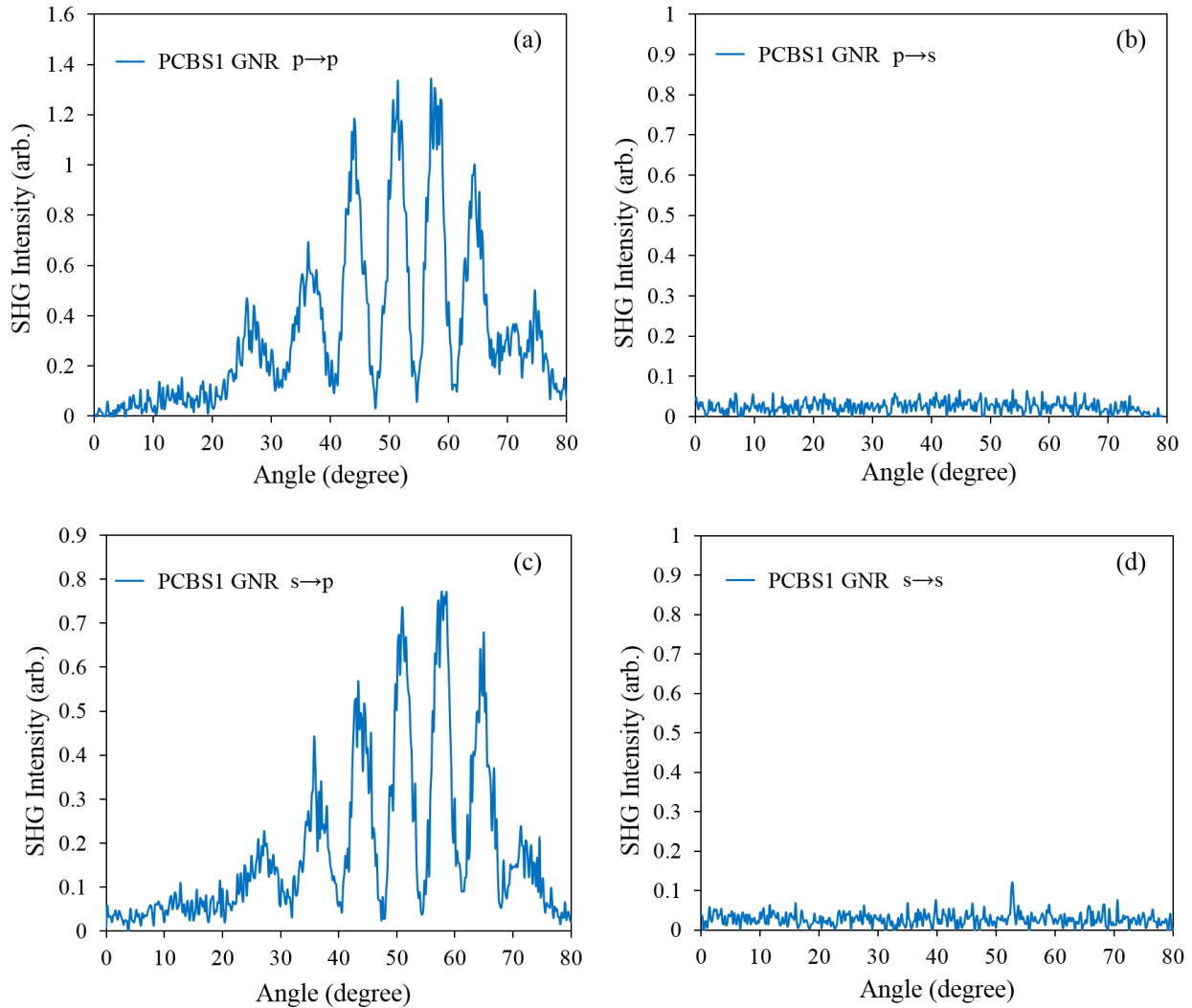


Figure 4.35 SHG intensity of PCBS1 GNRs deposited on (PAH/PCBS)₃PAH film for different fundamental and second-harmonic polarizations. (a) p-polarized fundamental light and p-polarized SH light, (b) p-polarized fundamental light and s-polarized SH light, (c) s-polarized fundamental light and p-polarized SH light, and (d) s-polarized fundamental light and s-polarized SH light.

4.8.2 GNRs on PAH/PSS ISAM Film

Similar to the case of PCBS film, only p-polarized incoming pump light generate p-polarized SHG light for 3.5 bilayer PAH/PSS film, as shown in the plot (a) of **Figure 4.36**. However, the SHG intensity from the PSS film was smaller compared to that from the PCBS film in **Figure 4.34a** due to weak SHG light generated at the film-air interface where the inversion symmetry is broken.

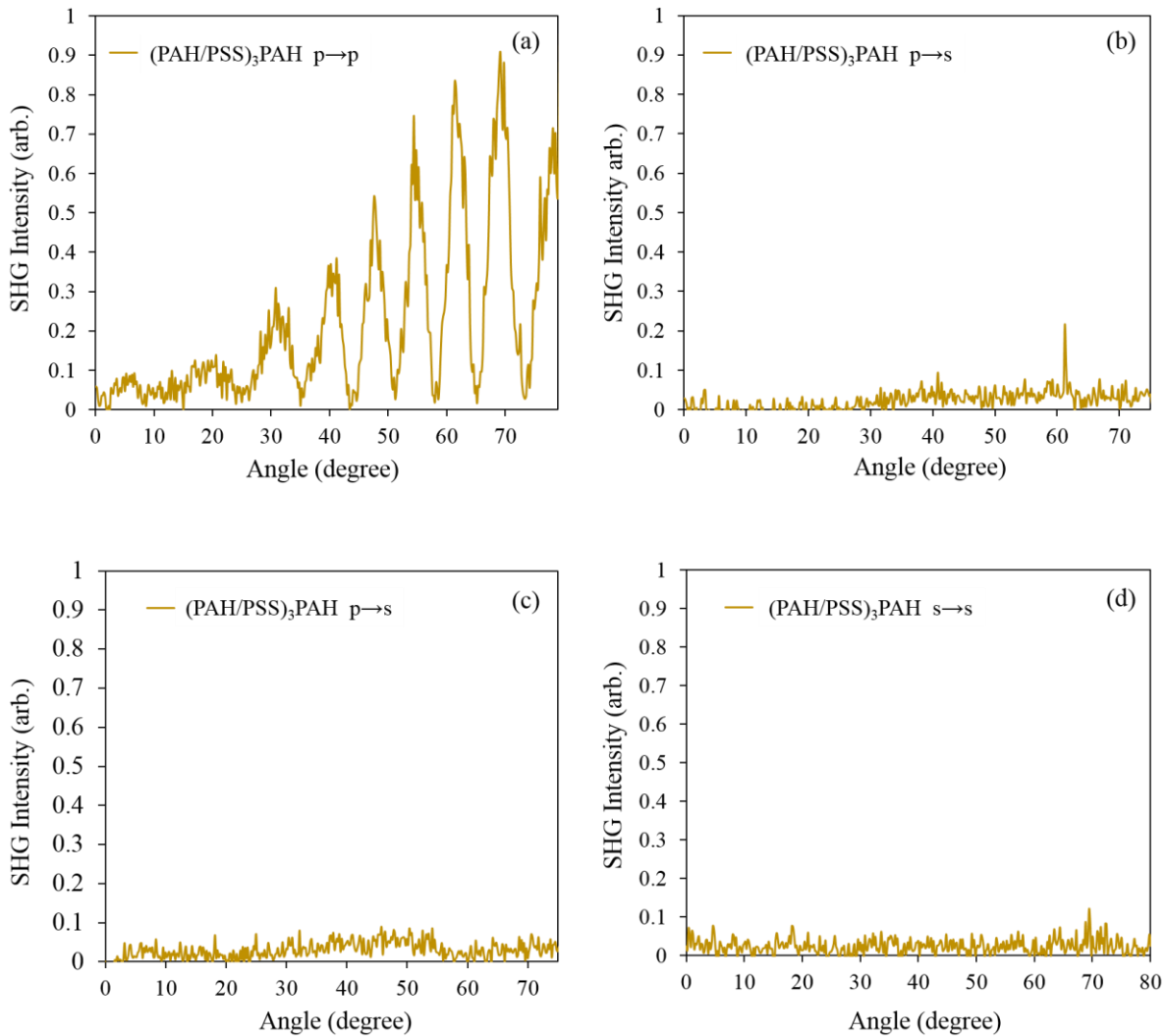


Figure 4.36 SHG intensity of (PAH/PSS)₃PAH film for different fundamental and second-harmonic polarizations. (a) p-polarized fundamental light and p-polarized SH light, (b) p-polarized fundamental light and s-polarized SH light, (c) s-polarized fundamental light and p-polarized SH light, and (d) s-polarized fundamental light and s-polarized SH light.

For PCBS1 GNRs deposited on (PAH/PSS)₃PAH film, both p- and s-polarized pump beams generated p-polarized SHG light same as the case of PCBS1 GNRs deposited on (PAH/PCBS)₃PAH film. The plots in (a) and (c) of **Figure 4.37** show the SHG intensity generated from nanorods by p-polarized pump light and s-polarized pump light, respectively.

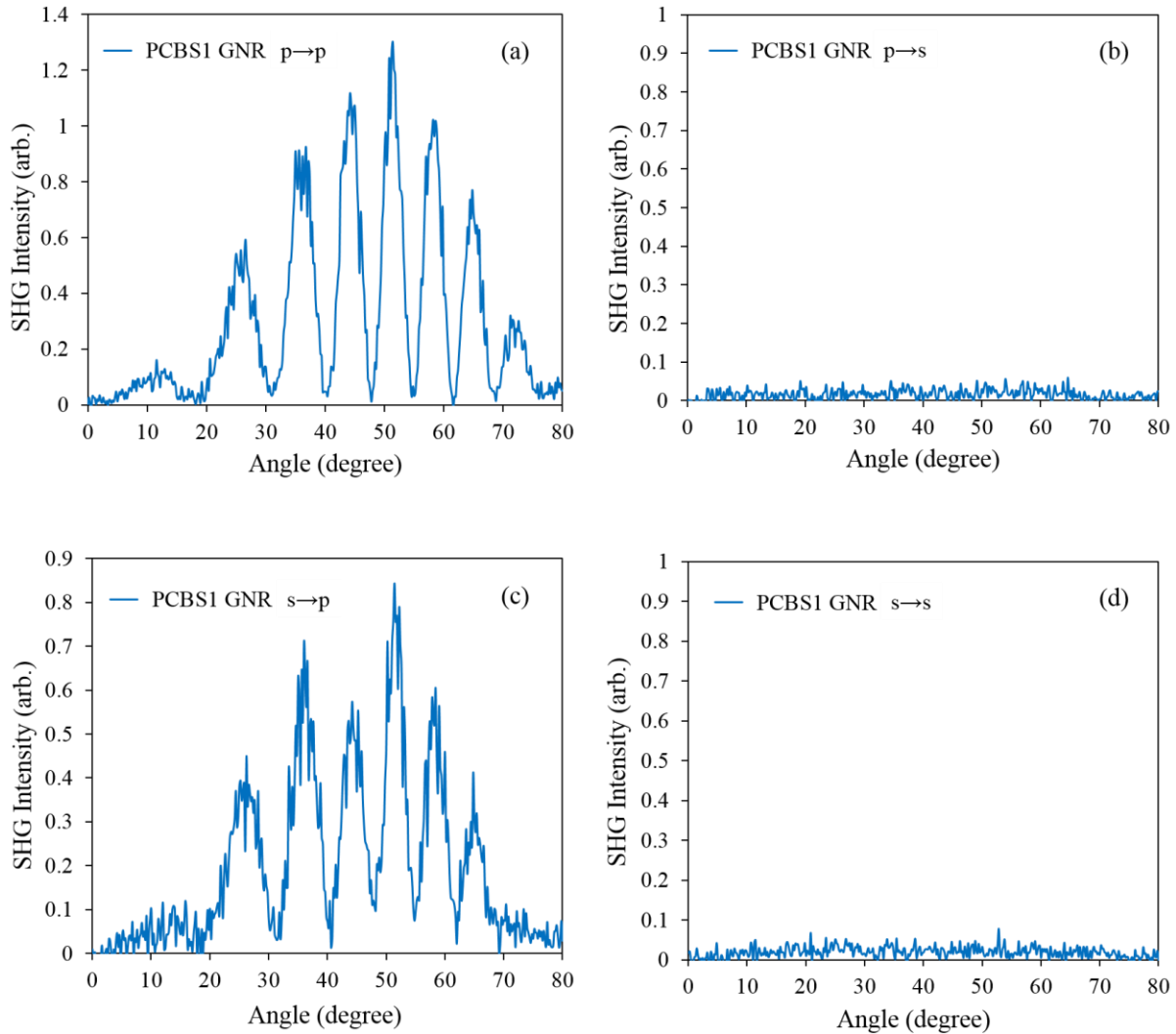


Figure 4.37 SHG intensity of PCBS1 GNRs deposited on (PAH/PSS)₃PAH film for different fundamental and second-harmonic polarizations. (a) p-polarized fundamental light and p-polarized SH light, (b) p-polarized fundamental light and s-polarized SH light, (c) s-polarized fundamental light and p-polarized SH light, and (d) s-polarized fundamental light and s-polarized SH light.

4.8.3 Summary of Polarization Dependent SHG Measurement

The results of the polarization dependent SHG measurements clearly show that only p-polarized second harmonic light is generated from both (PAH/PCBS)₃PAH and (PAH/PSS)₃PAH films with or without GNRs. For orientation of the chromophore dipoles perpendicular to the substrate, the s-polarized component of the second harmonic intensity vanishes when the fundamental beam is p- or s-polarized.¹² Therefore, this is in agreement with the uniaxial systems of C_{∞v} symmetry group with the axis perpendicular to the plane of substrate. The nonlinear optical susceptibility tensor d_{IJK} for the point group C_{∞v} is given by

$$d_{IJK} = \begin{pmatrix} 0 & 0 & 0 & 0 & d_{15} & 0 \\ 0 & 0 & 0 & d_{15} & 0 & 0 \\ d_{31} & d_{31} & d_{33} & 0 & 0 & 0 \end{pmatrix}. \quad (4.5)$$

By applying Kleinman symmetry, $d_{15} = d_{31}$, therefore there are only two independent coefficients, d_{31} and d_{33} .

The polarized pump light incident to the ISAM film is illustrated in **Figure 4.38a**. The PCBS chromophore dipoles are in the plane of incidence to which s-polarized light is perpendicular. Therefore, only p-polarized pump light can be coupled with the chromophore dipoles. However, the relative contribution of the interface SHG and the bulk SHG will differ depending on the thickness of the ISAM film. In thicker films (~ 40 bilayers), there is an average tilt angle in the bulk chromophores and thus the s-polarized incoming light contributes to the p-polarized SHG signal. Here, the ISAM film was only 3.5 bilayers and the SHG contribution was from the air-film interface.

The fact that s-polarized pump light can generate second-harmonic response from gold nanorods can be explained by considering arbitrary deposition of nanorods on the substrate. As can be seen in **Figure 4.38b** some of the nanorods can be oriented in such a way that PCBS chromophores on the nanorod tip are directed out of the page. Also in these nanorods, longitudinal surface plasmon resonance modes oscillate into and out of the page. Therefore, the s-polarized pump light can interact with the PCBS chromophores on the nanorod tip to generate SHG which is plasmonically enhanced by the longitudinal mode of nanorods.

Since the plots in **Figure 4.35** and **Figure 4.37** were normalized neither by pump intensity nor the nanorod density, comparison of corresponding subplots in these figures is not appropriate. However, since the pump power used here was the same in comparison to the plots (a) and (c) in the same figure is appropriate. Given a randomly oriented nanorod distribution on the film, the SHG intensity from nanorods should be generated equally from either s- or p-polarized pump light. However, the measured SHG intensity by p-polarized incoming light is about 38% higher. This may be partially attributed to different Fresnel reflections and transmissions for s- and p-polarized incident light at the air-glass interfaces. As is well known, the envelope of the measured SHG interference fringe directly depends on the Fresnel coefficients as a function of both incident polarization and incident angle.

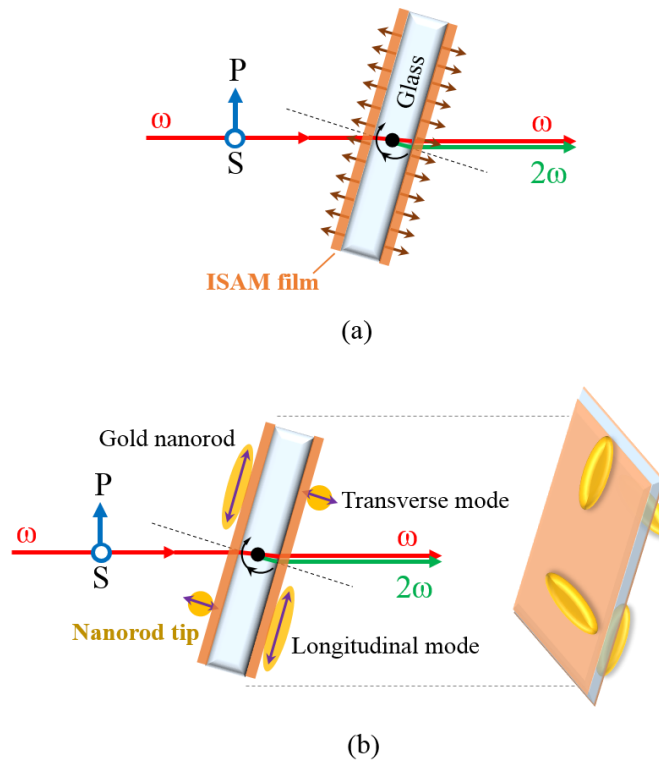


Figure 4.38 Illustration of fundamental and second-harmonic light passing through the substrate containing (a) ISAM film without nanorods and (b) with nanorods. Arrows on the surface of the substrate in (a) indicate the chromophore dipoles perpendicular to the substrate surface. Gold nanorods in (b) have longitudinal and transverse resonance modes indicated with arrows and dots. P-polarized light is vertical and s-polarized light is out of the page.

References

1. Maker, P. D., Terhune, R. W., Nisenoff, M. & Savage, C. M. Effects of Dispersion and Focusing on the Production of Optical Harmonics. *Phys. Rev. Lett.* **8**, 21–22 (1962).
2. Jerphagnon, J. & Kurtz, S. K. Maker Fringes: A Detailed Comparison of Theory and Experiment for Isotropic and Uniaxial Crystals. *J. Appl. Phys.* **41**, 1667–1681 (1970).
3. Bechthold, P. S. Ph.D. dissertation. (Universität Köln, 1976).
4. Herman, W. N. & Hayden, L. M. Maker fringes revisited: second-harmonic generation from birefringent or absorbing materials. *J. Opt. Soc. Am. B* **12**, 416 (1995).
5. Abe, M., Shoji, I., Suda, J. & Kondo, T. Comprehensive analysis of multiple-reflection effects on rotational Maker-fringe experiments. *J. Opt. Soc. Am. B* **25**, 1616 (2008).
6. Park, D. H. & Herman, W. N. Closed-form Maker fringe formulas for poled polymer thin films in multilayer structures. *Opt. Express* **20**, 173 (2012).
7. Boyd, R. W. *Nonlinear optics*. (Academic Press, 2008).
8. Verbiest, T., Clays, K. & Rodriguez, V. *Second-order nonlinear optical characterization techniques: an introduction*. (CRC Press, 2009).
9. Link, S., Burda, C., Mohamed, M. B., Nikoobakht, B. & El-Sayed, M. A. Laser Photothermal Melting and Fragmentation of Gold Nanorods: Energy and Laser Pulse-Width Dependence. *J. Phys. Chem. A* **103**, 1165–1170 (1999).
10. Chang, S.-S., Shih, C.-W., Chen, C.-D., Lai, W.-C. & Wang, C. R. C. The Shape Transition of Gold Nanorods. *Langmuir* **15**, 701–709 (1999).
11. Zdanowicz, M. *et al.* Ordered multilayer silica-metal nanocomposites for second-order nonlinear optics. *Appl. Phys. Lett.* **103**, 251907 (2013).
12. Kajikawa, K., Kigata, K., Takezoe, H. & Fukuda, A. Second Harmonic Generation from Langmuir-Blodgett Films in Various Optical Geometries. *Mol. Cryst. Liq. Cryst. Inc. Nonlinear Opt.* **182**, 91–101 (1990).

Chapter 5

Conclusions and Future Work

This dissertation described the fabrication of NLO-functionalized gold nanorods whose second harmonic generation (SHG) conversion efficiencies are larger than in conventional ISAM films and the measurement of SHG from these gold nanorods to demonstrate plasmonic enhancement. As is well known, the second harmonic intensity increases quadratically with the intensity of the fundamental wave. By matching the fundamental wavelength (1064 nm) of the laser to the resonant wavelength of the localized surface plasmon resonance of the nanorods, it was possible to obtain a high SHG intensity via surface plasmons up to 115 and 500 times from the nanorods deposited on 3.5 bilayer PAH/PCBS and PAH/PSS film, respectively, compared to the bare films.

In the preliminary study using PSS-coated gold nanorods on NLO-active ISAM film, there was no enhancement of SHG in comparison with the SHG signals from the ISAM film. It was demonstrated in the previous work¹ done in our group using silver nanotriangles on ISAM film that the longitudinal surface plasmon resonance (LSPR) modes can penetrate only about 3 – 4 nm. Therefore, the lack of SHG enhancement from the PSS-coated nanorods may be due to the thick layer of CTAB bilayer (3.4 nm)² and PSS (~ 0.5 nm) on the nanorods. A follow-up study on interface effects of SHG³ also revealed that only the top few bilayers of the NLO films took advantage of plasmonic enhancement. Hence, a direct attachment of nonlinear chromophores to the surface of nanorods was considered and a comprehensive method of nanorod surface modification using an NLO-active polymer (PCBS) was studied.

Gold nanorods were synthesized via the seed-mediated method with hydroquinone reduction to yield their LSPR peak around 1100 nm. Due to the shifts towards the near-infrared region by surface modification and towards the visible range after nanorod deposition on ISAM film, the resonance peak of gold nanorods in suspension was chosen using insight from repeated trials. The

resonance peak was tuned by adjusting the silver ion content. It was observed experimentally that an increase of the silver nitride concentration led to a redshift of the LSPR mode up to a certain point.

In order to replace a thick CTAB bilayer with a thin dithiocarbamate (DTC) anchored PAH layer, CTAB-coated nanorods were dialyzed for more than a day. Functionalization of gold nanorods was performed via the Layer-by-Layer method by alternating PAH and PCBS. In consideration of the decay length of LSPR modes, up to 3 bilayers of PAH/PCBS were adsorbed on the nanorod surface.

The last step of sample fabrication was the deposition of PCBS-functionalized gold nanorods on NLO-active (PCBS) and NLO-inactive (PSS) ISAM films. ISAM films were fabricated using PAH as the polycation and either PCBS or PSS as a NLO-active polyanion and a NLO-inactive polyanion, respectively. An in-depth study regarding the concentration of functionalized nanorod solution and the nanorod density was also conducted. It was found that diluting of nanorod solution caused a better coverage of nanorods on the film surface. The deposition was performed by the immersion (dipping) method in which the ISAM films were dipped into a small beaker containing different types of PCBS-functionalized gold nanorods: PCBS0, PCBS1, PCBS2, and PCBS3 GNRs, which had zero, one, two, and three layers of PCBS on the nanorods. Characterization of the samples was done using a reflectometer for spectrum measurement and DLS (dynamic light scattering) for zeta potential measurement. FESEM images showed how the nanorods deposited on the ISAM film and the corresponding surface density. Depositing the PCBS0 GNRs onto PAH/PCBS ISAM films was consistently difficult and the resulting low nanorod density samples did not enhance SHG.

The SHG measurement was conducted by a Maker-like fringe setup using a 1064 nm Nd:YAG laser as a fundamental light source. Various optical components were included and tested to ensure a proper polarization of pump light and a detection of the SHG signal via a PMT. Due to the large electrical noise generated by the laser power supply, a variety of noise reduction techniques, such as ferrite beads and a Faraday cage, were explored and applied to the optical setup. Even so, the low pump energy threshold of the SHG measurement of gold nanorods made it difficult to observe detectable signals from the PMT. By using a preamplifier to amplify the signal from PMT, it was

possible to perform ensemble averaging to extract the signal embedded in the noise pattern. A LabVIEW program was written for data acquisition and signal processing. A signal processing sub-function removed the DC bias from the oscilloscope and performed ensemble averaging for at least 50 waveforms from the oscilloscope. Finally, the SHG intensity for each angle step was then displayed on the front panel.

Since even a slight difference in thickness of the substrate (glass slide) can affect the angular position of the fringe maxima, a comparison of SHG intensity between nanorods on ISAM film and the bare ISAM film was made by the SHG data obtained from the same substrate. For this reason, the ISAM films were created on the glass slide first and then immersed into a gold nanorod solution that covered 2.5 cm from one end of the substrate. Samples were mounted in a rotational stepper motor which rotated the samples to change the angle between the incoming pump light and the plane of incidence of the samples. A small portion of the pump light was split to a photodiode to monitor the pump power, which was used to normalize the SHG intensity. Polarization of the incoming light was fixed at p-polarization for all measurements except for the polarization dependent measurement conducted in the last part of this dissertation. A large enhancement was achieved when the pump fluence for nanorods was 0.012 J/cm^2 . For ISAM films, it was necessary to increase the pump fluence and it was chosen to be 0.12 J/cm^2 .

The normalized SHG signal from PCBS-functionalized nanorod samples were compared to that from the bare 3.5 bilayer ISAM film. Due to a substantial SHG from the PCBS film, the enhancement from the gold nanorods deposited on a $(\text{PAH/PCBS})_3\text{PAH}$ film were not as large as from the nanorods deposited on a $(\text{PAH/PSS})_3\text{PAH}$ film. Nevertheless, the SHG enhancement was 105, 65, and 8 times from PCBS1, PCBS2, and PCBS3 nanorods deposited on a 3.5 bilayer PAH/PCBS film and 450, 600, 500, and 220 times from PCBS0, PCBS1, PCBS2, and PCBS3 nanorods deposited on a 3.5 bilayer PAH/PSS film.

There were two distinct features of the SHG interference fringe from the nanorods. First, the shape of the envelope was rather symmetric with the maximum envelope around 50° , while the envelope of the ISAM film peaked around 60° . Second, the SHG intensity fringe showed a 180° phase shift compared to the case of ISAM film. In order to fully understand these phenomena, it is necessary to look into the full SHG intensity formula and investigate it carefully. The extension

of this formula to include the effects of plasmon coupling to the nanorod deposition layers is not trivial. However, the difference in $\chi_{eff}^{(2)}$ value and the Fresnel transmittance coefficients between PCBS film and gold nanorods are likely key factors.

To investigate chromophore dipoles on nanorods, a polarization dependent SHG measurement was conducted. The polarization of incoming light was adjusted by using a polarizer and an additional polarizer was added right before the PMT to select the polarization of interest. The combination of polarizations from incoming light to SHG light was (p-p), (p-s), (s-p), and (s-s), where (p-p) denotes p-polarized incoming light and p-polarized SHG light measured. From this experiment, three observations were made. The first one was rather obvious and expected. In the case of both ISAM film and nanorods, only p-polarized SHG light was measured. Since it was implied that the overall orientation of the chromophores is perpendicular to the substrate, s-polarized component of the SHG intensity vanishes with either p- or s-polarized fundamental light. Thus, this follows the uniaxial systems of $C_{\infty v}$ symmetry group with the axis perpendicular to the plane of substrate. The second observation was more interesting. In the case of the nanorods, both p- and s-polarized pump light generated p-polarized SHG. For the not so obvious case of s-polarized incoming light, it can be understood by considering the randomly oriented nanorods on the film. It is likely that the PCBS chromophores at the ends of the nanorod may align in the same direction as the s-polarized light, generating a non-zero p-polarized SHG signal. Lastly, due to the random orientation of the nanorod distribution on the film, the SHG intensity due to the s-polarized pump light should be comparable to the SHG from the p-polarized pump light. However, the SHG generated from the p-polarized light was about 38% higher than the case with s-polarized light. This may be due to the difference in Fresnel coefficients between s- and p-polarized incident beams at the air-glass interfaces.

To improve the SHG efficiency and understanding of the enhancement, several ideas are suggested here. First, it has been proven that the SHG signal from the PMT is larger for a sample with a higher nanorod density. Therefore, a study of how nanorod density affects the SHG intensity would be very useful. Secondly, it is important to match the LSPR of nanorods on the ISAM film close to the pump wavelength to achieve maximum enhancement. However, since the LSPR mode is very sensitive to the surrounding dielectric medium, it is not easy to control the LSPR mode on

the film. Instead of tuning the resonance peak of the nanorods, tuning the fundamental wavelength may be more controllable by using a tunable laser, such as Ti:sapphire, more commonly used in nonlinear plasmonics. Another possibility is to include an optical parametric oscillator (OPO) in the current SHG measurement setup, but the free-space alignment is not a trivial task in this case. Lastly, bilayers and multilayers of gold nanorods by self-assembly would be an interesting study to investigate the trend of SHG intensity and number of gold nanorod bilayers. A similar study was conducted by Zdanowicz et al.^{4,5} where metal-silica nanocomposites were fabricated by alternating layers of pure silica and silica nanoparticles coated with silver nanodots. They demonstrated that the SHG intensity increases with the number of nanocomposite layers.

References

1. Chen, K., Durak, C., Heflin, J. R. & Robinson, H. D. Plasmon-Enhanced Second-Harmonic Generation from Ionic Self-Assembled Multilayer Films. *Nano Lett.* **7**, 254–258 (2007).
2. Gómez-Graña, S. *et al.* Surfactant (Bi)Layers on Gold Nanorods. *Langmuir* **28**, 1453–1459 (2012).
3. Chen, K. *et al.* Interface effects in plasmon-enhanced second-harmonic generation from self-assembled multilayer films. *J. Opt. Soc. Am. B* **27**, 92 (2010).
4. Zdanowicz, M. *et al.* Ordered multilayer silica-metal nanocomposites for second-order nonlinear optics. *Appl. Phys. Lett.* **103**, 251907 (2013).
5. Zdanowicz, M. *et al.* Second-harmonic response of multilayer nanocomposites of silver-decorated nanoparticles and silica. *Sci. Rep.* **4**, (2014).